

Numerical investigations of classical spin
models: the impact of lattice geometry,
confinement and long-range interactions

SUBMITTED BY

Marion Elizabeth Brooks-Bartlett

FOR THE DEGREE OF

Doctor of Philosophy

SUPERVISED BY

Dr Simon T. Banks and Prof Björgvin Hjörvarsson
and Prof Steven T. Bramwell

University College London, 2015

This thesis is dedicated to my Adonai Eloheinu.

Du har räddat mig

I, Marion Elizabeth Brooks-Bartlett confirm that the work presented in this thesis is my own. Where information has been derived from other sources, I confirm that this has been indicated in the thesis.

Abstract

This thesis addresses the nature of magnetic phases and phase transitions in a number of classical spin systems in which the magnetic behavior is governed by lattice geometry, the range of interactions and dimensional confinement.

The work presented here is underpinned by the use of classical Monte Carlo methods incorporating both long-range exchange and dipolar contributions to the magnetic Hamiltonian. These numerical simulations are used not only to test the theoretical concepts presented in this thesis, but also as a means for arriving at a more detailed understanding of the results of previous experimental studies.

Results are presented for a frustrated Ising model on a pyrochlore lattice (closely related to spin ice), along with studies of proximity effects in magnetic multilayers. The first of these systems reveal a previously unknown magnetic phase – a monopole crystal – which is shown to exist against a background spin liquid phase. The coexistence of these apparently mutually exclusive phases is shown to result from magnetic moment fragmentation. Studies of the proximity effect demonstrate the effects of magnetic induction at the interface between a single layer of a strong magnet and a thin layer of a weaker magnet. It is shown here that the transition temperature of both layers is enhanced by this interaction, with the effect in the stronger magnetic layer being a result of an increased effective thickness. Similar proximity effects are examined in the context of a magnetic trilayer exhibiting the exchange spring effect.

Contents

List of Figures	9
List of Tables	14
Symbols and Abbreviations	15
I Theory	21
1 Introduction	22
1.1 An overview of magnetic theory	22
1.2 The thermodynamics of phase transitions	29
1.2.1 Critical phenomena	32
1.2.2 Correlations and finite size effects	34
1.2.3 Fluid and magnetic phase transitions	36
1.3 Magnetic interactions	40
1.3.1 Mean field theory: no explicit interactions	41
1.3.2 Direct exchange interactions	44
1.3.3 Indirect exchange interactions	44
1.4 Classical spin models	47
1.4.1 Spin and spatial dimensionality	48
1.5 The impact of lattice geometry, spatial confinement and long range interactions	54
1.5.1 Magnetic multilayers	56

1.5.2 Frustrated spin systems	62
2 Spin ice background	69
2.1 The structure of spin ice	69
2.1.1 The pyrochlore and diamond lattice	69
2.1.2 Spin configuration in spin ice	71
2.1.3 Water ice to spin ice analogy	72
2.2 Other related spin systems	73
2.3 Dipolar interactions	74
2.3.1 The dumbbell model and magnetic monopoles	76
3 Monte Carlo simulations	82
3.1 Markov chain and Markov process	85
3.2 Ergodicity	86
3.3 Detailed Balance	86
3.4 Metropolis algorithm	87
3.5 Simulations of classical spin models on the pyrochlore lattice	89
3.5.1 Ewald summation	89
3.5.2 The Worm Algorithm	94
3.5.3 Autocorrelation functions	97
3.5.4 Neutron scattering and the Coulomb phase	98
 II Non-uniform finite systems with non-homogeneous interactions	 102
4 Magnetic monopole crystal	103
4.1 From the spin ice phase to a monopole crystal	103
4.2 Our analytical approach to the monopole crystal	104
4.3 Numerical results	107
4.3.1 Measuring the charge density	108
4.3.2 Spin and charge order parameters	111

4.3.3	Chemical potential – temperature phase diagrams	114
4.3.4	Analytical investigation of the monopole crystal	119
4.3.5	Simulated magnetic neutron scattering	120
4.3.6	Spin and charge autocorrelation functions	122
4.3.7	Susceptibility as a function of temperature	127
4.4	Experimental relevance	131
4.4.1	Applying a multiaxial external magnetic field	131
4.4.2	Quantum spin liquids	133
4.4.3	Pressure and lattice distortions	135
4.4.4	The kagomé system	136
5	Double proximity effect in magnetic multilayers	140
5.1	The proximity effect and long range interactions	140
5.2	Experimental relevance to simulations	142
5.3	Simulating further range exchange interactions	145
5.3.1	Comparing nearest neighbour and further ranged exchange interactions in the $2d$ XY model	151
5.4	Proximity effect results: A two-way T_c enhancement in a ferromagnetic weak/strong coupled trilayer	157
5.4.1	Simulation results for a weakly coupled ferromagnetic slab	158
5.4.2	Simulation results for a strongly coupled ferromagnetic monolayer	161
5.4.3	Simulation results for the ferromagnetic weak/strong coupled tri- layer	162
5.4.4	Simulation results for the ferromagnetic weak/strong coupled mul- tilayer with more repeat units	174
5.4.5	Conclusion	181
6	Towards modelling the exchange spring effect	183
6.1	An indirect interaction in the trilayer	183
6.2	The exchange spring effect	185
6.3	Experimental background to simulations	188

6.4	Simulation details	190
6.4.1	Method 1- system developed using experimental details	191
6.4.2	Method 2- system developed using experimental results	195
6.5	Results and discussion	203
6.5.1	Method 1	203
6.5.2	Method 2	213
6.6	Conclusion	218
III Final remarks and perspectives		220
Appendices		225
A Code development summary		226
A.1	For chapter 4	226
A.2	For chapters 5 and 6	226
B Equilibration of the energy in Monte Carlo simulations		228
B.1	Equilibration in the modified spin ice system	229
B.2	Equilibration in the magnetic multilayer systems	230
C Neutron scattering theory		232
D Proximity effects in the strong/weak coupled trilayer: beyond the monolayer		236

List of Figures

1.1	Simple schematic of a magnetic moment in a one-electron atom	23
1.2	Order of transition behaviour	30
1.3	Generalised phase diagram of water	31
1.4	Finite size effects in the magnetisation and susceptibility	35
1.5	$M(H)$ for a ferromagnet and $p(\rho)$ for a fluid	36
1.6	$H(T)$ for a ferromagnet and $p(T)$ for a fluid	40
1.7	Landau free energy vs magnetisation for the $2d$ Ising system	43
1.8	Example spin structure resulting from Dzyaloshinskii-Moriya interactions	45
1.9	The Ising, XY and Heisenberg classical spin types	49
1.10	The $1d$, $2d$ and $3d$ hypercubic structure	50
1.11	Vortex pairs in the $2d$ XY system	53
1.12	An A/B multilayer system	57
1.13	The β_{eff} exponent as a function of film thickness	61
1.14	Geometrical frustration on an antiferromagnetic Ising triangle	62
1.15	The pyrochlore lattice	63
1.16	Kagomé, honeycomb and square lattices	65
1.17	Vertex types of square ice and kagomé ice	67
1.18	Pd/Fe trilayer used in artificial spin ice	67
2.1	The diamond lattice	70
2.2	A single tetrahedron demonstrating the two-in two-out configuration . .	72
2.3	Schematic of a spin to dumbbell model mapping	77
2.4	Magnetic monopoles in spin ice, artificial spin ice and real monopoles .	79

3.1	Schematic demonstrating the Ewald summation	90
3.2	Hexagonal spin flip loop in the pyrochlore system	95
3.3	Neutron scattering showing diffuse pattern for the spin ice state	100
4.1	Phase diagram for the spin ice, pyrochlore spin system	105
4.2	Zincblende structure	107
4.3	Density of charges vs reduced temperature for different reduced chemical potential, μ^*	109
4.4	Density of charges vs reduced temperature for higher temperatures	110
4.5	Monopole order parameter vs reduced temperature for different μ^*	113
4.6	Phase diagrams for the modified spin ice pyrochlore system	115
4.7	Finite-size scaling for the specific heat and susceptibility	118
4.8	Diffuse pattern of the simulated neutron scattering	121
4.9	Charge and spin autocorrelation functions at $\mu^* = 0.41$	124
4.10	Charge and spin autocorrelation functions at $\mu^* = 0.90$	125
4.11	Charge and spin autocorrelation functions at $\mu^* = 0.57$	126
4.12	Magnetic susceptibility as a function of the reduced temperature	128
4.13	Curie constant crossover for monopole crystal	129
4.14	Phase diagram for quantum spin liquids $\text{Yb}_2\text{Ti}_2\text{O}_7$ and $\text{Yb}_2\text{Sn}_2\text{O}_7$	135
4.15	Charge and spin order in the kagomé structure	137
4.16	Simulated magnetic neutron scattering of kagomé ice II phase	138
5.1	Amorphous and crystalline cubic structures	143
5.2	The unit cell of closed packed crystal structures	144
5.3	Schematic of the further ranged interactions used in the simulations	146
5.4	Using the same energy scale for NN and further ranged (FR) systems	149
5.5	Magnetisation vs temperature for a NN and FR $2d$ XY system	152
5.6	Spin stiffness vs temperature for NN and FR systems	153
5.7	Universality class of strongly coupled layer using magnetisation vs T/T_c for NN and FR systems	155

5.8 Power law relationship of critical temperature with range of interaction for $2d$ XY model	156
5.9 Critical temperature as a function of Co layer thickness	158
5.10 A general ABA (weak/strong/weak) coupled trilayer	159
5.11 Magnetisation for the A layer as a function of temperature and layer	160
5.12 Magnetisation for selected monolayers in the A layer vs temperature	161
5.13 Magnetisation for the B layer vs temperature (equivalent of figure 5.5)	162
5.14 Magnetisation for the ABA trilayer vs temperature and layer	164
5.15 Varying the interlayer coupling strength in the trilayer	165
5.16 B layer magnetisation with varying interlayer coupling strength and range	166
5.17 Increase in effective thickness of B layer	166
5.18 Magnetic induction in the A layer by analysis of A monolayers	168
5.19 Increased A layer thickness in ABA multilayer	169
5.20 $3d$ to $2d$ crossover in spin dimensionality of B layer	170
5.21 $3d$ to $2d$ crossover in B layer using Bloch's law	172
5.22 Magnetisation vs layer profiles for the trilayer with varying range of interactions	173
5.23 Critical temperature in the B layer as a function of range and interspecies coupling strength	174
5.24 An $ABABABA$ multilayer	175
5.25 Magnetisation profile of the multilayer with varying temperature and thickness	177
5.26 Magnetisation profile of the multilayer with varying temperature and interspecies coupling strength	178
5.27 Multilayer with more repeat units with varying thickness and coupling	180
6.1 SmCo/CoAlZr multilayer used in the experimental system	184
6.2 Exchange spring effect in a magnetic hard/soft trilayer	186
6.3 Characteristic hysteresis loop of the exchange spring effect	187

6.4	Coercive field of the soft, strongly coupled top layer with varying thickness of the soft, weakly coupled central layer	189
6.5	A general <i>BAC</i> (soft strong / soft weak/ hard strong) coupled trilayer	191
6.6	Magnetic moment of magnetic layer as a function of amount of non-magnetic dopant	192
6.7	Susceptibility for each component in the <i>BAC</i> trilayer	194
6.8	Average susceptibility for various intra- and interspecies coupling strengths and spin dimensionalities in the <i>BAC</i> trilayer	196
6.9	Induced magnetisation in the <i>A</i> layer as a function of temperature for varying intraspecies coupling strength	198
6.10	Varying the rate of decay of interactions, σ , in the <i>A</i> layer	199
6.11	Varying σ in the context of the trilayer	200
6.12	Induced magnetisation as a function of temperature for varying σ . . .	202
6.13	Confirming the bulk <i>A</i> critical temperature	204
6.14	Critical temperature as a function of <i>XY</i> layer thickness	205
6.15	Extent of magnetic induction in the <i>A/B</i> bilayer	206
6.16	Extent of magnetic induction in the <i>A/C</i> bilayer	207
6.17	Effect on the <i>B</i> layer upon varying the <i>A</i> layer thickness	209
6.18	Magnetisation profile for the <i>BAC</i> trilayer at different temperatures . .	210
6.19	Extent of magnetic induction in trilayer	211
6.20	Magnetisation in <i>A</i> layer with varying <i>A</i> thickness	212
6.21	Magnetic induction extent in <i>A</i> layer for different interaction ranges at fixed temperature	213
6.22	Magnetisation profiles for different temperatures and intraspecies coupling strengths	215
6.23	Magnetic induction in <i>A</i> layers for temperatures greater than $T_c(A)$ for different interaction ranges and intraspecies coupling strengths	216
6.24	$m(T)$ of the <i>B</i> layer with varying <i>A</i> layer thickness using method 2 . .	218
B.1	Energy equilibration in the modified spin ice system	229

B.2 Energy equilibration in the *ABA* multilayer system 230

B.3 Energy equilibration in the *BAC* multilayer system 231

D.1 Increased *B* layer thickness in *ABA* trilayer 237

List of Tables

1.1	β critical exponents for the hypercubic spin and spatial dimensionalities	51
-----	---------------------------------------------------------------------------------	----

Symbols and Abbreviations

Please note vector quantities are in bold font.

$\langle \dots \rangle$	Statistical average
$ \dots $	Absolute value
a	Lattice constant
B	Magnetic induction
b	Exponent in fitted equation (relating to Bloch's law)
C	Heat capacity
\mathcal{C}	Curie constant
c	Heat capacity per spin
\mathbf{D}_{ij}	Dzhaloshinskii-Moriya vector
D	Dipolar interaction
d	Spatial dimensionality
E	Energy
e	Electrical charge
F	Helmholtz free energy
FR	Further ranged interaction
G	Torque
G	Gibbs free energy
\mathcal{G}_c	Two-point spin correlation function
$g_{\mathcal{J}}$	Landé g-factor
g_s	g-factor = 2.0023
H	Magnetic field strength

H	Applied magnetic field <i>or</i> enthalpy
\mathcal{H}	Hamiltonian
\hbar	Planck's constant divided 2π
I	Current
J	Exchange coupling
J_{AA}	Intraspecies exchange coupling between species A and A
J_{AB}	Interspecies exchange coupling between species A and B
J_{eff}	Effective J for temperature scale comparing range of interaction
\mathcal{J}	Total angular momentum quantum number
K	Anisotropy term
k_B	Boltzmann constant
L	Dimension length of a system
l	Orbital angular momentum
\mathbf{M} and M	Magnetisation
\mathcal{M}_{ij}	Total field of a magnetic moment
m	Magnetisation per spin
m_e	Mass of electron
m_s	Secondary spin angular momentum quantum number
$m_{\mathcal{J}}$	Secondary total angular momentum quantum number
MCS/s	Monte Carlo Step per spin
MDG	Melko-den Hertog-Gingras spin ice ground state
N	System size/ total number of spins
N_d	Demagnetising tensor
n	Spin dimensionality <i>or</i> amount of single component substance
NN	Nearest neighbour
OP ^C	Order parameter normalised by number of magnetic charges
OP ^D	Order parameter normalised by number of diamond sites
P	Probability
p	Pressure
\mathbf{p}	Linear momentum

Q	Net magnetic charge on diamond sites
\mathcal{Q}	A certain physical quantity
q	General charge <i>or</i> monopole charge in units of $2\mu/a$
\mathbf{q}	Structure vector
r	Radius of current loop <i>or</i> sometimes distance between spins
r_c	“Cut off” range for FR interactions
r_{nn}	Distance between nearest neighbour spins
r_{ij}	Distance between two spins
S	Spin length <i>or</i> entropy
$S(\mathbf{Q})$	Magnetic scattering function
s	Spin angular momentum quantum number
\mathbf{s}_i	Spin vector of spin i
T	Temperature
T^*	Reduced T (chapter 4)
T'	Upper limit T for $2d$ behaviour (chapter 5)
T''	Lower limit T for $3d$ behaviour (chapter 5)
T_{BKT}	Berezinskii-Kosterlitz-Thouless temperature
T_c	Critical temperature
t	Time
t_{eq}	Equilibrium Monte Carlo time
t_{obs}	Observation Monte Carlo time
U	Internal energy
u	Magnetic moment
U_C	Coulomb energy
U_L	Landau energy
u_l	Magnetic moment dependent on orbital angular momentum
u_s	Magnetic moment dependent on spin angular momentum
V	General volume
\mathcal{V}_{ij}	Coulombic potential
V_m	Molar volume

v	Velocity
W	Width of magnetisation profile
$w_A(t)$	Probability that the system will be in a state A at time t
Z	Partition function
z	Coordination number <i>or</i> charge number
α	Heat capacity critical exponent
α_M	Madelung constant
β	Order parameter critical exponent <i>or</i> inverse temperature
β_T	Inverse temperature
Γ_s and Γ_c	Autocorrelation function for spin and charge, respectively
γ	Gyromagnetic ratio <i>or</i> response function critical exponent
Δ	Sublattice type
δ	Less than a monolayer of a material
κ_T	Compressibility dependent on T
μ	Chemical potential
μ_0	Permeability of free space
μ^*	Reduced chemical potential (chapter 4)
μ_B	Bohr magneton
ν	Correlation length critical exponent
ν_0	on-site Coulombic interaction
ξ	Correlation length
ρ	General density
ρ_m	Density of magnetic monopoles
σ	Varying parameter for power law (chapters 5 and 6)
σ_i	Pseudo spin i
τ	Reduced temperature
Υ	Spin stiffness
ϕ_i	Electrostatic potential for spin i
χ	Magnetic susceptibility
ω_L	Larmor frequency

Acknowledgements

I would like to thank my primary supervisors Simon Banks at UCL and Björgvin Hjörvarsson at Uppsala Universitet, for all their support and guidance concerning the projects I have been involved with during my PhD. Two different but complementary characters, both of whom have imparted a lot of knowledge and understanding in me (a four-year proximity effect, which continued far past my critical temperature!). Thank you Simon for continually believing in me and all the invaluable conversations we have had both academically and professionally. The coding would also have never been possible without you. Thank you Björgvin for working on my character and pushing me to think independently and thoroughly on my work and also for my numerous trips to Sweden, which has given me the chance to meet many people, learn a “lite Svenska” and develop my confidence.

Thank you to my secondary supervisor, Steven Bramwell, for all the advice, most importantly, for telling me to get on writing my thesis when you did. I have thoroughly enjoyed the time spent with you and your group – Laura, Jonathan and Michael – all the support and the socials. I am most grateful to Peter Holdsworth, Ludovic Jaubert, Adam Harman-Clarke and Simon Banks for my first paper. I am so privileged to have worked with you all and for the trip to the ENS Lyon that came with it (thanks Peter!).

Thanks to all the Hjörvarsson group in Ångströmlaboratoriet – the presentations on Mondays, the Friday Fika and all the jokes!– Avi Saini, Sebastian George and Aron Mirwald...! To my experimental counterparts: thank you for your patience Fridrik Magnus, we got there in the end with the exchange spring paper, thank you Unnar Arnalds

ACKNOWLEDGEMENTS

for the time spent on the asymmetric $2d$ Ising model (unfortunately I was unable to use it here) and a special thanks to Martina Ahlberg for taking the time to help me understand the proximity effect when I just started my PhD.

Thank you to all my many supporters in the UCL chemistry department! Thanks to those past and present in my office (okay so I gate-crashed the femtosecond laser group). Special thanks to Michael Parkes for the support. You may not have known it but I've really appreciated your encouragement; my precious Wei Wen – so many times we would be typing away in the early hours of the morning! Nafisa and Zainab Sharif – my cheerleaders for my presentations, Liz Read – thank you for looking out for me, it will not be forgotten! To my security guard friends who always had words of wisdom for me and I would not forget Dr Aisha Rahman – you have been a major inspiration in making me believe this is even achievable.

Thank you to Uppsala Universitet (for a STINT award) and UCL (for a UCL Impact award) for both funding my doctorate and the UCL Graduate school for funding one of the conferences I attended.

I have had so many people cheering me on, friends and family and it is impossible to fit them all here but financially and emotionally thank you to: my twin soon to be Dr Jonathan Brooks-Bartlett, Rochelle Brooks-Ford, Sonia Brooks, Cecelia Brooks, Rodney Williams, Kudra Nagingo (incl. Rayaana), Church of Pentecost international, Nathaniel Johnson, Ken Bartlett, Finn Wolfreys, Croydon Supplementary Education Project, Sangeeta Bhagat and TMAN. There are two that have carried me when I have been “paralysed” in this race to finish- my mother Jacqueline Brooks and Kwame Agyei Marfo. God knows how much I have needed you both, you have gone through all of the seasons and the roller coaster of emotions! Finally, thank you to my grandmother Christiana Brooks – I know you are rejoicing up there!

Part I

Theory

Chapter 1

Introduction

The magnetic properties of a magnetic system are generally dependent on three factors: 1) the direction of the magnetic moments of individual atoms/ions, 2) the magnitude of these magnetic moments and 3) the strength of interaction between the magnetic moments in the system. Spin models provide a framework within which the direction and interaction of magnetic moments (otherwise referred to as spins) may be described and quantified. With this information, one can model the magnetic behaviour of the system.

1.1 An overview of magnetic theory

A moving charge is an electric current and one travelling in a circular motion forms a current loop, which yields a magnetic field. The field produced from the charge moving around in a current loop of radius, r , and current, I , is otherwise known as a magnetic moment, u_l , expressed as,

$$u_l = I\pi r^2 \tag{1.1}$$

with the units A m^2 (see figure 1.1). This is the magnetic moment found for a current generated by one electron orbiting a fixed centre of mass, however, this becomes more complex for many-electron systems. In the subsequent account, I provide a brief summary of the theory of magnetism. The reader is referred to Blundell [1] and Kittel [2] for a more in-depth explanation.

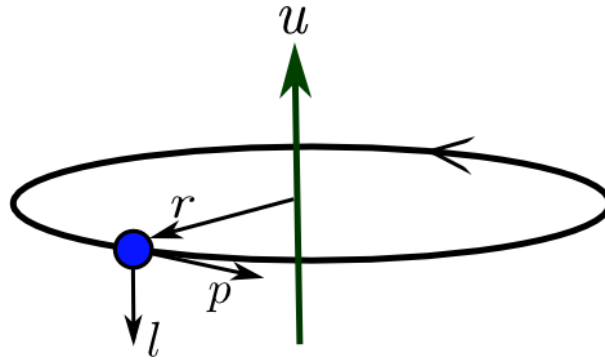


Figure 1.1: A simple schematic of a magnetic moment produced from a single electron (light blue circle) orbiting a nucleus. Also indicated are the vectors of the electron: the angular momentum, \mathbf{l} , the linear momentum, \mathbf{p} and the instantaneous position \mathbf{r} .

An electron in motion around a nucleus, has an angular momentum. From a classical perspective, the angular momentum \mathbf{l} is defined by the cross product of the linear momentum, \mathbf{p} and the instantaneous position \mathbf{r} :

$$\mathbf{l} = \mathbf{r} \times \mathbf{p} = \begin{vmatrix} i & j & k \\ x & y & z \\ p_x & p_y & p_z \end{vmatrix},$$

This is such that \mathbf{l} is perpendicular to the plane that the electron is rotating in. The magnetic moment is also perpendicular to the plane of rotation and it can be deduced that the angular momentum and the magnetic moment are associated. The magnetic moment of the electron is antiparallel to the angular momentum and directly proportional according to the relationship:

$$u_l = \gamma l \quad (1.2)$$

where γ is the gyromagnetic ratio and is negative due to the negative charge on an electron.

Upon substitution of $I = q/t$ into equation 1.1, where $t = 2\pi r/v$, another classical definition of the angular momentum, $l = m_e v r$ can be substituted to obtain the

following expression:

$$u_l = I\pi r^2 = -\frac{e}{2m_e}l \quad (1.3)$$

for an electron of electrical charge, $-e$, and mass m_e moving in a circular orbit around a nucleus assumed to be stationary. From equations (1.2) and (1.3), an expression for the gyromagnetic ratio can be obtained:

$$\gamma = -\frac{e}{2m_e}. \quad (1.4)$$

In quantum mechanics, the magnitude of the quantised orbital angular momentum is given by $l = \sqrt{l(l+1)}\hbar$ so that $u_l = -\frac{e}{2m_e}\sqrt{l(l+1)}\hbar$. This gives rise to another quantity known as the Bohr magneton, μ_B , so that,

$$u_l = -\sqrt{l(l+1)}\mu_B \quad (1.5)$$

$$\mu_B = \frac{e\hbar}{2m_e}. \quad (1.6)$$

The Bohr magneton, μ_B , is used as a unit to describe the size of a magnetic moment. Its definition is the magnitude of the magnetic dipole moment of an orbiting electron with a quantised angular momentum of \hbar and has the value $\mu_B = 9.2732 \times 10^{-24} \text{ A m}^2$ [3].

The orbital angular momentum is fixed along an axis $m_l\hbar$, where m_l can take the values $l, l-1, \dots, -l$. The m_l states are degenerate until some perturbation is applied such as a magnetic field in what is known as the Zeeman effect. This effect was key in discovering spin angular momentum, which is described later in the text.

Before considering the effect of an applied magnetic field on a magnetic moment, it is important to note the subtle difference in the magnetic induction, \mathbf{B} , in units of Tesla, and the magnetic field strength, \mathbf{H} , in units of A m^{-1} . When in a vacuum state, these quantities only differ by a constant $\mu_0 = 4\pi \times 10^{-7} \text{ H m}^{-1}$, which is the permeability of free space. However, for a magnetic solid, \mathbf{H} is the driving magnetic influence from external currents in a material independent of the material response, whilst \mathbf{B} is characterised by currents in the material and externally that generate a

magnetic field. Therefore in a magnetic solid, \mathbf{B} and \mathbf{H} are related by,

$$\mathbf{B} = \mu_0(\mathbf{H} + \mathbf{M}) \quad (1.7)$$

where \mathbf{M} is the magnetisation, which plays a major role in the projects in this report, and is defined as the magnetic moment per unit volume.

The energy, E , of a magnetic moment in a field \mathbf{B} is,

$$E = -\mathbf{u} \cdot \mathbf{B} \quad (1.8)$$

The magnetic moment couples to the magnetic field and precesses about it, consequently possessing a torque \mathbf{G} that is given by:

$$\mathbf{G} = \mathbf{u} \times \mathbf{B}. \quad (1.9)$$

The torque is equal to the rate of change of angular momentum and hence the magnetic moment must precess about the magnetic field as this allows the angular momentum to change direction without changing its magnitude. Therefore, the magnetic moment does not tend toward the magnetic field \mathbf{B} but precesses around it with an angle, θ and Larmor frequency, ω_L ,

$$\omega_L = \gamma \mathbf{B} \quad (1.10)$$

Had there been no angular momentum, the magnetic moment would have tended towards the magnetic induction \mathbf{B} , though it is only a non-uniform magnetic field that can exert a force on a magnetic moment.

It is very important in ferromagnets that the applied magnetic fields are distinguished from the internal fields of the magnetic solid. If the applied magnetic fields are defined by \mathbf{B}_a and \mathbf{H}_a , then these fields applied to a magnetic solid will not be the same magnitude as those within the solid \mathbf{B}_i and \mathbf{H}_i , since the magnetic moments within the solid would produce their own magnetic field and vary in the solid. To correct for this requires the demagnetising tensor, N_d , so that

$$\mathbf{H}_i = \mathbf{H}_a - N_d \mathbf{M} \quad (1.11)$$

where $-N_d\mathbf{M} = \mathbf{H}_d$ is the demagnetising field, and

$$\mathbf{B}_i = \mathbf{B}_a + \mu_0(1 - N_d)\mathbf{M} \quad (1.12)$$

The demagnetising field refers to a source of magnetisation which forms perpendicular to the plane of magnetisation within the material, particularly if there is some anisotropy. This is accounted for by N_d , which is a matrix that is dependent on the shape of a material.

To further develop an understanding of magnetic theory one needs to take into account that an electron possesses another momentum other than the orbital angular momentum. This intrinsic angular momentum is known as “spin” and is the point where classical theory meets quantum theory.

The spin component, s , can take the values $m_s\hbar$, where m_s is between s , $s - 1$, ..., $-s$. Therefore the intrinsic spin angular momentum is quantised just like the orbital angular momentum but it can additionally take half integer values. For an electron, $s = \frac{1}{2}$, so the possible orientation this spin could have is either $m_s = +\frac{1}{2}$ or $m_s = -\frac{1}{2}$. The electron also has an associated spin magnetic moment as shown in equation 1.13, but unlike γ in the $u_l = \gamma l$ relationship, the constant of proportionality between u_s and s is not easily calculated and must be obtained from experiment or relativistic quantum theory [4].

$$u_s = -\frac{g_s\mu_B}{\hbar}s \quad (1.13)$$

The constant is $-g_s\mu_B/\hbar$ where g_s is required as the g -factor for the spin and has a value of 2.0023 (independent of \mathbf{B}) [2, 5], making the constant almost twice as large as γ . However the g -factor can take various values when considered in many-electron atoms as shown below, due to the contributions of both L and S .

Spin-orbit coupling is when the spin and orbital angular momenta interact and the quantum number, J (denoted in this thesis as \mathcal{J}), can be obtained by $\mathcal{J} = |L + S|, |L +$

$S - 1, \dots, |L - S|$. The magnetic moment operator then becomes:

$$u = -\frac{g_{\mathcal{J}}\mu_B}{\hbar}\mathcal{J} \quad (1.14)$$

where the Landé g -factor, $g_{\mathcal{J}}$, is given by,

$$g_{\mathcal{J}} = \frac{3\mathcal{J}(\mathcal{J} + 1) + S(S + 1) - L(L + 1)}{2\mathcal{J}(\mathcal{J} + 1)} \quad (1.15)$$

(Note: the change to upper case letters for L and S is to take into account many-electron systems which consider the total of the angular momenta and spin momenta, respectively). The spin-orbit coupling gives rise to different $m_{\mathcal{J}}$ states, which take the values $\mathcal{J}, \mathcal{J} - 1, \dots, -\mathcal{J}$. However, in a zero magnetic field each state with a given value of \mathcal{J} is $(2\mathcal{J} + 1)$ -fold degenerate. Placing atoms into a uniform magnetic field, will perturb the $(2\mathcal{J} + 1)$ -fold degenerate ground states into non-degenerate $m_{\mathcal{J}}$ states known as anomalous Zeeman splitting.

Only the electrons in the outer electron shell contribute to whether an atom/ion is magnetic, as these may have net angular momenta[†]. For the systems described in this thesis, the ions have uncompensated spins (unpaired electrons) and hence have a non-zero magnetic moment. This is characteristic of paramagnets and ferromagnets.

In a paramagnet there is a tendency for the magnetic moments to align parallel to an applied field in order to minimise the energy and maximise the overall magnetisation. However, this tendency to align competes with thermal disorder and hence there is an inverse relationship of the magnetic susceptibility, χ_T (a response function of a magnet) to the temperature [6]. When the applied field is removed, the net magnetisation falls to zero again.

A ferromagnet has a spontaneous magnetic moment even in the absence of an applied magnetic field, which is known as the saturation moment, and this occurs because of the exchange interaction, J , otherwise thought of as the exchange field. The exchange

[†]Considering materials in the absence of an applied magnetic field.

interaction is a consequence of the symmetrisation postulates of the electron wavefunctions, the Pauli exclusion principle (i.e. that no two electrons can have the same quantum numbers) and the concept of electrostatic interactions between two charges (i.e. same sign charges cost energy being in close proximity to one another and cost less energy when further apart) [7]. To describe electron exchange in atoms, one must know that the wavefunction of a set of electrons consists of a spatial and spin part. For example, taking the simple case of two electrons (i.e. fermions), electron 1 and electron 2 with spatial and spin identities a and b will have the overall wavefunction $\Phi(a, b) = \Phi(r_1 s_1, r_2 s_2) = \phi_1(a)\phi_2(b)$. Swapping the electrons must cause a change in the sign of the total wavefunction of the pair of electrons since for fermions, the overall wavefunction must be antisymmetric with respect to the exchange of identical fermions. Therefore, $\Phi(a, b) = -\Phi(b, a)$. The pair of electrons with spins s_1 and s_2 , both with a value of one half, have an overall spin, S , which can either be $S = s_1 + s_2$ or $S = s_1 - s_2$, which gives $S = 1$, a triplet state, or $S = 0$, a singlet state. Singlet states are antisymmetric and triplet states are symmetric. Therefore, since the overall wavefunction must be antisymmetric and the singlet state has an antisymmetric spin state $S = 0$, then its spatial part must be symmetric, and a triplet state has a symmetric spin state $S = 1$, hence it must have an antisymmetric spatial state. Taking the difference of the energy for these two states decides which spin state is preferred in a crystal by [1]:

$$J = \frac{E_S - E_T}{2} \tag{1.16}$$

where E_S and E_T are the energy of the singlet and the triplet states, respectively. Though equation 1.16 has been determined in a two electron case, the equation and understanding applies for many-electron systems, as long as the total wavefunction of the many-electron system is antisymmetric under exchange coupling.

According to equation 1.16, for $E_S < E_T$, then $J < 0$ and the singlet state is preferred, which means that the spins align antiparallel to one another to obtain a zero net magnetisation and the system is known as an antiferromagnet. If $E_S > E_T$ such that $J > 0$, then the triplet state is favoured so the spins remain aligned spontaneously

as is the case for a ferromagnet, with the electrons in different orbitals. Interorbital spin exchange dynamics has only recently been observed experimentally for the first time using ultracold ^{173}Yb fermions [8].

1.2 The thermodynamics of phase transitions

Phase transitions are discussed extensively throughout this thesis and therefore this section is dedicated to introducing the key concepts.

A phase is a homogeneous state [9] whereby all its physical properties are uniform throughout. A material undergoes a phase transition from one phase to another when the thermodynamic densities change [10]. Thermodynamic densities are, e.g. the molar volume, the entropy and the thermodynamic potentials (U , G , F and H), which are defined later in this section. Variation in the thermodynamic fields (e.g. temperature and pressure) does not imply a phase transition has occurred, rather these quantities determine if a system is in thermal equilibrium. There are two types of phase transition as classified by Ehrenfest (1880-1933): first order or second order transitions [11]. These are distinguished by identifying which order of derivative of the Gibbs free energy with respect to either the temperature or pressure, has a discontinuity.

The differential of G is given by:

$$dG = -SdT + Vdp + \sum \mu dn \quad (1.17)$$

where μ is the chemical potential of a single component and n is the amount of this component. Taking the first derivative of G with respect to T or p gives,

$$S = -\left(\frac{\partial G}{\partial T}\right)_{p,n} \quad \text{and} \quad V = \left(\frac{\partial G}{\partial p}\right)_{T,n} \quad (1.18)$$

and the second derivatives are known as the response functions – the heat capacity C_p and the isothermal compressibility κ_T :

$$C_p = -T\left(\frac{\partial^2 G}{\partial T^2}\right)_{p,n} \quad \text{and} \quad \kappa_T = -\frac{1}{V}\left(\frac{\partial^2 G}{\partial p^2}\right)_{T,n} \quad (1.19)$$

For first order transitions, the discontinuity occurs in the first derivative of the free energy at a specific temperature, whilst the discontinuity occurs in the second derivative of the free energy for second order transitions at the critical temperature. Knowing this, the first and second order phase transitions can be identified and summarised by figure 1.2.

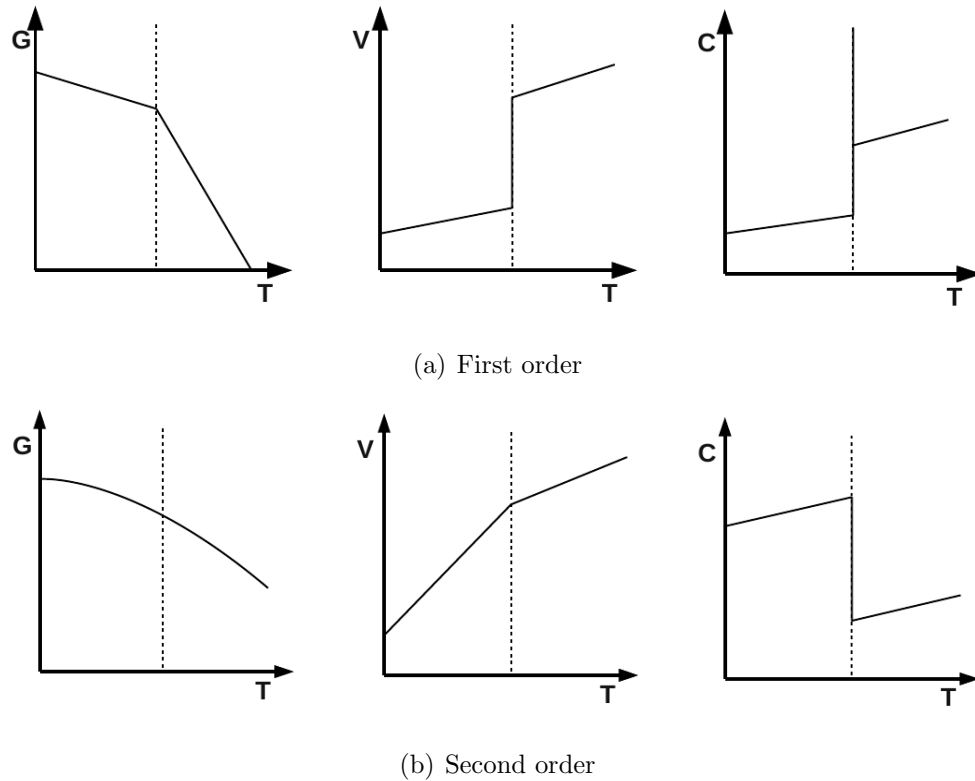


Figure 1.2: First (a) and second (b) order behaviour:- Gibbs free energy, G , volume, V and heat capacity, C , as a function of temperature. These properties are effectively zeroth, first and second order derivatives of the Gibbs free energy, respectively. Images replicated from reference [11].

The two types of phase transition are more appropriately described as discontinuous or continuous rather than first and second order. This is because Ehrenfest's description only takes into account the discontinuities in thermodynamic potentials and not the divergences recognised in continuous, critical transitions [12]. A discontinuous transition corresponds to shifting from one local minimum in the Gibbs potential to another

corresponding to distinct states in the thermodynamic space. This is in contrast to a continuous transition where the two states are neighbouring in thermodynamic space. This can be represented on a plot of the Gibbs potential vs molar volume as shown in the insets of figure 1.3.

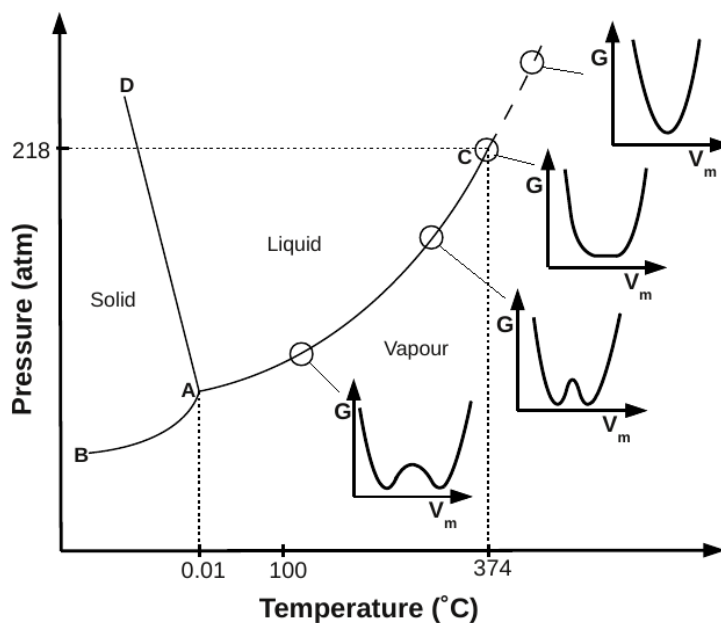


Figure 1.3: Phase diagram of water (pressure vs temperature) showing the three states- solid, liquid and gas. The coexistence line $A-B$ represents a line of sublimation/ deposition transitions, $A-D$ represents a line of melting/ freezing transition and $A-C$ represents condensation/ evaporation transitions. Point A is the triple point, where all three phases coexist, whilst point C is the critical point. The transitions along the $A-C$ line are first order. Beyond the critical point C , the system is in the single supercritical phase. The insets show plots of the Gibbs free energy vs molar volume corresponding to (p_i, T_i) along the $A-C$ coexistence line, indicated by round circles.

It is easier to describe these transitions using the phase diagram of water as shown in figure 1.3. Crossing the coexistence line between the liquid and gas phase of water corresponds to a first order phase transition. Either side of the coexistence curve one of the minima is lower in energy corresponding to the more stable phase. Increasing

the temperature and pressure along the liquid-gas coexistence line (along the direction $A \rightarrow C$ in figure 1.3), a decrease in the separation of local minima of the Gibbs free energy is observed so that the two states are closer in the thermodynamic configuration space. Point C is a critical point where the two minima coalesce, such that the two-phase coexistence terminates and is represented in a plot of the Gibbs-molar volume in figure 1.3 with a flat-bottomed single minimum. This demonstrates that there is no restoring force from the critical state [13] (since force $\propto (\partial G/\partial V_m)$) and hence divergent fluctuations are observed for this second order transition. Beyond the critical point, there is a theoretical single minimum where the coexistence line is extrapolated [13] and is shown in figure 1.3 representing the one-phase supercritical fluid.

1.2.1 Critical phenomena

Critical phenomena are exclusive to second order phase transitions and arise due to the flattening of the thermodynamic potential at the critical point. The phenomena encompass the fact that thermodynamic functions become singularities at the critical temperature leading to interesting properties of the system.

Theories developed by Lev Landau [14] lead the way when discussing phase transitions and though all were not quantitatively true, because of deviations from classical theory, the concepts are still pillars in the field. Landau recognised that all second order transitions should have an order parameter (OP), which is zero at high temperatures and non-zero at low temperatures ($0 \leq \text{OP} \leq 1$) [13]. In the liquid-gas transition, the order parameter commonly chosen to be the density difference $\rho - \rho_c$ where ρ is the density and ρ_c is the critical density, whilst the order parameter in magnetic systems is the magnetisation [15]. The order-disorder transition occurs at the critical temperature, T_c , which as previously shown has a flattened critical isotherm in the plot of G vs V_m and a divergence in the second derivatives of the Gibbs potential (response functions). Another way of identifying when the critical temperature is reached, is when the order parameter of the system becomes zero. For a magnetic material, this is when the spontaneous magnetisation becomes zero as a function of T at zero applied field.

For magnetic systems, the order parameter $M(T)$, the heat capacity $C(T)$ and the susceptibility $\chi(T)$ can be described by power laws in the vicinity of a critical point. The power law corresponding to each physical property is listed below. These equations describe the divergence in C , χ and ξ (the correlation length) and the vanishing of the magnetisation, m (lower case m is used conventionally for discussing numerical methods, which is the magnetisation per spin explained further in chapter 3).

$$\xi = |\tau|^{-\nu} \tag{1.20}$$

$$\chi = |\tau|^{-\gamma} \tag{1.21}$$

$$C = |\tau|^{-\alpha} \tag{1.22}$$

$$m = |\tau|^\beta \tag{1.23}$$

$$m = |H|^{1/\delta} \tag{1.24}$$

Here h is the magnetic field and τ is the reduced temperature given by:

$$\tau = \left| \frac{(T - T_c)}{T_c} \right|. \tag{1.25}$$

Hence, $\tau = 0$ implies $T = T_c$. All the relationships of the thermodynamic quantities to the critical exponents are the same whether approaching T_c from above or below except β whereby the relationship only holds for $T < T_c$.

These exponents give rise to a classification for systems at critical points, known as the universality class. The universality class is determined by the space-time dimension and the symmetries of the order parameter [16], i.e. the spatial and, for magnetic systems, spin dimensionality of the system. For instance, section 1.4.1 includes a table of β values, which are used to determine the universality class of a system. The ability

to classify different systems into the same universality class is independent of their macroscopic thermodynamics but is rather based on the statistical mechanical concept of correlations, discussed in the next section.

1.2.2 Correlations and finite size effects

The correlation between spins can be described by the two-point spin correlation function, \mathcal{G}_c ,

$$\mathcal{G}_c = \langle \mathbf{s}_i \mathbf{s}_j \rangle - \langle \mathbf{s}_i \rangle \langle \mathbf{s}_j \rangle \quad (1.26)$$

where \mathbf{s}_i and \mathbf{s}_j are the spin vectors of spin i and neighbouring spin j , separated by a distance r_{ij} . As indicated, this is averaged for all pairs of spins in the system. To lower the energy, in a ferromagnet for example, spins will generally align and hence be strongly correlated [9]. However, the entropy above the critical temperature of a ferromagnet opposes this and the correlation length of the spins, ξ , is finite. When the critical temperature is approached from high temperatures the system prepares to order from the disordered state and once T_c is reached there is no typical length scale of the correlation length and hence in the thermodynamic limit, the correlation length diverges. ξ diverges by the power law shown in equation 1.21, which has consequences for the susceptibility as described below. In a ferromagnet, ξ becomes finite again at temperatures below T_c as ξ measures the distance over which deviations occur from the spontaneous magnetisation [17].

The susceptibility is proportional to the two-point spin correlation between spins, as shown in equation 1.27 [18], where $\beta_T = 1/k_B T$ (conventionally denoted as β).

$$\chi \sim \beta_T \mathcal{G}_c. \quad (1.27)$$

Since ξ diverges at the critical temperature with an inverse power law rather than decaying exponentially with distance, the correlations at all length scales are equally important ensuring χ also diverges.

Finite size effects occur when the critical fluctuation of spins diverge in a finite size system, such that $L < \xi$, where L is the dimension length of the system. For temperatures far from T_c this effect is not a problem since generally $L > \xi$ [12]. Figure 1.4 shows the consequences of finite size effects. There is a pronounced curvature of the order parameter for $T > T_c$, shown in figure 1.4 (a) in a plot of M vs T , whilst the quantities mentioned in section 1.2.1, which would usually diverge, demonstrate a “cut off” and a small shift in the peak at T_c (figure 1.4 (b)).

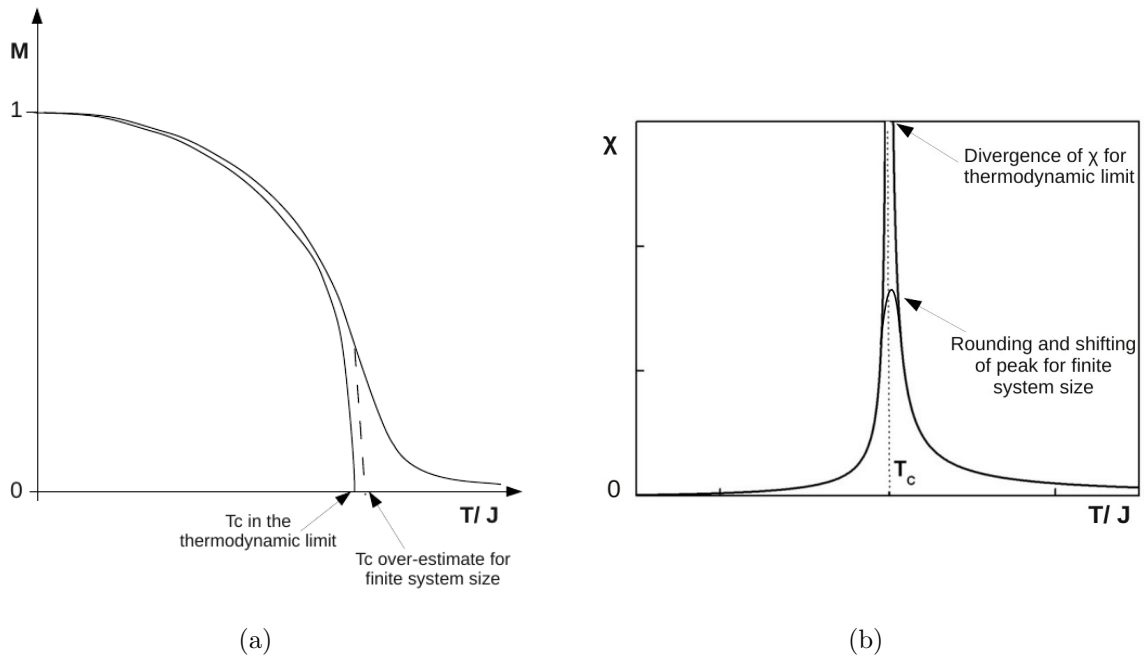


Figure 1.4: A schematic of critical behaviour in finite systems compared with the thermodynamic limit. The “curved tail” in (a) the magnetisation and the “cut off” in the divergence of (b) the susceptibility as a function of temperature are artefacts of finite size effects. Figure 1.4 (b) is a modified image from reference [19].

The scenario of an infinite system size, where the instabilities of the energy of the system become negligible [20], is known as the thermodynamic limit. There is no suppression of the divergence in the thermodynamic quantities when $L \approx \xi \rightarrow \infty$. The effects of finite size may be manifest in experimental systems where the thermodynamic limit is not experimentally accessible. However much of the time experimental systems

do exist in an effective thermodynamic limit and representing such systems in numerical simulations is a challenge. The best method of mitigating finite size effects is to obtain results for the thermodynamic quantities for increasing system sizes (linearly in dimension L) and extrapolate for $L = \infty$ [12]. This is known as finite size scaling.

1.2.3 Fluid and magnetic phase transitions

There exist magnetic analogues of the thermodynamic relations familiar to us from studying fluid systems. The comparison between the thermodynamics of magnetic and fluid systems is particularly clear when considering pressure versus density and magnetisation versus field isotherms (see figure 1.5). These isotherms will be explained later in this section.

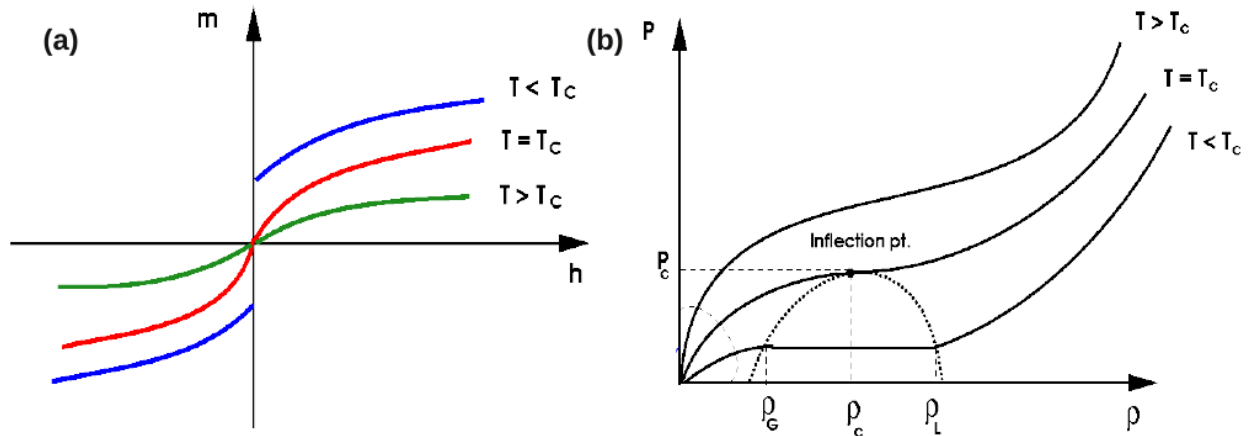


Figure 1.5: The critical behaviour in (a) a ferromagnetic-paramagnetic phase transition and (b) a liquid-gas transition where ρ_G is the gas density, ρ_L is the liquid density and ρ_c and p_c are the critical density and pressure, respectively. Isotherms in each figure are shown for temperatures above, at and below the critical temperature, T_c . There are very clear similarities between these systems with a discontinuous transition for $T < T_c$ and a continuous transition for $T = T_c$. Images are taken from reference [21].

The mapping [22],

$$p \rightarrow H \tag{1.28}$$

$$V \rightarrow -M \tag{1.29}$$

where p is the pressure exerted on the fluid system and V is the volume of the fluid system, provides a straightforward derivation of physical quantities for magnetic systems from their fluid analogues. For instance, the two thermodynamic potentials of most interest in this thesis are the Gibbs free energy, G and the Helmholtz free energy, F . In a one-component fluid system, the differentials of G and F are expressed as:

$$dG = -SdT + Vdp + \sum \mu dn \quad (\text{Gibbs free energy}) \tag{1.30}$$

$$dF = -SdT - pdV + \sum \mu dn \quad (\text{Helmholtz free energy}) \tag{1.31}$$

where n is the amount of the pure substance, μ is its chemical potential and S is the entropy. The decrease of the Gibbs and Helmholtz free energy indicate a spontaneous process both at constant temperature and at constant pressure or volume, respectively [23]. With the mapping in expressions 1.28 and 1.29, dG and dF in the magnetic analogy can easily be derived as,

$$dG = -SdT - MdH + \sum \mu dn \quad (\text{Gibbs free energy}) \tag{1.32}$$

$$dF = -SdT + HdM + \sum \mu dn \quad (\text{Helmholtz free energy}) \tag{1.33}$$

Other physical quantities which can be derived include the heat capacity and the isothermal and isentropic response functions. Rather than C_V and C_p in a fluid, these become C_H and C_M for a magnet; rather than the compressibilities, κ_T and κ_S , for a fluid, they become the susceptibilities, χ_T and χ_S , for a magnet.

In fluids, p and V have an inverse relationship, where a decrease in the volume increases the pressure. This is shown by κ_T ,

$$\kappa_T = -\frac{1}{V} \left(\frac{\partial V}{\partial p} \right)_T. \tag{1.34}$$

In contrast, an increase in the magnetic field applied to the system will cause a corresponding increase in the magnetisation in ferromagnetic systems. This is shown by the isothermal magnetic susceptibility, χ_T , which was discussed earlier,

$$\chi_T = \left(\frac{\partial M}{\partial H} \right)_T. \quad (1.35)$$

Note that the magnetic susceptibility is dimensionless with both \mathbf{M} and \mathbf{H} having SI units A m^{-1} . Sometimes the susceptibility is denoted as χ_v or χ_m to represent the volume or molar susceptibility, since the susceptibility is actually defined as the magnetic moment induced by a magnetic field \mathbf{H} per unit volume. There is much confusion in the literature with the use of \mathbf{B} instead of \mathbf{H} in the definition of χ . Use of \mathbf{B} would only be appropriate if in a vacuum, where $\mathbf{B} = \mu_0 \mathbf{H}$ and using cgs units, where μ_0 is unity, otherwise the SI units of \mathbf{B} are $\text{kg A}^{-1} \text{s}^{-2}$ and the substitution would not yield a dimensionless susceptibility.

There is another fluid-magnet mapping, given by [22]:

$$\rho - \rho_c \rightarrow M \quad (1.36)$$

$$\mu - \mu_c \rightarrow H \quad (1.37)$$

where ρ and μ are the density and chemical potential of the fluid system respectively and the subscript c indicates the respective property at the critical point. This is a more appropriate transformation, according to Stanley [24], as the chemical potential is the thermodynamic variable conjugate to the density (via the number of particles) and the density difference $\rho - \rho_c$ is the order parameter.

$M(H)$ and $p(\rho)$ isotherms

The order parameter, $\rho - \rho_c$, vanishes as $T \rightarrow T_c^+$ (to approach T_c with a decreasing temperature), such that $\rho \rightarrow \rho_c$. In this case,

$$\kappa_T = -\frac{1}{V} \left(\frac{\partial V}{\partial p} \right)_T \equiv \frac{1}{\rho} \left(\frac{\partial \rho}{\partial p} \right)_T. \quad (1.38)$$

The critical isotherm in a plot of ρ vs p (in figure 1.5 (b)) has a point of inflection and hence κ_T becomes infinite. The behaviour of the response function in the critical region can be expressed as

$$\kappa_T = (T - T_c)^{-\gamma} \quad (1.39)$$

which diverges when the critical exponent γ is greater than zero.

In the magnetic system, T_c can be approached from above or below, ($T \rightarrow T_c^+$ or $T \rightarrow T_c^-$ respectively) with χ_T expressed as,

$$\chi_T = (T - T_c)^{-\gamma} \quad (1.40)$$

when $H = 0$ and where χ_T diverges for $\gamma > 0$. This corresponds to the critical isotherm with a point of inflection in the plot of M vs H (in figure 1.5 (b)).

The isotherms for fluid and magnetic systems in the vicinity of a critical point are functionally similar (see figure 1.5). The liquid-gas transition is first order for the points on the coexistence curve ($T < T_c$), but at the critical point ($T = T_c$), the transition becomes second order, such that $\rho - \rho_c$ diminishes continuously. The order of transitions for the respective isotherms are the same for the magnetic system. When $T > T_c$ in a ferromagnet, the system is in the paramagnetic region and $M \propto H$ for small fields. When $T < T_c$, the material is magnetised even when $H = 0$ and this is the ferromagnetic region (see figure 1.6(a)). If a field is applied when the system is in this phase, then the magnetic moments will align with the field. When $T = T_c$, small fluctuations in the magnetic field, cause the susceptibility to become infinite because the correlation length has all length scales, hence a continuous phase transition at this temperature. The plot of $H - T$ for a ferromagnet in figure 1.6(a) is analogous to the $p - T$ curve for a fluid shown in figure 1.6(b).

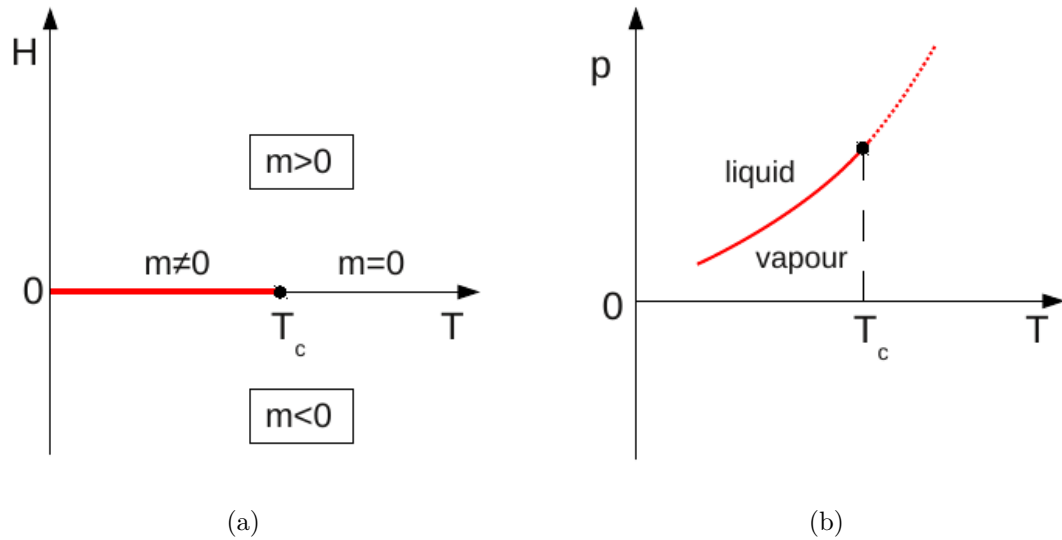


Figure 1.6: (a) H vs T for a ferromagnetic-paramagnetic phase transition and (b) p vs T for a liquid-gas transition. Below the critical temperature, T_c , both the magnetic and fluid system have a line of first order phase transitions. The point indicated at T_c is where this first order line terminates and second order phase transition occurs for $T = T_c$. In (a), the magnet has a spontaneous magnetisation ($m \neq 0$) for $T < T_c$ and $m = 0$ above T_c . For a non-zero applied magnetic field, the magnetisation is in the direction of the field ($m > 0$ or $m < 0$).

1.3 Magnetic interactions

The spins on a lattice can interact with each other in several ways. Examples include:- exchange interactions (otherwise known as J -coupling), which is via the electrons in bonds; dipolar interactions, caused by the magnetic moment of the spins being large enough to give rise to a sizeable dipole-dipole coupling; and Coulombic interactions, which consider the interaction between emergent magnetic charges that are formed in the lattice. Both dipolar and Coulombic interactions are direct (through space) and long ranged and will be discussed further in section 4.

Direct exchange interactions between nearest neighbours (NN), give rise to the simplest Hamiltonian that is used to evaluate the energy of a classical spin system. Equa-

tion 1.41 shows the conventional Heisenberg Hamiltonian, which is the energy for an isotropic spin system with zero applied magnetic field [25] and with the J term, representing the strength of interaction between the spins. In this case, the equation is presented such that $J < 0$ or $J > 0$ depending on whether the system is antiferromagnetic or ferromagnetic, respectively, as explained in section 1.1).

$$\mathcal{H} = -J \sum_{\langle ij \rangle} \mathbf{s}_i \cdot \mathbf{s}_j \quad (1.41)$$

The summation in the equation is over all nearest neighbour pairs of spins. Other Hamiltonians, such as dipolar, are developed from the NN exchange Hamiltonian.

1.3.1 Mean field theory: no explicit interactions

The transitions undergone by the systems studied in this thesis are generally second order, continuous, changing from an ordered ferromagnetic state to a disordered paramagnetic state or vice versa. Mean field theory is the earliest method used for describing such transitions [26] and is therefore a reasonable place to start. It is a simple method that does not directly consider fluctuations or correlations of spins in the system. Below is a brief example for the mean field theory for the Ising model, otherwise known as the Weiss molecular field theory [27].

Mean field theory can be described as an infinite dimensional approach [28] as all spins in the system experience an identical average exchange field produced by all the other spins in the system. It is, as a result, recursive in nature. Analytically, this approximation is shown starting with the Hamiltonian:

$$\mathcal{H} = -J \sum_{\langle ij \rangle} \sigma_i \sigma_j - H \sum_i \sigma_i \quad (1.42)$$

where $\sigma_i = \pm 1$ is the pseudo spin for spins i and σ_j , the pseudo spin of the neighbours, j . Pseudo spins can be used when describing Ising spins as these either have one of two orientations denoted by ± 1 . The applied magnetic field is given by H . At a certain

temperature the expectation value of the magnetisation, m , is given by:

$$\langle \sigma_i \rangle = m. \quad (1.43)$$

So that for a particular spin, σ_0 [27],

$$\mathcal{H}(\sigma_0) = -\sigma_0(zJm + H) - J\sigma_0 \sum_j (\sigma_j - m), \quad (1.44)$$

where z is the coordination number of σ_0 . Mean field theory neglects the terms which include correlations between neighbouring spins and so the second term of equation 1.44 is disregarded, hence giving rise to the approximation of the mean field. The intensive m is then simply equal to the average value of any given spin,

$$m = \langle \sigma_0 \rangle = \langle \sigma_j \rangle. \quad (1.45)$$

This assumes that the configurations of the spins do not deviate very much from the average or that sufficient spins contribute to the effective field so that individual spin fluctuations about the average cancel out. The average value of the magnetisation can then be shown as [28]:

$$m = \tanh \left[\frac{1}{k_B T} (zJm + h) \right]. \quad (1.46)$$

Weiss [29] was the first to propose mean field theory, which relates strongly to Landau's theory of phase transitions. Landau uses the Helmholtz free energy as a function of the order parameter in order to determine the magnetisation at different T when $H = 0$ [30]. This is achieved by describing the free energy in terms of a power series of m given by:

$$F(m) = F_0 + \alpha(T)m^2 + \beta m^4 + \dots \quad (1.47)$$

such that F_0 and β are constants and $\alpha(T)$ is dependent on T as indicated. The behaviour of $F(m)$ as a function of m for three different T at $H = 0$ is shown in figure 1.7, where the temperatures correspond to $T < T_c$, $T = T_c$ and $T > T_c$ (these are similar to the plots of G vs V_m shown in the insets of the water phase diagram in figure 1.3). When $T < T_c$, the system is said to have broken symmetry by which the spins in the system order in one of two preferential directions. These two configurations are

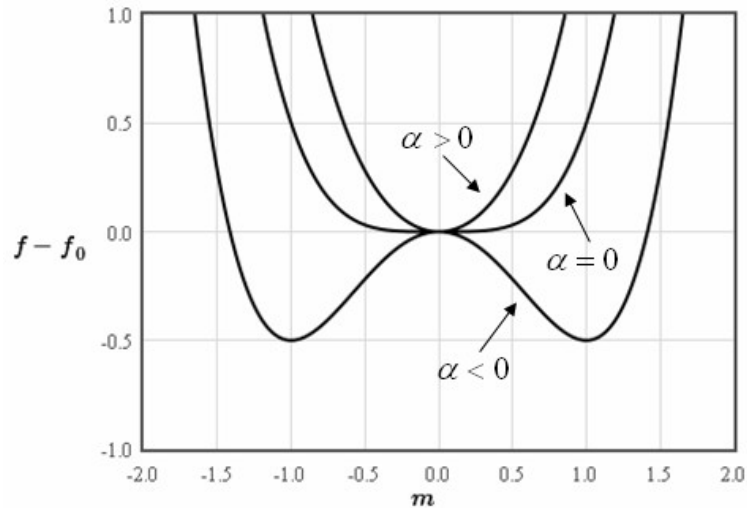


Figure 1.7: Landau free energy vs magnetisation for the $2d$ Ising system showing how α , a function of T , affects the free energy when $h = 0$. When $\alpha < 0$, the system has two minima, which correspond to two degenerate ordered states antiparallel to one another. When $\alpha = 0$, the minima coalesce to a single flat minimum with finite curvature. When $\alpha > 0$, a single minimum is obtained at $m = 0$, where the system is paramagnetic [31].

degenerate but the magnetisation is either positive or negative (i.e. either $-m(T)$ or $+m(T)$). Unlike the fluid example presented in section 1.2, the two degenerate phases cannot coexist. The sign of the magnetisation can easily be chosen by setting $H \neq 0$ in which case the spins will point in the direction dictated by the field.

When $T = T_c$, the minimum at $m = 0$ in figure 1.7 becomes broad and flat so that $(\partial^2 F / \partial m^2)_{m=0} \rightarrow 0$. This relates to equation 1.46 since only $m = \tanh[m]$ satisfies this condition and hence $T_c = zJ/k_B$. The critical temperature in the mean field approximation, therefore only depends upon the exchange constant and the coordination number of the lattice. The theory usually makes an over estimation of the critical temperature (due to the neglect of fluctuations) [30]. This can differ by up to a factor of 2 of the critical temperatures in low-dimensional systems [26]. The accuracy of the method increases with dimensionality and coordination number and is more appropriately applied further from the critical region [26].

1.3.2 Direct exchange interactions

The fundamental concept underlying nearest neighbour exchange interactions is the symmetry of the total wavefunction of electrons swapping either the spin or spatial part between electrons in neighbouring atoms (explained in section 1.1). For exchange interaction between atoms, it is more favourable to have a greater orbital overlap between two atoms and to form bonds. The concept of a particle in a box (PIB) can be used to rationalise this [1]. If the box in which a particle is able to move around is small, then the kinetic energy (and hence, the total energy of the system), is higher since energy is inversely proportional to the length of the box squared, L^2 . By creating a bond between the atoms, the energy is minimised since the size of the “box” in which a particle can move is larger and therefore the electrons can easily move between the two atoms.

A bonding molecular orbital is spatially symmetric and therefore singlet states are favoured such that spins preferentially align antiparallel to one another [1]. Antibonding molecular orbitals are spatially antisymmetric and less energetically favourable. Direct exchange is therefore most effective when there is sufficient orbital overlap between the atoms for bonding to occur and produce antiferromagnetism. However, in reality rare earth metals have poor orbital overlap whilst transition metals, though comparatively better than rare earths, do not always have sufficient orbital overlap also[1]. Therefore, indirect exchange interactions via itinerant electrons are more often considered.

1.3.3 Indirect exchange interactions

There are several models of indirect exchange interactions, however I will focus on the three most common: Superexchange, Ruderman, Kittel, Kasuya and Yosida (RKKY) and Dzyaloshinskii-Moriya (DM) interactions. DM and RKKY interactions are of particular interest when describing the form of interactions in magnetic multilayers (a system studied in chapter 5) [32–37]. The concept of superexchange is complimentary to DM interactions and therefore is introduced first.

Superexchange

Superexchange occurs as a consequence of non-neighbouring magnetic ions exchanging electrons via a mediating non-magnetic ion. This type of interaction usually enables antiferromagnetic coupling, such as in crystalline MnO, but can also mediate ferromagnetic coupling [1]. Once again, minimising the kinetic energy is key, but rather than effectively increasing L^2 as in direct exchange, this minimisation results from the ground state mixing with excited states, enabling the electrons to delocalise over the whole system. Superexchange is therefore dependent on the overlap of the orbitals of the non-magnetic ion with those of the magnetic ions and is why the angle of the Mn-O-Mn bonds are so important in determining the type of coupling in crystalline MnO.

Dzyaloshinskii-Moriya (DM)

DM interactions are similar to superexchange which also undergo a mixing of ground and excited states in an antiferromagnet. Rather than the interaction of a non-magnetic ion with a magnetic ion, DM interactions involve two adjacent magnetic ions which must have a broken space-inversion symmetry between them [38]. DM interactions arise due to spin-orbit interactions [39], where the strength of DM is linearly proportional to the spin-orbit coupling [40]. An excited state is produced by the spin-orbit coupling within one of the magnetic ions which then interacts with the ground state of the other magnetic ion via an exchange interaction. This is given the name anisotropic exchange or Dzyaloshinskii-Moriya.

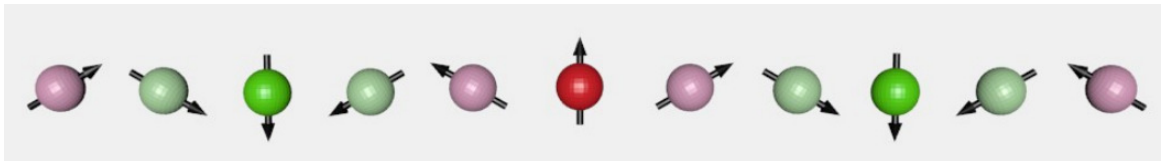


Figure 1.8: Schematic of a spin spiral generated from DM interactions. Image modified from reference [41].

DM interactions promote weak ferromagnetism, as the anisotropic term added to the conventional Heisenberg Hamiltonian is:

$$\mathcal{H}_{\text{DM}} = \sum_{\langle ij \rangle} \mathbf{D}_{ij} \cdot (\mathbf{s}_i \times \mathbf{s}_j) \quad (1.48)$$

which cants the spins perpendicular to the spin axis of an antiferromagnetic system [42]. The canting of spins results in a spin system with non-collinear magnetic order, known as a spin spiral (see figure 1.8). In equation 1.48, \mathbf{s}_i is the vector of the spin on magnetic ion i and \mathbf{s}_j is the vector of the spin on the neighbouring magnetic ion j and \mathbf{D}_{ij} is the DM vector. The DM vector is obtained from a combination of the second order perturbation of the spin-orbit coupling and the antiferromagnetic interaction, whilst its direction is determined by the symmetry of the crystal structure [43]. DM interactions particularly play a role when the inversion symmetry of the crystal is broken [39, 41], which is the case at the surface of a material (see section 1.5.1).

Ruderman, Kittel, Kasuya and Yosida (RKKY)

RKKY interactions occur via conduction electrons (otherwise known as itinerant electrons), which mediate the coupling between ions. A magnetic ion i polarises the conduction electrons, which in turn couple to/polarise a second magnetic ion j at a distance r_{ij} . The conventional Heisenberg Hamiltonian is modified as in equation 1.49 [44].

$$\mathcal{H} = \sum_{\langle ij \rangle} J(r_{ij}) \mathbf{s}_i \cdot \mathbf{s}_j = J_0 \sum_{\langle ij \rangle} \frac{\cos(2k_F r_{ij})}{r_{ij}^3} \mathbf{s}_i \cdot \mathbf{s}_j \quad (1.49)$$

where k_F defines the radius of the spherical Fermi surface (explained below).

The theory behind RKKY interactions in metals is based on the free electron model [1]. Electrons fill the energy levels in pairs of spin up and spin down until the Fermi energy level is reached, which is the highest occupied energy level at $T = 0$ K. In k -space, each energy level has a corresponding wavevector. The relationship of the energy of the Fermi energy level, E_F , to the maximum wavevector, k_F , is $E \propto k^2$. By knowing the wavevector, one can determine the density of states at the Fermi energy

level, $g(E_F)$, as given in equation 1.50.

$$g(E_F) = \frac{m_e k_F}{(\pi \hbar)^2} \quad (1.50)$$

Together, $g(E_F)$ and the occupancy of each of these states, $f(E)$, can be used to determine the value of the Fermi energy level.

When $T = 0$ K, the Fermi energy is equal to the chemical potential. As this is for the free electron gas model, the chemical potential relates to the number of electrons filling the energy levels. In real materials the value of the chemical potential determines whether the material is metallic, a semiconductor or an insulator. For a metallic material, there must be a set of points in k -space which have an energy equal to the chemical potential (the Fermi surface). The existence of a Fermi surface is therefore characteristic of a metallic material.

Since RKKY interactions take place in metallic materials and occur via itinerant electrons, it is not surprising that the coupling strength is related to the Fermi surface (where the Fermi sphere has a diameter $2k_F$):

$$J_{\text{RKKY}}(r) \propto \frac{\cos(2k_F r_{ij})}{r_{ij}^3}. \quad (1.51)$$

This interaction has an alternating effect between ferromagnetic and antiferromagnetic coupling as a function of distance and hence also causes oscillations in the magnetisation and susceptibility at long distances [1].

1.4 Classical spin models

Spin models are used to imitate and aid understanding of real systems. This is achieved by identifying the dimensionality of the spin, that is whether the spins are able to rotate freely in a three-dimensional space or are confined to a plane by repulsion of neighbouring spins, for instance. It is also achieved by identifying how the spins in the system interact, either directly or indirectly, short or long ranged and the nature of the interaction. Lastly, it is achieved by identifying the dimensionality and geometry of the

lattice these spins are located on.

If the universality class of a real material is known then its critical exponents are known and it is simple to represent the system with spin models. If the universality class is not known then these spin models are used to characterise the magnetic behaviour of the material, including finding its universality class (if it falls into one).

To obtain accurate critical exponents of a statistical mechanical system and hence its universality class, it is necessary to evaluate the partition function. However, it is difficult to solve the partition function exactly for systems with more than one dimension and therefore numerical methods such as Monte Carlo (discussed in chapter 3) are employed.

1.4.1 Spin and spatial dimensionality

Spin models can either be treated with a classical or quantum model. Classical spins can be represented as n dimensional vectors, e.g. Ising ($n=1$), XY ($n=2$) and Heisenberg ($n=3$) spins. The vector of the spin is denoted by $\mathbf{s}_i = (s_x, s_y, s_z)$ and has length $S_i = \sqrt{(s_x)^2 + (s_y)^2 + (s_z)^2}$. In quantum spin models, the Hamiltonian is an operator and the spins are treated quantum mechanically [45]. For spin- $\frac{1}{2}$ particles, the spin vectors are Pauli spin-1/2 matrices, which are shown below:

$$s_x = \begin{pmatrix} 0 & 1 \\ 1 & 0 \end{pmatrix}, \quad s_y = \begin{pmatrix} 0 & -i \\ -i & 0 \end{pmatrix}, \quad s_z = \begin{pmatrix} 1 & 0 \\ 0 & -1 \end{pmatrix}.$$

In this thesis, I have chosen to use classical spin models and assume the spin length to be $S_i = 1$. For the systems modelled, this is not considered to be too serious an approximation.

As shown in figure 1.9, the Ising spins are able to point parallel or antiparallel to a particular defined axis (e.g. $\mathbf{s}_i = (s_x, 0, 0)$). The axis is defined by the “easy axis” of the system which is the energetically favourable direction. The magnetocrystalline

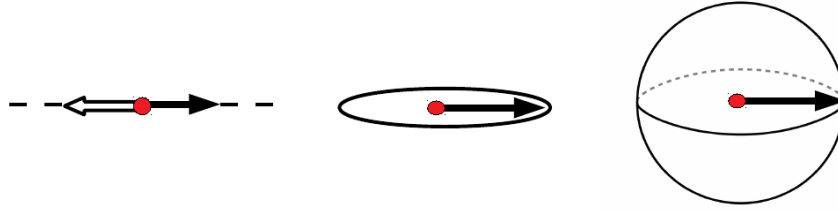


Figure 1.9: A schematic of the three classical spin types: Ising, XY and Heisenberg, from left to right. Ising spins are able to point parallel or antiparallel to a particular defined axis (denoted by open arrow and filled arrow), XY spins can point anywhere in a circular space and Heisenberg spins can point anywhere on a sphere in a $3d$ space.

anisotropy contributes to the easy axis and is determined by the principal axis of the crystal lattice, which is ultimately influenced by spin-orbit coupling [46]. To obtain the one-dimensional spin then there must be a biaxial anisotropy, whilst a two-dimensional spin (XY) has a uniaxial anisotropy and hence has an “easy plane”. Therefore, XY spins can point anywhere in a circular space (e.g. $\mathbf{s}_i = (s_x, s_y, 0)$, where these are local x and y co-ordinates). Heisenberg spins can point anywhere on a sphere in a $3d$ space as there is zero anisotropy (i.e. $\mathbf{s}_i = (s_x, s_y, s_z)$).

These Ising, XY and Heisenberg spins with n dimensional vectors can be placed on lattices with different spatial dimensionality, d , e.g. ($d=1$) a row of spins, ($d=2$) a square lattice and ($d=3$) a cubic lattice if considering hypercubes (see figure 1.10).

As mentioned previously, the universality classes are grouped by the spin, n , and spatial, d , dimensionalities. Using the hypercubic system as an example of spatial dimensionality (line $1d$, square $2d$, cube $3d$, ...), a table of the β critical exponents are given in table 1.1 showing the differences between these spin models.

Some significant differences between the spin models can be inferred from the table since from section 1.2.1, the presence of a critical exponent implies a phase transition at some finite critical temperature for hypercubic lattices. A phase transition at a non-zero temperature is only observed in three-dimensional systems [53] with the exception

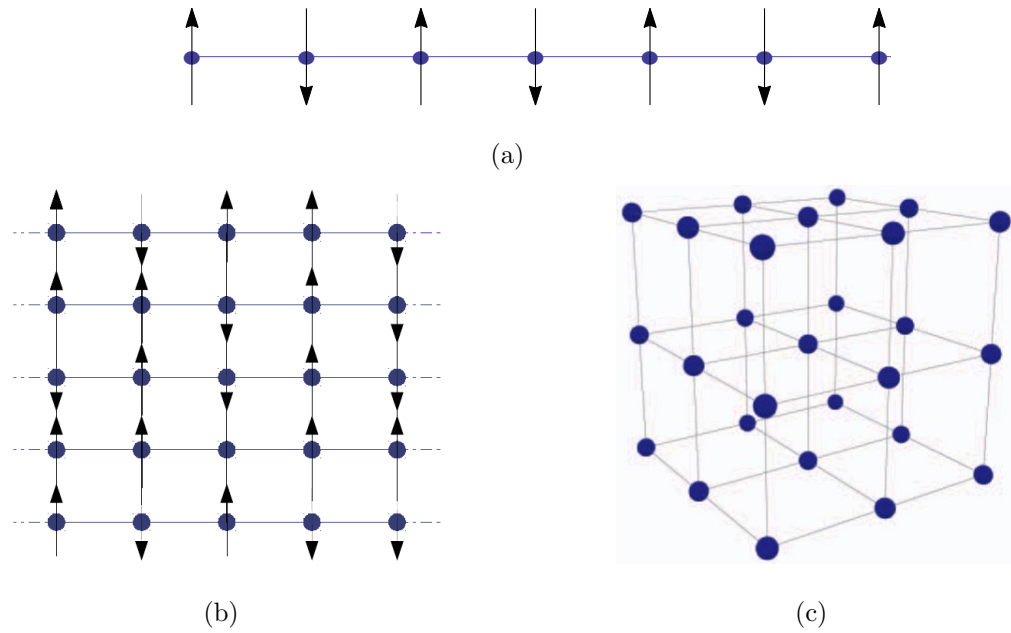


Figure 1.10: Hypercubic schematics of the (a) $1d$ and (b) $2d$ spin models and (c) of the $3d$ structure (spins are omitted for clarity). If one considers these as Ising spins (denoted by arrows), then the spins can only point parallel or antiparallel to the specified axis. The cubic image is taken from reference [47].

of the $2d$ Ising system at $T_c \simeq 2.269J$ [18]. This is because the two spin correlations of the spins in $3d$ structures survive by decaying to a non-zero constant as $r \rightarrow \infty$ [27, 54, 55]. For an infinitely large system size, the low-dimensional systems ($d \leq 2$) with continuous spins (XY and Heisenberg) have low energy excitations, known as spin waves quantised into magnons [1], which can destroy long range order. The spins are not stable enough to overcome thermal fluctuations, creating small angle deviations between spins which may occur in a continuous fashion [30] and hence develop a full twist in the spins at a vanishingly small energy cost. These low-dimensional systems therefore obey the *Mermin and Wagner theorem*, which states that it is not possible to observe long range magnetic order (spontaneous symmetry breaking) at finite temperatures for a continuous spin system when the dimensionality is $d < 3$ [56]. The one-dimensional Ising model has been solved exactly by Ising [48] showing that the phase transition takes place at $T = 0$ K when $H = 0$ since at any non-zero temperature

Spatial dimensionality	β values for each spin dimensionality		
	Ising	XY	Heisenberg
$1d$	-	-	-
$2d$	0.125 [48]	0.23 [49]	-
$3d$	0.325 [50]	0.349 [51]	0.36 [52]

Table 1.1: Critical β for the hypercubic spatial and spin dimensionalities, which is a key exponent used to determine the universality class of a system.

the correlation between spins decay exponentially.

Exactly solved models include the one-dimensional spin systems which have a finite range of interaction, decaying exponentially or which interact Coulombically [28] and also the $2d$ Ising system [57]. Additionally, some $2d$ Ising systems with different geometries, e.g. the honeycomb lattice with $S = 1$ [58] and $S = 3/2$ [59], have also been solved exactly. Heisenberg spins in low-dimensional systems have not been exactly solved and neither are they known to represent real systems. Ferromagnetic rare earth Gd^{3+} was thought to be a good candidate for isotropic Heisenberg spins because it is an S-state ion and has a large localised magnetic moment [60]. S-state ions have half-filled shells, which produce an orbital singlet as their ground state and should not show any hyperfine splitting in a small magnetic field [61]. Therefore, a very small magnetocrystalline anisotropy is expected. However, investigations found that there will always be a dipolar interaction between magnetic moments or a magnetocrystalline anisotropy present to create a uniaxial anisotropy [60]. Due to the complexity of the partition function, $3d$ systems have also not been solved exactly and therefore the β exponents for this spatial dimensionality, shown in table 1.1, are approximations.

The $2d$ XY system behaves quite differently to the other spin models mentioned so far, in that an effective T_c and β exponent can be extracted when the system size is finite [49]. This is despite the fact that it does not undergo a phase transition by

spontaneous symmetry breaking but rather by topological ordering. The Hamiltonian for the nearest neighbour XY exchange only system is given in equation 1.52:

$$\mathcal{H} = -J \sum_{\langle ij \rangle} \cos(\theta_i - \theta_j) \quad (1.52)$$

where θ_i and θ_j are the angle of the spin i and spin j with respect to some arbitrary direction. The spin stiffness is then a measure of how much free energy is required to create a twist in the spins. As mentioned before, for an infinitely large system size, the free energy cost is zero in creating a twist of the spins, hence the magnetisation is zero at all temperatures. This can be viewed as long wavelength spin waves (a long twist in the spins) destroying long range order. For finite system sizes, a cut-off in the correlation length and consequently in the spin waves with long wavelengths mean that a finite magnetisation per spin, $m(L)$, can exist at low temperatures [49]. For $m(L) \rightarrow 0$, the system size would have to be of the order of the size of Texas [20]! Since it is unlikely that a thermodynamic system size of $2d$ XY spins will be obtained physically, then the $m(L)$ result found for finite systems is important.

Although there is no symmetry breaking in the $2d$ XY system, the finite size ensures a nonzero magnetisation at low temperature and a slow decay in the order parameter to zero as a function of system size. The slow decay is characterised by an algebraic decay in the spin correlations. An algebraic decay is generally related to a critical temperature of a second order phase transition, but since all points up to a certain temperature, $T_c(L)$ have an algebraic character, then all $T < T_c(L)$ are considered critical [49].

Vortices are created in the $2d$ XY system when small angle deviations between spins become multiples of 2π (see figure 1.11). Vortices exist as pairs at temperatures below the Berezinskii-Kosterlitz-Thouless transition temperature, T_{BKT} [53, 62]. They are paired at low temperatures because a single vortex in the thermodynamic limit has an infinite energy [30].

Vortices also contribute to the destruction of long range order [53] as there is a de-

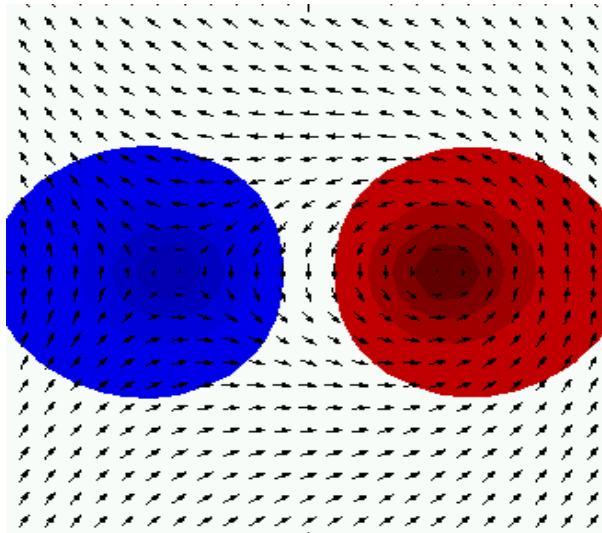


Figure 1.11: This is a schematic of a vortex pair (the red and blue shaded areas) created at low temperatures in the $2d$ XY system [63].

crease in the spin stiffness [55]. However there is a different type of order at $T < T_{BKT}$, which is a topological order of these defects. Once $T = T_{BKT}$ vortex pairs unbind [64] and isolated vortices can exist, however isolated vortices can only exist providing the total vorticity is zero [30]. This is the only notable transition which takes place in the $2d$ XY system in the thermodynamic limit. When T_{BKT} is approached from $T > T_{BKT}$, an exponentially diverging correlation length appears but the magnetisation remains zero throughout the temperature range ($T = 0$ to $T > T_{BKT}$).

For a finite system, T_{BKT} becomes less important than in the infinite system, as the spin stiffness does not become zero at this temperature. The power law decay is bounded between $T^*(L)$ and $T_c(L)$, where $T^*(L) < T_c(L)$ is the Berezinskii-Kosterlitz-Thouless transition temperature shifted as a result of the finite size [65] and $T_c(L)$ marks the T at which $\xi \simeq L$. The associated effective β exponent is found to be universal for this region, $\beta = 0.23$ and can be observed for real systems [49]. As $L \rightarrow \infty$, β becomes undefined and both $T^*(L)$ and $T_c(L)$ converge on T_{BKT} .

Therefore it is shown that by confining the lateral dimensions of the $2d$ XY system,

one can alter the magnetic system from having no phase transition to one that appears to have a second order, critical phase transition. Similarly, a finite $2d$ XY system with long range dipolar interactions exhibits a spontaneous ordering transition [66–68]. This shows that even changing the range of interactions from nearest neighbour exchange to long range dipolar can alter the magnetic system from having an apparent phase transition to having a true spontaneous phase transition. With finite dipolar interactions, the system does not have a Kosterlitz-Thouless transition neither is it considered that topological defects of vortices exist [69]. Debates around the true nature of this phase transition has been evident from Mol and Costa [67] compared with Maier and Schwabl [70], as to whether the transition has algebraic behaviour as in all second order phase transitions or an exponential behaviour similar to that in the BKT transition, respectively. Both, however, agree that there is a phase transition and the critical exponents are unusual, whether this is characteristic of a new universality class is still under investigation. Nevertheless, one can see how changing the range and nature of interactions can alter the finite $2d$ XY system to have a true phase transition. In chapter 5, I present findings on the finite $2d$ XY system with a varying range of exchange interactions.

1.5 The impact of lattice geometry, spatial confinement and long range interactions

When discussing the concept of lattice geometry, spatial confinement and long range interactions, it is essentially how lattice points are arranged in space and to what extent spins on these lattice sites are dependent on the behaviour of all the other spins in the system. The arrangement of lattice points give rise to the number of neighbouring spins, which is of course controlled by both the spatial dimensionality and the lattice geometry. The impact of the number of neighbours can mean more or less attraction/repulsion experienced by any one spin from those surrounding it and hence determine its spin dimensionality (note: ignoring the contribution from the magnitude of the mag-

netic moment itself for now). Knowing the spin and spatial dimension will effectively provide the universality class of the material and therefore the critical exponents. Using these exponents, it has been possible to observe crossovers from $3d$ to $2d$ spin behaviour in magnetic multilayers as the system is increasingly confined in one dimension [71]. The number of neighbours for each spin become more important with increased confinement, which gives rise to significant surface effects in thin films.

The arrangement of the lattice points also has an indirect effect. If each spin on the lattice is constrained in its dimensionality by the crystal field from surrounding spins or by some other external factor, then the arrangement may give rise to *frustration* of the spins. Frustration describes a system where all pairwise interactions cannot be satisfied simultaneously. When this frustration arises as a consequence of the geometry of the lattice it is known as “geometrical frustration”, which is found in magnetic pyrochlore oxides [72], for instance. However, frustration can impact on systems where there are non-homogeneous competing interactions and this is the case for both the magnetic multilayers and frustrated monopole pyrochlore studied in this thesis.

The number of neighbours of each spin feeds well into the impact of the range of interactions, since by having a greater proportion of the system interacting with any one spin, is as though that spin has numerous close neighbours in a nearest neighbour only picture. It is for this reason that a one-dimensional system with an infinite range of interactions has a phase transition with a critical exponent, because the system becomes, in some sense, infinite-dimensional [28]. The range of interactions is therefore important in all the systems I investigate and the differences in the nearest neighbour system and a further ranged analogue are explored.

A description of the systems investigated in this thesis are in the sections below. The next chapter has been dedicated to one of the systems, the frustrated pyrochlore, as the concepts which are utilised in understanding the project require a more thorough explanation.

1.5.1 Magnetic multilayers

Consider a slab of iron, which consists of numerous layers of Fe atoms and where each Fe atom only interacts with other Fe atoms (known in this thesis as the intraspecies coupling). It has a single magnetic domain so that the spin of each Fe atom points in one and the same direction so the material is ferromagnetic. If one were to increase the temperature beyond the critical (Curie) temperature of iron, $T_c(\text{Fe})$, the slab of iron would no longer be ferromagnetic, but rather paramagnetic with all the spins randomised (when $\mathbf{H} = 0$).

Now if the iron slab system were modified by adding several layers of a different magnetic material on top (another slab), one would expect that the properties of the slab of iron would be affected in some way by this alteration. In layering the iron material with another magnetic material, the smallest unit of a magnetic multilayer is created, known as a magnetic bilayer. This is generally where a system has two magnetic species in a layered arrangement. Consider for this example that this other material is cobalt (Co), which is another ferromagnet. One would have to additionally take into account the intraspecies coupling of Co atoms to other Co atoms but also interactions of Co atoms to Fe atoms (the interspecies coupling). Interspecies coupling takes place at and close to where different species meet, known as the interface. In this case, it is where the top surface of the Fe slab meets the bottom surface of the Co slab.

Cobalt has a higher Curie temperature than iron [46], therefore order in the Co layers will remain intact at higher temperatures than for iron. Consequently, when $T_c(\text{Fe})$ is reached, the order in the Co atoms at the interface influence the behaviour of the Fe atoms coupling with them. This will have a cascading effect as these Fe atoms affected by the Co atoms, are also interacting with the other Fe atoms in the Fe slab. The influence from one species with higher magnetic ordering to another with lower (or zero) magnetic ordering is known as the *proximity effect* [73, 74].

The proximity effect has great prospects for use in spintronic devices [75, 76] and in understanding frustrated spin systems [77] (discussed later). Magnetic multilayers in general have already been used in magnetic recording devices [78, 79] and spintronics [80] such as magnetoresistive Random Access Memory (mRAM) [81]. Similar to alloys, magnetic multilayers enable one to take advantage of the benefits of several species in one system and is largely the reason to study them. The general definition of magnetic

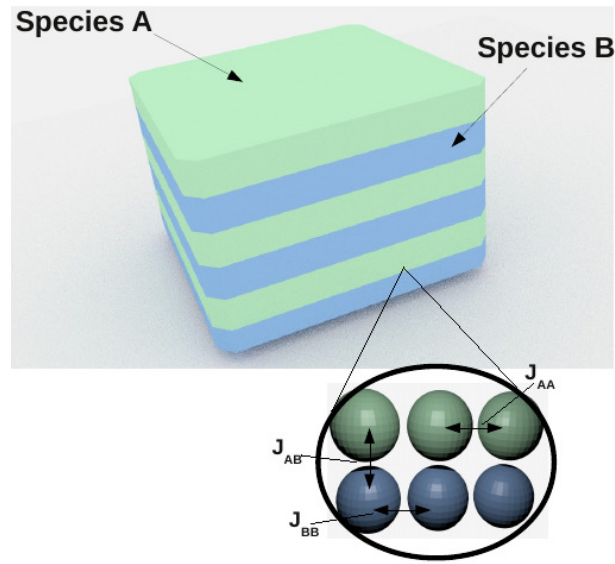


Figure 1.12: An A/B multilayer system, where A and B are different magnetic species. The intraspecies couplings, J_{AA} , J_{BB} and the interspecies coupling J_{AB} , are indicated by a magnified interface.

multilayers is that they are compositionally modulated layers of magnetic materials [82]. With the previous example of the bilayer of iron/cobalt, one could form a trilayer by adding another slab of Fe on top of the cobalt. The bilayer, trilayer and other multilayer forms of this system would be referred to as Co/Fe multilayers [83] and hence the name is independent of the number of repeat units.

Figure 1.12 presents a general A/B magnetic multilayer system, where A and B represent two different magnetic species. In reality, the Co/Fe example is a very simple example of a magnetic multilayer, firstly because magnetic multilayers can have anti-ferromagnetic layers e.g. CoMn or FeMn [84] and/or non-magnetic layers e.g. Co/Au

and Co/Pt [85, 86]. They can have the same magnetic component in both layers but compositionally different, such as CoO/CoPt multilayers [87]; each species layer does not need to be several layers thick (a slab), but can consist of a single layer of the species (a monolayer) [88, 89] or less than a monolayer [71] and the multilayer can have more than two species [90]. Most often magnetic transition metals are used in magnetic multilayers [91–93], however they are not limited to this as magnetic rare earth elements have also been used, such as Dy [94, 95].

The composition of magnetic multilayers is not the only aspect of these systems which have been exploited, but also the ability to confine them into thin films, particularly useful in small devices such as memory storage. However, this also gives rise to effects which cannot be seen in the bulk equivalents and can be a disadvantage.

Surface effects in magnetic thin films

It is easiest to describe surface effects in magnetic thin films when considering a system which only consists of one species, referred to as a slab in this thesis, since unlike a multilayer, there are no interfacial effects to take into account. The extent to which the surface affects a slab system is dependent on the thickness [96–98]. When a slab system decreases in thickness, there is a higher proportion of atoms forming the surfaces, therefore the surface has a much greater influence on the overall system. Surface effects are relevant when comparing thin film and bulk systems. Thin films are generally $< 1000 \text{ \AA}$ thick [99], which is the order of a domain wall in a bulk system and ultrathin films are $\lesssim 7 \text{ ML}$ thick [100], which is $\sim 21 \text{ \AA}$ using an approximate $(3 \text{ \AA}):(1 \text{ ML})$ ratio [101][‡]. Thin films are therefore defined by a relatively small dimension in the z direction compared with the xy -plane.

The lower coordination of the surface and broken symmetry contributes to the increase in magnetocrystalline surface anisotropy such that the easy axis of magnetisation

[‡]the $\text{\AA}:\text{ML}$ ratio is highly dependent on the atoms used and a more in depth investigation can be found in reference [102]

is altered to favour that of the perpendicular plane upon overcoming the demagnetising field [103–106]. This results in a lowering of the critical temperature in magnetic thin films [107–109] compared with the bulk systems. In fact, generally a lower coordination number decreases T_c when comparing different crystal structures in $3d$ systems [110]. The critical temperature of bulk Fe is $T_c = 1043$ K [108], whilst for ultrathin films of Fe(100) 2.2 ML grown on W(100) $T_c = 306$ K [111]. Disordering the system from a crystalline to an amorphous structure by inserting other elements also decreases the critical temperature [112] (e.g. the amorphous $\text{Fe}_{93}\text{Zr}_7$ thin film discussed in chapter 5 has a critical temperature $T_c \sim 150$ K [71]).

The effects from thickness and structure change is not element specific. Another example is cobalt which has bulk $T_c = 1394$ K [113]. The T_c of bulk amorphous $\text{Co}_{95}\text{Zr}_5$ is only slightly affected compared to the T_c of pure Co, with a gradual reduction in magnetisation from room temperature up to $T_c > 950$ K [114] (measurements were not made beyond this temperature). This follows from a 19% reduction in the magnetic moment of pure bulk Co [114]. However, overall it is evident that there is a large effect in the magnetic ordering of bulk vs thin films and those which are amorphous.

Theoretical studies using first principles calculations [115, 116] and the Green’s function technique [88, 117, 118] show that it is the electronic states of the d orbitals that control the magnetic behaviour of the surface and the surface anisotropy which influences the thickness dependence of magnetic quantities of the system. This is because of differences in the overlap integrals between electronic wavefunctions or the lattice parameters being perturbed at the surface, such that the exchange interaction is directly affected at the surface, J_s [119]. In some simulations, J_s is used distinctly from J_{bulk} with a reduction of even up to half the bulk value [97].

Interfacial effects in magnetic multilayer thin films

In thin film magnetic multilayers, the interface is where two surfaces meet and therefore multilayers have competing surface and interfacial effects. One can determine to

what extent the interfacial effects are experienced by a single species in a multilayer by studying the simplest unit, a bilayer [120–122]. The interface effects are evident when the magnetising strength of one species dominates the magnetic behaviour in another such as Co to Cr in Co/Cr multilayers [123], Fe to Pd in a Pd/Fe trilayer [89] and Fe to Dy in a Fe/Dy bilayer [124]. There is particularly good experimental evidence that varying the thickness of the different layers can give rise to changes in the spin anisotropy in the layers [71, 85, 92, 125–129].

Although decreasing the thickness in magnetic thin films and magnetic multilayer thin films may seem to be the same, there is a subtle difference. To describe this it is easier to demonstrate using a specific subset of magnetic multilayer systems in which the multilayer is composed of ferromagnetically coupled species with different coupling strengths. This can be represented by the general scheme $ABABA$, where A is less strongly coupled than B (i.e. $J_{AA} < J_{BB}$). In such systems, magnetic order is induced in A as a consequence of proximity to the strongly coupled B species [71]. This induction plays a greater role in the system as the thickness of A decreases and gives rise to an increased critical temperature in A , resulting in an increase in the average T_c of the system [130]. A result which is unlike that given by surface effects (discussed in the previous section), where the critical temperature decreases when the thickness decreases. The difference is the proximity effect, where the higher T_c material influences the lower T_c material in a magnetic multilayer [131, 132]. Therefore competing interactions are present in the system.

***3d-2d* crossover**

Characteristic of decreasing the film thickness is a crossover from $3d$ to $2d$ interactions, which for example, has been observed in pure Fe films between 100-200 nm thickness [133] and in pure Ni on W(100) [134] (see figure 1.13).

All thin film systems with a single species exhibit two-dimensional critical properties, but this is not observed in temperature regions far from the critical temperature

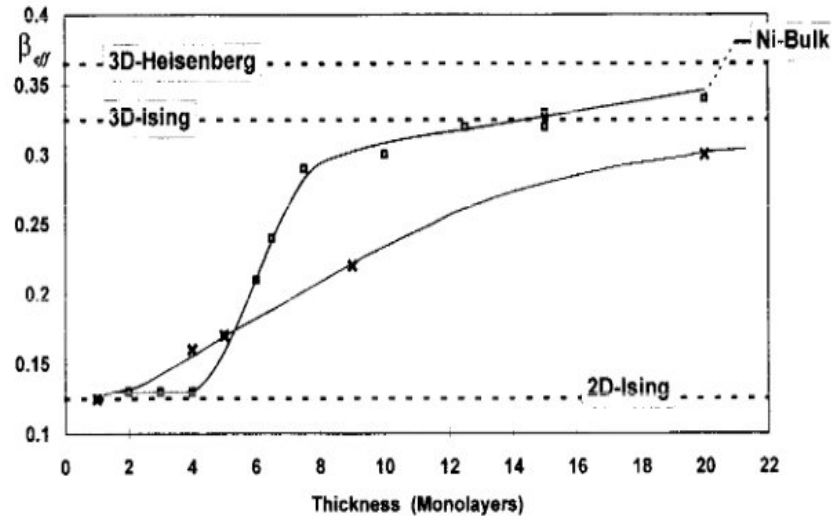


Figure 1.13: β_{eff} exponent as a function of film thickness for Ni on W(100). The squares are from reference [134] with regards to the Ni on W(100) thickness and the crosses are from Monte Carlo simulations conducted on Ising 200×200 systems in reference [135] with varying thicknesses (1-20 layers).

[135]. When ξ diverges at T_c , the correlation length of spins is a length scale beyond the perpendicular lattice dimension, which causes a cut off in perpendicular spin waves and gives rise to two-dimensional critical behaviour regardless of the film thickness [135]. This differs somewhat in a multilayered/ doped system where critical exponents have been shown to be dependent on a relationship between the critical temperature, T_c and the temperature by which z magnons are excited, T'' , in CoZr/FeZr [71] and δ -doped Pd(Fe) [136]. For instance, if T_c is greater than T'' then one will observe three-dimensional critical behaviour as the perpendicular magnon modes are active.

In this thesis, trilayers with the general formula ABA (chapter 5) and BAC (chapter 6) are discussed in regards to the proximity effect, which is an interfacial effect, whilst surface effects are also evident in the results.

1.5.2 Frustrated spin systems

The first example of frustration was found in an antiferromagnetic spinel lattice and was explained by Anderson [137], however one of the simplest examples that encom-

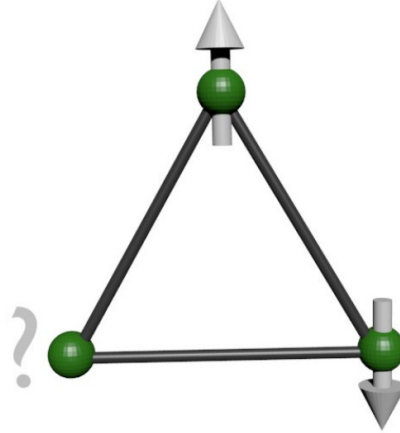


Figure 1.14: This triangular Ising antiferromagnet is frustrated since the site with the question mark can only satisfy one antiferromagnetic interaction and the other has to be ferromagnetic, i.e. all pairwise interactions cannot be satisfied in this system.

passes the concept of frustration is a triangular system of antiferromagnetically coupled Ising spins which have a common axis (see figure 1.14). Notice that from figure 1.14, two of the spins have an antiferromagnetic pairwise interaction whilst continuing this trend of antiferromagnetism one can easily see that the site with the question mark cannot satisfy all of its pairwise interactions. This limitation defines frustration in that all pairwise interactions cannot be simultaneously satisfied.

When a spin system is frustrated, a single ground state cannot be obtained when $T \rightarrow 0$ K, since $S \rightarrow 0$ JK⁻¹ [25].

Spin ice

Geometrical frustration in three-dimensional structures have included magnetic rare earth pyrochlore oxides, which are arranged as a lattice of corner sharing tetrahedra (see figure 1.15) and have additionally shown some exotic behaviour due to this frustration

[25, 138], as will be discussed in the next section. These structures are known as spin ices.

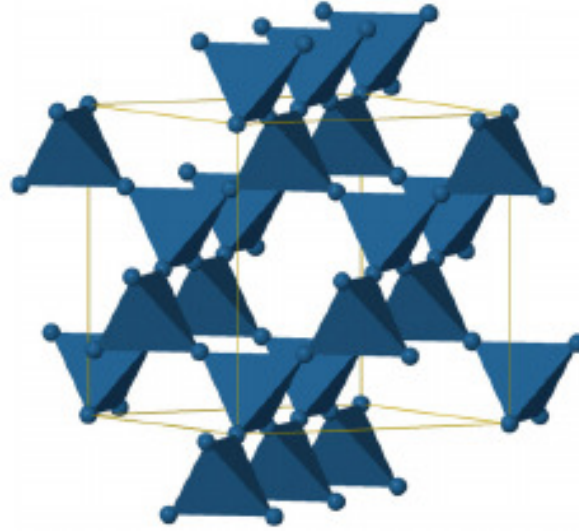


Figure 1.15: A schematic of a pyrochlore system, where each sphere represents a magnetic ion and the yellow lines represent the boundaries of a cubic unit cell. Image taken from reference [139].

Pyrochlores can have more than one type of magnetic ion at the vertices. In spin ice, these ions are rare earth ions and their magnetic moments are “Ising-like” due to the crystal field of surrounding ions imposing the constraint on the spins [140]. The Ising spins for each tetrahedra also favour an uncommon axis between them. Therefore, the tetrahedral geometry of the system collectively with the constraint on the spin dimensionality and direction causes geometrical frustration in spin ice.

As a frustrated system, spin ice is known to disobey the third law of thermodynamics since $S \not\rightarrow 0$ when $T \rightarrow 0$ (this has been disputed in $\text{Dy}_2\text{Ti}_2\text{O}_7$ where considerably long equilibration times in the specific heat in the low temperature region show some evidence to be contrary [141]). However, by confining the bulk system of $\text{Dy}_2\text{Ti}_2\text{O}_7$ into a thin film on a substrate of $\text{Y}_2\text{Ti}_2\text{O}_7$, the third law is restored in spin ice [142]. By studying thickness sizes from 5 nm - 60 nm, a loss of entropy is observed with a smaller

thickness, which is considered to be due to strain induced by lattice mismatch between the film and substrate [142]. Thin film $\text{Ho}_2\text{Ti}_2\text{O}_7$ has also been studied between 9 nm - 120 nm thickness [143], with the magnetic properties specifically investigated for 80 nm - 120 nm thickness. It is found in this range that these thin films still demonstrate spin ice magnetic behaviour, however, thin films with 9 nm thickness do not show strain to the substrate [143] as observed in the $\text{Dy}_2\text{Ti}_2\text{O}_7$ thin film study. It is still interesting that different properties can be observed upon spatial confinement of a spin system even with different geometries, which relies on the lattice arrangement of the film and the substrate.

More on the bulk spin ice is given in the next chapter as the concepts are key to one of the projects presented in this thesis. In the next section, a system related to spin ice is discussed as much of the understanding in spin ice can easily be visualised and explained using this system.

Artificial spin ice

The exotic features in spin ice, which are explored more in chapter 2, can only be observed at extremely low temperatures (< 4 K [144]). This is due to the susceptibility of thermal fluctuations by the atomic sized magnetic moments. As a consequence of this dilemma, artificial spin ices (ASI) were introduced, which are effectively $2d$ projections of spin ice fabricated using lithographic techniques [145]. ASI systems consist of typically $\sim 80,000$ magnetic nanoislands [145] with dimensions ranging from 100 nm – 1000 nm [146]. These nanoislands are made up of microscopic spins aligning along one axis (a single domain), forming a macrospin. The microspin alignment is due to the shape anisotropy of the elongated nanoislands and consequently makes these macrospins “Ising-like”.

When ASI was introduced, these nanoislands were by no means susceptible to thermal fluctuation due to the size and material initially used (energy barrier to spin flip was $\sim 10^5$ K [147]) and had restricted thermal equilibration of these nanoarrays [148].

However, since these systems can be studied at room temperature [149], they have been valuable in the study of “spin ice-like” behaviour.

The two ASI geometries presented below are those of kagomé [150] and square [145] artificial spin ice, where kagomé ice is a projection of spin ice along the (111) plane [72] and square ice is a projection of spin ice along the z direction [151] (see figure 1.16).

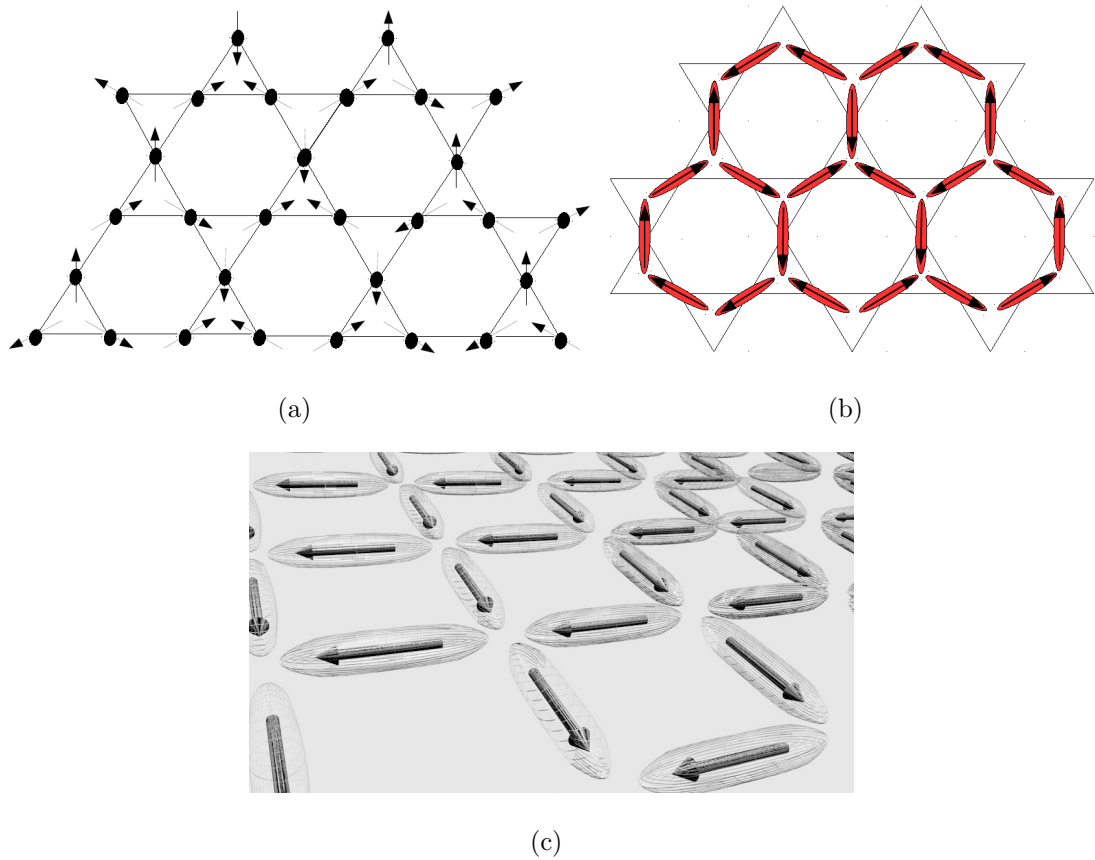


Figure 1.16: A schematic of the two-dimensional frustrated (a) kagomé spin model, (b) islands (denoted by red ellipses) in a honeycomb geometry and (c) the square ice model. The honeycomb structure is the premedial lattice of the kagomé lattice. In ASI, the spins are Ising due to a strong shape anisotropy and the spins point toward or away from the centre of a triangle in the kagomé lattice.

The frustrated spin systems have a spin lattice and a premedial lattice. From figure

1.16 (a) one can see the spins occupy the vertices of the kagomé lattice but not the vertices of the premedial honeycomb lattice (shown superimposed in red in figure 1.16 (b)). The centres of the triangles in the kagomé lattice correspond to the vertices of the honeycomb lattice and three spins can point toward or away from these centres. As a general definition for frustrated systems, the centres for which spins point toward or away from is commonly known as a *vertex*. Square ice, shown in figure 1.16 (c), has four spins associated with each vertex and has two different square lattices for the premedial and parent lattice, whilst in the next chapter, the diamond lattice is shown to be the premedial lattice of the pyrochlore and this structure also has four spins associated with each vertex.

Both square ASI and spin ice are 16-vertex models. This means that there are sixteen possible ways of arranging a vertex of spins in the system, whilst kagomé is an 8-vertex model. The overall energy of favourable and unfavourable interactions of spins at a vertex determine the energy of the vertex, which is then classified accordingly as either Type I, Type II, etc. (see figure 1.17).

The ground state square ASI, a completely Type I arrangement (see figure 1.17 (a)), is lower in energy than the Type II arrangement because the 90° interactions contribute more to the energy than the 180° . This is dissimilar to kagomé and spin ice, where all interactions at a vertex are equivalent and yield a six-fold degenerate ground state.

The Type I ground state for square ice has been difficult to observe because of the limitations in the thermal dynamics of the nanoislands, as mentioned previously. There has been developments in the field with Morgan *et. al.* [148] obtaining domains of ground state vertices during thermal growth of permalloy nanoislands. However, this is limited to a small time frame since once a critical thickness is reached ($\lesssim 1$ nm [148]), the spins are frozen into state and no further thermal fluctuations can occur.

As mentioned before, magnetically soft permalloy (NiFe) is commonly used to fab-

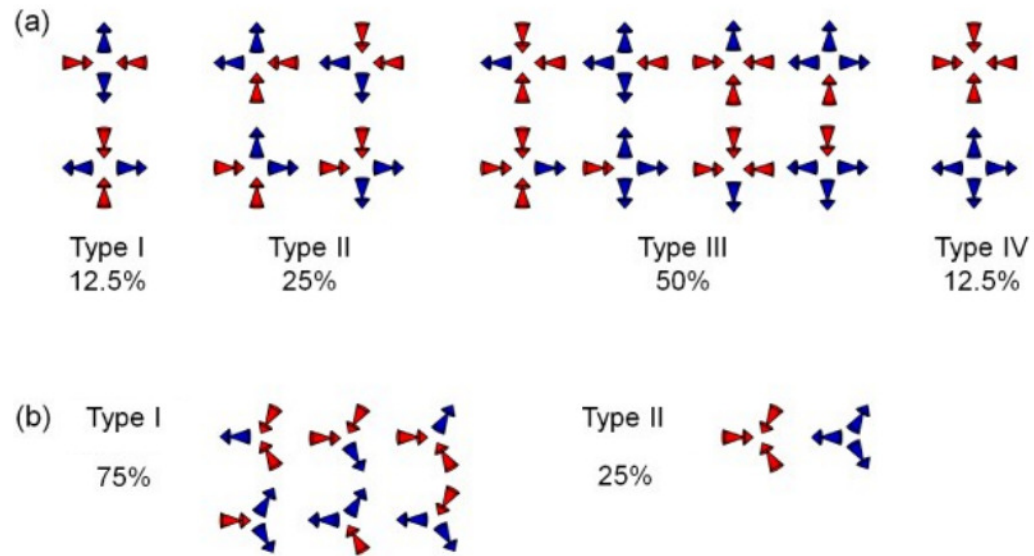


Figure 1.17: The vertex types of (a) square ice and (b) kagomé ice. The percentages below the square and kagomé ice vertices represent the statistical population of the vertex types in the respective systems. The lowest energy vertex type is Type I in both the square and kagomé geometries and correspond to the ground states. Modified image taken from reference [152].

ricate the nanoislands [145, 153–156]) and also magnetically hard cobalt [157]. Both materials have been useful in imaging the excitation vertices (Type II in the kagomé lattice and Type III and IV in the square lattice) [146, 158, 159]. For instance, a distribution of switching fields in cobalt nanoarrays enables simple creation of these excitations [146] as well as improved imaging since the excitations are stabilised by large pinning fields [158]. However, for studying the ground state, Pd/Fe trilayers (see figure

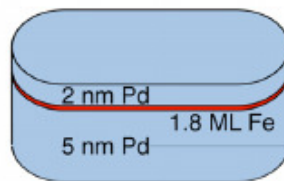


Figure 1.18: A schematic of the Pd/Fe trilayer used to achieve thermal equilibration in both square and honeycomb artificial spin ice to observe the ground state Type I vertices. Image taken from reference [160].

1.18) are a good candidate which have shown thermally driven ground state vertices in the honeycomb and square ice structures [77, 161]. The tunability of the anisotropy and hence, the variation of the Curie temperature in these multilayers, can be controlled by the thickness of the iron layer [160]. By using a material which has a lower Curie temperature than the typical permalloy or cobalt, it has been possible to make observations at and around room temperature since the island array is not quasi-static at these temperatures. This study demonstrates the benefits of integrating magnetic multilayers within the structures of these frustrated artificial spin ice.

Chapter 2

Spin ice background

A major result of this thesis involves a model closely related to spin ice. In order to understand the context of this model it is essential to have an understanding of the background theory of spin ice; this background is presented here.

2.1 The structure of spin ice

2.1.1 The pyrochlore and diamond lattice

The class of pyrochlores known as spin ice, have a general stoichiometry of $A_2B_2O_7$ [38], where A is a magnetic rare earth 3+ ion, B is a transition metal 4+ ion and O is symbolic of the oxide 2- ion. In short, these are rare earth pyrochlore oxides and these magnetic materials can behave differently depending on the composition of A and B . Two of the most studied systems are $\text{Ho}_2\text{Ti}_2\text{O}_7$ and $\text{Dy}_2\text{Ti}_2\text{O}_7$ [25].

The rare earth ions used in spin ice have large magnetic moments of $u \sim 10\mu_B$ [72], which is in contrast to the approximate $5\mu_B - 7\mu_B$ for a Co^{2+} ion [162]. The fact that there is a range ($5\mu_B - 7\mu_B$) for the transition metal and not for the rare earth magnetic moments is due to the relatively small effect from chemical bonding and crystal structure in rare earths [162]. This is since the valence $4f$ electrons in the rare earth ions are shielded from the outer $5s$ and $5p$ electrons and stay close to the

nucleus, hence the behaviour is close to that of a free ion. The exchange, J coupling is from the $4f$ electrons in the rare earth system and the shielding is large in comparison to the transition metal systems and so the coupling is of the order of ~ 1 K [163]. The dipolar coupling is also of the order ~ 1 K [1] and the large magnetic moments of the rare earth ions mean dipolar interactions play a significant role in spin ice.

The rare earth ions in spin ice make up one pyrochlore lattice and the transition metal ions make up an inter-penetrating pyrochlore lattice of the overall cubic structure of spin ice, whilst some of the oxide ions are at the centres of the tetrahedra. The network connecting the centres of the pyrochlore lattice is known as the diamond lattice (the premedial lattice of the pyrochlore). Figure 2.1 shows how the pyrochlore and diamond lattices relate.

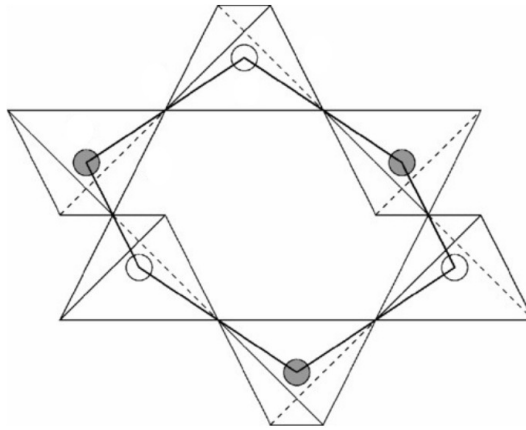


Figure 2.1: A schematic showing how the parent lattice (the pyrochlore tetrahedral structure), relates to the diamond lattice (the joint white and grey circles in the centre of the tetrahedra). The white circles represent one sublattice (i.e. the tetrahedra containing these white circles have the same orientation), whilst the grey circles represent another sublattice. Please keep in mind that these circles do not represent an atom/ ion but rather a source/ sink of magnetic field or divergent free field, as will be discussed later in the text. Image taken from reference [164].

2.1.2 Spin configuration in spin ice

Any one rare earth ion, which resides at a vertex of a tetrahedron, is co-ordinated by two oxide ions lying along the trigonal axis given by the local $\langle 111 \rangle$ cubic direction [72]. The vectors of the magnetic moments of these rare earth ions coincide with the point symmetry of their position, so that they either point toward or away from the centre of any one tetrahedron. The crystal field on each rare earth ion [140], lifts their free ion degeneracy and leaves a ground state doublet far lower in energy compared with its first excited state. This large energy difference of ~ 300 K [72], mean the spins behave almost purely as classical Ising spins. Comparitively, quantum spin ices, which will be introduced later, have a separation between the ground and excited states of ~ 10 K [165], which mean the spins do not behave as perfect classical Ising spins and hence quantum effects play a major role in these systems.

At low temperatures in spin ice[†], the cubic symmetry causes these “Ising-like” magnetic moments to orient along the local $\langle 111 \rangle$ easy axis [167] and not a global axis. The combination of the crystal field and the interactions between the magnetic moments, such as dipolar and exchange, ensures the formation of an energetically favourable configuration. This configuration has two spins pointing toward the centre of any one tetrahedron and two spins pointing away. This produces a state of divergent free tetrahedra, such that each tetrahedron has a magnetic field of zero (see equation 2.1) [3], as the tetrahedron is neither a source or sink of magnetic field such that

$$\nabla \cdot \mathbf{B} = 0 \tag{2.1}$$

It is possible to rationalise the favoured two-in, two-out configuration as each magnetic moment interacts favourably with another when opposite poles interact, much like a bar magnet. This is represented in figure 2.2 by the head of an arrow to the tail of another arrow. Each magnetic moment therefore interacts unfavourably when “like” poles interact (e.g. head of an arrow to the head of another arrow). Therefore, referring to the tetrahedron in figure 2.2 with two spins in and two spins out, one will

[†]Refer to reference [166] for high temperature properties of spin ice.

notice that for every pair of magnetic moments, only four of the possible six interactions are satisfied in this configuration, however, this is the configuration with the least unfavourable interactions. The inability to minimise the energy of all pairwise interactions simultaneously defines *frustrated magnetism* and is the reason why spin ice is a frustrated magnet.

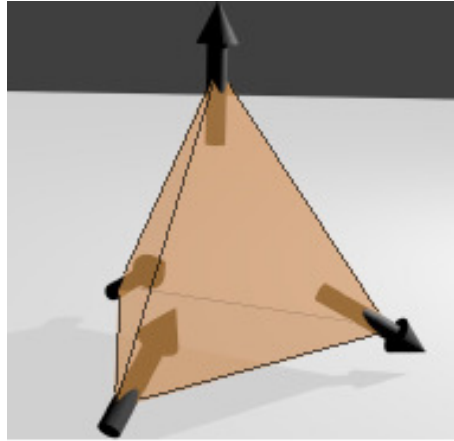


Figure 2.2: A schematic showing a tetrahedron with the rare earth magnetic moments depicted as arrows. One pole of the moment is denoted by the head of the arrow and the other pole of the moment is denoted by the tail of the arrow. Here is a two-in two-out configuration which satisfies 4 of 6 favourable pairwise interactions (head to tail).

Six different configurations in each tetrahedron of spin ice correspond to the lowest energy state of two spins in and two spins out, therefore, the ground state is 6-fold degenerate [168].

2.1.3 Water ice to spin ice analogy

Water ice has a stable hexagonal structure, however, it is found that when water ice is supercooled, the structure contains random metastable cubic stacking faults in the hexagonal structure [169]. This result was contrary to the previous literature which identified water ice only with cubic symmetry in powder diffraction results [170–172].

When water ice is in the cubic arrangement, each oxide ion is connected with four protons, where two protons are covalently bonded to the oxide ion and two protons are hydrogen bonded. Each hydrogen bonded proton belongs to another water molecule. The covalently bonded protons have a shorter bond length than the hydrogen bonded due to the relative bonding strengths. The displacement vector of the protons in water can then be mapped onto the spins in spin ice so that cubic water ice has an analogous arrangement to spin ice. This is such that two protons are close to an oxide ion (two spins in) and two protons are further away (two spins out).

The proton arrangement in water ice was first noted by Pauling in 1935 [173], who identified that water ice has a non-zero entropy upon approaching absolute zero temperature (breaking the third law of thermodynamics). His motivation for this was based upon previous studies of the water ice structure and confirmed by experimental work conducted by Giauque and Stout [174], who found discrepancies in the entropy of water ice when calculated using different techniques. Prior to this, Bernal and Fowler in 1933 [175], had suggested that the protons in water ice lie between the O-O “bonds”. The 4-fold coordination of the oxide ion was known and so these constraints led to the ice rules which state that two protons are in near positions to the oxide (covalent bonds) and the other two protons are further away from the oxide (hydrogen bonds). Spin ice also follows the ice rules by analogy.

2.2 Other related spin systems

The thermal fluctuations in spin ice being of the same order as the interaction strength (both dipolar and exchange) means that spin ice is not suitable for studying under ambient conditions. The physics of two-dimensional artificial spin ice is fundamentally different to that given by spin ice (described more in section 2.3) and so although investigations can be made in ambient conditions, there are limitations on the analogies that can be made between spin ice and ASI. However, if two of the islands in every vertex of

square ASI were elevated by a particular height, h , then it would be possible to observe the features currently unique to spin ice [176, 177] but under ambient conditions. If it is possible to fabricate, the system could also prove there to be a ground state lower than degenerate spin ice, where the most likely candidate is the MDG (Melko, den Hertog, Gingras) state [178]. This state has an ordering vector parallel to $\mathbf{q} = (0, 0, 2\pi/a)$ such that there are stacked planes of the ferromagnetic two-in two-out configuration similar to the order by disorder transition in the antiferromagnetic FCC Ising model, which finds an ordered antiferromagnetically stacked ferromagnetic state [179]. The state is only possible if long range dipolar interactions can lift the ground state degeneracy and favour a particular configuration of the spin ice states.

Other rare earth pyrochlore oxide systems include spin glasses, e.g. $\text{Y}_2\text{Mo}_2\text{O}_7$ [180, 181] and spin liquids e.g. $\text{Tb}_2\text{Ti}_2\text{O}_7$ [182, 183]. These will be discussed later in the text in relation to the results found in chapter 4.

2.3 Dipolar interactions

The ice-rule obeying spin ice states can be reproduced using the nearest neighbour ferromagnetic model of the pyrochlore spin structure, with Ising spins aligned along the local $\langle 111 \rangle$ axis [184]. However, this model is a first approximation and the exact behaviour of spin ice is derived from a combination of short range exchange coupling and long range dipolar interactions. The energy of dipolar interactions and nearest neighbour exchange coupling are of the same order of magnitude in spin ice, since orbital overlap is poor between the rare earth ions [185]. The dominating interaction is via superexchange, which is mediated by the oxygen $2p$ orbitals [72]. However, the dipolar model is used to model spin ice since the energy of dipolar interactions is of the order of thermal fluctuations and the strength of the magnetic moments in these systems is $u \sim 10\mu_B$ [72], which is large enough not to neglect these long range interactions.

Spin ice has local order, as all tetrahedra have a two-in, two-out configuration, how-

ever, there is no long range ordering of the spins. This is significant because the two-in two-out degenerate ground states have a net magnetic moment [167], whilst the true bulk magnetisation of spin ice is known to be zero [72]. Therefore, it is deduced that long range contributions must play a major role in spin ice and need to be known up to an infinite distance.

Besides all the reasons above for considering dipolar interactions in spin ice, it was still a mystery how spin ice behaviour could be observed in $\text{Ho}_2\text{Ti}_2\text{O}_7$ when it was known to have antiferromagnetic exchange interactions [144].

The Hamiltonian for spin ice is a contribution from both the exchange and dipolar interactions [72]:

$$\mathcal{H} = -J \sum_{\langle i,j \rangle} S_i \cdot S_j + Dr_{nn}^3 \sum_{i>j} \frac{S_i \cdot S_j}{|r_{ij}|^3} - \frac{3(S_i \cdot r_{ij})(S_j \cdot r_{ij})}{|r_{ij}|^5} \quad (2.2)$$

Where D is the dipolar interaction defined by $D = \mu_0 u^2 / 4\pi r_{nn}^3$, r_{nn} is the nearest neighbour distance such that $r_{nn} = (a/4)\sqrt{2}$ and the lattice parameter $a \sim 10 \text{ \AA}$ for a cubic unit cell [72]. S_i and S_j are three-component unit vectors, which have a unit length ($|S_i| = 1$). The four body centred cubic axes of the spins are given in equation 2.3 [163]:

$$S_1 = \frac{\sigma_1}{\sqrt{3}} \begin{pmatrix} -1 \\ -1 \\ +1 \end{pmatrix} S_2 = \frac{\sigma_2}{\sqrt{3}} \begin{pmatrix} +1 \\ +1 \\ +1 \end{pmatrix} S_3 = \frac{\sigma_3}{\sqrt{3}} \begin{pmatrix} +1 \\ -1 \\ -1 \end{pmatrix} S_4 = \frac{\sigma_4}{\sqrt{3}} \begin{pmatrix} -1 \\ +1 \\ -1 \end{pmatrix} \quad (2.3)$$

If these spin identities are substituted into the dipolar Hamiltonian then taking the dot product of S_i with neighbouring S_j results in $S_i \cdot S_j = (-1/3)\sigma_i\sigma_j$. The terms $\sigma = \pm 1$ are the pseudo spins (or Ising variables) to denote whether a spin points into a tetrahedron or out of a tetrahedron, which was described for the ice rules previously. Since $r_{ij} = 1/\sqrt{2} \times (1, 1, 0)$ where $(1, 1, 0)$ is the vector of the nearest neighbour spin, then $(S_i \cdot r_{ij})(S_j \cdot r_{ij}) = -(2/3)\sigma_i\sigma_j$ and the Hamiltonian in equation 2.2, can be rewritten as the nearest neighbour dipolar and exchange Hamiltonian:

$$\mathcal{H}_{\text{eff}} = \sum_{\langle ij \rangle} J_{\text{eff}} \sigma_i \sigma_j \quad (2.4)$$

This holds for the nearest neighbour exchange and dipolar interactions, so that $r_{ij} = r_{nn}$, $J_{\text{eff}} = J_{\text{nn}} + D_{\text{nn}}$, where $J_{\text{nn}} = J/3$ and $D_{\text{nn}} = 5D/3$, with $D > 0$. This way of describing the Hamiltonian ensures that an antiferromagnet should demonstrate spin ice behaviour when $J > -5D$. Holmium and Dysprosium titanate have $J \approx -1.65$ and $J \approx -3.72$, respectively, so that $J_{\text{eff}} > 0$ and the spin ice criterion is obeyed with $H_{\text{eff}} < 0$ in equation 2.4. This is deduced when only taking into account nearest neighbour dipolar and exchange interactions.

Dipolar interactions are complicated, since the interactions decay slowly as $1/r_{ij}^3$ and the interactions are anisotropic in that they depend on the relative orientation of the interacting moments with respect to the separation vector, hence the $(S_i \cdot r_{ij})$ terms. Therefore in actual fact, even when $J < 0$, which it is for the spin ice state, if $|J_{\text{nn}}| \gg D_{\text{nn}}$, then the system undergoes a transition into an all-in all-out ground state from the two-in two-out state. It is from the ratio of nearest neighbour exchange interactions, J_{nn} and the nearest neighbour dipolar interactions, D_{nn} that one can obtain the phase diagram with respect to temperature shown in figure 4.1 of section 4.1.

Longer range effects from the dipolar interactions (when $J_{\text{nn}}/D_{\text{nn}} \rightarrow 0$) are “screened” to obtain the short range behaviour from the nearest neighbour model [72]. Hence, the simplicity of the nearest neighbour behaviour that comes from the spin ice rules are almost sufficient in describing the spin ice system with long and short range interactions.

2.3.1 The dumbbell model and magnetic monopoles

Castelnovo *et. al.* [186] formulated the “dumbbell model”. This takes the point dipoles of the dipolar model (a magnetic moment) and stretches them the length of one diamond site to another to form infinitesimally thin needles such that each pole resides on the ends of the needle (see figure 2.3). The length of the needle coincides with connect-

ing the centres of the two tetrahedra that the point dipole resided upon, so the poles are exactly on the centres of the two tetrahedra. It becomes clear that this is not reasonable physically to have same sign magnetic poles overlapping exactly, however the dumbbell model exactly reproduces the interaction between real neighbouring dipoles separated by a large distance [186].

With all the point dipoles of every tetrahedron approximated with the dumbbell model and the overlap of the poles at the centres, the long range part of the dipolar interaction is perfectly screened [72]. This screening of the long range dipolar interactions in the model mean that the Pauling entropy from the ice rules is the same entropy as it is in spin ice (represented by the long range dipolar model).

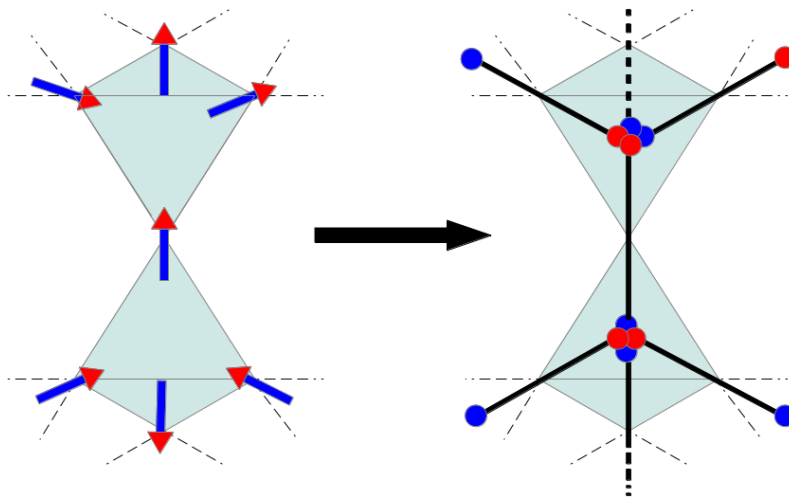


Figure 2.3: A schematic of how the point dipole arrangement in the magnetic rare earth pyrochlore system maps onto the dumbbell model. This is shown for two tetrahedra which obey the spin ice rules with a two-in, two-out spin configuration. The black lines represent the infinitesimally small needles that terminate with the poles equivalent to that of the point dipole. Each pole in the dumbbell model is located in the centre of the tetrahedra (a diamond site).

The dumbbell model has made it possible to identify the net pole/ net magnetic charge, Q , at the centres of every tetrahedron (the diamond lattice). The charge on a

diamond site i is given by Q_i , such that,

$$Q_i = \sum_j M_{ij} \quad (2.5)$$

where,

$$M_{ij} = \pm \left(\frac{u}{a}\right) \quad (2.6)$$

j indicates the neighbouring tetrahedra that the magnetic moment is shared with, u is the strength of the magnetic moment and a is the length of the dipole. Due to the summation in equation 2.5, the two-in two-out spin ice state, has $Q = 0$, which is true for any divergence free state. Excitations from this lowest energy ground state, $Q = 0$, produce monopole-antimonopole pairs (M-AM) with $Q = \pm 2u/a$. The singly charged monopoles have “three-in one-out” or “one-in three-out” magnetic moment configurations on a tetrahedron and further excitation cause the formation of “four-in” and “four-out” states with $Q = \pm 4u/a$. If q is defined as Q in units of $2u/a$ then one can say a spin ice state has $q = 0$, the monopoles and antimonopoles have $q = \pm 1$ (singly charged) and the all-in all-out configuration has $q = \pm 2$ (doubly charged). This is how the states are defined by convention.

The monopoles in the pyrochlore system must always be created and destroyed in pairs as the overall charge in the system must always remain equal to zero. Flipping a spin to form these oppositely charged poles (excitations) costs energy. In the nearest neighbour model, the energy cost is $\sim 4J_{\text{eff}}$ [185], however, in reality the energy of a spin flip is dependent on the random fields created by close proximity bound monopole pairs and therefore can have a range of energies [187]. To separate monopole pairs further with subsequent spin flips costs a finite amount of energy because including the dipolar Hamiltonian leads to an effective Coulombic interaction for monopole pairs separated by a distance r [185]. However this finite energy cost never diverges in spin ice, and so these monopole pairs can separate as far apart as the lattice which could be infinite [186] and as though the monopoles were “freely moving” (deconfined), with a chain of flipped spins showing their paths. The monopoles in artificial spin ice, on the other hand, can only be described as emergent magnetic monopoles – quasiparticles –

that form as a consequence of the spin configuration [188].

Strings in the rare earth pyrochlore lattice

For a real monopole (see figure 2.4 (a)), otherwise known as Dirac monopoles and still unobserved, the M-AM pair must be connected by an unphysical, unobservable string [189]. These must be a tensionless string of flipped dipoles in the continuum limit [163], whereby increasing the length of the string should not affect the energy of creating more overturned dipoles. This is the case for the classical magnetic monopoles observed in spin ice, where the energy cost of flipping spins does not diverge with the length of the string as no domain walls form along the string and hence the monopoles behave as though they are deconfined [186]. However, the strings are observable, as can be seen in figure 2.4 (b) and compensating flux travels along these strings since the monopoles in spin ice are not quantised [186] (discussed further in the next section).

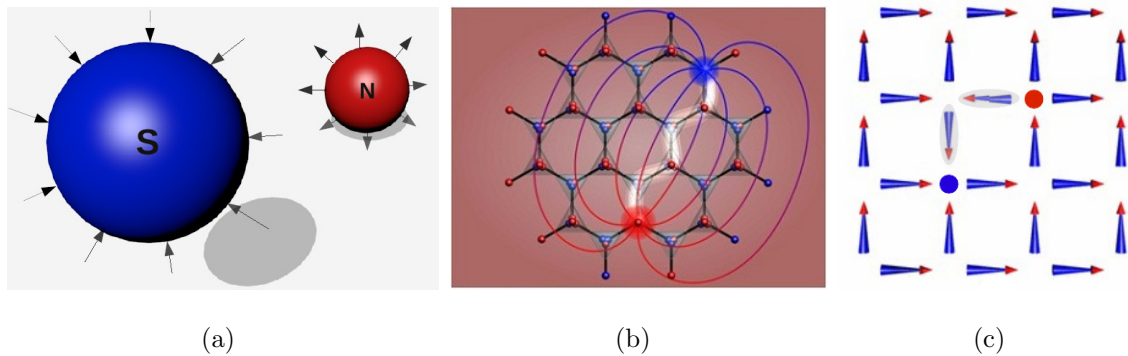


Figure 2.4: Magnetic monopoles. In all three figures the largest red and blue circles represent the south and north polarity of the M-AM pair. The white/shaded areas in (b) and (c) are the observable strings. (a) “real” magnetic monopoles with an unobservable Dirac string and field lines; (b) magnetic monopoles in spin ice with an observable but tensionless string and (c) effective magnetic monopoles in artificial spin ice, which are observable and have a tension of the order bX (described in the text). Images were taken and modified from references [186] and [190] for (b) and (c), respectively.

In artificial spin ice, spin flips have an associated energy cost behaving as bX [191],

where X is the length of the spin flips (otherwise referred to as strings in relation to Dirac strings) and $b > 0$ is the effective string tension (see figure 2.4 (c)). As the monopoles are separated further from each other, the energy coming from the bX term increases. The authors in reference [191] claim that at a certain temperature proportional to the string tension, b , that the string tension vanishes due to entropic effects and hence the charge defects would freely move as real monopoles do.

Coulombic interaction with monopoles

The monopoles in spin ice interact via Coulombic interactions [186]. Therefore, the Coulomb potential between pairwise magnetic charges is given by,

$$\mathcal{V}_{ij} = \begin{cases} \frac{\mu_0}{4\pi} \frac{Q_i Q_j}{r_{ij}} & i \neq j \\ \frac{1}{2} \nu_0 Q_i^2 & i = j \end{cases} \quad (2.7)$$

where μ_0 is the magnetic permeability in free space, ν_0 is the on-site Coulombic interaction, which corresponds to the J_{eff} that was derived earlier and r_{ij} is the distance between the monopole charges $i = 1, \dots, N_d$, where N_d is the number of diamond sites.

In the dipolar model the lattice of interest is the pyrochlore lattice, whilst in the dumbbell model, the lattice of interest is the diamond lattice. Therefore neighbouring dipoles on the same tetrahedron of the pyrochlore lattice are related with the dumbbell model by the charges on the ends of dumbbells that overlap at the corresponding diamond site. This is what is meant by the on-site Coulomb interaction. In equation 2.7, the on-site charge is the Q_i^2 term for the charge on the diamond site of interest and for $i \neq j$, the $Q_i Q_j$ term is for the interaction between charges on diamond site i and its neighbour j .

Dirac monopoles also interact via Coulombic interaction so the free monopoles and the spin ice monopoles are the same in this sense, however, they differ since the monopoles in spin ice are not quantised to the fundamental electric charge [192] as they are in real monopoles. In fact, the magnetic charges in spin ice can vary with the diamond lattice constant. Monopoles in spin ice also correspond to divergences in the

magnetic field \mathbf{H} or magnetic moment \mathbf{M} but not the magnetic induction \mathbf{B} [163], so that:

$$\nabla \cdot \mathbf{B} = \mu_0 [\nabla \cdot (\mathbf{H} + \mathbf{M})] = 0 \quad (2.8)$$

The monopole charges in artificial spin ice do not interact solely via Coulombic interactions. Rather, in addition, the monopoles are attracted by an entropically driven force when they are close to one another [191, 193]. This is because there are more ways of rearranging the surrounding dipoles, when the charges forming a given pair are in close contact than when they are further apart. This yields an additional ‘ $\ln r_{ij}$ ’ term with the $1/r_{ij}$ Coulombic relationship [191]. However, with the development of a stacked square artificial spin ice, as mentioned in section 2.2, giving rise to the MDG state [177], there is a debated possibility that monopoles interacting with Coulombic interactions, as seen in spin ice, could exist in these nanoscaled systems [176, 177, 190, 194].

Chapter 3

Monte Carlo simulations

Monte Carlo (MC) methods can be used for calculating a variety of quantities including integrals, probabilities, confidence limits and partition functions, for which this is the only known numerical method for large lattices. To enable flexibility in the use of this method, a specific probability density function ($P_{DF}(x)$) is chosen to model the behaviour of the system of interest. This explanation of MC methods will follow the account by Newman and Barkema [18].

The use of MC simulations in spin ice and in the magnetic multilayer systems, is to obtain a thermodynamic distribution that mimics the real system as closely as possible. This enables one to extract physical quantities that describe the system at a particular temperature. For the thermodynamic distribution of a system, it is necessary to simulate the thermal fluctuations of the system from one state to another, as governed by a Boltzmann distribution. One must find the expectation value of a certain physical quantity, \mathcal{Q}_A , in state A and specifically for the simulations in this thesis, this is given by the time average over the states that the system has passed through, $\langle \mathcal{Q} \rangle$, as given by equation 3.1 [18],

$$\langle \mathcal{Q} \rangle = \sum_A \mathcal{Q}_A w_A(t) \quad (3.1)$$

where $w_A(t)$ can also be defined as the probability that the system will be in a state A at time t . We can see from this equation that the most probable states will therefore

contribute most to the time averaged physical quantity. Alternatively, $\langle \mathcal{Q} \rangle$ can be expressed in terms of the equilibrium occupation probabilities, p_A , given by:

$$p_A = \lim_{t \rightarrow \infty} w_A(t). \quad (3.2)$$

As $t \rightarrow \infty$, the equilibrium state of the system is reached so that w_A is equal to the equilibrium occupation probability. Hence when the system is in thermal equilibrium with its surroundings at a temperature T , then equation 3.2 can be re-written as equation 3.3,

$$p_A = \frac{1}{Z} \exp(-\beta_T E_A) \quad (3.3)$$

where Z is the partition function $Z = \sum \exp(-\beta_T E_A)$, $\beta_T = \frac{1}{k_B T}$, k_B is the Boltzmann constant and E_A is the energy of the state A . Using equation 3.3 one can obtain the following expression,

$$\langle \mathcal{Q} \rangle = \sum_A \mathcal{Q}_A p_A = \frac{1}{Z} \sum_A \mathcal{Q}_A \exp(-\beta_T E_A) \quad (3.4)$$

which corresponds to a Boltzmann distribution.

The physical quantities can be obtained easily from the partition function due to the relationship with the Helmholtz free energy, F :

$$F = U - TS = -k_B T \log Z \quad (3.5)$$

where U is the internal energy and S is the entropy of the system. Other thermodynamic quantities, such as the heat capacity, can be derived from U and S .

The systems studied in this thesis each possess a large set of states, A , too numerous to possibly sample every one. Importance sampling is the means by which a subset of configurations is chosen to find an approximate $\langle \mathcal{Q} \rangle$. This method takes into account only the states which contribute most importantly to the sums in equation 3.4 (the expectation value) and in terms of the Boltzmann distribution, this means to sample states with a probability according to their Boltzmann weight and not with equal sampling probability.

By following this method, only a small portion of states need to be sampled to obtain accurate results for the physical quantities. Most of the error in the results of the simulations stem from statistical errors in the calculation arising because the whole system is not sampled [18]. In this thesis, the expectation values of the physical quantities are a time average and therefore the errors may be minimised by increasing the length of time for which the simulations run. This provides the system the opportunity to approach equilibrium, which one can then observe multiple expectation values and average them.

The dynamics of the MC simulation must follow,

$$\frac{dw_A}{dt} = \sum_B \left[w_B(t)R(B \rightarrow A) - w_A(t)R(A \rightarrow B) \right] \quad (3.6)$$

which shows the rate of transition, R , of the system into an initial state (A) and the rate of transition of the system into another state, B . If one term is greater than the other then the system has not reached equilibrium, but if $\frac{dw_A}{dt} = 0$ then the system has reached equilibrium and an expectation value can be observed.

In addition to finding the expectation values of the physical quantities, the fluctuations in these quantities is also of importance. Fluctuations are most usefully represented by the mean squared deviation:

$$\langle (x - \langle x \rangle)^2 \rangle = \langle x^2 \rangle - \langle x \rangle^2 \quad (3.7)$$

where x is some fluctuating quantity in the system. Referring to section 1.2.3, it is known that every thermodynamic variable X has a conjugate variable Y . Therefore, using the free energy whilst keeping Y fixed, the fluctuation in quantity X can be deduced by:

$$-\frac{\partial F}{\partial Y} = \langle X \rangle = \frac{1}{\beta_T} \frac{\partial \log Z}{\partial Y} = \frac{1}{Z} \sum_A X_A e^{-\beta_T E_A} \quad (3.8)$$

$$-\frac{\partial^2 F}{\partial Y^2} = \frac{\partial \langle X \rangle}{\partial Y} = \frac{1}{\beta_T} \frac{\partial^2 \log Z}{\partial Y^2} = \beta_T (\langle X^2 \rangle - \langle X \rangle^2) \quad (3.9)$$

Two of the most important quantities investigated in the magnetic systems in this thesis are the magnetisation and the fluctuations in the magnetisation, given by the magnetic susceptibility, χ_T . Since M is coupled with H as the conjugate variable then,

$$\frac{\partial \langle M \rangle}{\partial H} = \beta_T (\langle M^2 \rangle - \langle M \rangle^2). \quad (3.10)$$

However, conventionally, the susceptibility and magnetisation are measured as the susceptibility per spin and magnetisation per spin, so that:

$$\langle m \rangle = \frac{1}{N} \left\langle \sum_{i=0}^N s_i \right\rangle \quad (3.11)$$

$$\chi_T = \beta_T N (\langle m^2 \rangle - \langle m \rangle^2). \quad (3.12)$$

In the simulations, temperature is in energy units [18] of $k_B T/J$. The Boltzmann constant, k_B is taken to be 1. The heat capacity is found by equation 3.13, which is the first derivative of the internal energy with respect to temperature.

$$c = \frac{\partial \langle E \rangle}{\partial T} = \frac{k_B \beta_T^2}{N} (\langle E^2 \rangle - \langle E \rangle^2) \quad (3.13)$$

3.1 Markov chain and Markov process

As mentioned previously, there is a subset of states that need to be sampled based on their Boltzmann weighting to eventually obtain the time averaged physical quantity $\langle Q \rangle_{\text{approx}}$. The Markov process generates the set of states, where state B is generated from state A with the transition probability $P(A \rightarrow B)$, which obeys the following two rules:

- the transition probabilities do not vary over time and
- depends only on the configuration of state A and B , and not any other state.

The sequence of states generated by successive application of the Markov process is known as the Markov chain.

There are constraints on the simulations which ensure the states generated obey the Boltzmann distribution, known as ergodicity and detailed balance and these are explained in the next two sections.

3.2 Ergodicity

The probability of a transition from state A to another state B must satisfy the *closure relation*:

$$\sum_B P(A \rightarrow B) = 1 \quad (3.14)$$

This avoids a high number of rejected states, though $P(A \rightarrow A)$ is also allowed (this is to say there is a finite probability that the system remains in state A).

Ergodicity ensures that all states should be accessible from any other state through a finite number of intermediate states if the simulation is given a long enough time to run. If this were otherwise, then equation (3.14) could be zero. Ergodicity demonstrates that there must be at least one accessible pathway to get from state A to B , which obeys Boltzmann statistics, as required in this thesis.

3.3 Detailed Balance

Detailed balance ensures that upon reaching equilibrium, the desired distribution is generated and p_A is attained for any state A when the simulation is run for long enough. For this to be the case, equation (3.15) must hold [18]:

$$p_A = \sum_B p_B P(B \rightarrow A) \quad (3.15)$$

where the closure relation has been incorporated in this expression. This indicates that the overall rate at which transitions occur from state A is equal to the overall rate for which transitions occur to state A (i.e. on average, A to B transitions take place as often as B to A).

As a result of the detailed balance condition and ergodicity, the transition probabilities should satisfy expression (3.16):

$$\frac{P(A \rightarrow B)}{P(B \rightarrow A)} = \frac{p_B}{p_A} = \exp(-\beta_T(E_B - E_A)) \quad (3.16)$$

Using the Boltzmann distribution is specific to this study, such that the ratio of the probability of being in state B to that in state A is set to a Boltzmann distribution. This would differ depending on the distribution of interest. I only focus on classical MC methods in this thesis, but quantum MC methods differ here since the distribution is not known and has to be solved for [195]. Quantum MC methods are however, more accurate in obtaining the variational energy of the system since parameters can be altered in the trial wavefunctions of the Hamiltonian to minimise the error in this value [196].

3.4 Metropolis algorithm

The Metropolis algorithm was introduced by Metropolis *et. al.* in 1953 [197]. This method uses a set of selection probabilities $g(A \rightarrow B)$, to generate a new state B and then a set of acceptance ratios, $A(A \rightarrow B)$, are chosen to decide whether to reject or accept the new state. If the state is accepted then the system is updated to this new state otherwise it remains in its present state A and this is repeated continuously.

For each of the possible states B , $g(A \rightarrow B)$ is set to $\frac{1}{N}$ (since there are N selection probabilities in a system size N with single spin flips). As $P(A \rightarrow B) = g(A \rightarrow B)A(A \rightarrow B)$ and $P(B \rightarrow A) = g(B \rightarrow A)A(B \rightarrow A)$, then the detailed balance condition, as shown in equation 3.16, becomes [18],

$$\frac{A(A \rightarrow B)}{A(B \rightarrow A)} = \exp(-\beta_T(E_B - E_A)). \quad (3.17)$$

This specific choice of the acceptance ratio defines the Metropolis algorithm, where one of the acceptance ratios can be set to one to maximise the acceptance rate. This is chosen to be the most favourable transition, i.e. going from a state of high energy to

low energy.

Below is an outline of the single spin flip Metropolis Monte Carlo method used in the simulations in 7 steps:

1. Evaluate the energy, E_A , of the initial state A of the system.
2. Pick a random spin and flip the spin temporarily. For an Ising spin, the spin flip is a simple case of flipping the spin antiparallel to its current direction, whilst for XY and Heisenberg spins, a random angle of the spin is chosen and polar co-ordinates are used to find the cartesian equivalents.
3. Evaluate the new energy of the system, E_B .
4. If $E_B \leq E_A$, then $A(A \rightarrow B)$ is set to one and the transition is always accepted.
5. If $E_B > E_A$, then $A(A \rightarrow B) = \exp(-\beta_T(E_B - E_A))$, which means the transition could be accepted as long as this value is greater than some uniform random number generated, z (such that $0 \leq z < 1$), otherwise it is rejected.
6. If the flip is accepted set $E_A = E_B$ and update the spin configuration of the system permanently. If it is rejected then $E_A = E_A$ and do not change the spin configuration.
7. Repeat the steps from point 2 onwards.

Since single spin flip dynamics have been chosen to carry out the Metropolis method, then the difference in state A to the next state B is by the flip of one spin. The algorithm can equally be implemented with multiple spin flips at once or with cluster updates. Multiple spin flips in frustrated systems are often known as loop algorithms. Loop algorithms are particularly useful at low temperature when the dynamics of a system are slow and single spin flips are too high in energy. The MDG state, mentioned in chapter 2 was found using a numerical loop algorithm [178]. Given that this state could not be found using single spin flips emphasises how important it can be to sample the low temperature system with loop updates. The loop algorithm used to determine

some of the results in chapter 4 is explained in the next section.

Since the Metropolis algorithm follows the Boltzmann distribution, then the system will always sample near the lowest energy configuration over time. Time, in these simulations, is measured by the number of Monte Carlo steps per spin (MCS/s). A single MCS is following the 7 steps above (i.e. undergoing a single spin flip attempt), 1 MCS/s is undergoing $N \times \text{MCS}$ (i.e. the number of spin flip attempts should be the order of the system size). It is after 1 MCS/s that a physical quantity of the system is observed. This is to allow an opportunity for every spin to undergo the Metropolis algorithm. Increasing the MCS and MCS/s increases the validity of the results as the system is thoroughly sampled. For most of the simulations in this thesis, I use 10^5 MCS/s for observations, which is to say that a physical quantity is extracted 10^5 times, summed together and then averaged. Equilibration of the energy as a function of MC time for the main system in each project can be found in appendix B. The number of equilibration MCS/s are justified by these results.

3.5 Simulations of classical spin models on the pyrochlore lattice

The following sections are dedicated to the simulation and analytical methods used with the Monte Carlo simulations for investigating the system in chapter 4.

3.5.1 Ewald summation

The Ewald method [198] is used to help evaluate the energy of states more efficiently when long range interactions are considered in a system. In chapter 4, magnetic monopoles in a “spin-like” system are investigated and therefore long range Coulombic interactions between these magnetic charges are of interest in the Ewald summation. Therefore I will briefly summarise the basic theory of this method.

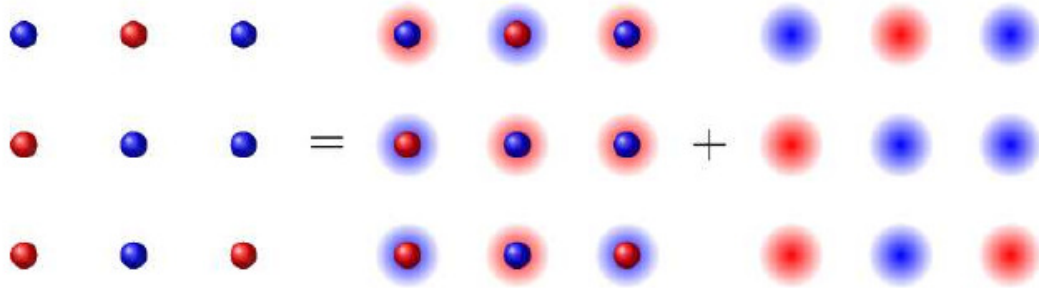


Figure 3.1: A schematic of the two fast converging potentials which sum to the direct space of the electrostatic potential. The real point charges are shown on the left side of the equation. On the right side of the equation, the left figure is the real point charges with a Gaussian charge distribution of opposite sign added to it ϕ_b , whilst the right figure is the Gaussian charge distribution of the point charges ϕ_a [167].

The total energy of the system is determined by the Coulombic energy, U_C , between N magnetic charges (considered as point charges), q_i , which is given by:

$$U_C = \frac{1}{2} \sum_{i=1}^N q_i \phi_i. \quad (3.18)$$

ϕ_i is the electrostatic potential,

$$\phi_i = \sum_{j=1}^N \frac{\mu_0 q_j}{4\pi r_{ij}}, \quad (3.19)$$

where the summation is for $j \neq i$, r_{ij} is the separation between the magnetic charge of interest and the magnetic charge it is interacting with. Obtaining the electrostatic potential is very slow and inefficient for all the point charges i in the system as there are a vast number of interactions. The Ewald summation solves this problem by splitting the slow converging total potential, ϕ_i , into the sum of two fast converging potentials given by:

$$\phi_i = \phi_a + \phi_b \quad (3.20)$$

See figure 3.1 for a depiction of this equation.

The system is treated with periodic boundaries and each point charge is considered

to be the centre of a spherical Gaussian charge distribution with a density $\rho(\mathbf{r})$,

$$\rho(\mathbf{r}) = q_t \left(\frac{\eta}{\pi} \right)^{3/2} \exp(-\eta r^2), \quad (3.21)$$

where q_t is the total charge associated with a point charge and η is the range parameter (width of the Gaussians) which should be chosen carefully to ensure both sums (ϕ_a and ϕ_b) converge rapidly [2] (usually chosen to be 1 [167]).

One of the fast converging potentials, ϕ_a , is a continuous series of Gaussian charge distributions of each charge site, which have the same signs as those of the real point charges. Since the electrostatic potential is calculated for $j \neq i$, then the charge distribution at the site of interest i does not contribute to the potential ϕ_a (or ϕ_b) and hence this potential, ϕ_{self} , is subtracted from ϕ'_a (where ϕ'_a is the potential ϕ_a before ϕ_{self} is subtracted).

The other fast converging potential, ϕ_b , consists of a lattice of point charges with opposite sign Gaussian distributions superimposed on the real point charges, which yields a net neutrality over the system. It can already be deduced that by adding the Gaussian distribution in ϕ_a (the same charge as the real point charges), to the opposite sign Gaussian distribution in ϕ_b , that the two potentials will cancel and result in the real point charges remaining from ϕ_b . So this method is not altering the system, it is just a manipulation of it.

To ensure the convergence of these two potentials is fast, both potentials are dependent on the width of the Gaussian peaks, η and whilst ϕ_a is evaluated in Fourier space, ϕ_b is evaluated in direct space.

To begin the derivation of ϕ_a , the Fourier series of ϕ'_a and the charge density $\rho(\mathbf{r})$ are:

$$\phi'_a = \sum_{\mathbf{G}} c_{\mathbf{G}} \exp(i\mathbf{G} \cdot \mathbf{r}) \quad (3.22)$$

and

$$\rho(\mathbf{r}) = \sum_{\mathbf{G}} \rho_{\mathbf{G}} \exp(i\mathbf{G} \cdot \mathbf{r}) \quad (3.23)$$

where \mathbf{G} is 2π times a vector in the reciprocal lattice.

The Poisson equation combines these two equations by the relationship:

$$\nabla^2 \phi'_a = -4\pi\rho(\mathbf{r}) \quad (3.24)$$

and it is then possible to solve for the coefficient, $c_{\mathbf{G}}$, in equation 3.22 by inserting equation 3.22 and 3.23 into equation 3.24,

$$c_{\mathbf{G}} = \frac{4\pi\rho_{\mathbf{G}}}{G^2}. \quad (3.25)$$

The next step is to integrate the charge density over a single cell multiplied by $\exp(-i\mathbf{G} \cdot \mathbf{r})$ over all space. This is possible by multiplying both sides of equation 3.23 by $\exp(-i\mathbf{G} \cdot \mathbf{r})$, substituting in $\rho(\mathbf{r})$ for a single cell, where r is replaced with $r - r_t$ and integrating over all space.

$$\rho_{\mathbf{G}}\Delta = \int_{\text{allspace}} \sum_t \rho(\mathbf{r}) \exp(-i\mathbf{G} \cdot \mathbf{r}) .d\mathbf{r} \quad (3.26)$$

$$\rho_{\mathbf{G}}\Delta = \int_{\text{allspace}} \sum_t q_t \left(\frac{\eta}{\pi}\right)^{3/2} \exp(-\eta(r - r_t)^2) \exp(-i\mathbf{G} \cdot \mathbf{r}) .d\mathbf{r} \quad (3.27)$$

where Δ is the volume of one unit cell. With some mathematical manipulation, equation 3.27 yields the Fourier transform of $\rho(\mathbf{r})$, which is $\rho(\mathbf{G})$, in terms of the structure factor $S(\mathbf{G})$ (Fourier transform of the correlation function).

$$\rho_{\mathbf{G}}\Delta = S(\mathbf{G}) \exp(-G^2/4\eta), \quad (3.28)$$

where $S(\mathbf{G}) = \sum_{q_t} \exp(-i\mathbf{G} \cdot \mathbf{r})$. Substituting equations 3.28 and 3.25 into ϕ'_a in equation 3.22 gives,

$$\phi'_a = \sum_{\mathbf{G}} \frac{4\pi}{\Delta} G^{-2} S(\mathbf{G}) \exp(i\mathbf{G} \cdot \mathbf{r} - (G^2/4\eta)) \quad (3.29)$$

and when at the origin, $\mathbf{r} = 0$, which gives:

$$\phi'_a = \sum_{\mathbf{G}} \frac{4\pi}{\Delta} G^{-2} S(\mathbf{G}) \exp(-G^2/4\eta). \quad (3.30)$$

ϕ_{self} is the interaction of the point charges with the Gaussian charge distribution surrounding it. Using the Poisson equation with spherical coordinates at the reference point i ($r = 0$), ϕ_{self} is given by:

$$\phi_{\text{self}} = \int_0^\infty (4\pi r^2 dr) (\rho/r) \quad (3.31)$$

$$= 2q_i \left(\frac{\eta}{\pi}\right)^{1/2}. \quad (3.32)$$

Therefore, overall $\phi_a = \phi'_a - \phi_{\text{self}}$ as shown below,

$$\phi_a = \frac{4\pi}{\Delta} \sum_{\mathbf{G}} S(\mathbf{G}) G^{-2} \exp(-G^2/4\eta) - 2q_i \left(\frac{\eta}{\pi}\right)^{1/2}, \quad (3.33)$$

where q_i is the charge on the diamond lattice point of interest.

The other potential, ϕ_b , required to obtain ϕ_i is evaluated in direct space at the reference point. Unlike ϕ_a , the self interaction is not subtracted from the potential because the tails of the Gaussian distributions from surrounding point charges overlap with this site. It is also important to take into account the surrounding Gaussian distributions of opposite charge. One can summarise that these contributions pertain to:

$$q_l \left[\frac{1}{r_l} - \frac{1}{r_l} \int_0^{r_l} \rho(\mathbf{r}) d\mathbf{r} - \int_{r_l}^\infty \frac{\rho(\mathbf{r})}{r} d\mathbf{r} \right]. \quad (3.34)$$

The first term is from the point charges themselves, where q_l is the charge on the site and r_l is a particular radius around the point charge. The second term is from the surrounding spherical point charges which have their Gaussian distribution tails overlapping within the radius r_l from the site of interest. The third term is from the remaining end of the oppositely charged Gaussian distributions that lay outside r_l .

Determining the interaction of point charges with a surrounding Gaussian charge distribution has already been found for ϕ_{self} (equation 3.31) and the same principal

is applied to ϕ_b , which has an oppositely charged Gaussian distribution from the real point charges. Therefore, it is again necessary to use the Poisson equation for a charge at the origin $r_l = 0$. In the mathematical steps between equations 3.31 and 3.32, there is an error function generated $\text{erf}(\sqrt{\eta}r)$ where $\text{erf}(x) = \frac{2}{\sqrt{\pi}} \int_0^x \exp(-u^2) du$. In this case, because the charges are of an opposite sign, the error function is $\text{erfc}(\sqrt{\eta}r) \equiv 1 - \text{erf}(\sqrt{\eta}r)$ as shown below.

$$\phi_b = \sum_l \frac{q_l}{r_l} \text{erfc}(\eta^{1/2} r_l) \quad (3.35)$$

such that,

$$\text{erfc}(x) = \left(\frac{2}{\sqrt{\pi}} \right) \int_x^\infty \exp(-u^2) du \quad (3.36)$$

Overall, the Ewald summation, showing the total potential of the magnetic charge of interest in a field caused by all its surrounding magnetic charges, is given by:

$$\phi_i = \left[\frac{4\pi}{\Delta} \sum_{\mathbf{G}} S(\mathbf{G}) G^{-2} \exp\left(-\frac{G^2}{4\eta}\right) - 2q_i \left(\frac{\eta}{\pi}\right)^{\frac{1}{2}} \right] + \left[\sum_l \frac{q_l}{r_l} \text{erfc}\left(\eta^{\frac{1}{2}} r_l\right) \right] \quad (3.37)$$

where the two fast converging sums, ϕ_a and ϕ_b , are distinguished by the square brackets in equation 3.37.

3.5.2 The Worm Algorithm

Single spin flips are not always sufficient to obtain the lowest energy configuration of a system, particularly at low temperatures and at the critical point [199]. This is because using these dynamics with a low thermal energy is unfavourable when sampling between low energy states that can only be accessed via the creation of an excitation. Single spin flips that would introduce an excitation in the system are more likely to be rejected by the Metropolis algorithm at these temperatures and hence the numerous rejections slow the dynamics of the simulation. In my experience and more generally, even when an update is accepted to form the excitation, if that spin is chosen again, the likelihood is that it will flip back to its original state so that over time no change in the configuration of the system occurs. This means it is not possible to sample the configurational space at the current energy of the system and therefore requires another

method which can sample the lower energy states at low temperatures and within the critical region.

In spin ice, there is a six-fold degenerate ground state and to access each degenerate state would require at least the consecutive spin flip of six spins making a hexagonal loop (see figure 3.2).

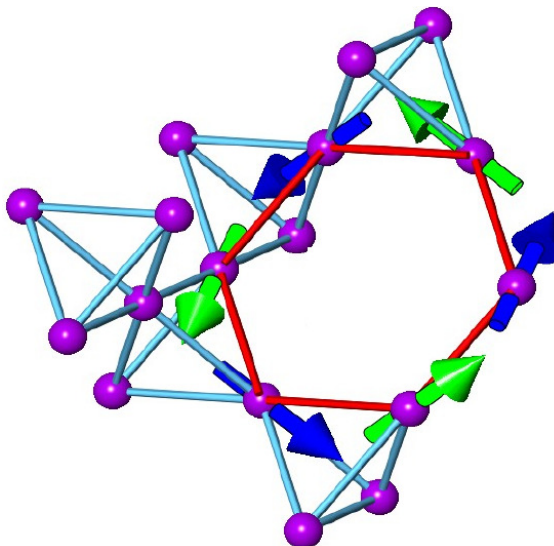


Figure 3.2: The smallest spin flip loop that can be implemented in spin ice. Only the blue and green spins contributing to the hexagonal loop are shown, whilst all other spins on each tetrahedron have been omitted from the diagram for clarity. Image taken from reference [200].

The hexagonal loop is the smallest spin flip loop that can be made in spin ice [201] that will not cost any overall energy but change the spin configuration. Loops generated from the worm algorithm can be much longer, particularly in $3d$ systems such as the pyrochlore with periodic boundaries. In these cases, there are a greater number of loops produced from closing after crossing the periodic boundary of the system (winding loops), than there are short loops produced from loops closing before passing the periodic boundary (non-winding loops) [201].

The worm algorithm uses a looping method as shown above to sample the energy configuration [199, 202, 203], however, unlike general loop algorithms, the worm algorithm samples alternating orientations of spins (specific definition relating to spin ice Ising spins) [201]. For instance, if a spin pointing toward the centre of a tetrahedron is denoted by i and a spin pointing away from the centre is denoted by $-i$; then in the simulations, if a worm enters a tetrahedron via a spin with orientation i , it is predetermined to exit the tetrahedron via a spin with orientation $-i$ [201]. This loop ends when it reaches the initial spin.

The difference in the resulting configurations produced by using these updating methods (a general loop algorithm and the worm algorithm), is made most evident when magnetic excitations are present in the spin ice system. For a general loop algorithm, the net magnetic charges residing on the diamond lattice from a three-in one-out or one-in three-out configuration of the respective pyrochlore spin lattice can change between updates. For instance, diamond site 10 could have a $+1$ net charge and after a loop update, have a -1 net charge. This is because a three-in one-out tetrahedron can become a one-in three-out tetrahedron. This is not possible using the worm algorithm due to the constraint that flipping an “in” spin must be followed by flipping an “out” spin and vice versa. Therefore, the charge on the respective diamond site will remain unchanged whilst the spin configuration is sampled. The worm algorithm is used to sample the spin configuration of the monopole crystal at low temperatures and low chemical potential and it is because of its ability to conserve the net magnetic charge on the diamond lattice that it has supported the remarkable result in chapter 4.

In brief, a simple worm algorithm works by creating two defects in the system and moving them around in a random walk independently of one another until they meet at the same vertex and annihilate one another [199, 204]. To do this, one chooses the defect v to move with a probability P , otherwise the other defect is chosen. A neighbouring site v' of the chosen defect is then uniformly and randomly chosen and an update is proposed to move $v \rightarrow v'$ and to change the occupation status of the

edge vv' . With the configuration A , the new status of the edge should increase the worm by $A \rightarrow A\Delta vv'$. $A\Delta vv'$ denotes the symmetric difference of A with vv' [204], which means if vv' has an existing edge, it will be deleted by this update. Lastly is to apply the Metropolis acceptance criterion to the update proposal and if it is accepted then all the steps are repeated until the neighbouring site of v is $v' = \nu$, where ν is the other defect (both defects annihilate) and observables can then be measured. This example is simple though requires non-local connectivity queries to determine the cyclomatic number is changing, which controls the minimum number of edges that need to be deleted to make the system cycle-free [204]. A *self-avoiding* algorithm can be used instead known as the colouring algorithm, which does not require these queries.

Overall the worm algorithm increases the configurational space that is sampled and is a solution to the dynamical issues which arise with single spin flip dynamics.

3.5.3 Autocorrelation functions

To analyse the fluctuations in the magnetisation in the Ising model, Barkema and Newman [203] used the following time displaced autocorrelation expression, χ_T :

$$\chi_T = \int dt' [m(t) - \langle m \rangle][m(t+t') - \langle m \rangle] \quad (3.38)$$

where $m(t)$ is the instantaneous magnetisation at time t , $\langle m \rangle$ is the statistical average magnetisation over Monte Carlo time and $m(t+t')$ is the magnetisation after a time lapse t' from t . From this equation, one can obtain how the spin configuration changes over time. If the orientations of the spins fluctuate in random arrangements relative to their neighbouring spins then this number will be < 0 , but if it is > 0 then there are correlated fluctuations (i.e. spins fluctuate in similar arrangements relative to neighbouring spins). For example, consider the Ising model, if all spins in a region collectively fluctuate between the $+z$ direction and the $-z$ direction, then these spins are correlated; whilst if the fluctuation of spins in another region were such that some spins randomly align parallel and others align antiparallel to one another, these spins

are not correlated. Integrated over time, χ_T is between 1 or 0, where 1 represents correlation and 0 denotes disorder.

The autocorrelation function is known as a one-site, two-time method, which as described, identifies the configuration of the spins (or other properties such as magnetic charges) at time $t = 0$ and later at a time $t = t + t'$. In this thesis, the autocorrelation method is slightly modified from that used by Barkema and Newman to not only monitor the order/disorder of spins, but also that of magnetic charges in the “spin ice-like” system presented in chapter 4.

3.5.4 Neutron scattering and the Coulomb phase

The ground state of spin ice is known to be a Coulomb phase. To date, it has been accepted that the Coulomb phase is defined by the following characteristics [205]:

1. Each spin can be mapped onto a signed flux directed along a bond in a bipartite lattice.
2. The sum of the incoming fluxes at each vertex (parent lattice) is zero – *i.e.* divergence free. In the case of pyrochlore structures, this means the total magnetic flux entering a tetrahedron is equal to the flux leaving it such that it satisfies:

$$\nabla \cdot \mathbf{B} = 0 \tag{3.39}$$

3. The spin system has no long range order and behaves “liquid-like”.

Due to the degeneracy of the ice rule states for each tetrahedron, the magnetic moments in the spin ice system are free to fluctuate so that each tetrahedron accesses the 6 degenerate ground states. As mentioned in section 3.5.2, this is possible by a closed hexagonal “loop” of single spin flips [206] or longer [167]. These dynamics are such that the configuration is altered but the overall energy remains the same upon closure of the loop. These dynamics mean that the spin ice phase behaves as a cooperative paramagnet.

One signature of the presence of a Coulomb phase, is through the famous pinch points in the diffuse neutron scattering [138, 207]. Neutron scattering is a method used to study the structural and magnetic correlations in materials. This technique is useful, since the beams of radiation used to probe the material consist of neutrons, which do not interact with the charge of the electrons from the atoms in the target sample. This is because neutrons do not have an electrical charge and hence, unlike electrons used in X-ray diffraction, the scattering length of neutrons is not particularly related to the atomic number [208]. However the different scattering lengths can be used to distinguish isotopes, which become important when dealing with rare earths like dysprosium, which naturally have seven isotopes [209].

Neutron scattering can probe the static and dynamical magnetic correlations of a material as neutrons can interact with the spin of unpaired electrons [210]. This is since neutrons carry a magnetic moment (spin- $\frac{1}{2}$) and hence have an associated magnetic field. Spin correlations in experimental systems are used to produce plots of the magnetic structure factor, defined as the fourier transform of the spin-spin correlation function. This can simply be translated into computational simulations by knowing the location and vectors of the spins of the systems being simulated. A brief outline of the theory of neutron scattering can be found in appendix C.

The plots of the intensity of the magnetic structure factor as a function of the scattering vector are chosen to be in the $(00l)$ and $(hh0)$ plane, where $k = h$, for studying the rare earth pyrochlore spin structure. This is because this plane contains a number of high symmetry points in the underlying lattice and therefore bright spots can be obtained in the neutron scattering figures. The $(00l)$ and $(hh0)$ plane has also been used in previous results found for spin ice (see figure 3.3) and therefore comparison with these results can be made.

Diffuse patterns are of lower intensity than the Bragg peaks and arise from local magnetic spin order. Fennell *et. al.* conducted experimental and Monte Carlo simulated

neutron scattering on a spin ice material [138]. The intensity of the magnetic structure factor calculated using nearest neighbour interactions is displayed in figure 3.3 capturing some key features which are shown in the experimental results. The dipolar

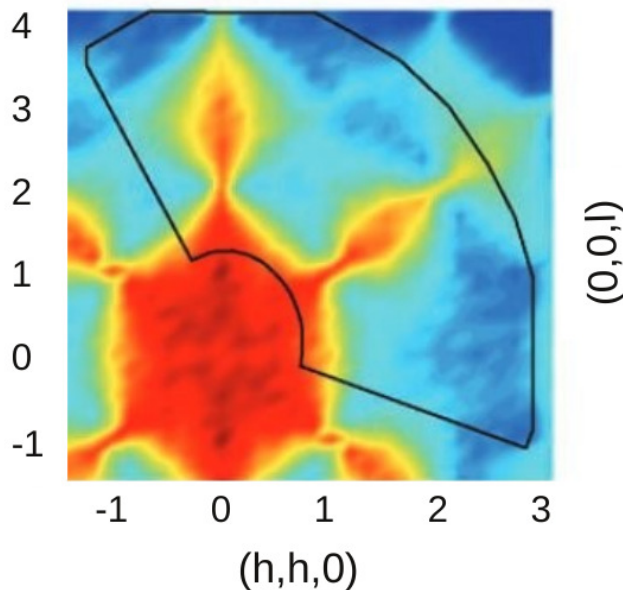


Figure 3.3: Simulated diffuse pattern of the spin flip component in nearest neighbour neutron scattering for $\text{Ho}_2\text{Ti}_2\text{O}_7$. This is calculated for the (hhl) plane, where $k = h$. The red coloured areas are the most intense magnetic scattering regions, whilst the blue coloured areas are the least intense. Image taken from reference [25]

model, however, is required for the true results. The red areas are the most intense magnetic scattering regions and the blue regions are the least intense. The Bragg peaks in the experimental plot of the structure factor of $\text{Ho}_2\text{Ti}_2\text{O}_7$ are said to be nuclear and have no magnetic component [25]. This is due to the degeneracy of the ice rule states. However, when a magnetic field is applied in the $[110]$ direction then the ground state symmetry is broken and the diffuse pattern disappears, leaving $\mathbf{q} = 0$ magnetic Bragg peaks unique to ferromagnetic interaction [211].

As has been mentioned, a Coulomb phase must have divergence free plaquettes, which is consistent with the two-in two-out topological constraint in spin ice. The local

two-in two-out configuration means that the relationship of the susceptibility with the scattering function [38] causes a vanishing scattering near the zone-centre [205] which are known as pinch points in reciprocal space (see figure 3.3 at the centres of the “bow-ties”). To obtain perfect singularities in the diffuse pattern would require observing infinite correlations in real space, however, due to exceptions in the topological constraints of a real finite spin ice system, this is not a perfect singularity [3].

The correlation between spins greater than nearest neighbours are weak [212] and hence magnetic order found by neutron scattering, is only from the local two-in two-out constraint in the system. These correlations do not decay exponentially as in a liquid-like state, but rather by a power-law, which makes the system appear to have long ranged dipolar interactions. The long range nature actually derives from tetrahedra in adjacent (100) planes being antiferromagnetically correlated [212], which only occurs when the spin configuration is in the ground state.

Part II

Non-uniform finite systems with non-homogeneous interactions

Chapter 4

Magnetic monopole crystal

It is known that as spin ice is cooled down, monopoles disappear because the ground state has a two-in, two-out spin configuration. However, what if cooling down meant an increase in the number of monopoles? What would the ground state be then?

4.1 From the spin ice phase to a monopole crystal

In this project, jointly conducted by Peter Holdsworth's group in École Normale Supérieure (ENS), Lyon, France and our group in UCL, London, we have investigated the ground state of a model system similar to spin ice, but filled with singly charged magnetic monopoles. To alter the nature of the ground state from spin ice, our model utilises the chemical potential (μ) in the grand canonical ensemble, which controls how favourable it is to form a pair of magnetic monopoles. By using μ as a varying parameter and the temperature, a ground state filled with magnetic monopoles can be achieved when starting from a spin ice configuration. Our model excludes double charges so we explicitly investigate a singly charged system. This means we do not allow the all-in or all-out spin configurations in our classical system, which consequently means we use a fourteen vertex model rather than the sixteen vertex model as in spin ice.

Due to the constraint in the spin configurations, our model is not physical, however the results are valuable to real systems. This is because it was thought that the

Coulomb phase (see section 3.5.4) was only exhibited in systems with no long range interactions [205], whilst this investigation demonstrates the Coulomb phase can be observed in a system with long range order and completely filled with magnetic charges [213]. The possibility of this result is shown to be through fractionalisation of the magnetic moments in our model, making it possible for the coexistence of two magnetic phases. This understanding could be of interest in studies of real systems such as the disputed nature of quantum spin ices e.g. $\text{Tb}_2\text{Ti}_2\text{O}_7$, where experimental analysis yields contradicting results.

4.2 Our analytical approach to the monopole crystal

A system of a fixed number of charges on the diamond lattice has an internal energy given by the sum of the pairwise Coulomb energies, U_C . However, we are interested in a system where the number of charges is free to vary. Therefore we must work in the grand canonical ensemble, in which the internal energy is given by the Legendre transform of U_C according to the equation:

$$U_L = U_C - \mu N_c. \quad (4.1)$$

We refer to this as the “Landau Energy”, U_L , where μ is the chemical potential in the grand canonical ensemble (this has a negative value by definition) and N_c is the number of monopoles in the system.

The energy cost in creating a monopole pair in a vacuum is 2μ . Since μ determines the potential of the system to do work through change, then by making μ less negative, is to drive the formation of magnetic monopoles in the system. This can be understood using equation 4.1 where the μN_c term (or the energy cost in creating monopoles) becomes less negative with a less negative μ and hence decreases the value of U_L . With decreasing $|\mu|$, more excitations are introduced and a system fully occupied with double charged monopoles form (the ground state for low $|\mu|$) [38]. This was shown by den

Hertog and Gingras [184] and is represented in figure 4.1.

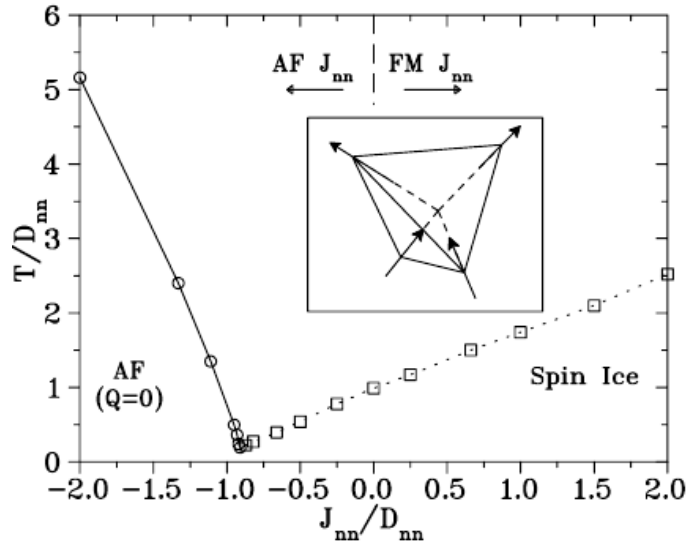


Figure 4.1: The phase diagram for the spin ice pyrochlore structure, in the $T/D_{nn} - J_{nn}/D_{nn}$ plane. The constants J_{nn} and D_{nn} are the nearest neighbour exchange and dipolar interaction strengths, respectively. At positively large ratios of J_{nn}/D_{nn} , the spin ice phase is the ground state, whilst low ratios produce the all-in all-out antiferromagnetic state. The inset is a schematic of the ground state ice rule obeying two-in, two-out tetrahedron. This image is taken from reference [184].

The phase diagram in figure 4.1 is in the temperature vs J_{nn}/D_{nn} plane. The constants J_{nn} and D_{nn} are the nearest neighbour exchange and dipolar interaction strengths, respectively and it is clear to see that their ratio at low temperatures determine the ground state phase of spin ice. At high temperatures, the phase is considered to be a fluid of monopoles.

The dipolar picture of spin ice can be related to the dumbbell model [186], such that J_{nn}/D_{nn} is equivalent to $|\mu|$. In the dumbbell model the magnetic moment is the length of the diamond lattice constant, a_d , which is $a_d = \sqrt{3/2}a$ (a is the length of a unit cell in the pyrochlore) and the magnetic moment of the dumbbell is given by $u = q\tilde{a}$, where \tilde{a} is the separation of the point charges on the ends of the dumbbells.

When $\tilde{a} \rightarrow 0$, one obtains the dipolar system which are point dipoles, whilst for the dumbbell model $\tilde{a} = a_d$. Q is the total charge on a diamond site given by $Q = 2u/a$ for a singly charged monopole site, discussed earlier, J is the antiferromagnetic exchange interaction for the pyrochlore and D is the dipolar interaction given by $D = u^2\mu_0/4\pi a^3$. To find the overall magnetic Coulomb interaction between charges on the diamond lattice, it is necessary to evaluate how the poles on the ends of the dumbbells interact. This includes needing to find the on-site Coulombic contribution (on a diamond site), ν_0 , of the charge of interest. Holdsworth determines the relationship between $J_{\text{nn}}/D_{\text{nn}}$ and $|\mu|$ for the singly charged system we investigate in this project.

By excluding doubly charged diamond sites, the model has a chemical potential that corresponds to:

$$|\mu| = -\frac{\nu_0 Q^2}{2} = -\left[\frac{2J}{3} + \frac{8}{3}\left[1 + \sqrt{\frac{2}{3}}\right]D\right] \quad (4.2)$$

Now using equation 4.2 and equation 4.3 below, where α_M is the Madelung constant,

$$\frac{2J}{3} + \frac{8}{3}\left(1 + \sqrt{\frac{2}{3}}\right)D = \frac{\alpha_M}{2}\frac{8}{3}\sqrt{\frac{2}{3}}D, \quad (4.3)$$

we can deduce that,

$$\frac{J_{\text{nn}}}{D_{\text{nn}}} = -\frac{4}{5}\left[1 + \sqrt{\frac{2}{3}}\left(1 - \frac{\alpha_M}{2}\right)\right]. \quad (4.4)$$

In the left-most part of the phase diagram in figure 4.1 labelled AF, is the doubly charged crystal with the all-in, all-out configuration. The arrangement of the doubly charged crystal corresponds to a zincblende structure with 2+ and 2- charges decorating the lattice (e.g. FeF₃ [214]), which has a Madelung constant of $\alpha_M = 1.638$ and both the anion and cation have a four-fold coordination (see figure 4.2).

In this study, we exclude these double charges to analyse a system filled with single charges. However, the single charges are related to the double charges in that they are later shown to also form a crystal in the zincblende structure, but with 1+ and 1- charges. Therefore the chemical potential for which this structure forms is given by $\mu^* < \mu_0^* = \alpha_M/2 = 0.819$. Using the Madelung constant in equation 4.4 to find $\frac{J_{\text{nn}}}{D_{\text{nn}}}$

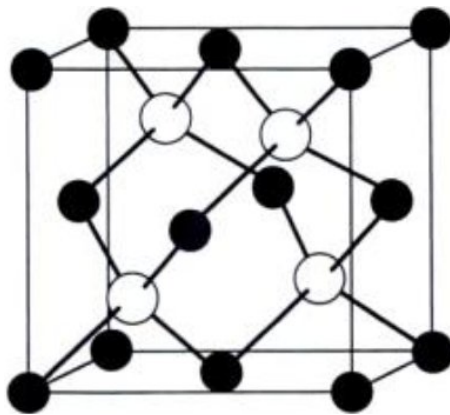


Figure 4.2: A schematic of the zincblende structure, which corresponds to a 2+ cation (black) and a 2− anion (white) each with four-fold coordination. A well known example of this is ZnS (zincblende). Image taken from reference [215].

for the crossover from spin ice to a monopole zincblende crystal gives $\frac{J_{nn}}{D_{nn}} = -0.918$. This is a similar value for the crossover from spin ice to the doubly charged zincblende structure (see figure 4.1) and hence the relationship between the singly charged crystal and the doubly charged crystal imply that the observations made in our project were likely to be similar to the phases shown for dipolar spin ice.

4.3 Numerical results

Monte Carlo methods with a combination of single spin flip dynamics and the worm algorithm were used in most of these simulations. Existing Fortran 90 code created by Jaubert included a Monte Carlo method with single spin flip dynamics, which specifically kept track of the charges on the diamond lattice, the Landau energy and ensured the formation of doubly charged diamond sites were forbidden. My contribution to this project has been to manipulate this code and include the evaluation of the density of monopoles, the order parameter, the heat capacity and the spin and charge autocorrelation functions. With my preliminary results using single spin flip dynamics, we decided that the density and order parameter of the monopoles as shown in figures 4.3 and 4.5 should be generated using the worm algorithm at low temperatures. I simulated and created the phase diagrams in figure 4.6 and the autocorrelation functions in figures

4.9-4.11.

4.3.1 Measuring the charge density

To ensure that we create a monopole filled system we first define the density of monopoles, ρ_m , in our system by equation 4.5:

$$\langle \rho_m \rangle = \frac{\langle N_c \rangle}{N_d} \quad (4.5)$$

where $\langle N_c \rangle$ is the statistical average (over Monte Carlo time) of charges in the system and N_d is the number of diamond sites (the maximum number of sites available for occupation by a charge). The density of monopoles depends on the chemical potential and temperature since the configuration of the spins and charges are dependent on these parameters. Note that from now on in this study, we refer to the reduced temperature, $T^* = k_B T / |\vartheta|$ and reduced chemical potential, $\mu^* = \mu / \vartheta$, where $\vartheta = -\mu_0 Q^2 / 4\pi a$. This is to generalise the results so they are irrespective of the material being analysed. For instance, the simulations run in this project are specific to $\text{Dy}_2\text{Ti}_2\text{O}_7$, due to the requirement of the length of the unit cell, a , therefore we account for this by dividing through by ϑ which is a quantity that includes the lattice constant of the material.

Figure 4.3 produced by Jaubert shows a plot of the statistical average density of charges as the temperature is varied. Each line represents a different chemical potential from $\mu^* = 0.767 - 0.801$. The simulations were run for a system size of $L = 8$ so that the number of diamond sites were $8L^3 = 4096$. The system was equilibrated for $t_{eq} = 10^4$ MCS/s, observed for $t_{obs} = 10^5$ MCS/s and averaged over 4 independent simulations. We used the worm algorithm for 100 different temperatures between $T = 0.2 - 0.6$ K to avoid inaccurate results from the slow dynamics in this temperature region. This consisted of 50 worm updates every 10 MCS/s. The error bars are the standard deviation of the 4 independent simulations.

Excluding the line for $\mu^* = 0.801$, we can see that as the temperature decreases, the density of monopoles increases. This implies that when the chemical potential is

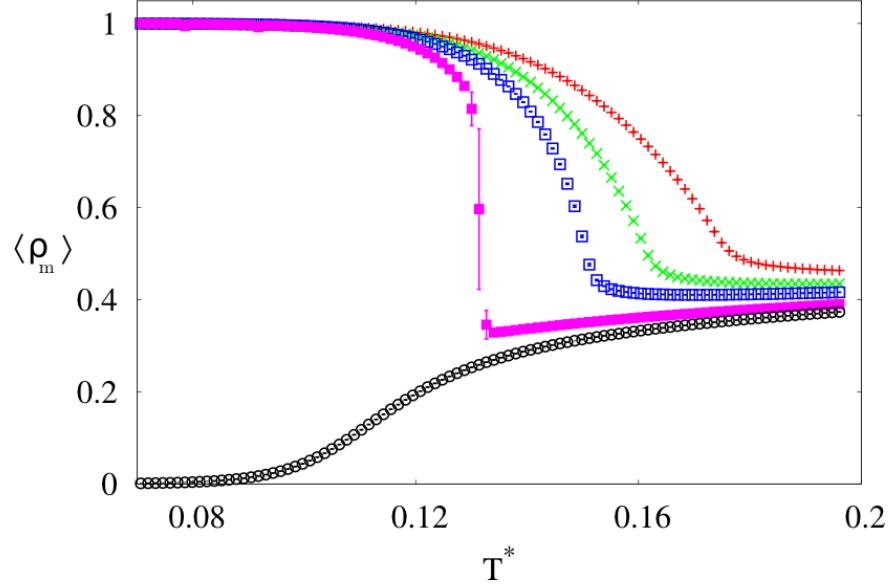


Figure 4.3: Average density of charges $\langle \rho_m \rangle$, as a function of reduced temperature T^* . This is simulated for chemical potentials $\mu^* = 0.767$ (+), 0.778 (\times), 0.784 (\square), 0.794 (\blacksquare), 0.801 (\circ) with $L = 8$, $t_{eq} = 10^4$ MCS/s and $t_{obs} = 10^5$ MCS/s and the worm algorithm used at low temperatures for further thermal equilibration.

$\mu^* < 0.801$, then a monopole filled diamond lattice is the ground state of the system. At high temperatures this is a system almost half filled with monopoles. It is clear to see that as the chemical potential increases from $\mu^* = 0.767$, the gradient representing the transition region from this half filled system to the fully filled monopole system, becomes steeper. The error in these points also become larger between the independent simulations.

When increasing the chemical potential to $\mu^* \gtrsim 0.801$, the system favours the spin ice vacuum as the ground state. This is when all the diamond sites have zero charges with the two-in, two-out spin configuration. To add context, previous literature has reported that the spin ice phase exists at $\mu^* \approx 1.42$ when simulating $\text{Dy}_2\text{Ti}_2\text{O}_7$ using the dumbbell model [163] so we know that the spin ice phase extends from $\mu^* = 0.801 - 1.42$. Once again in the high temperature region, the density curve appears to plateau to a similar density as for low $|\mu|$. This is because, regardless of the value

of μ , the high temperature region provides the system with a sufficient amount of thermal energy to obtain randomly distributed magnetic charges, which is expected for non-interacting, randomly orientated magnetic moments [145]. Since we use a 14 vertex model as opposed to the 16 vertex model in spin ice (as we exclude the doubly degenerate double charged sites), then we would expect the fraction of monopoles present in a randomly distributed vertex system to be $8/14 \simeq 0.57$.

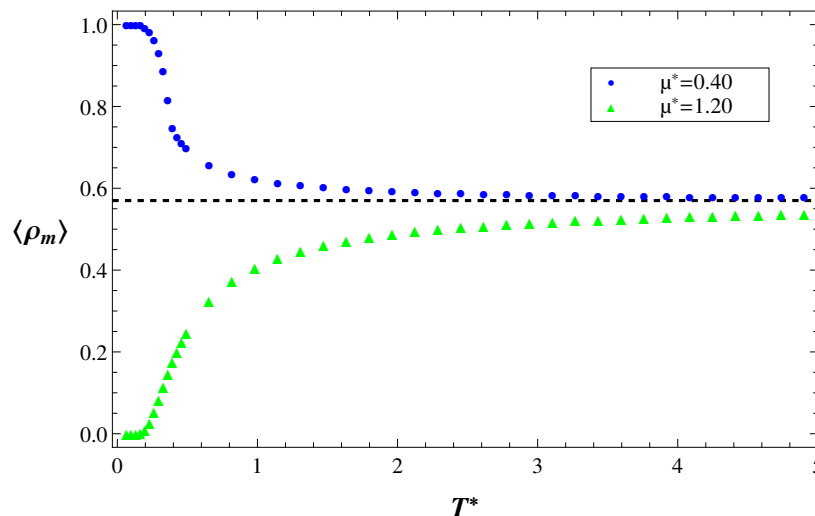


Figure 4.4: Average density of charges $\langle \rho_m \rangle$ vs T^* for higher temperatures than in figure 4.3. Single spin flip Monte Carlo simulations were run using chemical potentials $\mu^* = 1.20$ (\blacktriangle) and $\mu^* = 0.40$ (\bullet) with $L = 5$, $t_{eq} = 10^4$ MCS/s and $t_{obs} = 10^5$ MCS/s.

The plot shown in figure 4.4, is similar to the plot in figure 4.3 of the charge density vs temperature but I have included higher temperatures up to $T^* = 4.90$. Figure 4.4 also differs from figure 4.3 by the method of equilibration at low temperatures. No worm algorithm was used as this plot is simply to demonstrate that higher temperatures approach this value of $\mu^* = 0.57$. The system size is $L = 5$ so diamond sites are $8L^3 = 1000$. The equilibration time was $t_{eq} = 10^4$ MCS/s, observed for $t_{obs} = 10^5$ MCS/s and was only observed for one independent simulation. Figure 4.4 shows the high temperature region for chemical potentials which favour two different ground states: $\mu^* = 1.20$, which favours the spin ice state and $\mu^* \approx 0.40$, which favours

the monopole filled state. The $\langle \rho_m \rangle = 0.57$ limit for a random distribution is indicated on the plot by a dotted line. It is clear to see that the low $|\mu|$ system approximates to this value at relatively lower temperatures than the high $|\mu|$, but the high $|\mu|$ may require considerably higher temperatures to plateau.

These charge density vs temperature results have shown the ground states change with the chemical potential, which indicates that there are two different phases here. Figure 4.3 shows that there is a possible phase boundary at around $\mu^* \approx 0.801$. The nature of these states, with different chemical potentials, are investigated further by analysing the order parameter vs temperature in the next section.

4.3.2 Spin and charge order parameters

To measure the order of the monopoles in our diamond lattice, we need to define an order parameter. The order parameter is a quantity which must be between 0 and 1, where 0 is completely disordered and 1 is completely ordered. Symmetry must be broken for order to occur in a crystal structure. The pyrochlore lattice is bipartite, so it has two sublattices, one consisting of “down” tetrahedra and the other consisting of “up” tetrahedra. When one type of monopole charge (e.g. +1) is located on one sublattice and the other charge (e.g. -1) is on the other sublattice, then symmetry is broken in the pyrochlore structure, which implies ordering. Due to the mapping of the pyrochlore and the diamond lattice, there are consequently two sublattices for the diamond lattice and hence order can be identified using the same methodology as in the pyrochlore structure. We have chosen the diamond lattice in our simulations to find the order of magnetic charges in our model. It is therefore necessary that our order parameter takes into account both the sublattice type and the magnitude of the charge. The normalisation of the charge order parameter was debated as there is information which can be drawn from normalising with the number of diamond sites rather than the number of charges in the system and vice versa. This gives rise to two slightly different definitions of the charge order parameter, where equation 4.6 is normalising with the

number of charges, OP^C and equation 4.7 with the number of diamond sites, OP^D .

$$OP^C = \left\langle \left| \frac{1}{N_c} \sum_{i=1}^{N_d} q_i \Delta_i \right| \right\rangle \quad (4.6)$$

$$OP^D = \left\langle \left| \frac{1}{N_d} \sum_{i=1}^{N_d} q_i \Delta_i \right| \right\rangle \quad (4.7)$$

The order parameter is dependent on T^* and μ^* , since the configuration of the spins and charges are dependent on T^* and μ^* . The charge on each diamond site is denoted by q_i and the sublattice type is assigned a value Δ_i , which is either +1 or -1. This order parameter demonstrates that when a particular sign of charge is on one sublattice then the summation will result in $\pm N_c$, however to ensure the order parameter is between 0 and 1, we find the modulus of the summation and divide by the number of charges. When there are no charges in the system then all $q_i = 0$ and the order parameter is zero. Even though this state is not necessarily disordered, the order parameter only measures the order of the charges providing they are actually present in the system.

The disadvantage of normalising to the number of charges in the order parameter (as in equation 4.6) is that whether there are for example, 2, 50 or 500 positive and negative charges on opposite sublattices, all three would return $OP^C = 1$ corresponding to 100% charge order. This would mean our order parameter does not provide any information on the scale of order in the system and hence must be analysed alongside the density of monopoles result. The issue can be alleviated by normalising with the number of diamond sites, N_d (as in equation 4.7). However then we would have the issue that even with a 90% filling of magnetic monopoles with opposite charges on opposite sublattices would return an order parameter $OP^D < 1$ as all the diamond sites would not be filled. The phase diagrams in this report were created using OP^C , whilst every other result presented in this chapter in regards to the order parameter uses $OP^{D\dagger}$.

[†]This was an accidental approach but as will be seen later, the results from the two definitions provide results which are not too dissimilar to one another except in one instance explained in section 4.3.3 of this thesis.

Figure 4.5, produced by Jaubert shows a plot of the order parameter vs T^* . Each line of points corresponds to a different chemical potential and these are the same μ^* used in the charge density plot in figure 4.3. The simulation details were the same used to create figure 4.3 and were plotted using the same temperature range. The density

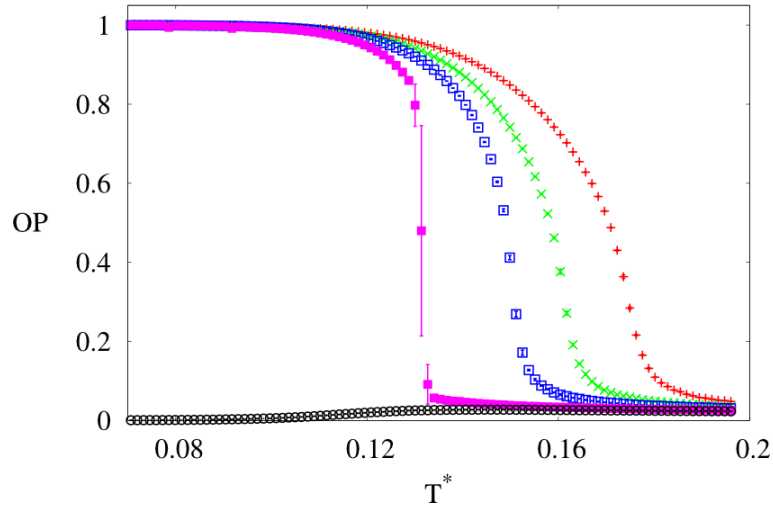


Figure 4.5: Monopole order parameter, OP^D , vs T^* for $\mu^* = 0.767$ (+), 0.778 (x), 0.784 (□), 0.794 (■) and 0.801 (○). The simulation details here are the same as was used for the density plot in figure 4.3.

results show that for $\mu^* < 0.801$ with low T^* , that the density of monopoles is at its greatest, but figure 4.5 shows that this phase is also ordered with $OP^D \rightarrow 1$. When the temperature increases, the density and ordering of the monopoles decrease to $OP^D \rightarrow 0$. At approximately $\mu^* = 0.801$ and above, where the vacuum/ spin ice phase is the most favoured ground state, the order parameter is zero as there are no charges. Increasing the temperature at these chemical potentials increases the density of monopoles but barely increases the order parameter. This is not to say that there is necessarily more order in these higher temperature states compared with the spin ice ground state, but rather is an artefact of the definition of the order parameter (given by equation 4.7), which highlights its limitations.

4.3.3 Chemical potential – temperature phase diagrams

We summarise all the phase changes identified in the previous section with phase diagrams that I produced. Several plots of $\langle \rho_m \rangle$ vs T^* are combined for different μ^* to obtain a 3d surface plot. The same is produced for the order parameter and the heat capacity. By viewing this 3d surface in the $T^* - \mu^*$ plane, one can obtain the respective 2d density plots shown in figure 4.6. The density results are found using equation 4.5, the order parameter results are found using equation 4.6 and the heat capacity (at a fixed external field, where $H = 0$ in this case), C_H , is found using the statistical definition:

$$C_H = \frac{\beta_T}{T} \langle \langle U_L^2 \rangle - \langle U_L \rangle^2 \rangle \quad (4.8)$$

where $\langle \dots \rangle$ is the statistical average.

These phase diagrams were produced with data from a system size of $L = 5$ and hence $N_d = 1000$, a simulation time $t_{eq} = 10^4$ MCS/s and $t_{obs} = 10^5$ MCS/s and averaged over one independent simulation. The temperature steps varied over the T^* range, with more observations in the transition region. We used the pre-built interpolation function in Wolfram Mathematica v9.0 [216], which interpolates the respective $\langle \rho_m \rangle$, OP^C and C_H data in the $T^* - \mu^*$ plane with an interpolation order of 0. The intensity of $\langle \rho_m \rangle$, OP^C and C_H is indicated in the phase diagrams from red (highest intensity) to yellow (lowest intensity). We tried higher orders of interpolation and they produced less pixelated phase diagrams, however, these created unreal features in the plots such as a line of intense spots along $T^* \approx 1$.

The density phase diagram shown in figure 4.6 (a) and the heat capacity phase diagram shown in figure 4.6 (c) indicate three phase regions. In figure 4.6 (a), region **I** is the state of the system filled with monopoles and hence the dark red colour, whilst region **III** is yellow, indicating the spin ice state which has no monopoles. With high T^* , region **II** is considered a dense charge gas (or liquid). It is not clear whether region **II** is in fact a separate phase, as the evidence for a coexistence curve is ambiguous

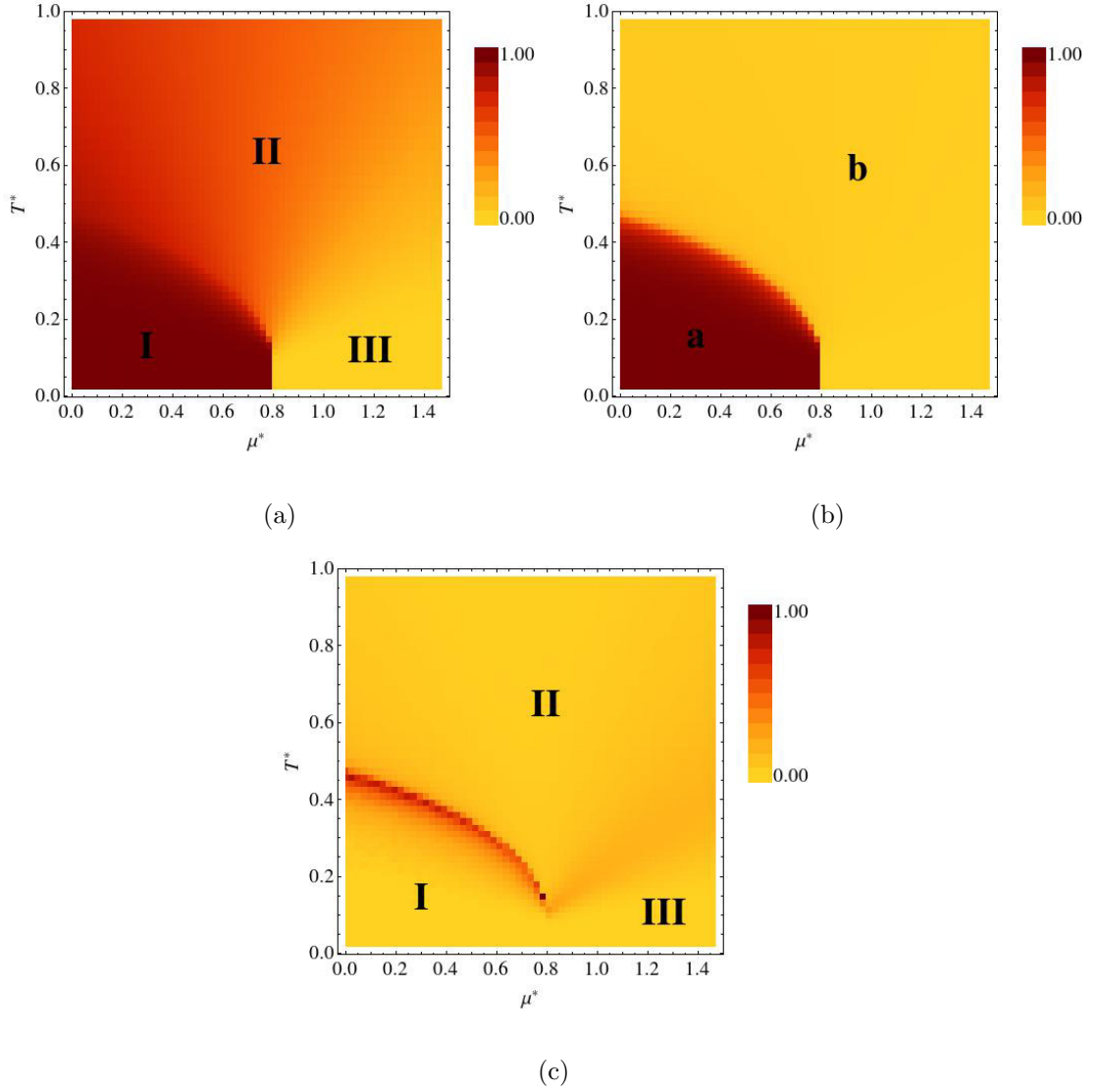


Figure 4.6: Phase diagrams of the modified spin ice system for the (a) density, (b) order parameter and (c) heat capacity of the monopoles. Phase **I** in (a) and (c) indicate the monopole crystal, whilst the order of the crystal is denoted as “**a**” in (b). Phase **II** in (a) and (c) indicate a possible charge liquid. The order parameter only shows complete disorder (denoted as **b**) in this liquid phase and phase **III** in (a) and (c) corresponds to the Coulomb gas phase. Simulation details were: $L = 5$ such that $N_d = 8L^3 = 1000$, $t_{eq} = 10^4$ MCS/s and $t_{obs} = 10^5$ MCS/s.

from the heat capacity phase diagram. For spin ice, the literature shows the crossover, from spin ice to the high temperature region, with a dotted line (see figure 4.1 [184]).

This is because though it is difficult to violate the ice rules in the spin ice state by spin flipping, the dynamics are very slow and absent of long range order. Therefore, as the temperature increases, the spin ice state must be smoothly connected to the high temperature paramagnetic phase [38].

The order parameter phase diagram in figure 4.6 (b) only shows two states which are “**a**”, a completely ordered monopole crystal, and “**b**”, a completely disordered phase. Similar results are shown in figure 4.5, where the results for $\mu^* \leq 0.801$ were either $OP^D \sim 1$ at low T^* or $OP^D \sim 0$ at high T^* . It must be remembered that the order parameter in figure 4.5 is defined by OP^D whilst in figure 4.6 (b) the order parameter is defined by OP^C . Both definitions of the order parameter result in only two regions in the phase diagram since regions **II** and **III** are considered disordered (the order parameter is set to zero for a system with no charges). Figure 4.5 shows a slight increase in the order of the monopoles when $\mu^* = 0.801$ with increasing temperature. This is not evident at the same chemical potential in the order parameter phase diagram shown in figure 4.6 (b) because of the differing normalisation factors in the order parameter definitions.

The heat capacity phase diagram (figure 4.6 (c)) shows a red line of points on a background of low intensity data points. The red line of points correspond to the peak in C_H versus T^* plot for a range of low μ^* . Since each peak represents a transition temperature, then this line of peaks help to confirm that there is a phase transition from the monopole solid to the dense monopole gas. On the other hand, for high μ^* , a faint shade of orange is observed, which may be an indication that there is a phase transition from the monopole gas (region **III**) to the dense monopole gas/ liquid (region **II**). This faint shaded feature also poses the question as to why there is a broadening of these low intensity peaks with μ^* .

We are able to identify some differences for region **II** compared with the other two regions by the $3\chi T$ results shown in section 4.3.7, which indicates a difference in mag-

netic spin behaviour. However, the fact that there is a range of charge densities in this region (i.e. the spectrum of colour) from the Coulomb gas to almost that of the monopole crystal could indicate a more subtle explanation. No conclusive result on the nature of region **II** can be drawn until further investigation.

The heat capacity phase diagram also indicates the order of transition. A tricritical point is commonly known to be an indicator of where three-phase coexistence terminates, but another definition is the point where a second order line of transition points become first order [217]. In this plot the dark red point at $\mu^* \simeq 0.78$ is the tricritical point. We used finite-size scaling on the maxima of the heat capacity and susceptibility to classify the order of transition. It happens that the chemical potential window of first order transitions is small (from $0.78 < \mu^* < 0.80$) so that distinguishing first order and tricritical behaviour is very difficult. This becomes more difficult when trying to increase the system size beyond the correlation length due to the long range nature of the Coulomb interactions. However, even with this difficulty, further work by Jaubert has been conducted using finite-size scaling (see figure 4.7) to consider the nature of the transitions.

Figures 4.7 (a) and (b) show finite size scaling[‡] for the heat capacity at a particular μ^* , C_μ , and the critical susceptibility, χ_c , with system sizes $L = 2$ up to $L = 10$. Each point represents the peak/ maximum height of the respective quantities. These plots show clearly that when $\mu^* = 0.801$ and the system size is larger than $L = 4$, the peak heights in C_μ and χ_c remain fairly constant, which is consistent with the two-in two-out configuration. This is because the density of the monopoles becomes so small that compared with system size, the monopoles in the system no longer “feel” its boundaries/ finite size so that larger system sizes return the same response function. Whilst with smaller system sizes, the scaling of the maxima are comparable with the chemical potentials in the first order region. This could indicate that at low temperatures the spin ice regime could exhibit the dynamics observed in the monopole crystal. We can

[‡]The simulation details for the finite size scaling is the same as was mentioned for figure 4.3.

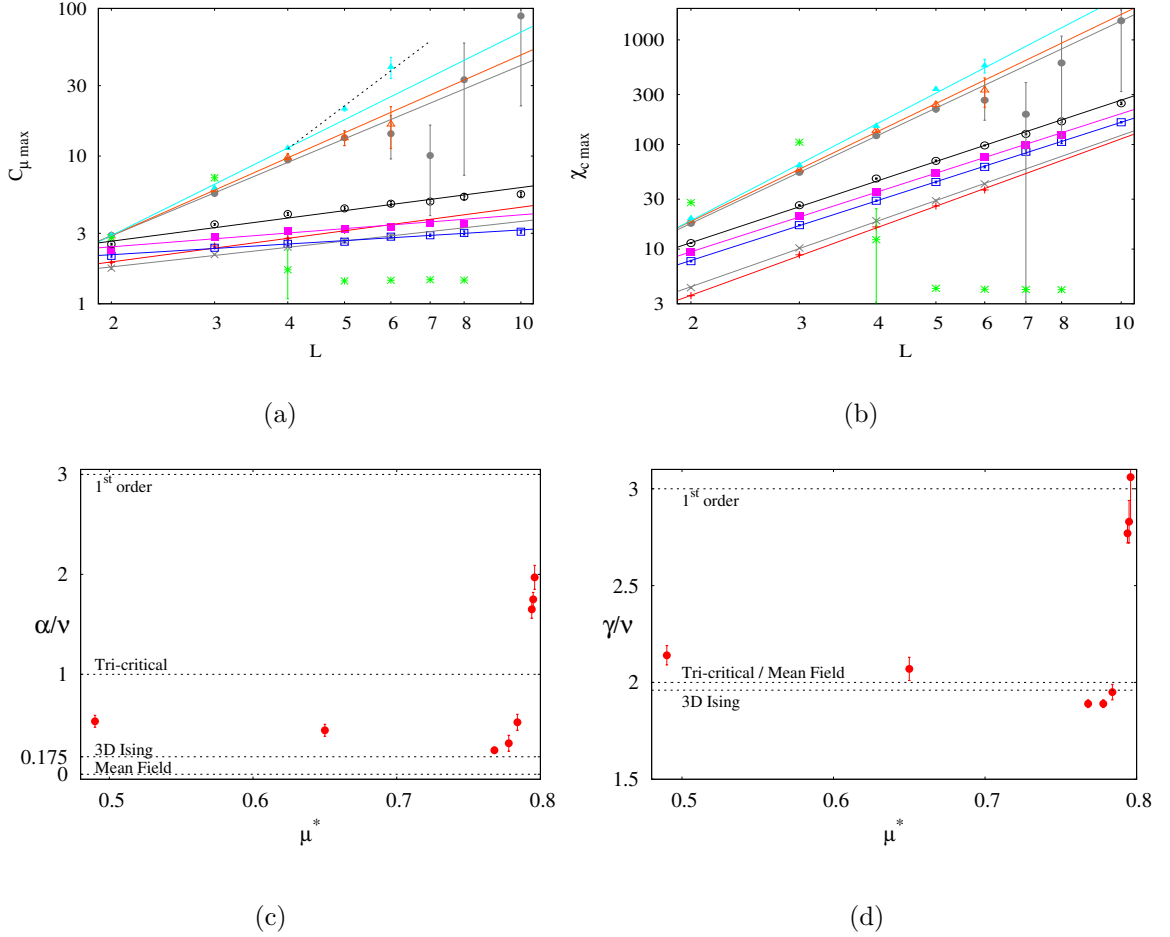


Figure 4.7: Finite-size scaling of the maxima of (a) the specific heat, C_{μ} and (b) the susceptibility, χ_c as a function of linear system size, L , for $\mu^* = 0.490$ ($+$), 0.654 (\times), 0.768 (\square), 0.778 (\blacksquare), 0.784 (\circ), 0.794 (\bullet), 0.795 (\triangle), 0.796 (\blacktriangle), 0.801 (\ast). This is observed close to the low temperature phase boundary. The dashed line in (a) is the cubic power law ($\propto L^3$) appearing in the first order region for $L \geq 4$. The scaling exponents ratio (c) α/ν and (d) γ/ν as a function of μ^* .

see the distinct gradient change in the plots when moving from the second order regime to the first order regime, which occurs here for $\mu^* > 0.784$ and is consistent with our results thus far. At $\mu^* = 0.796$ the scaling has a cubic law behaviour (peak height $\propto L^3$), which is characteristic of a first order phase transition [218]. The corresponding scaling exponents, shown in figures 4.7 (c) and (d), reinforce the crossover in order of transition with increasing μ^* , but also help us to identify a possible 3d Ising universality

class for the system in the second order, continuous region of the phase diagram.

The heat capacity finite size scaling results were generated using equation 4.8 and the critical susceptibility produced using equation 4.9.

$$\chi_c = \frac{1}{N_d T} \langle M_c^2 \rangle - \langle M_c \rangle^2 \quad (4.9)$$

The error bars in figures 4.7 (a) and (b) are the standard deviation σ over 4 independent simulation outcomes. The error bars in figures 4.7 (c) and (d) represent a confidence level of 90%, based on the statistical uncertainty of the data plotted in figures 4.7 (a) and (b). A line of best fit function has been used in Wolfram Mathematica v9.0 [216] to create the solid lines shown. It includes all the data points for a given μ^* and each data point is weighted by $1/\sigma^2$, where σ is the standard deviation.

4.3.4 Analytical investigation of the monopole crystal

The numerical simulations so far indicate that the tricritical point occurs at $\mu^* \sim 0.78$ and the first order transitions terminate at $\mu^* \sim 0.80$, however, the analytical investigation initiated by Holdsworth, disagrees slightly with this result.

The Coulomb energy is a contributor to the Landau energy given in equation 4.1, whilst a term known as the Madelung constant, α_M , contributes to the Coulomb energy. This constant is specific to the crystal structure and is defined as,

$$\alpha_M^i = \sum_j \frac{z_j}{r_{ij}/r_{nn}} \quad (4.10)$$

where the summation is for $j \neq i$, z_j is the charge number/ coefficient of the interacting monopole j , which multiplied by e , the elementary charge, gives the charge of the monopole ($q = ze$) and r_{ij} is the separation between the two interacting monopoles normalised by r_{nn} .

As mentioned previously, the doubly charged system in the spin ice model has a zincblende structure, where the coordination number of the 2+ and 2- ions is 4 in this

structure, which is also the case for the sites on the diamond lattice. It was earlier derived that the diamond lattice with single charges transitions from the spin ice phase to the monopole crystal at $\alpha_M/2 = 0.819$ in our model. One can see that this result is not $\mu^* = 0.80$ as predicted by our numerical simulations, but our simulations make a good approximation.

4.3.5 Simulated magnetic neutron scattering

For our project we use neutron scattering simulations, produced by Banks, to identify the nature of the magnetic correlations in our system. We simulated 2000 distinct configurations in a system size $L = 8$, $N_d = 4096$ of the monopole crystal ground state. This consists of three-in one-out and one-in three-out spin configurations of spin (dumbbell) length $S = 1$. The result is an output of the structure factor $S(\mathbf{Q})$, which is shown in figure 4.8. Intense Bragg peaks at $\mathbf{q} = (220)$ and a lower intensity diffuse pattern is observed. To show this diffuse pattern, the Bragg peaks had to be pictured as contours superimposed on the diffuse scattering background. It is possible to see from this figure, the resemblance of our results with the calculated nearest neighbour results in figure 3.3 in chapter 2, which would suggest some similarities between the spin ice system and our model.

The Bragg peaks at $\mathbf{q} = (220)$ are indicative of an all-in, all-out spin arrangement, which is an ordered antiferromagnet. This is the same for antiferromagnetic FeFe_3 , where the Bragg peaks appear due to the equivalent spins on every other tetrahedra being aligned and hence ordered [38, 214], however, the diffuse scattering with pinch points coincide with a disordered spin system.

The fact we have diffuse scattering with pinch points, as for a Coulomb phase, is an indication of no long range spin order in the system and the vertices are divergence free. However, the presence of antiferromagnetic Bragg peaks, corresponds to the all-in all-out spin configuration, for which there is a non-zero divergence at each diamond lattice site. Additionally, because the magnitude of magnetic charge on a diamond site

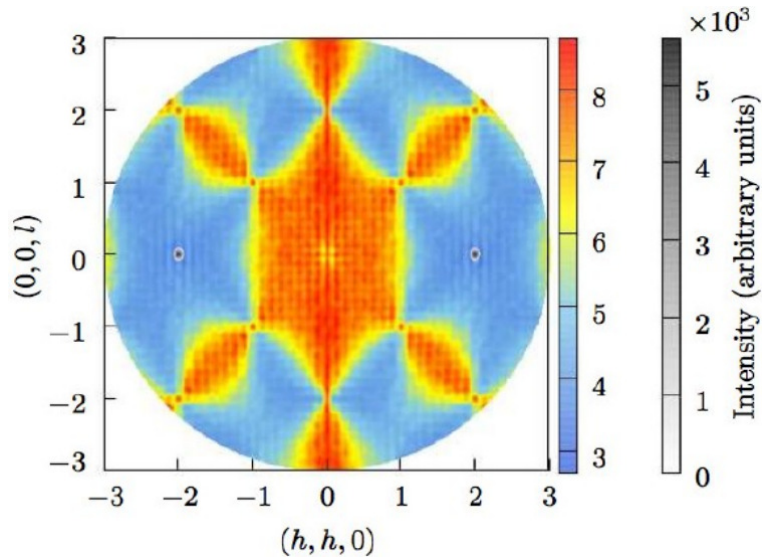


Figure 4.8: Diffuse pattern of the spin flip component in simulated unpolarised neutron scattering for the system in region **I**, the monopole crystal. The pyrochlore $S(\mathbf{Q})$ has been calculated by averaging over 2000 distinct monopole crystal ground states with system size $L = 8$. The Bragg peaks at $\mathbf{q} = (220)$ have been plotted as contours in grayscale superimposed on the contribution to $S(\mathbf{Q})$ from the dipolar field due to their relatively high intensity.

is defined by the summation of magnetic moments into and out of a tetrahedron, then according to equation 2.5 in section 2, an all-in all-out configuration with spin length of 1 should produce a double charge on the diamond site. However, as emphasised previously, these all-in, all-out states are disallowed in these simulations, to avoid double charges.

In this monopole crystal state, the single charges are an ordered network on the diamond sites, therefore the spin configuration should only consist of three-in one-out and three-out one-in of every tetrahedron. However, these neutron scattering results challenge this implication with the Bragg peaks and hence we consider the possibility of the pseudo-spins[§] of length 1 fractionalising into two parts: one which contributes to the monopolar part of the system and the other which contributes to the dipolar

[§]The pseudo-spins are related to the real spins by equation 2.3 in chapter 2.

part of the system. This leads to the following description of our model proposed by Holdsworth [213]:

$$[\mathcal{M}_{ij}] \left(\frac{a}{u} \right) = (-1, -1, -1, 1) = \left(-\frac{1}{2}, -\frac{1}{2}, -\frac{1}{2}, -\frac{1}{2} \right) + \left(-\frac{1}{2}, -\frac{1}{2}, -\frac{1}{2}, \frac{3}{2} \right), \quad (4.11)$$

If we take $[\mathcal{M}_{ij}] \left(\frac{a}{u} \right) = (-1, -1, -1, 1)$ as a three-out one-in tetrahedron, then -1 denotes a pseudo-spin pointing out of the tetrahedron and $+1$ denotes a pseudo-spin pointing into the tetrahedron. The first term on the right side of equation 4.11 is the monopolar part, \mathcal{M}_m , given by $(-\frac{1}{2}, -\frac{1}{2}, -\frac{1}{2}, -\frac{1}{2})$. This is an all-out state, which is antiferromagnetic with half the originating spin length. \mathcal{M}_m does not produce a doubly charged site since the spins are half a unit length, therefore it will produce a singly charged site. It is therefore, \mathcal{M}_m that gives rise to the Bragg peaks in the neutron scattering. The second term on the right side of equation 4.11 is for the dipolar part, \mathcal{M}_d , given by $(-\frac{1}{2}, -\frac{1}{2}, -\frac{1}{2}, \frac{3}{2})$. This is a three-out one-in state but produces no magnetic charge since the spin pointing into the tetrahedron is 3 times the length of the other three spins. Therefore, it is this fragmented part of our magnetic moments that contribute to the divergence free signature in the neutron scattering.

Overall, our model can be described by:

$$\mathcal{M}_{ij} = \mathcal{M}_m + \mathcal{M}_d \quad (4.12)$$

4.3.6 Spin and charge autocorrelation functions

Spin and charge autocorrelation functions are calculated to confirm that the model has spin dynamics with simultaneous charge order. With reference to equation 3.38 in section 3.5.3, we formulated the following spin autocorrelation function, $\Gamma_s(t)$ (equation 4.14):

$$\Gamma_s(t) = \left\langle \frac{1}{N_s} \sum_{i=1}^{N_s} [S_i(0) - \langle S(0) \rangle] [S_i(t) - \langle S(t) \rangle] \right\rangle \quad (4.13)$$

$$= \left\langle \left(\frac{1}{N_s} \sum_{i=1}^{N_s} S_i(0) S_i(t) \right) - \langle S(0) \rangle \langle S(t) \rangle \right\rangle \quad (4.14)$$

Where N_s is the number of spins, $S_i(t)$ is the i^{th} spin value at time t and $\langle S(t) \rangle$ is the mean spin value of the system at time t . Since the overall magnetisation of the spins in the pyrochlore structure must add up to zero, then the overall number of spins with a +1 charge must be equal to the number of spins with a -1 charge. This means that both $\langle S(0) \rangle$ and $\langle S(t) \rangle$ must be zero. Therefore, the expression for the spin autocorrelation can be simplified to equation 4.15.

$$\Gamma_s(t) = \left\langle \frac{1}{N_s} \sum_{i=1}^{N_s} S_i(0) S_i(t) \right\rangle \quad (4.15)$$

The same principle applies to the autocorrelation function of the charges (see equation 4.16), however extra care must be taken here. Unlike the Ising spins on the pyrochlore structure that we model, the charges on the diamond sites can take values +1, 0 or -1 rather than just -1 or +1, due to working in the grand canonical ensemble.

$$\Gamma_c(t) = \left\langle \frac{1}{N_c} \sum_{i=1}^{N_c} q_i(0) q_i(t) \right\rangle \quad (4.16)$$

This means that if the system were filled with vacuum sites and hardly fluctuated, maintaining zero charges over time, the autocorrelation function would still return a zero. This is not the correct measure as the system is technically ordered, however, our aim with these results is to understand how the order of the charges vary given that they are present in the system. Therefore, if there are no charges in the system then there is no charge order to measure so a return of zero is appropriate. This conclusion can be rationalised by the fact that zero charges are indistinguishable and hence, it is not possible to determine the sublattice a vacuum site resides.

Figure 4.9 shows the spin and charge autocorrelation functions that I produced for a system size $L = 7$ ($N_s = 5488$ and $N_d = 2744$) and $t_{eq} = 10^4$ MCS/s. Each point is an average of 100 simulations of $\Gamma_s(t)$ (blue line in figure 4.9) and 100 simulations of $\Gamma_c(t)$ (red line in figure 4.9). The total Monte Carlo time taken for the spin autocorrelation to plateau varies depending on the chemical potential. An indication of this can be seen by comparing the time ordinate of figure 4.9 ($\mu^* = 0.41$) with figure 4.10 ($\mu^* = 0.90$).

An autocorrelation function will always start at 1 by virtue of the fact that simultaneous observations of the same classical variable will always yield identical results, $\langle S_i(0) S_i(t) \rangle = 1$. When a spin is flipped the total correlation changes by

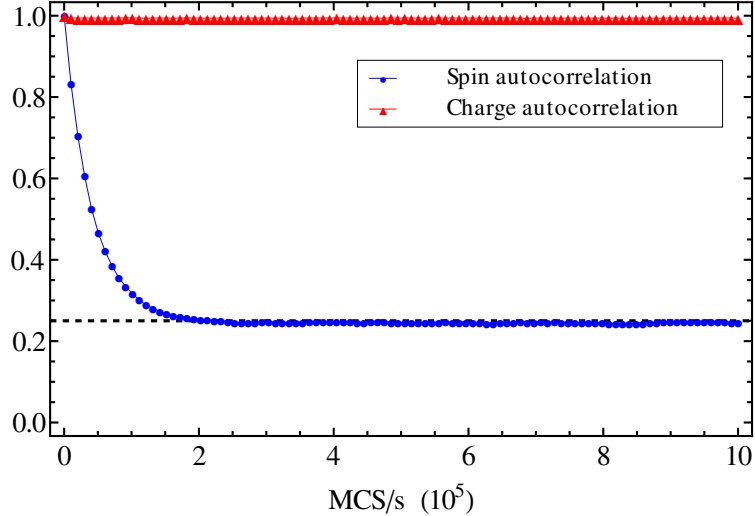


Figure 4.9: Charge and spin autocorrelation functions vs MCS/s for $T^* = 0.20$ and $\mu^* = 0.41$, which is in phase **I** of the phase diagram in figure 4.6. The solid lines through the points are a guide for the eye. The dotted line indicates the asymptote at $\Gamma_s(t = \infty) = 1/4$. The time scale for equilibration of the spins is relatively long compared to higher μ^* , due to the slow dynamics in the monopole solid.

$-2(S_i(0) S_i(t))$. Therefore, the total correlation is updated after every spin flip but since the change in order would not be significant with a single spin flip, we take an observation of $\Gamma_s(t)$ after N single spin flips (i.e. 1 MCS/s). For the charge autocorrelation, the correlation of a charge at two times cannot be updated by just $-2(q_i(0) q_i(t))$ due to the possibility of zero charges and so the system is updated by recalculating $\sum_{i=1}^{N_c} q_i(0) q_i(t)$ after every 1 MCS/s.

It can be seen from figure 4.9 that when the chemical potential is small, the autocorrelation of the charges is fixed at 1, which is expected considering the order parameter at this temperature and chemical potential. This is also understandable with regards to phase **I** of the phase diagram shown in figure 4.6. The decline in the spin autocor-

relation plot shows that the spins fluctuate even though we have identified that the charges remain ordered with a low chemical potential.

If we are then to look at the autocorrelation of the charges and the spins in phase **III** of the phase diagram (figure 4.10), when the chemical potential is high, we see that the spins and the charges are completely uncorrelated. This is understandable as the charges present are few or none and the spins are fluctuating as the phase is a constrained paramagnet sampling through the six degenerate ice rule configurations. There are correlations in the ice rule obeying ground states but as all spins are of equal length, the autocorrelation function cannot determine this. It is in $3\chi T$ vs T plots that the differences between a paramagnet and a cooperative paramagnet can be viewed as the magnetic fluctuations, which carry a magnetic moment, are proportional to changes in the topological sector [219]. The results of this method is discussed in the next section.

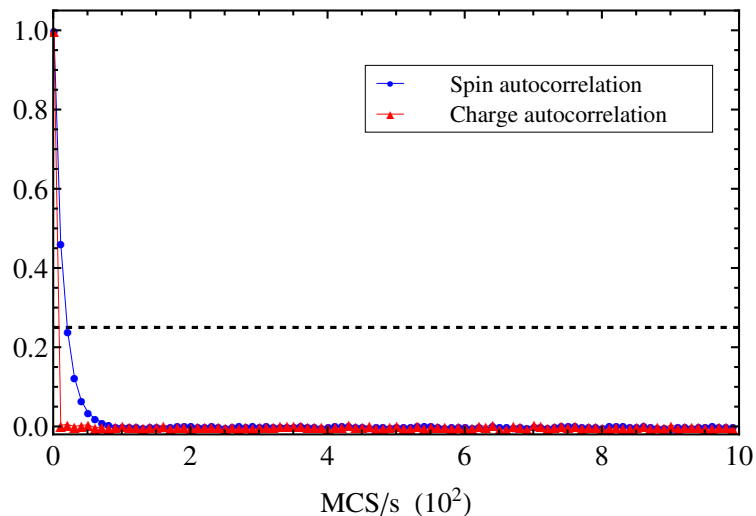


Figure 4.10: Charge and spin autocorrelation functions vs MCS/s for $T^* = 0.20$ and $\mu^* = 0.90$, which is in phase **III** of the phase diagram in figure 4.6. The dotted line indicates the asymptote at $\Gamma_s(t = \infty) = 1/4$. The time scale for equilibration of the spins is significantly faster than in phase **I** of the phase diagram.

Lastly in figure 4.9, we observe that the autocorrelation of the spins decline to a fixed value of $\Gamma_s(t) = 1/4$ over Monte Carlo time, which is quite remarkable. For there to be a non-zero autocorrelation means that there is some correlated fluctuation. It is through the the neutron scattering results and the expression derived from heuristic reasoning in equation 4.11 that we can explain the limit of $\Gamma_s(t = \infty) = 1/4$ in figure 4.9. The \mathcal{M}_d component involves a spin three times the length of the other three spins on a tetrahedron, known as the “minority spin”. This minority spin can occupy any one of the four sites on a tetrahedron and still ensure the divergence free criterion is satisfied and hence supports the spin dynamic nature of our system. By equally choosing 1 of the 4 possible sites on the vertices of the tetrahedron to reside on, the spins in the system are on average, ordered 1/4 of the time. The correlated fluctuation is mandatory for the diamond sites to maintain the same charges on the same sites on average. We can see how the constraint on the position of the minority spin relaxes with higher chemical potentials in figure 4.11.

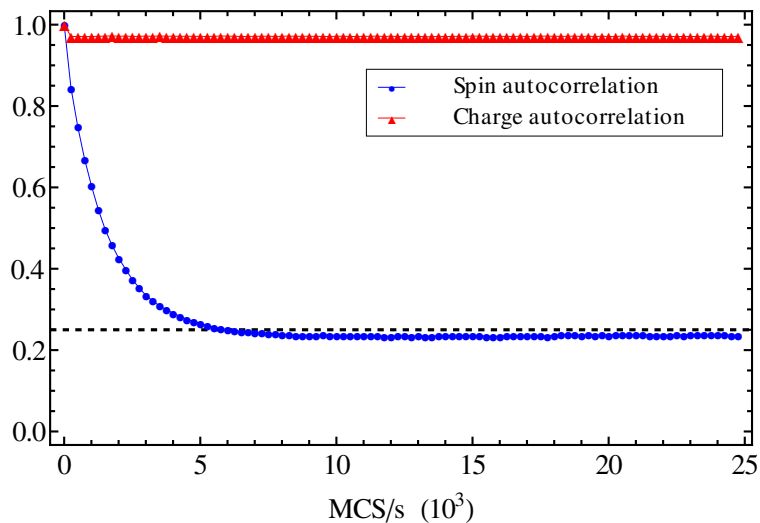


Figure 4.11: Charge and spin autocorrelation functions vs MCS/s for $T^* = 0.20$ and $\mu^* = 0.57$, which is in phase **I** of the phase diagram 4.6, but closer to the ‘monopole crystal – spin ice vacuum’ phase boundary than $\mu^* = 0.41$ shown in figure 4.9. The dotted line indicates the asymptote at $\Gamma_s(t = \infty) = 1/4$.

From figure 4.11, we can see that the spin autocorrelation plateaus to $\Gamma_s(t) < 1/4$. This is because the system is not completely filled with monopoles at this chemical potential and therefore, spins can fluctuate more freely than for a lower chemical potential such as $\mu^* = 0.41$ shown in figure 4.9. We can see that when $\mu^* = 0.57$ in figure 4.11, there is a sharp initial decline in the charge order and then the line plateaus.

Spin dynamics have been investigated using the autocorrelation functions before but particularly for the spin ice system [163]. Separation of M-AM pairs create the classical Dirac string of overturned dipole moments. These strings are not easy to determine in the monopole solid phase due to entanglement but the dynamics in the system are limited, particularly for $T^* = 0.20$ when monopoles are most likely to be bound tightly together as pairs [191]. The constraint of removing double charges means that only one of three spins can flip [185], e.g. for a tetrahedron with a three-in, one-out spin configuration, only the three-in spins can be flipped without correspondingly forming a doubly charged diamond site. This also means that monopole hopping or creation/annihilation can only occur in one of the three neighbouring tetrahedra. We have considered that on average monopoles remain on the same sites by annihilation and instant creation. The static ability of the charges on the diamond sites would require further investigation to support this hypothesis.

4.3.7 Susceptibility as a function of temperature

The neutron scattering results have identified our system to show both antiferromagnetic and cooperative paramagnetic behaviour. Therefore we expect to see the characteristic cusp in a susceptibility vs temperature plot, which appears as a consequence of the presence of an antiferromagnetic phase. We have simulated χ vs T^* for a system size $L = 4$ and hence $N_d = 512$. This was achieved by first annealing from high temperatures to the temperature of interest over a period of 10^5 MCS/s and then equilibrating the system at temperature T for a further $t_{\text{eq}} = 10^5$ MCS/s. The data collection period lasted 10^6 MCS/s where observations were made every 10 MCS/s. The worm algorithm was also used to facilitate thermalisation by 50 worm updates every 10 MCS/s. The

data is averaged over six independent simulations for each value of the parameter μ^* and the error bars are the standard deviations of these six samples at each temperature.

Figure 4.12, produced by Jaubert, shows the susceptibility result, which is clearly not representative of an antiferromagnet. Evidently featureless of the “cusp” which should occur at the phase transition temperature. For the range of μ^* we simulate here (region **I**), only the behaviour of a paramagnet are seemingly present. This is probably due to the fluctuating background of the cooperative paramagnet [220] such that the Coulomb phase is obscuring the antiferromagnetic behaviour.

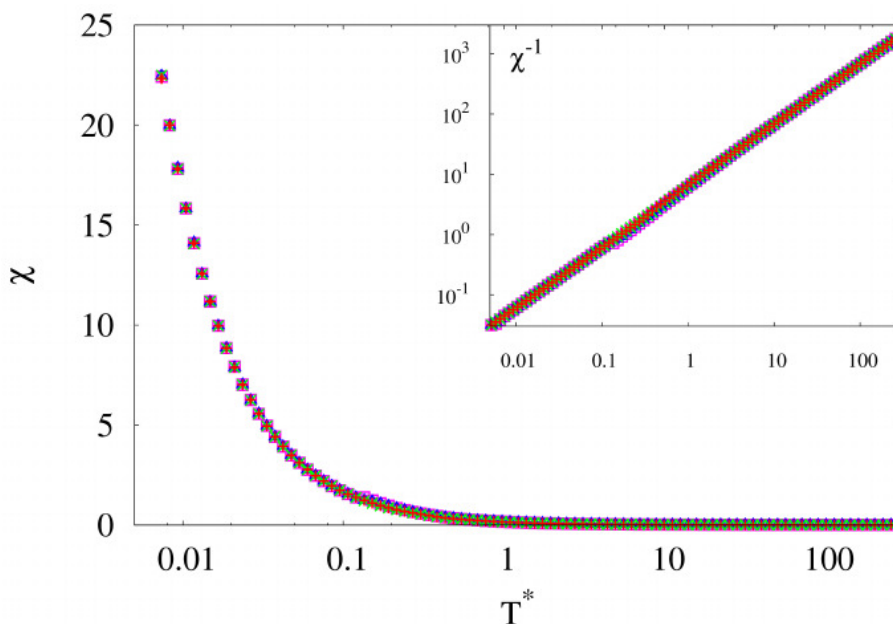


Figure 4.12: Magnetic susceptibility as a function of T^* for the monopole crystal system, simulated for $\mu^* = 0.33$ (+), 0.65 (\times), 0.784 (\triangle), 0.794 (\square) $< \alpha_M/2$. Clearly, the results only show the presence of a paramagnet. The inverse susceptibility is plotted in the inset on a log-log scale.

Despite the result shown in χ vs T^* in figure 4.12, we are still able to obtain information from the susceptibility, but using a plot of $3\chi T$ vs T^* . This method has measured topological sector fluctuations in the Coulomb phase [219] and hence could distinguish between the dynamics in the high temperature paramagnet and the low

temperature cooperative paramagnet. In our investigation, we analysed the change in the Curie constant, \mathcal{C} , as the monopole density changes as a function of temperature.

If the dumbbells on the tetrahedra are described as scatterers of unit length, then there should be a crossover in the Curie constant from the paramagnet with $\mathcal{C} = 3\chi T = 1$ to the cooperative paramagnet with $\mathcal{C} \approx 2$, as discussed by Jaubert *et. al.* [219]. We have simulated $3\chi T$ vs T^* with the same input parameters and simulation details that were used to create figure 4.12.

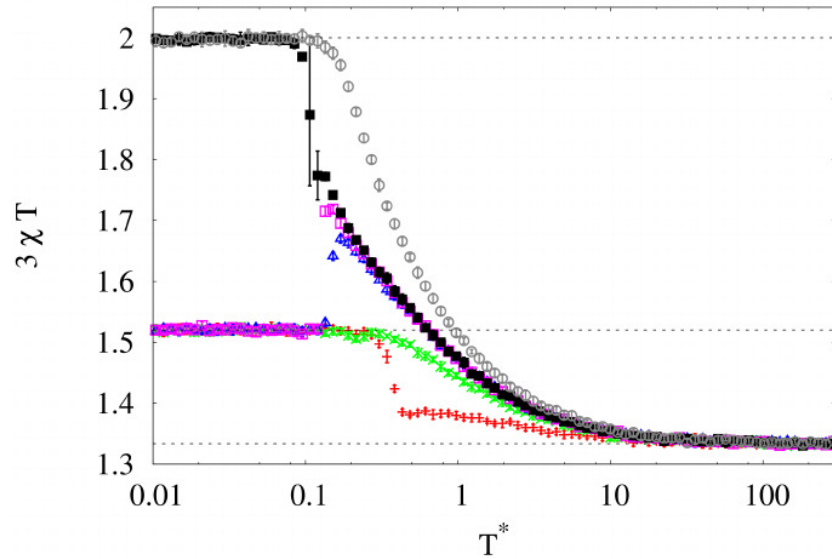


Figure 4.13: Curie constant, $3\chi T$ vs reduced temperature for our model. This is simulated for $\mu^* = 0.33$ (+), 0.65 (\times), 0.784 (Δ), 0.794 (\square) $< \alpha_M/2$ and including $\mu^* = 0.801$ (\blacksquare) and 0.98 (\circ) $> \alpha_M/2$. For each chemical potential there is a Curie constant crossover. The behaviour of the transition also seems to be unique to the phase (i.e. phase **I**, **II** and **III**), where the phase region is identified via the chemical potential in this case. The dashed lines are theoretical expectations for the spin liquid Curie law prefactor, \mathcal{C} , of the Coulomb phase ($\mathcal{C} \approx 2$) and the singly charged monopole fluid ($\mathcal{C} = 4/3$), while the line at $\mathcal{C} = 1.52$ is a guide to the eye for the monopole crystal. Equilibration has been ensured down to $T = 20$ mK ($T^* \approx 0.007$) by the worm algorithm [213].

One can see from the results in figure 4.13 that at high temperatures (region **II**) the Curie constant is $\mathcal{C} \sim 4/3$ regardless of the chemical potential. The paramagnetic regime is not $\mathcal{C} = 3\chi T = 1$ due to our 14-vertex model rather than the 16-vertex in spin ice. As the temperature decreases we can see that the $3\chi T$ measurement is not only able to determine the difference of unconstrained and constrained paramagnets, but also indirectly provide information on different orders of transition.

A crossover from $\mathcal{C} \sim 4/3$ to $\mathcal{C} = 2$ is shown for $\mu^* = 0.801$ and 0.98 (region **III**), with decreasing temperature. In this region, the $\mathcal{C} = 2$ Curie constant does not differ from that reported in low temperature spin ice. This is because the high μ^* , low T^* state corresponds to the spin ice ground state, which includes the six-fold degenerate ice-rule vertices that are present in both the 14- and 16-vertex models. For $\mu^* = 0.33$ and 0.65 , the system is in phase **I**, the monopole solid. The Curie constant shifts from $\mathcal{C} \sim 4/3$ to $\mathcal{C} \sim 3/2$ from high to low temperature. This indicates that the constrained fluctuations in the monopole crystal are different to that found in spin ice, since at low temperatures $\mathcal{C} \neq 2$. In fact, with a lower Curie constant this would imply that there are more unconstrained fluctuations in the monopole crystal than for spin ice. For $\mu^* = 0.784$ and 0.794 , the system is in the tricritical and first order region, respectively. Decreasing the temperature shows crossovers in this region to occur from $\mathcal{C} \simeq 4/3$, to a rise beyond $\mathcal{C} = 3/2$, followed quickly by a decline to the monopole crystal Curie constant of $\mathcal{C} \simeq 3/2$ at low temperatures. This is unique compared to the other chemical potentials in this plot and can be considered as an indicator for a change in the order of transition. We attribute this “peak-like” feature to an initial decrease of the monopole density in the fluid phase and then a sudden creation of monopoles to form the monopole crystal.

In the heat capacity phase diagram (see figure 4.6 (c)), μ^* with first order transitions demonstrate that the phase in region **II** is stable at relatively lower temperatures compared to other chemical potentials. Considering this region represents paramagnetic disorder as shown by all the results we have analysed and with $\Delta G = \Delta H - T\Delta S$ (where

H is enthalpy and S is entropy), then this would imply that the region is stabilised entropically rather than energetically. From the $3\chi T$ plots, we can see the difference between the plots of $\mu^* = 0.794$ and the next chemical potential measured at $\mu^* = 0.801$ and that through the susceptibility we can identify that there is an energy barrier that is overcome from this small difference in chemical potential.

4.4 Experimental relevance

At present, there is no known material that behaves in an analogous way to our model and hence we need to consider methods which would effectively tune the chemical potential of current materials to favour that of the singly charged magnetic phase. A staggered chemical potential is necessary to ensure the system does not favour the doubly charged magnetic system.

Possible areas for investigation were discussed in our paper [213], which we felt could be fruitful in looking for systems that may exhibit the monopole crystal phase. I follow the arguments that were presented in the paper (listed below).

- Applying a multiaxial external magnetic field,
- quantum spin liquids,
- applying an external pressure to cause lattice distortion and
- artificial spin ice.

4.4.1 Applying a multiaxial external magnetic field

We consider the possibility of using a magnetic field to stabilise the formation of the monopole crystal phase of a pyrochlore magnet, as it has been observed that applying a magnetic field to $\text{Tb}_2\text{Ti}_2\text{O}_7$ in the (110) direction can stabilise single magnetic charges [221]. However, Sazonov *et. al.* [221] report that this system consists of double layered monopoles and antimonopoles, which is not observed in the conventional spin

ice $\text{Ho}_2\text{Ti}_2\text{O}_7$. This stabilisation of single charge monopoles could be achieved by a distortion from e.g. the Jahn Teller effect. Application of a magnetic field in spin ice ($\text{Dy}_2\text{Ti}_2\text{O}_7$) in the (110) direction is otherwise known to create pinned ferromagnetic chains (known as α and β chains) [222], which are chains that are parallel and perpendicular to the magnetic field respectively. This still produces vacuum sites and so we would have to consider applying this perturbation in other spin systems such as the quantum spin ices.

Applying a field in the (111) direction in spin ice would likely constrain monopole movement since this would fix one of the spins to give $2d$ kagomé planes [72]. Hence the movement will only occur in these planes, which are perpendicular to the magnetic field. The field creates a staggered chemical potential and it becomes possible to have symmetry breaking so as to access the monopole crystal state [186]. Our hypothesis and future studies will involve coupling a magnetic field to the dipolar field, \mathcal{M}_d , in the magnetic monopole crystal state. With this coupling there should be a $3d$ Kasteleyn transition analogous to the transition in $2d$ kagomé ice, which is driven by weakly tilting the field off the (111) axis [3, 223].

On a slightly related topic, it could be possible to apply a DC or AC electrical field to a quantum spin ice just as one would use an external magnetic field. As discussed in chapter 1.1, electrons have an electrical charge and a magnetic dipole (spin), but magnetic monopoles have a magnetic charge and an electric dipole [224]. Khomskii [224] shows that magnetic textures breaking inversion symmetry are required to create electric dipoles. Therefore, a four-in or four-out configuration and the two-in, two-out have an electrical dipole moment of zero due to the symmetry. The three-in one-out or three-out one-in spin configurations produce an antiferroelectric effect, which is created by charge redistribution. These configurations are considered to be dominated by antiferromagnetic spin orientations. Therefore, applying the electrical field in the (110) and (111) direction is another possibility that could equally be explored.

4.4.2 Quantum spin liquids

The spin ice Coulomb phase is classical and described by the exchange interactions and more significantly, the dipolar interactions. A quantum spin ice (QSI) is quite like spin ice but rather use spin matrices. QSI differ from classical SI since the easy axis anisotropy is not so strong compared with the spin-spin interaction (i.e. exchange coupling or dipole-dipole interaction) [225]. This means the local Ising spins are not fixed by the usual anisotropy in classical spin ice and can quantum tunnel between ice states at low temperatures. Therefore magnetic order can be obtained more easily in these systems and hence, QSI's are generally less frustrated than the classical systems. Quantum fluctuations in the classical Coulomb phase correspond to the quantum spin liquid (QSL) in a quantum spin ice [226]. The magnetic monopoles in quantum spin ice are carried by pseudo-spin 1/2 quantum mechanical quasiparticles, spinions, which hop through the lattice via pseudo spin flip exchange interactions [227].

Quantum spin liquids have strongly correlated spins, unbroken crystalline symmetry and the magnetic moments are dynamic [226]. For more details of their properties and temperature dependence, the reader is referred to reference [228]. It seems to be in these spin systems that features identified in experimental work could potentially be explained by our picture of magnetic moment fragmentation. For the QSL, $\text{Dy}_2\text{Ge}_2\text{O}_7$, the chemical potential can be reduced to increase the number of monopoles present [229], however, this predictably coincides with the formation of double charges. Through zero-point quantum fluctuations in the fragmentation of the dipolar field, there may be a possibility to stabilise a monopole crystal phase between the spin ice phase and the all-in, all-out phase [164, 230].

$\text{Tb}_2\text{Ti}_2\text{O}_7$ was previously considered as both a spin liquid [231] and quantum spin liquid [232]. However, it has recently been defined as a magnetoelastic spin liquid, which comes from the magnetoelastic modes (MEM) used to describe a system with hybrid fluctuations [233]. The characteristics of a quantum spin liquid are similar to this but

the MEM combines electronic and structural/vibronic excitations, rather than just photon modes. $\text{Tb}_2\text{Ti}_2\text{O}_7$ has antiferromagnetic behaviour due to its negative Curie-Weiss temperature $\Theta = -14\text{ K}$ [165]. At ambient pressure, no long range order is observed down to 50 mK [234] and even diffuse neutron scattering experiments show pinch points [235, 236], corresponding to a Coulomb phase. The dynamics are also quite similar to what we see in our results, with a fraction of the spins freezing [234, 237, 238] and it does not exhibit spin glass behaviour [238]. A MEM distinguishes the spin liquid phase as a Coulomb phase with propagating bosonic spin excitations [233]. It is possible that this is a consequence of magnetic moment fragmentation and therefore this could mean that hybrid fluctuations can stabilise the formation on an antiferromagnet coexisting with Coulomb phase spin fluctuations. With a larger lattice constant than $\text{Tb}_2\text{Ti}_2\text{O}_7$, studies into the ferromagnetically ordered $\text{Tb}_2\text{Sn}_2\text{O}_7$ [239, 240] are accompanied by a magnetic fluctuating background.

Quantum spin ices could potentially undergo magnetic moment fragmentation but with different magnetic arrangements to the antiferromagnet/cooperative paramagnetic coexistence we demonstrate. Much debate has taken place over the nature of the phase of $\text{Yb}_2\text{Ti}_2\text{O}_7$ at low temperatures (see figure 4.14).

For instance, in some cases $\text{Yb}_2\text{Ti}_2\text{O}_7$ is said to show a magnetic phase with no order (neither spin glass freezing [242]) below 200 mK in both single crystals and polycrystalline samples [243, 244], but at 250 mK shows ferromagnetic order [245]. Whilst in some instances, a single crystal of this compound shows ferromagnetic order even below 200 mK, dependent on the Yb content [227]. The discrepancies found in $\text{Yb}_2\text{Ti}_2\text{O}_7$ has led to the study of $\text{Yb}_2\text{Sn}_2\text{O}_7$, which differs by an increase in lattice parameter when comparing Sn^{4+} and Ti^{4+} [241]. However, differing results persist in polycrystalline samples with spin dynamics reported down to 50 mK [241], whilst in contrast to a first order transition into a ferromagnetic phase [246].

We can see that more investigations need to be conducted in these systems par-

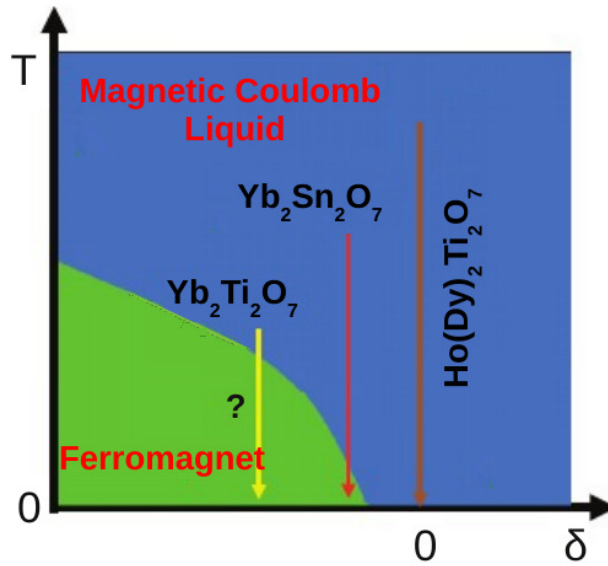


Figure 4.14: T - δ phase diagram of the potential QSL's $\text{Yb}_2\text{Ti}_2\text{O}_7$ and $\text{Yb}_2\text{Sn}_2\text{O}_7$ compared with the classical spin ices $\text{Ho}_2\text{Ti}_2\text{O}_7$ and $\text{Dy}_2\text{Ti}_2\text{O}_7$. δ is the relative strength of the U(1) symmetric planar exchange compared with the Ising exchange for Yb. The “?” represents this debatable transition. Image taken from reference [241].

ticularly when varying between single crystal and polycrystalline samples, as well as experimental methods. However, it is clear that there is unexplained behaviour occurring in these quantum spin ices and our picture of magnetic moment fragmentation could explain the possibility of a coexistence of two magnetic phases to demonstrate both order and disorder.

4.4.3 Pressure and lattice distortions

Another method for obtaining a staggered chemical potential could be by applying a pressure to distort the lattice structure of a pyrochlore magnet and breaking the electric field symmetry which enforces the spin type to be almost perfectly Ising. This method would lift the doublet degeneracy for the Ising-like spins in spin ice and could lead to a perturbation that couples only to the monopolar field and not the dipolar field and hence produce the monopole crystal.

High pressure work has been popular in studies on NH_3 [247] and NaCl [248] to form new solid ionic structures. The ammonia crystals are most interesting since at low temperatures ammonia is quite like water in that it has 4 sites for hydrogen bonding [249]. However at high pressures, ~ 70 GPa and temperatures ~ 750 K the hydrogen bonding of an ammonia molecule is six-fold and weak [250]. With a range of molecular forms, namely NH_3 , NH_4^+ and NH_2^- , the system can coexist as a solid crystal and a liquid via proton disorder in the c crystal axis [250]. This is the superionic phase which has layers of alternating NH_4^+ and NH_2^- similar to that in the low temperature, high pressure “ionic phase” recently found [247]. These alternating layers of anions and cations are similar to our broken symmetry monopole crystal where the ions are analogous to magnetic monopoles, which similarly as monopoles hop around the diamond lattice by single spin flip, the NH_4^+ and NH_2^- ions move by proton hopping [250]. In this structure we may have found our molecular equivalent, just as water ice is the molecular equivalent of spin ice. The formation of a similar structure with water (via H_3O^+ and OH^- ions) would cost more energy since water can create other preferentially symmetrical hydrogen bonded structures before deforming into these ions [251].

4.4.4 The kagomé system

The final possibility we consider in visualising magnetic moment fragmentation in a singly charged monopole system, is in an artificial spin ice system. The different artificial spin ice geometries have been introduced in chapter 1, however, in this section we focus on the kagomé geometry since there has been recent evidence for charge ordering in these structures with a non-zero entropy [252]. As mentioned previously, the monopoles in these systems do not have a tensionless and unobservable Dirac string linking two opposite magnetic poles and hence are not real monopoles. Instead, these charge defects are emergent. The spin flip dynamics and consequently the monopole positions, can be observed experimentally [146, 188], and they travel in a one-dimensional path.

The dumbbell model can be used on the kagomé system to observe magnetic charge

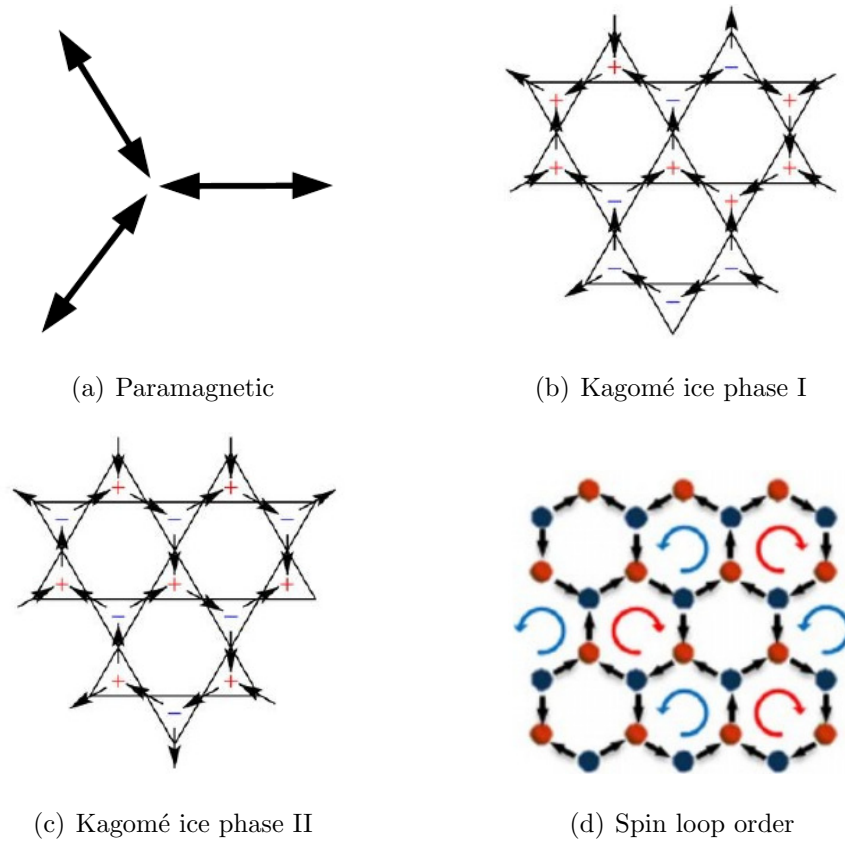


Figure 4.15: Dipolar kagomé spin ice demonstrating charge order. (a) paramagnetic phase such that the spins can point in any local Ising direction, (b) spin ice state with no order, (c) intermediate charge ordered phase with spin disorder and (d) is a kagomé phase with spin and charge order. The phases in (a) to (d) are obtained with decreasing temperature. Images (b) and (c) were taken from reference [253] and (d) was taken from reference [254].

ordering [194, 253, 255, 256]. Unlike the dipolar spin ice model on the pyrochlore lattice, the dipolar spin ice model on the kagomé lattice retains a net magnetic charge on the vertices as there is an uneven number of spins which form a vertex. At high temperatures the spins on the kagomé lattice behave paramagnetically (see figure 4.15 (a)), decreasing the temperature takes the system into a spin ice state (two-in one-out and one-in two-out vertices), which has no long range order and is known as the kagomé ice I phase (see figure 4.15 (b)). Of recent interest is what happens when the temperature is decreased further to what is known as the kagomé II phase [254] (see

figure 4.15 (c)). This is where the spins are still disordered but the magnetic charges are ordered in a similar way to our monopole crystal, with the same charges on one sublattice [253]. This is observed by breaking the Z_2 symmetry of the dumbbells on each vertex in kagomé ice and the state can be realised upon applying a (111) field along the pyrochlore lattice [257]. At low temperatures, the kagomé lattice is in its ground state, where magnetic charges are ordered and spins have a distinctive spin-loop order [113] (see figure 4.15 (d)).

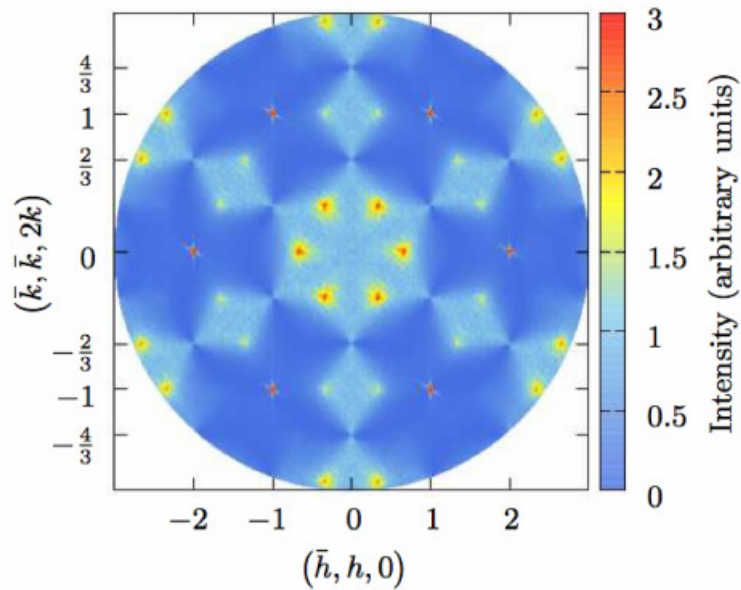


Figure 4.16: Simulated magnetic neutron scattering of the kagomé ice II phase, which has disordered spin structure still obeying the ice rules but simultaneously has magnetic charge order. Bragg peaks are shown as though there is a presence of antiferromagnetic all-in all-out vertices and diffuse scattering with pinch points indicate cooperative paramagnetism. Image taken from reference [3].

Simulated neutron scattering results of the kagomé ice II phase were produced by A. Harman-Clarke[3]. These indicate a presence of magnetic moment fragmentation with the presence of Bragg peaks and diffuse scattering. Figure 4.16, presents the neutron scattering which corresponds to fractionalisation of magnetic moments in the kagomé

system by:

$$[\mathcal{M}_{ij}] \begin{pmatrix} a \\ u \end{pmatrix} = (-1, -1, 1) = \left(-\frac{1}{3}, -\frac{1}{3}, -\frac{1}{3} \right) + \left(-\frac{2}{3}, -\frac{2}{3}, \frac{4}{3} \right).$$

In direct analogy with the fragmentation discussed above for the pyrochlore system, equation 4.17 explains the simultaneous charge order and spin disorder through a monopolar and dipolar part of the magnetic moment. This also explains the antiferromagnetic and cooperative paramagnetic results from the simulated neutron scattering. Experimental neutron scattering studies are required to confirm these results in real systems.

Chapter 5

Double proximity effect in magnetic multilayers

Magnetic multilayers have a wide variety of uses due to the exploitation of the composition of layers. The proximity effect as discussed in the introduction (section 1.5.1), has been shown to enhance the critical temperature of a low T_c , weakly coupled layer when in the proximity of a high T_c , strongly coupled layer [130]. In this chapter, the consequences of the strongly coupled layer are considered and particularly how increasing the interspecies coupling strength and range of exchange interactions affect the results. Since the strongly coupled layer is modelled as the $2d$ XY model in this project, further ranged direct exchange interactions are discussed in relation to the $2d$ XY nearest neighbour model.

5.1 The proximity effect and long range interactions

Monte Carlo methods are used to identify the magnetisation profile of an A/B trilayer, where A is a low T_c , weakly coupled layer and B is a high T_c , strongly coupled layer. Upon understanding the magnetic effects in both the A and B layers both as stand-alone components and then within the trilayer, an A/B multilayer with more repeat

units can be considered with varying A thickness. The motivation of this study was initiated by experimental investigations conducted by Ahlberg *et. al.* [71] on amorphous $\text{Fe}_{93}\text{Zr}_7(x \text{ \AA})/\text{Co}_{95}\text{Zr}_5(1 \text{ \AA})$ thin films. It was found in these experiments that decreasing the thickness of the FeZr layer causes a dimensionality crossover in the magnetic multilayer from $2d$ to $3d$ behaviour.

However, experimental analysis is limited and is unable to distinguish the magnetic behaviour of each monolayer in the multilayer thin film. Therefore, this theoretical approach is conducted in the attempt to shed more light on the microscopic properties of the system. Additionally, further ranged direct exchange interactions are used to model this system as the effects seen in these multilayers are unlikely to be short ranged nearest neighbour and the minimal literature on longer range direct exchange interactions with a power law decay can be developed with these results, particularly for the $2d$ XY model which is effectively the B layer in this system.

Please note the notation in this section is such that a *layer* corresponds to a particular magnetic species within a multilayer, e.g. there are two A layers in the ABA trilayer, whilst a *monolayer* refers to the thickness of a single layer of atoms, e.g. one A layer in the trilayer has a thickness of 10 monolayers. A *slab* is the term used to describe a system only consisting of a single species and is therefore not a multilayer, e.g. a system with only x monolayers of A spins is a slab of A . To avoid any further confusion, the coupling between the same species is known as the *intraspecies coupling*, e.g. coupling between A spins is given by J_{AA} , whilst coupling between different species is known as the *interspecies coupling*, e.g. coupling between A and B spins is given by J_{AB} . These couplings are fixed between species and independent of r , it is only by the power law decay given in the Hamiltonian that changes the overall interaction of one spin to another, which is dependent of r .

Before discussing the numerical details in this project, it is necessary to consider the composition and properties of the experimental system.

5.2 Experimental relevance to simulations

In the investigation conducted by Ahlberg *et. al.* [71], magnetic multilayers formed of amorphous $\text{Fe}_{93}\text{Zr}_7(x \text{ \AA})/\text{Co}_{95}\text{Zr}_5(1 \text{ \AA})$ were created using magnetron sputtering techniques with the respective zirconia compounds. These had 10 repetitions with an extra layer of $\text{Fe}_{93}\text{Zr}_7$ for symmetry purposes. The magnetisation and susceptibility were determined by the magneto-optical Kerr effect (MOKE), which measures the change in polarisation of visible light as a consequence of the magnetic properties of the system. Using this observation, a measure of the changes in magnetic moment with field and temperature can be studied. For bulk materials, MOKE is limited to only understanding the surface properties since polarised visible light can only penetrate $\sim 15 - 20 \text{ nm}$ in metals [258]. This is however, reasonable for thin film materials where the overall size is of the order of this penetration (e.g. when $x = 25 \text{ \AA}$ in $\text{Fe}_{93}\text{Zr}_7(x \text{ \AA})/\text{Co}_{95}\text{Zr}_5(1 \text{ \AA})$). In Ahlberg's work, the total sample size is $\sim 26 \text{ nm} +$ capping layers). Still a further limitation persists, which is that the results are not layer specific and can only measure the sample as a whole, therefore, these theoretical studies are partly an attempt to understand the layer specific magnetic properties of the multilayer system.

Ahlberg *et. al.* [71] use amorphous thin films with varying thicknesses, x / nm , of a weakly coupled layer ($\text{Fe}_{93}\text{Zr}_7$) and a fixed thickness of a strongly coupled layer ($\text{Co}_{95}\text{Zr}_5$). Amorphous materials were used in the thin films, since they are not as susceptible to issues arising from crystal structure mismatch between the modulated layers. This is due to the nature of the disordered, randomly arranged state. The definition of amorphous materials is quite obscure; with short range order like that of a crystalline structure and no long range order similar to the definition of a liquid, therefore it is difficult to categorise these materials [259]. Crystalline materials are grouped according to their periodic structure and are grouped according to this, e.g. body centered cubic (BCC), face centered cubic (FCC), etc., which is unlike for amorphous materials that have no measure on the amorphous quality of a sample [114]. Figure 5.1 shows calculated arrangements of amorphous and crystalline cubic structures using first principles

as a guide to visualising the difference between these structures.

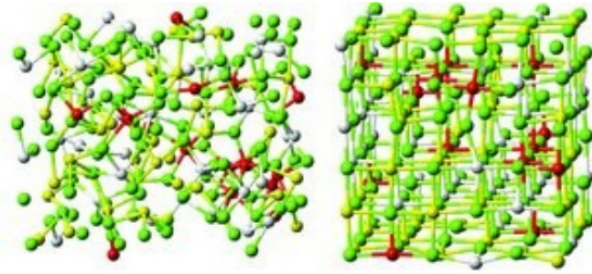


Figure 5.1: Amorphous (left) and crystalline (right) cubic structures calculated from first principles of 3d metal-doped $\text{Ge}_2\text{Sb}_2\text{Te}_5$ [260].

An attempt to define an amorphous system, is by identifying correlations in these materials that extend over atomic length scales [261, 262]. The use of Extended X-ray Absorption Fine Structure (EXAFS), which is an elemental specific measurement using X-ray absorption, is one way to identify these lengths [263]. Measuring the order is taken with respect to the coordination within a spherical shell (i.e. the number of atoms surrounding any one atom in concentric rings). Amorphous materials are also identified as densely packed structures, similar to crystalline materials [264]. For FeZr and CoZr, it is possible to dope pure Fe or Co with small amounts of Zr, which also stabilises the amorphous phase from structural relaxation when the doping is $\lesssim 7$ at.% [265, 266] or $\sim 5 - 7$ at.% [267, 268], respectively. This supports the idea that amorphous structures are densely packed as they stem from the crystalline structures with a small doping.

Though iron and cobalt are ferromagnetic, the disorder in the amorphous structures give rise to random electrostatic fields, which then influence the direction of the magnetic moments and are more likely to give rise to a ferrimagnetic system [269]. The magnitude of the magnetic moments in these structures can be influenced by its coordination number. For instance, the magnetic moments of transition metals in rare earth (RE)/transition metal (TM) amorphous systems can reduce to zero when the number of neighbouring TMs decrease [269]. This can occur with small TM doping and is due to a decrease in exchange interactions. In the experimental work of interest, there is a

small amount of non-magnetic Zr dopant in each layer, given by $\text{Fe}_{93}\text{Zr}_7$ and $\text{Co}_{95}\text{Zr}_5$.

In our theoretical study, we do not take into account any differing behaviour from the amorphous material and simply model the system as a simple cubic (SC) crystalline structure (the unit cell is shown in figure 5.2 (a)). There is some evidence that when simulating amorphous materials, the systems are best represented by face centred cubic (FCC) [124, 270] or body centered cubic (BCC) structures (see unit cells in figure 5.2 (b) and (c), respectively) for small doping, as in loosely packed random $\text{Fe}_{88}\text{B}_{12}$ [271]. However we have opted for the simplicity of the simple cubic (SC) structure in the anticipation that this choice will not significantly affect the results of our study.

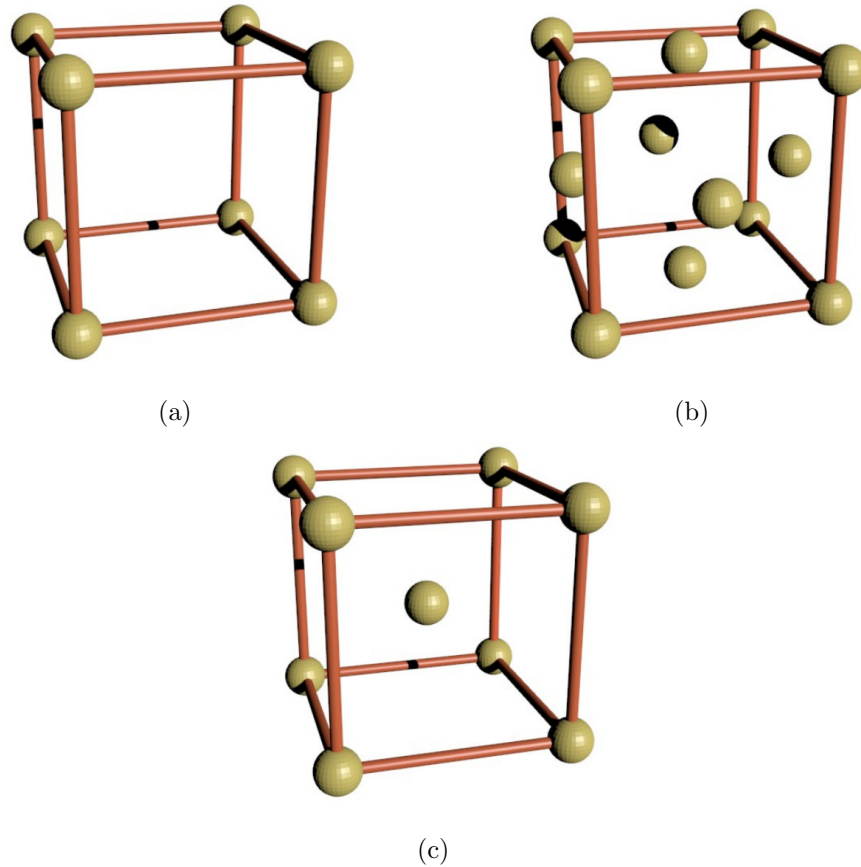


Figure 5.2: The unit cells of closed packed crystal structures (a) simple cubic (SC) (b) face centered cubic (FCC) and (c) body centered cubic (BCC). SC has 6 NN, FCC has 12 NN and BCC has 8 NN.

Pure iron has a BCC structure whilst $\text{Fe}_{(1-x)}\text{Zr}_x$ with $x \geq 0.07$ has a BCC/HCP (bimodal body centered and hexagonal close-packed) structure [272]. A thin film of pure cobalt is also found to have a metastable BCC structure when grown on a thin film of BCC Fe(001) [273] or GaAs(111) [274]. On GaAs(111), it is only once the cobalt thickness is beyond 2 nm that it transforms into the stable FCC crystallographic phase. Therefore with this information we can consider that a “BCC-like” structure dominates in the $\text{Fe}_{93}\text{Zr}_7$ thin film fabricated in the experiments by Ahlberg *et. al.* [71]. Though the FCC structure is reported to be most stable for CoZr [71], this layer is less than a monolayer and hence would likely adopt the arrangement of the FeZr surrounding it.

Consider the difference in results for a monolayer of magnetic ions with the three crystal structures shown in figure 5.2. Each ion in a unit cell of the BCC structure has 8 NN, however, unlike the FCC and SC structures, none of these neighbours are within the plane of the ion of interest and hence first NN interactions in the plane would correspond to the second nearest neighbours in the unit cell shown in figure 5.2. There are 4 of these neighbours in a single plane of a BCC crystallographic phase, which is in exactly the same geometry and separation as SC (studied in this thesis) and hence by the definition of the Hamiltonian, will give the same result with NN interactions. FCC also has 4 NN in the plane but the distance between the neighbours differs from the BCC and SC structures and since the Hamiltonian is distance dependent, then an FCC structure would give a different result to BCC and SC. Extending this observation to further range systems, one can notice that a single layer of BCC is the same structure as SC and therefore when choosing to model the CoZr layer as a monolayer in the simulations, the SC results will provide the same results as if it were modelled with a BCC structure.

5.3 Simulating further range exchange interactions

Exchange interactions have been explained in chapter 1.3, whereby these type of interactions were split into direct and indirect interactions. Direct interactions were

strictly defined as short ranged since they are dependent on the overlap of orbitals between atoms, whilst indirect exchange interactions could be long ranged via other non-magnetic atoms or through excited states. In the multilayer system we analyse in this chapter, we look at further range direct exchange interactions which extend to the 3rd coordination sphere of a simple cubic lattice (see figure 5.3).

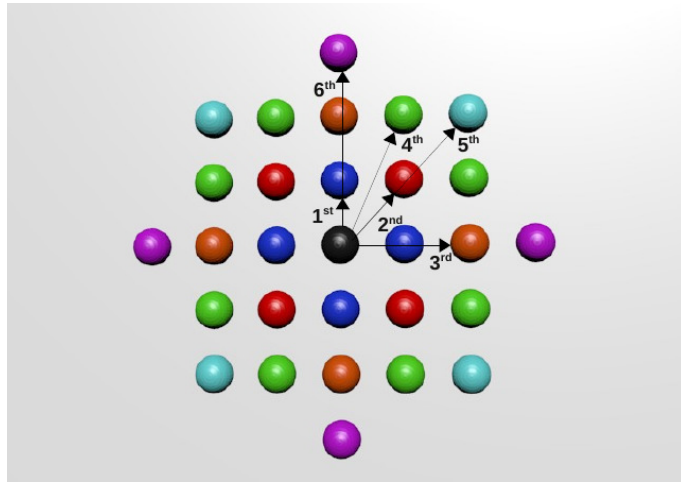


Figure 5.3: Schematic to show the further range interactions used in this study for the simple cubic structure. These interactions are modelled up to the 3rd coordination sphere for 2*d* systems, whilst due to out-of-plane interactions, the same extent would correspond to 8th NN in 3*d* systems. The colours indicate the range of interaction.

The hypothesis here is to consider the possibility that some of the interactions in these transition metal magnetic multilayers are from direct exchange interactions as opposed to only indirect exchange interactions and that the strength of this interaction decays quite rapidly as a power law.

Monte Carlo simulations conducted on 2*d* systems with these further range exchange interactions have been presented by Luijten and Blöte [275], who used a cluster algorithm. This algorithm was chosen as it was found in their study that with the single spin flip Metropolis algorithm, the time of the simulations increased dramatically with range. Luijten and Blöte also note that one should use a suitable range of interactions

to improve the validity of the results compromised by the “cut-off” in interactions.

The exchange coupling, J , between atoms decays quite rapidly with a distance r . In this project we model this decay with a power law relationship, as has previously been done [276–278] and first developed by Fisher and Privman [279]. This is such that J decays by $r^{-(d+\sigma)}$, where d is the dimension of the system and σ is a deviation from the decay occurring as the order of the dimension. The choice of $d + \sigma$ (otherwise known as the range of interactions $\alpha = d + \sigma$) is very important for specifying the weight of contribution that each interaction has to the energy.

For $d < 4$ dimensional systems, classical, mean field-like critical exponents are obtained when $0 < \sigma \leq d/2$ [280, 281] and a strong system size dependence in the one-dimensional Ising model [282]. When $\sigma = 0$, the energies diverge for an infinite system [283] and hence $\alpha = d$ is critical [284]. For a one-dimensional system, $\sigma \leq 1$ is system size dependent [282] and between $\sigma = 0.5$ and $\sigma = 1$, there is non-trivial long range critical behaviour [285]. When $\sigma = 1$ in the Ising model, the transition is governed by topological defects [285]. Bhatteerchagee *et. al.* [286], studied this for $n = d = \sigma = 1$ and $n = d = \sigma = 2$ (the short range $2d XY$ model) and found that generally for $n = d$ topological defects exist, where defects are domain walls for $n = d = 1$ and vortices for $n = d = 2$. For $d/2 < \sigma < 2$, the critical exponents are dependent on σ [281], until $\sigma \geq 2$, which is dimensionally independent [282], i.e. the system becomes thermodynamically extensive. A fast decay ($\sigma > 2$ [283]) in these interactions will mean an approach to the nearest neighbour model [276] (the short range limit), such that further ranged interactions provide a negligible contribution to the total energy. Whilst in contrast $d + \sigma \rightarrow 0$ has all spins interacting in the same way to one another, which is the infinite-ranged model [284].

The choice of σ depends on what is being investigated in a certain system. For instance, there are cases when one might want the decay of interactions to be dependent on the system size, using $\sigma = 0$, such as a study on the system size itself [284]. In our

study, the system size should not be a large factor in the effects observed, but rather the coupling effects. Therefore $\sigma = 1$ is chosen in the $2d$ and $3d$ systems, which gives an r^{-3} and r^{-4} decay, respectively. For the $2d$ simulations, I also used $\sigma = 2$ for a r^{-4} decay, which was to directly compare results with the $3d$ system also decaying by r^{-4} . The advantage of using $\sigma = 1$ in these systems is that the long range attractive interactions decay fast enough for the range of interactions that are simulated so that not accounting for spins beyond this range will not invalidate the results.

When the nearest neighbour exchange Hamiltonian is manipulated with this long range decay factor, we obtain the following modified Hamiltonian (equation 5.1):

$$\mathcal{H} = - \sum_{(i,j)}^N J_{ij} S_i \cdot S_j \quad (5.1)$$

such that,

$$J_{ij} = \begin{cases} \left(\frac{a}{r_{ij}}\right)^{d+\sigma} J'_{ij}, & \text{if } r_{ij} \leq r_c \\ 0, & \text{otherwise } r_{ij} > r_c \end{cases}$$

Where $S_i = (s_i^x, s_i^y, s_i^z)$ are the vectors of the spins. This is to find the pairwise interaction of the spins with their neighbours up to a specified range, r_c , hence (i, j) in the summation represents the sum over pairs of spins. The summation over pairs mean there is no double counting. The coupling strength between pairs is given by J'_{ij} , which is set to zero when i and j are coupling from the opposite surfaces in the z direction to ensure finite boundaries are satisfied. The coupling strength between a pair of spins, decays to J_{ij} with range and is set to zero if the range between neighbouring pairs, r_{ij} , is greater than the range of interest, r_c . The a term is the lattice parameter of the simple cubic structure and in the simulations is set to 1.

For all the results in this chapter that compare the NN and further ranged (FR) systems (shown in figure 5.4), it is necessary to relate both to the same energy scale. This ensures that the total energy of the system does not increase simply due to the number of interactions increasing. Additionally, one will notice that there are no units

in the quantities in figure 5.5 neither in all of the results to follow in this chapter and the next. This is because these quantities are all dimensionless.

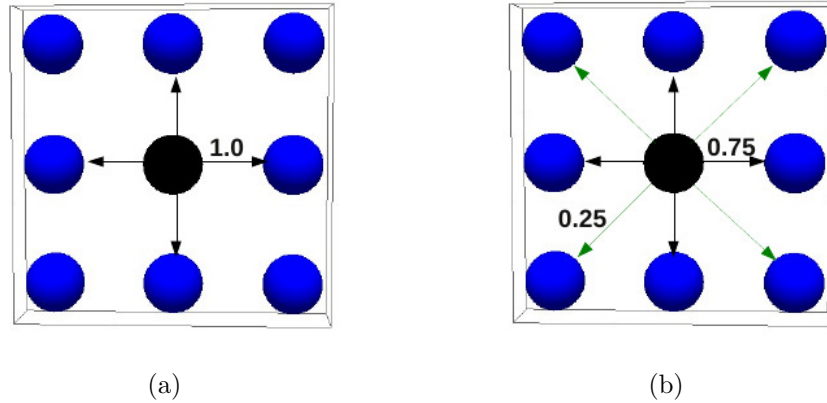


Figure 5.4: Schematic to demonstrate the rescaling of the energy for the FR system to that of the NN system. (a) NN interactions with $J = 1$ and an energy of $4J$ (4 upon substitution), as the energy is equal to the sum of J couplings. (b) Extended range of interactions to include 2^{nd} NN. In this case there are 8 interactions and J must be distributed so that the total energy still amounts to 4, where NN contributes more to the energy than the 2^{nd} NN. The weighting is determined by the range, r and the number of interactions and hence note this is not an exact calculation.

Figure 5.4 shows a schematic of rescaling the energy of the FR system (b) to equal that of the NN (a). By setting the FR system equal to the NN system, the relative coupling strengths must decrease with distance due to the weighting from the power law decay. It is easy to see that with longer ranges of interaction, the J couplings in the system become smaller, whilst the global J coupling remains constant.

An analytical interpretation of this energy rescaling can be obtained by considering a factor Λ such that $J_{\text{eff}} = \Lambda J_0$, where J_0 is the NN exchange constant and J_{eff} is the rescaled exchange of the further ranged system. To find the value of J_{eff} , the energies

of the two systems are set equal to one another:

$$\sum_{\langle i,j \rangle}^N J_{ij} S_i \cdot S_j = \Lambda J_0 \sum_{\langle i,j \rangle}^{n.n.} S_i \cdot S_j \quad (5.2)$$

where *n.n.* is the number of nearest neighbours. Here, $\sum_{\langle i,j \rangle}$ is over any pair of spins separated by up to r_c and $\sum_{\langle i,j \rangle}^{n.n.}$ is conventional for the sum over nearest neighbour pairs. Substituting for $J_{\text{eff}} = \Lambda J_0$ and rearranging to make J_{eff} the subject, then,

$$J_{\text{eff}} = \frac{\sum_{\langle i,j \rangle}^N J_{ij} S_i \cdot S_j}{\sum_{\langle i,j \rangle}^{n.n.} S_i \cdot S_j} \quad (5.3)$$

Therefore to change the energy scale, the long range energy is divided by J_{eff} to set the energy scale equivalent to that of the nearest neighbour.

In the experimental work by Ahlberg *et. al.*, the strongly coupled species in the multilayer is a δ layer, meaning it has less than a monolayer coverage. Despite the small coverage, δ layers are known to still have a large effect on the properties of a multilayered system [287]. *XY* spins on a two-dimensional lattice have been found to appropriately model a δ layer of 0.5 ML of Fe [288], hence we model a single layer of *B* spins with *XY* dimensionality. It is also known that layered Heisenberg spins with planar anisotropy behave like quasi- $2dXY$ systems [289], so even if the spins of the δ layer have a Heisenberg nature, their strong intra-species coupling mean they have a strong planar anisotropy. This is why understanding the $2d XY$ system is of relevance to this study.

XY spins are very sensitive to finite size effects, which means their critical behaviour is highly dependent on the system size. These finite size effects are revealed when the correlation length, ξ , of the spins is greater than the dimension size, L . At low temperatures, the *XY* monolayer has excitations known as spin waves and high energy excitations known as vortices, which can give a false result if their length/bound state is “cut-off” by the finite boundaries. In this study, the *xy* plane is fixed to a size of 32×32 to compromise between computational effort and the accuracy of results. This size was reasonable in finding the critical behaviour of the $2d XY$ system in Bramwell

and Holdsworth's work [49] and when this monolayer is inserted into the multilayer system, the finite size effects are smaller in the three-dimensional structure due to a smaller exponent relating the correlation length [97]. In terms of the demand on computer time, it has recently been shown that the entropic behaviour is dependent on the system size [290] such that as the system size increases, the entropy increases and the relaxation times grow exponentially. Hence larger systems would be computationally demanding.

This study uses periodic boundaries in the xy -plane and finite boundaries in the z direction with a simple cubic (SC) structure for the model to closely model thin films.

5.3.1 Comparing nearest neighbour and further ranged exchange interactions in the $2d$ XY model

Figure 5.5 shows the simulated plots of m vs T/J_{eff} the NN, 4^{th} NN and 6^{th} NN $2d$ XY system, which has a fixed J'_{ij} between NN spins equal to 1.

This figure shows a plot of magnetisation per spin vs T/J_{eff} for NN, which is simply a reproduction of Bramwell and Holdsworth's result [49], compared with further range exchange interactions. We can see that regardless of the decay rate given by α (r^{-3} with $\sigma = 1$ or r^{-4} with $\sigma = 2$), the transition temperature, T_c , increases as the range of interaction increases. The values were found to be: $T_c(\text{NN}) = 1.08$, $T_c(6^{\text{th}} \text{ NN with } \sigma = 1) = 1.42$, $T_c(6^{\text{th}} \text{ NN with } \sigma = 2) = 1.32$ and $T_c(4^{\text{th}} \text{ NN with } \sigma = 1) = 1.37$ using a χ^2 fitting method.

Within the transition region there has been $\sim 30\%$ increase in T_c when comparing 6^{th} NN with NN interactions for $\sigma = 1$ (difference corresponds to ΔT in figure 5.5) and $\sim 20\%$ increase in T_c when comparing 6^{th} NN with NN interactions for $\sigma = 2$. This is a significant difference between the further ranged (FR) and nearest neighbour (NN) interactions, as there is no variation in the total coupling strength and consequently

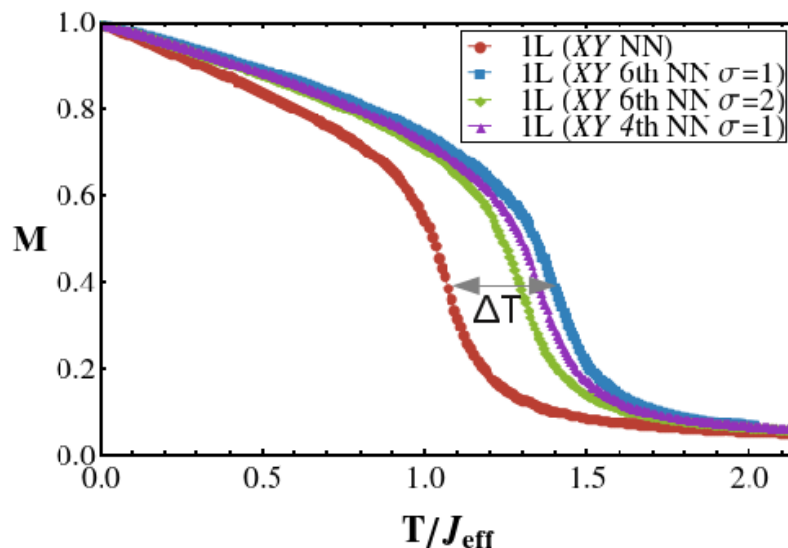


Figure 5.5: m vs T/J_{eff} of the $2d$ XY system with NN, 4^{th} NN ($\sigma = 1$) and 6^{th} NN ($\sigma = 1$ and $\sigma = 2$) interactions. 1L indicates “1 layer”. This is for a 32×32 system with $J'_{ij} = 1$ using $t_{eq} = 10^4$ MCS/s and $t_{obs} = 10^5$ MCS/s.

the energy due to the rescaling of the energies as mentioned in section 5.3. The range of attractive interactions is decaying faster with $\sigma = 2$ than $\sigma = 1$, as shown in figure 5.5, which is expected since it is known that beyond $\sigma = 2$ for all d dimensions, that the exponents obtain their short range values [276]. This would explain why $T_c(6^{\text{th}}$ NN with $\sigma = 2$) is shifted less from the NN result and why there is a greater difference in T_c from the decay rates (r^{-3} and r^{-4}) than there is for the range of interactions considered. It is more likely that a smaller range of interactions than 4th NN could correspond to the $\sigma = 2$ plot as both would tend towards NN interactions.

It was expected that the results in figure 5.5 would approach a behaviour similar to that predicted by mean field theory. This is because when the energy of the FR system is rescaled to that of the NN energy, the effective interaction of the closer neighbours decrease until in the limit of an infinite range of interactions where all J_{ij} are approximately zero and equal. Mean field theory predicts a system which is effectively infinite dimensionally since all spins interact equally with every other [28] and since only the thermal equilibrium average of the effective external field a spin experiences is

taken into account in the Hamiltonian [26]. Therefore with this knowledge, as the range of interactions increases in the $2d$ XY exchange coupling system, the system becomes “mean-field like” in the limit of an average J coupling equal to zero. This means the spins effectively become non-interacting and the only dependence in the system is the spin configuration.

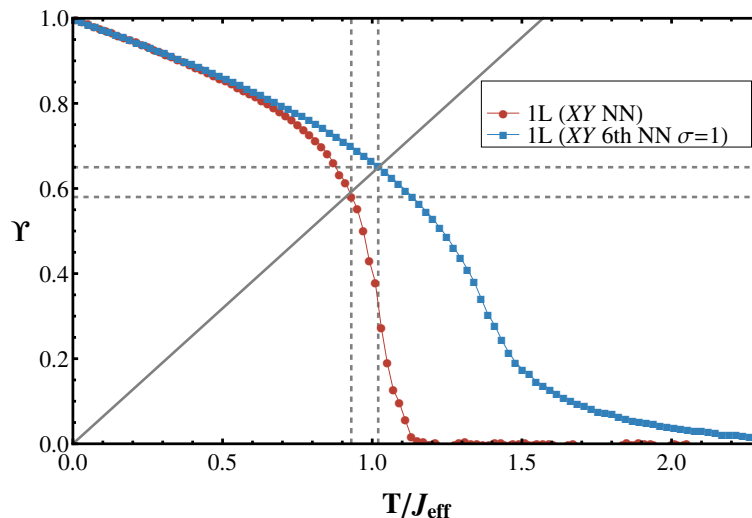


Figure 5.6: Spin stiffness vs T/J_{eff} comparing the NN and 6^{th} NN ($\sigma = 1$) $2d$ XY system. This is for the helicity in the y direction, the direction all spins initially are ordered in. The slope $f(T) = 2T/\pi$ is to show the universal jump in Υ at $T = T_{BKT}$, which is indicated by where the slope $f(T)$ crosses the two plots respectively (the gridlines also indicate the coordinates of these two points). For the NN system, $\Upsilon/T = 2/\pi$ when $T_{BKT} \simeq 0.93$ consistent with the result found by [49] and $T_{BKT} \simeq 1.02$ for the FR system.

To help explain why T_c of the FR system is greater than the NN system, the spin stiffness calculated for both systems (see figure 5.6). This is related to the helicity modulus, Υ , in equation 5.4 [68], which depends on the relative phase between neighbouring spins and how the system responds to a uniform rotation in one Cartesian direction

(here it is indicated by the y direction as it is in the code).

$$\Upsilon = -\frac{1}{2}\langle E \rangle - \frac{1}{T} \left\langle \sum_{\langle i,j \rangle} [\sin(\theta_i - \theta_j)(\vec{r}_{ij} \cdot \vec{y})]^2 \right\rangle \quad (5.4)$$

where $\langle E \rangle$ is the average energy of the nearest neighbour system at a particular temperature, T , θ_i and θ_j are the polar coordinates of neighbouring spins i and j , \vec{r}_{ij} is the distance between the two spins and \vec{y} is the unit vector in the Cartesian direction in which this helicity forms. It is only the second term ($\frac{1}{T} \langle \sum [\sin(\theta_i - \theta_j)(\vec{r}_{ij} \cdot \vec{y})]^2 \rangle$) which differs between the NN and FR systems as it identifies the interaction between neighbouring spins in the respective systems and subtracts this from the nearest neighbour energy. Figure 5.6, shows that the spins are stiffer in the FR system throughout the temperature range. A mean field system would imply that the fluctuations in the system are no longer of concern as correlations between spins are neglected. This is contrary to the possible hypothesis that due to the correlations in the FR system, the spins are stiffer. Rather, the neglect of correlations causes T_c to be entirely dependent upon the sum of all the exchange interactions that is experienced by any one spin regardless of their range and hence gives a higher critical temperature in the mean field limit [30].

Included in the plot of the spin stiffness is the slope $f(T) = 2k_B T/\pi$ where $k_B = 1$ as mentioned in the Methods chapter. The intersection of this dotted line with the plot of m vs T for the NN and FR system gives $\Upsilon(T_{BKT}) = \frac{2}{\pi} T_{BKT}$. A universal BKT-transition takes place at $\lim_{T \rightarrow T_{BKT}} \Upsilon(T)/k_B T = 2/\pi$, which for the NN system is $k_B T_{BKT}/J_{\text{eff}} = 0.95$ [68] (in my results this is 0.93 using the *FindRoot* function in Mathematica), due to finite size effects. This is universal for all system sizes with nearest neighbours providing the system has BKT-behaviour[†]. When $L \rightarrow \infty$, then there is an exponential increase in the free energy when T_{BKT} is approached from above. For $T > T_{BKT}$, $\Upsilon = 0$ in the infinite system [68] as there is no spin stiffness and vortices are unbound, whilst finite systems demonstrate finite size effects so the plots in figure 5.6

[†]BKT stands for Berezinskii-Kosterlitz-Thouless. Mentioned in the introduction, it is the point at which bound vortices become unbound in the $2d$ XY model.

show $\Upsilon \rightarrow 0$ for $T > T_{\text{BKT}}$. With this in mind it may be possible to use this method to determine T_{BKT} in the 6th NN system, which here is $k_B T / J_{\text{eff}} = 1.02$.

To further investigate the excitations and universality class in the FR and NN systems I plot m vs T/T_c shown in figure 5.7 (a) for each system and then find the gradients of these plots, shown in figure 5.7 (b). The gradient contains information about the modes of excitation since a zero gradient starting from an ordered state, would imply that there are no modes of excitation, whilst a non-zero gradient indicates that excitations are present.

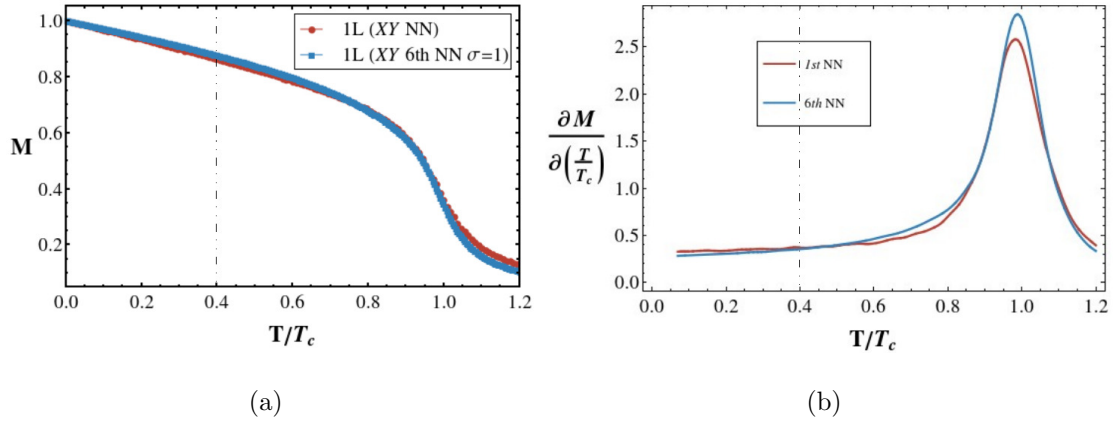


Figure 5.7: Magnetisation per spin vs T/T_c of the NN and 6th NN (a) and the corresponding $(\partial M / \partial (T/T_c))$ vs T/T_c plot (b). The gradients were obtained using Gaussian smoothing in one dimension (i.e. using a Gaussian filter).

To compare the gradients of these plots I particularly focus in the low temperature region (below $T/T_c = 0.4$), where Bloch's law holds. In a 2-dimensional system the reduction in the spontaneous magnetisation should behave as $\frac{M(0)-M(T)}{M(0)} \propto T$ [49] in this temperature region. This low temperature region only corresponds to low energy excitations present in the system [1], known as spin waves. Beyond this point higher energy excitations can exist, such as vortices and spin waves with shorter wavelengths such that Bloch's relation cannot be considered. From the gradients, one can deduce that the number of modes converting into excitations is greater in the NN system, since

the gradient is steeper than for the further ranged system.

The β exponents, found by fitting plots of m vs T with Matlab code developed by Ahlberg *et. al.*, remain characteristic of the $2d$ XY universality class [49] in the FR system. In the NN system $\beta = 0.21$ whilst $\beta = 0.23$ and $\beta = 0.22$ for the 6^{th} NN system with $\sigma = 1$ and $\sigma = 2$, respectively. The gradient plot in figure 5.7 (b) supports the spin stiffness results, since the smaller gradient in the FR system also indicates a greater spin stiffness than for the NN system. All of these results are consistent with the higher T_c observed in the further ranged system.

A more in depth analysis of how the range of interactions affect T_c (figure 5.8), reveals that $\log T_c \propto \log r$. This linear relationship indicates a power law behaviour of T_c with r related by $T_c = 1.09r^{0.248}$. Unfortunately it has been difficult to find

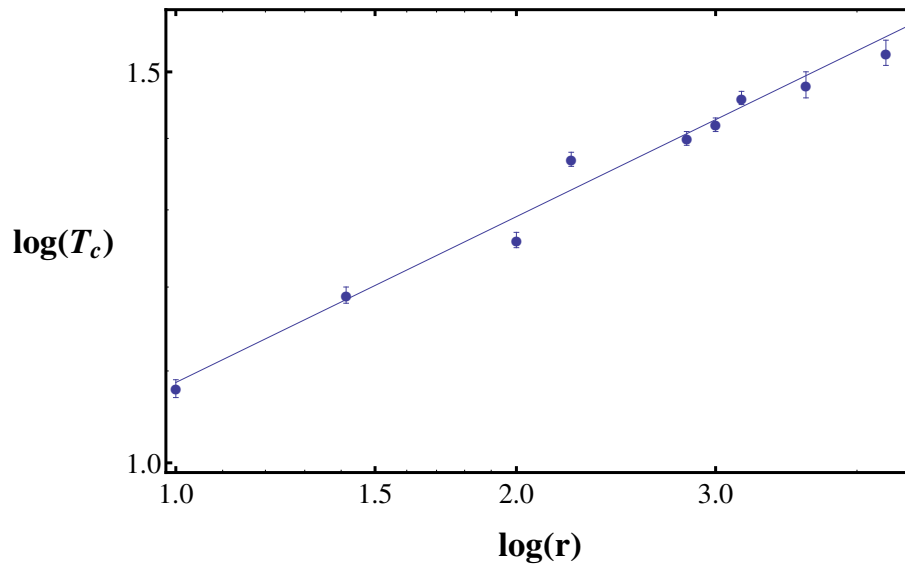


Figure 5.8: $\log T_c/J_{\text{eff}}$ vs $\log r$ with up to 9^{th} NN ($\sigma = 1$) in the $2d$ XY system. This spans all of the 3^{rd} coordination shell. The log – log plot demonstrates that there is a power-law relationship between the critical temperature and the range of interactions with the equation $1.09 + 0.248x$.

the literature corresponding to further ranged direct exchange interactions in $2d$ XY

systems with a power law decay. Extensive work has been conducted by Luijten and Blöte [275, 291, 292] on the range of interactions in $2d$ Ising systems using mean field theory and so a finite range of interactions has been considered before this study. My result for the $2d$ XY system with further ranged exchange interactions has at least shed light on a gap in the literature.

5.4 Proximity effect results: A two-way T_c enhancement in a ferromagnetic weak/strong coupled trilayer

It is known experimentally, that cobalt would not usually behave ferromagnetically in the monolayer limit [100]. Reasons for this range from: inefficient electron exchange for ferromagnetic coupling to simply only having islands of spins from a non-uniformly distributed layer. Below 1 ML thickness, $T_c \rightarrow 0$, as seen in figure 5.9. However, coupled to Fe in thin film CoZr/FeZr multilayers, ~ 0.5 ML (1 Å) Co becomes ferromagnetic by proximity with Fe [71]. This effect Fe has on Co is interesting since Fe is a weaker coupled species compared with Co so would not be expected to enhance the magnetic ability of Co. The aim of our study is to identify the intricate detail of the magnetisation throughout the CoZr/FeZr system by a general approach (i.e. how a harder magnetic material in the monolayer limit is affected by a slab of soft material when the coupling between them is varied).

Consider the generic system where B is the hard material like Co and A is the soft material like Fe, then the interspecies coupling strength, J_{AB} , is the coupling between them as shown in the schematic of the general multilayer system in figure 5.10. In the experimental work conducted by Ahlberg *et. al.* [71], the thickness of A was used as the main parameter to tune the interspecies coupling and therefore J_{AB} will be used in this study as the analogy to the thickness parameter. Key results in the experimental work showed a spin dimensionality crossover in the FeZr layers from $2d$ to $3d$ with

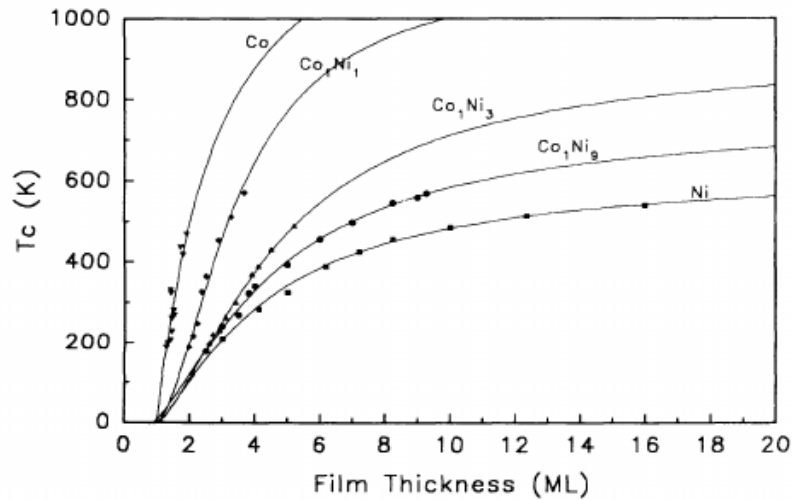


Figure 5.9: Experimental data [100] showing how the critical temperature varies with the layer thickness of Co, various CoNi alloys and Ni. Here we take particular interest in the plot for Co (first line on the left). The general trend is that upon reaching one monolayer, T_c approximates to 0.

decreasing thickness (L_{Fe}). To allow a crossover of spin dimensionality from $2d$ to $3d$, magnon modes perpendicular to the plane must be accessible [288], which is assisted by a high enough temperature and/or thickness. The interspecies coupling is highly relevant and important to this project since this can determine whether each layer is to behave independently or collectively in the multilayer system [293].

I will present the results of this study by analysing the A and B components separately, then together as a trilayer, before concluding with results on the multilayer with more repeat units.

5.4.1 Simulation results for a weakly coupled ferromagnetic slab

The coupling constants used in this study have been considered according to the Fe/Co multilayer used in Ahlberg's experiment, which effectively shows that the intraspecies coupling between A spins, J_{AA} , is four times smaller than between the B spins, J_{BB}

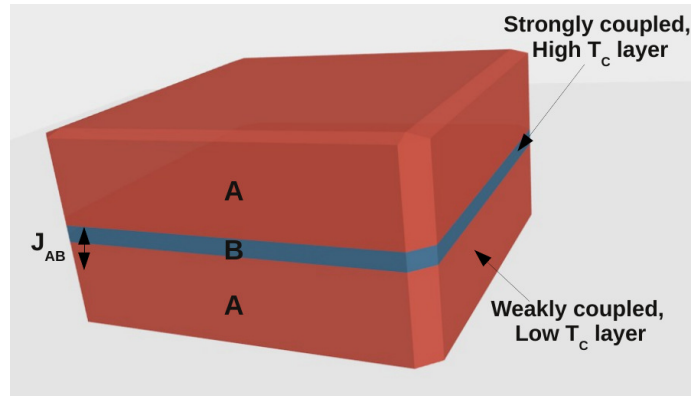


Figure 5.10: A schematic of the general ABA trilayer simulated in this study, where the A species is weaker coupled compared to the B species and consequently has a lower T_c than the B species. The interspecies coupling, labelled J_{AB} , is the coupling between these two species A and B .

[294]. Therefore I have chosen $J_{BB} = 1$ and $J_{AA} = 0.25$. In my simulations the set intra- and interspecies coupling in the bulk of the system is not different to the surface so that $J_s = J_{\text{bulk}}$, but due to the finite boundaries in the z direction and the power law factor in the Hamiltonian, a different energy at the surface can be obtained.

The following plot of magnetisation vs temperature vs layer in figure 5.11 is for a slab of A with 21 monolayers and is the equivalent size to that used in the simulated trilayer ($32 \times 32 \times 21$) for direct comparison.

The transition temperature for the A slab is shown in figure 5.11 at $T_c/J_{BB} = 0.91$, where the energy scale is set to T/J_{BB} for consistency in the results and $J_{BB} = 1$. The surface effects in the system, are indicated by a decline in the magnetisation, which is upon approaching monolayers 10 and -10 (the surface monolayers). This result is consistent with the plots of the magnetisation vs layer produced by Binder *et. al.* [97] who used the Ising model on a simple cubic lattice with thicknesses of up to 20 monolayers. As mentioned earlier, it is possible to simulate with $J_s \neq J_{\text{bulk}}$, however, this is accounted for in our model due to the finite boundaries.

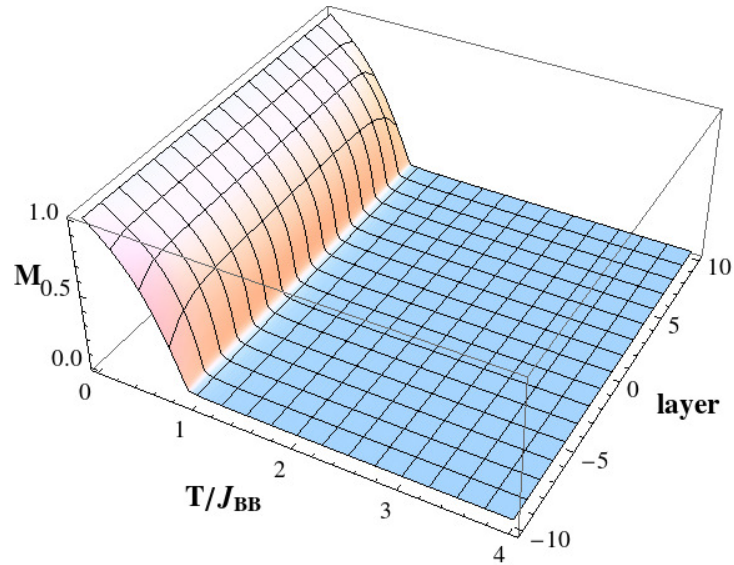


Figure 5.11: m vs T/J_{BB} vs layer $3d$ of an A slab, modelled with 21 monolayers of Heisenberg spins with further range exchange interactions (8^{th} NN).

A closer observation can be made by analysing plots of the magnetisation vs temperature for selected monolayers in the A slab (shown in figure 5.12). The surface monolayer (monolayer 10) clearly shows what has been discussed regarding surface layers and the lowering in magnetisation, whilst monolayers 6 and 1 are representative of the bulk of the system which is unaffected by reductions in magnetisation at the surface. However, the average magnetisation of the first 10 monolayers is very slightly reduced for all temperatures below the critical temperature compared with the magnetisation of the bulk system (e.g. monolayer 6), due to surface effects.

The results presented in figure 5.12 are only for the first 10 monolayers of the A slab as this will be used for comparison with the 10 A monolayers used in the trilayer given in section 5.4.3. The monolayers near to the surface which show this decline in magnetisation, in figure 5.11, are at least 3 layers deep from the surface monolayer as the range of interactions extend up to this coordination sphere in the simple cubic structure. Justification for this depth can be seen in figure 5.12 where the magnetisation in monolayer 6 corresponds well to the magnetisation in monolayer 1, which is almost the centre of the slab. Therefore a total of 4 monolayers are affected by surface effects

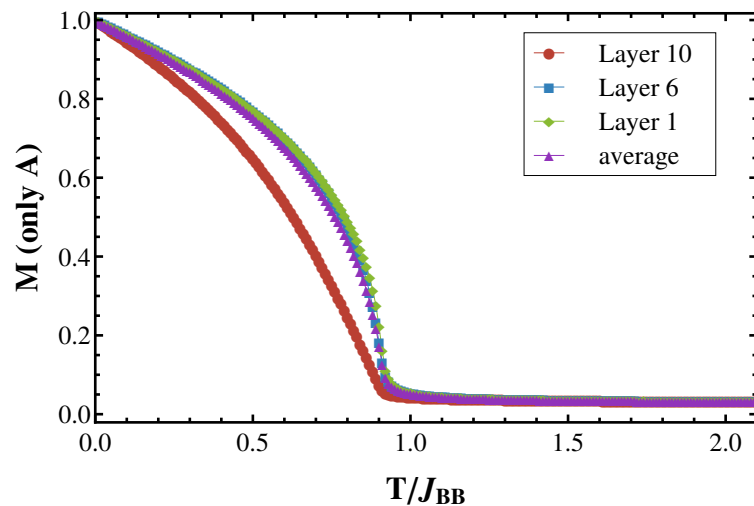


Figure 5.12: Magnetisation vs T/J_{BB} for individual monolayers in the A slab (21 monolayers thick). Comparison is made between monolayers 10 (surface), 6, and 1 (neighbouring the central monolayer). The average magnetisation of the first 10 monolayers is also included specifically as a direct comparison with the layer A used in the multilayer system (10 monolayers thick) in section 5.4.3.

(including the surface monolayer). This penetration would have been different for other crystal structures which have a greater proportion of neighbouring spins out of the plane. Taking the NN coordination as an example for the SC structure, only $1/3$ of its coordination are out of the plane, whilst the other $2/3$ are within the plane.

5.4.2 Simulation results for a strongly coupled ferromagnetic monolayer

In this study, the B layer is modelled as XY spins since the xy plane is the easy plane and also because a $2d$ layer with isotropic Heisenberg spins does not exist. The single layer of XY spins with $J_{BB} = 1$, periodic boundaries and further range exchange interactions was thoroughly investigated in section 5.3, however, for completeness we show the plot of $m(T)$ for the single layer here again.

One can see there is an increase in T_c from NN to 6^{th} NN and that T_c is greater for

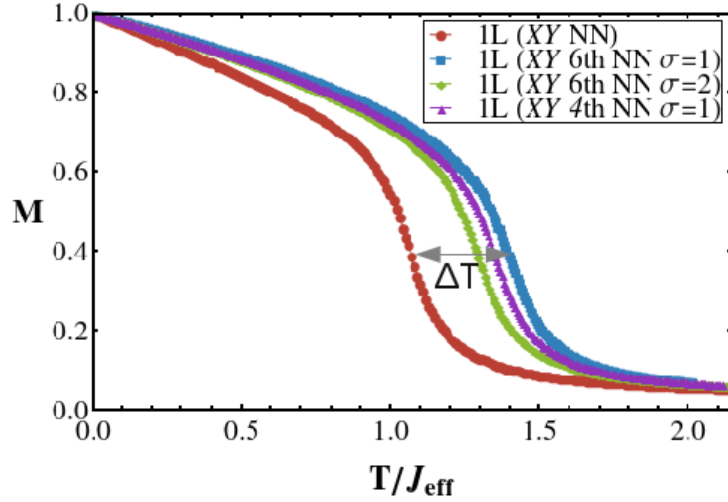


Figure 5.13: m vs T/J_{eff} of the $2d$ XY system with NN, 4^{th} NN ($\sigma = 1$) and 6^{th} NN ($\sigma = 1$ and $\sigma = 2$) interactions. 1L indicates “1 layer”. This was for a 32×32 system with $J_{BB} = 1$ using $t_{eq} = 10^4$ MCS/s and $t_{obs} = 10^5$ MCS/s. As shown before in figure 5.5.

the B layer than for the A slab due to a stronger intraspecies coupling. Specifically, $T_c(B) = 1.90$ with ($\sigma = 2$) and $T_c(A) = 0.91$, using the same T/J_{BB} energy scale as with the slab in section 5.4.1. Choosing $\sigma = 2$ is because then both the A and B would have the same rate of decay.

5.4.3 Simulation results for the ferromagnetic weak/strong coupled trilayer

The $2d$ XY monolayer (otherwise denoted as B), presented in section 5.4.2 replaces the middle monolayer of the A slab, presented in section 5.4.1 to form the magnetic trilayer. A schematic of this weak/strong/weak coupled trilayer is shown in figure 5.10.

The exchange coupling strengths are $J_{AA} = 0.25$, $J_{BB} = 1$ and the variable $J_{AB} = 0.20$, 0.30 , 0.45 , 0.60 , 0.75 . The Fe-Co coupling (as it would be in the experiment) is a stronger coupling than Fe-Fe coupling [269], so generally $J_{AB} > J_{AA}$. However, $J_{AB} = 0.20$ has been used for further comparison to see if there are any differences

in having $J_{AA} > J_{AB}$. This study does not consider dipolar interactions because in three-dimensional systems, dipolar interactions are small corrections to the exchange interactions [70]. However, dipolar interactions are important near the transition region and are very important for stabilising order particularly in the $2d$ XY and single-ion anisotropic Heisenberg systems [66].

The notation for these multilayer systems are defined in the following way: H = Heisenberg spins, X = XY spins, therefore HA corresponds to treating the A layer with Heisenberg spins and XB is to treat the B layer as XY spins. It is due to the relatively weak coupling in A compared with B , that the A spins are modelled as Heisenberg spins. For HA:XB:HA (10:1:10), this is to say that there are 10 monolayers of Heisenberg A spins, 1 monolayer of XY B spins sandwiched between another 10 monolayers of Heisenberg A spins.

Varying the interspecies coupling in the trilayer

Figure 5.14 shows $3d$ plots of the magnetisation vs temperature vs layer position of the trilayer for different interspecies coupling strengths. The influence of the strongly coupled layer on the weakly coupled layer is instantly noticeable when comparing a slab of A in the absence of a B layer (figure 5.14 (a)), to a weak interspecies coupling between A and B ($J_{AB} = 0.20$ in figure 5.14 (b)), to a strong interspecies coupling between A and B ($J_{AB} = 0.75$ in figure 5.14 (c)).

It can be seen that even when $J_{AB} < J_{AA} < J_{BB}$ (in figure 5.14 (c)), the A monolayers either side of the central B layer have a higher magnetisation than the other A monolayers. This is due to the strong coupling in the B layer which induces order in the neighbouring spins.

Since interactions extend to 8^{th} NN, the B layer directly couples to monolayers 1, 2, 3 and -1 , -2 , -3 . Seeing as the B layer is the only source of magnetic order then it is understandable why these neighbouring A monolayers are most affected. When the

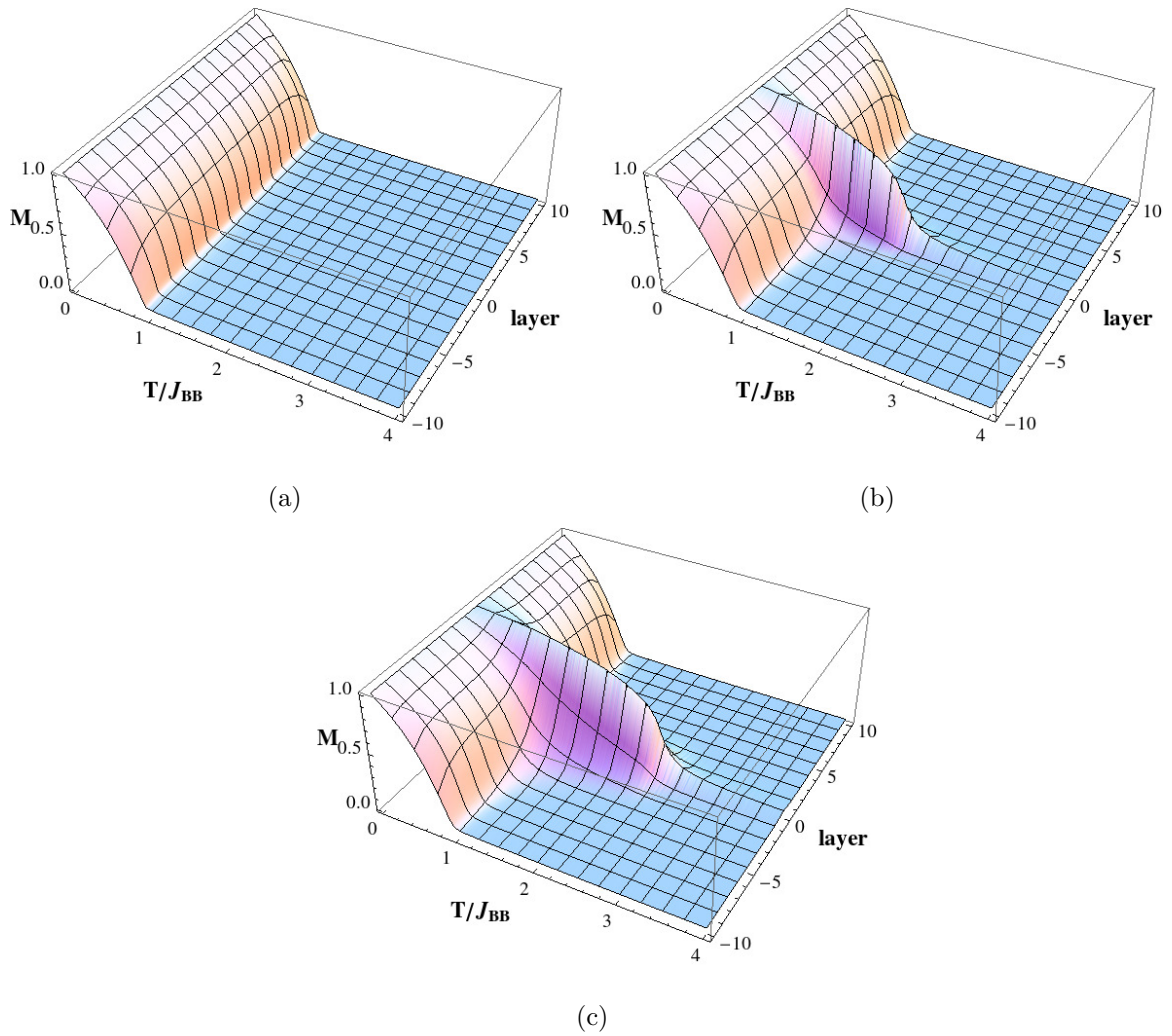


Figure 5.14: 3d plots of m vs T/J_{BB} vs layer in the trilayer system with HA:XB:HA (10:1:10) using 8th NN and 32×32 lateral size. (a) A slab with 21 monolayers and the trilayer with (b) $J_{AB} = 0.20$ and (c) $J_{AB} = 0.75$. The other couplings are $J_{AA} = 0.25$ and $J_{BB} = 1$.

interspecies coupling is increased to $J_{AB} = 0.75$ (see figure 5.14 (c)), there is not only an increase in the number of layers affected by the strong ordering of the B layer, but there is also an increase in $T_c(B)$, which can be seen more clearly in the m vs T/J_{BB} plot shown in figure 5.15 for the B layer with varying interspecies coupling.

From fitting the results in figure 5.15, T_c is found to increase by $\sim 27\%$ from $J_{AB} = 0.20$ to $J_{AB} = 0.75$. This increase in the ordering temperature is due to the

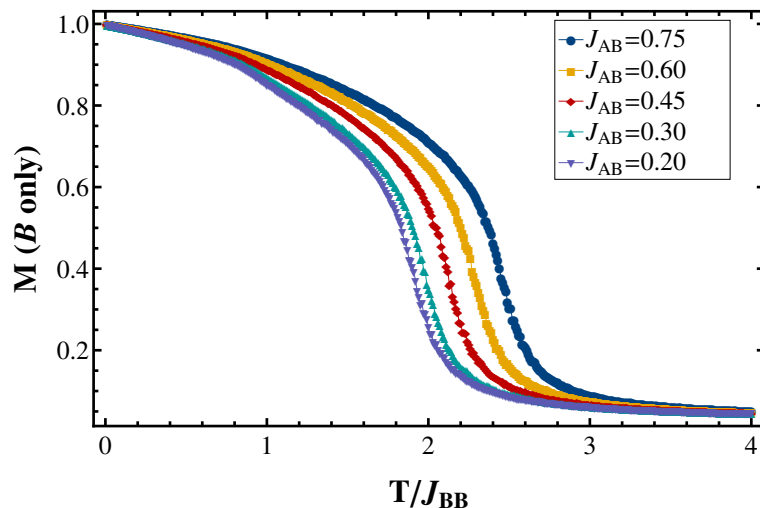


Figure 5.15: m vs T/J_{BB} for the B layer in the trilayer with different J_{AB} couplings indicated in the legend. One can see that as the interspecies coupling increases, T_c of the B layer increases.

decoupling region increasing, the region in which A decouples from B when $T > T_c(A)$. When the interspecies coupling is small in the trilayer, the B layer behaves as it would for a single layer of B , which can be seen in figure 5.16(a) (for 8th NN). This is consistent with the analytical work done by Griffiths in 1970 [295] where they state that as $J' \rightarrow 0$ ($J' \equiv J_{AB}$ in this study), the exponents of the physical quantities obtain their $2d$ values and the Curie temperature decreases continuously.

The deviation from the single layer behaviour is particularly seen when further ranged interactions are present, highlighting the importance of using longer range interactions when studying interfacial effects in magnetic multilayers. There is a greater deviation of the B monolayer from the single layer with a stronger interspecies coupling. This is due to the A monolayers which are in closest proximity to the B layer becoming more “ XY -like” with increasing interspecies coupling. To demonstrate this finding, plots of the average magnetisation per spin vs T/J_{BB} for monolayers 1 and -1 modelled as XY spins are shown in figure 5.17 and compared with the original model.

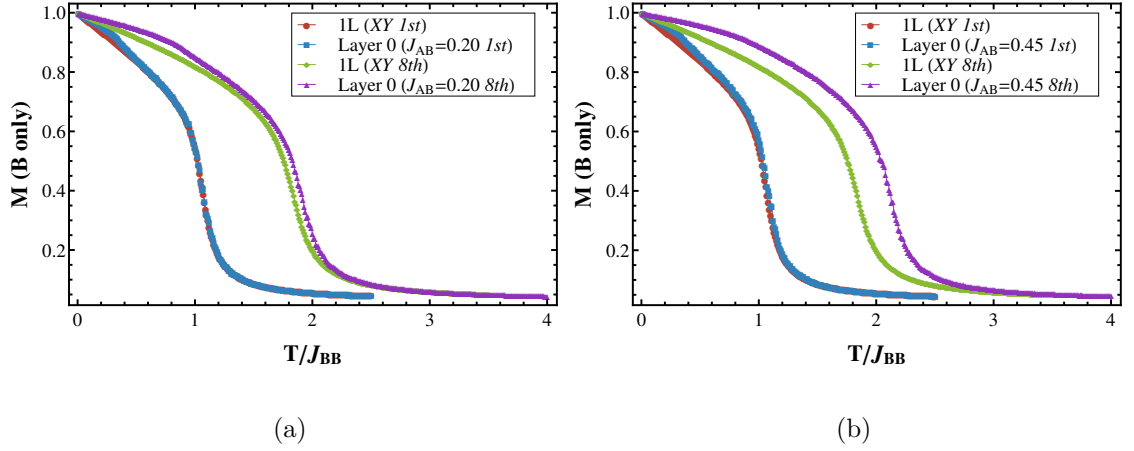


Figure 5.16: m vs T/J_{BB} comparing a single layer of XY B spins with the monolayer of XY B spins in the trilayer. This is for the trilayers when (a) $J_{AB} = 0.20$ and (b) $J_{AB} = 0.45$. Each plot is shown for 1st NN NN and 8th NN. Comparing the interspecies coupling strengths with a fixed range of interaction, shows that the B layer in the trilayer behaves more like the monolayer of B when the interspecies coupling is small.

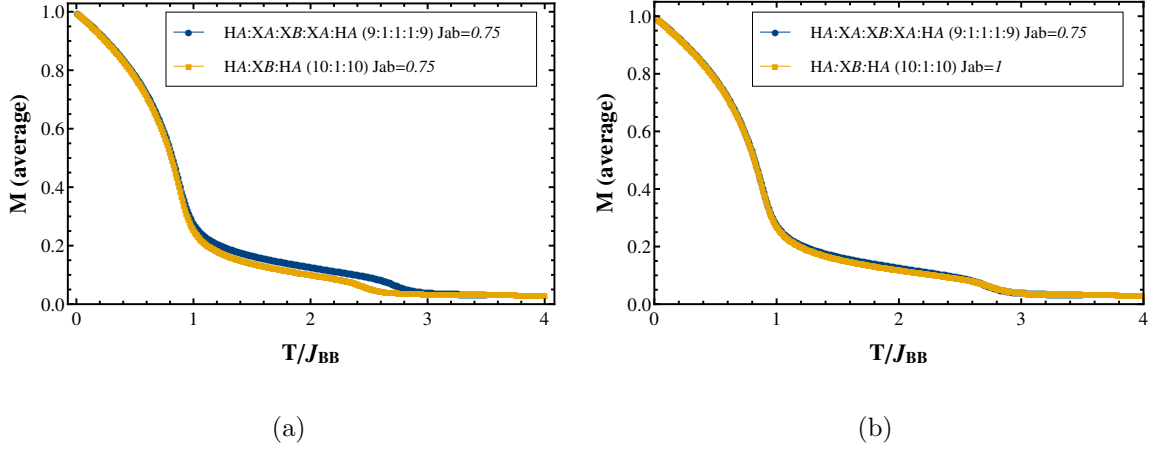


Figure 5.17: Average m vs T/J_{BB} comparing the trilayer $HA : XA : XB : XA : HA$ (9:1:1:1:9) with $J_{AB} = 0.75$ fixed and the original $HA : XB : HA$ (10:1:10) for (a) $J_{AB} = 0.75$ and (b) $J_{AB} = 1$. All plots have the coupling $J_{BB} = 1$ and $J_{AA} = 0.25$.

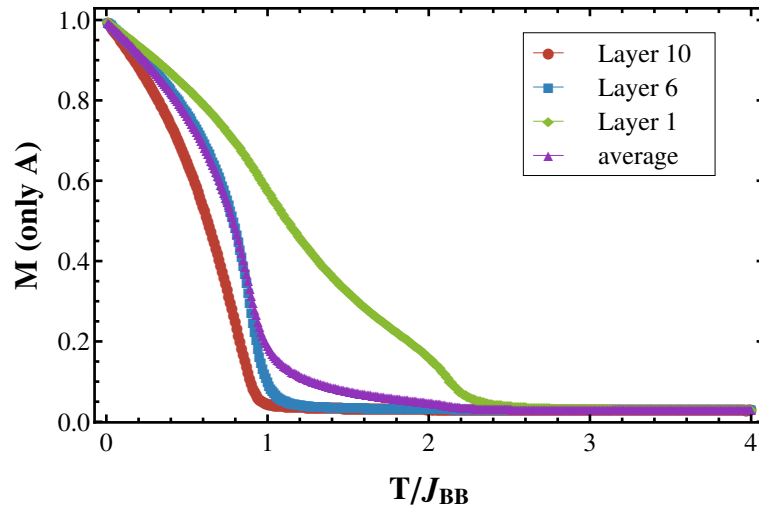
The modified system is denoted as $HA : XA : XB : XA : HA$ (9:1:1:1:9) whilst the original (modelling all A spins as Heisenberg), is denoted as $HA : XB : HA$ (10:1:10). The coupling strengths for the modified system and the original are the same in figure 5.17 (a) and one can see that these two systems do not behave exactly same. However, by increasing the interspecies coupling to 1 in the original system (figure 5.17 (b)) seems to show that considering the monolayers 1 and -1 as XY spins is a reasonable approximation. These plots show the average magnetisation of the entire system so they show the magnetisation contributions from the A layers (low T transition feature) and from the B layer (high T transition feature). These results are evidence of a limiting factor, that as $J_{AB} \rightarrow 1$ these Heisenberg A spins in the $HA : XB : HA$ (10:1:10) become more “ XY like”. Please note it has not been possible to determine the critical exponent of the interfacial A monolayers because of the odd shape of m vs T/J_{BB} .

Extent of magnetic induction in the weakly coupled layer of the trilayer

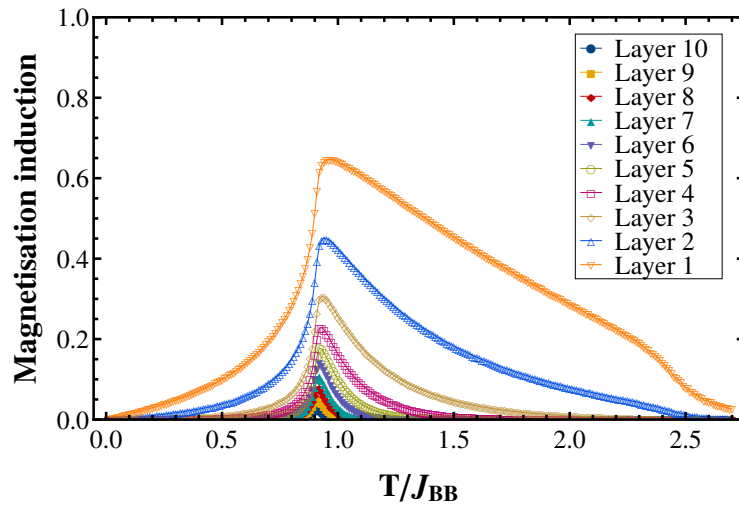
As was mentioned in the introduction to this chapter, the magnetic induction from the strongly coupled species into the weakly coupled species has been studied thoroughly and will be discussed in this section specifically for our model.

Figure 5.18 (a) shows the magnetisation distribution in individual monolayers of A in the trilayer. This plot is exactly the same as in figure 5.12, except rather than the monolayers being from a slab of A , it is for the respective monolayers in a layer of A in the trilayer and hence direct comparison can be made.

Figure 5.18 (a) demonstrates that with the inclusion of the B layer, the average magnetisation for one layer of A cannot capture the magnetisation in each monolayer of A , particularly the monolayers closest to the B layer. Maccherozzi *et. al.* [296] described the different regions of their Fe/(Ga,Mn)As bilayers, where (Ga,Mn)As is a paramagnetic semiconductor and iron is a ferromagnet, as a bulk region of the soft material (represented by monolayer 6 in figure 5.18 (a)), an interfacial region with induced



(a)



(b)

Figure 5.18: (a) m vs T/J_{BB} for individual monolayers of A in the trilayer with $J_{AB} = 0.45$ and 8^{th} NN (b) the amount of magnetisation induced in each monolayer of A when $J_{AB} = 0.75$ as a function of temperature. This is found by subtracting the magnetisation of a monolayer in the A layer of the trilayer system from the magnetisation of the respective A monolayer in an A slab.

ferromagnetic order (represented by monolayer 1) and a harder ferromagnetic region (monolayer 0). Figure 5.18 (b) shows how the induction of ferromagnetism evolves with layer distance with respect to temperature.

Figure 5.19 shows that the results in figure 5.18 (b) are system size independent for A layers closest to the B layer or at high temperatures[‡]. This plot shows the magnetisation vs layer results for a $HA : XB : HA$ (20:1:10) system with increasing temperature as indicated by the arrow. The system size with a smaller thickness “feels” the surface effects proportionally more and hence the equivalent layers in the two different systems sizes will not have the same magnetisation. The fact that these two system sizes do not show exactly the same decay in magnetisation for some temperatures, this indicates that there is some sort of “cut off” in the induction when using 10 monolayers of A and hence the extent of induction could be beyond the 20 monolayers of A , but would require further investigation. For temperatures exceeding T_c , it is clear that the decay in magnetisation is exactly the same regardless of the thickness because even the smaller system size is relatively larger than the extent of induction.

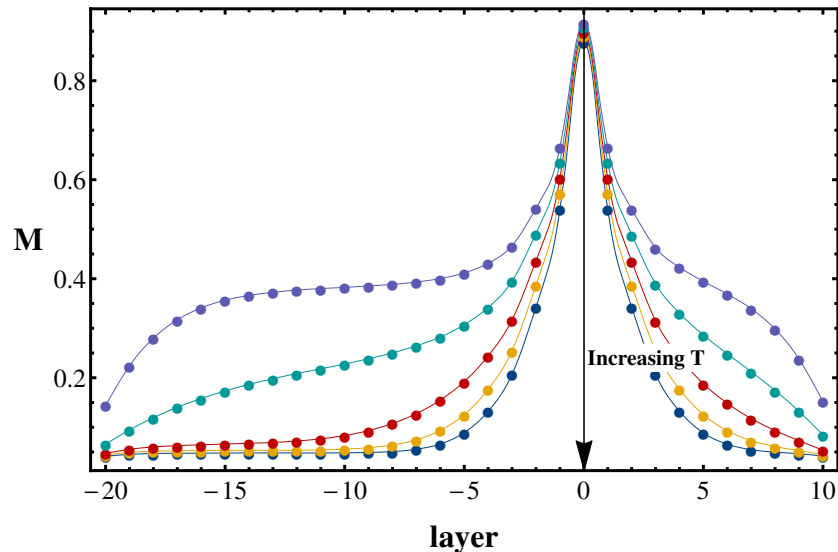


Figure 5.19: Magnetisation per spin vs layer for the trilayer system comparing the decay in magnetisation in 10 monolayers of A with that in 20 monolayers of A using the $HA:XB:HA$ (20:1:10) system. The increasing temperature is indicated in the plot, where the curve for $T_c(A)$ is the highest temperature plot (purple line for coloured version).

[‡]For temperatures within the decoupling region $T/J_{BB} = 0.86, 0.91, 0.96, 1.01, 1.06$.

Spin dimensionality analysis in the trilayer

So far, it is clear that the B layer is inducing magnetic order in the A layers, so that $T_c(A)$ increases and neighbouring A monolayers of the B layer become more “ XY -like” or in other words, “more B -like” in spin nature with increasing coupling strength. However, it has also been shown that the ordering temperature of the B layer increases with coupling strength. In this section we show that this is a consequence of an increase in *effective thickness* of the B layer.

The following spin dimensionality results are unique to ultrathin layers of B (ultrathin films are $\lesssim 7$ ML thick [100]), as ultrathin materials behave as $2d$ systems [288] so an increase in effective thickness will cause a crossover to $3d$ behaviour.

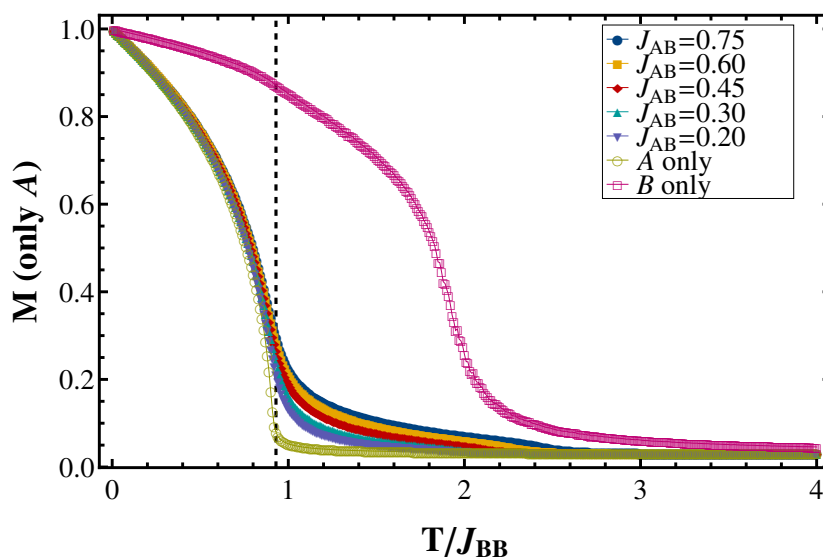


Figure 5.20: An average m vs T/J_{BB} for one A layer for different J_{AB} couplings using 8^{th} NN. Also included is the B layer from the trilayer with $J_{AB} = 0.20$ to show how the $3d$ feature in the decoupling region declines at the transition region of the A spins (indicated by the dotted line).

For the small coupling, $J_{AB} = 0.20$, J_{AA} dominates J_{AB} at temperatures close to $T_c(A)$ and decoupling occurs abruptly in this region (shown in figure 5.20). Hence the

B spins are left to behave more “ $2d$ -like” for $T > T_c(A)$ which is supported by figure 5.16(a). With a stronger interspecies coupling the A monolayers closest to the B layer remain ordered so that J_{AB} dominates J_{AA} even when $T > T_c(A)$. The order in the A layers then decline in the decoupling region at a rate dependent on the interspecies coupling strength. Due to the extended temperature range of ordering in the A layers, the B layer behaves as though it has a greater effective thickness. This would indicate a change in the exponent since the shape of the low temperature region of an m vs T/J_{BB} plot describes the universality class of the material.

Figure 5.21 demonstrates this change in shape, where (a)-(d) show plots of T/T_c for the single layer of B spins (NN and 6^{th} NN) and the B monolayer in the trilayer (8^{th} NN for $J_{AB} = 0.20$ and $J_{AB} = 0.45$).

Keeping in mind that Bloch’s law only holds for the low temperature region, the results from the single layers should show a linear relation with T/T_c as a $2d$ system, whilst a $3d$ system should follow the relationship $\frac{M(0)-M(T)}{M(0)} \propto T^{3/2}$. The fitting shown in figure 5.21 was found by fitting up to $T/T_c = 0.4$ to the equation $y = ax^b + c$. The results show that for the single layer of B with 6^{th} NN, $b = 1.09$, the monolayer of B in the trilayer with $J_{AB} = 0.20$, $b = 1.28$ and with $J_{AB} = 0.45$, $b = 1.47$. These findings strongly support that the dimensionality of B spins changed to $3d$ in a system with only one B monolayer. The ABA system with an increased B thickness is discussed in appendix D to compare with the results found here for B with an increased “effective thickness”.

Overview of varying the range and interspecies coupling in the weak/strong coupled trilayer

It has been shown that further ranged interactions are required to observe key features in these results which are inaccessible to NN interactions, such as the increase in effective B thickness. The difference between the two ranges, NN and 8^{th} NN, are shown more clearly in the magnetisation vs layer profiles in figure 5.22. These have been plotted

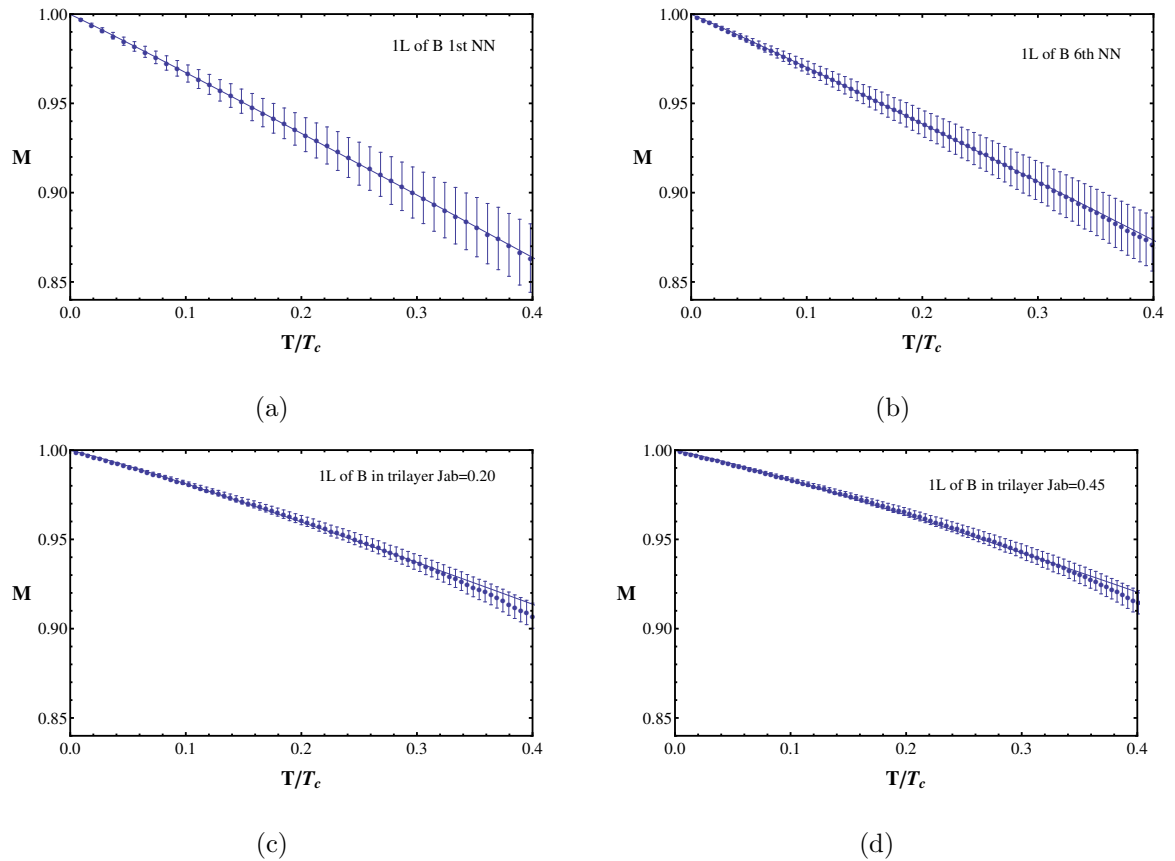


Figure 5.21: Fits to m vs T/T_c in the low temperature region according to Bloch's law. For (a)-(d), the change in exponent using Bloch's law, which shows that as the interspecies coupling in the trilayer increases, the relation approaches the $\frac{M(0)-M(T)}{M(0)} \propto T^{3/2}$, characteristic of a $3d$ system rather than the linear relation for a $2d$ system. This is found by fitting up to $T/J_{BB} = 0.4$ of the T/T_c plot to $y = ax^b + c$. (a) The monolayer of B with NN, $b = 1.06$, (b) the monolayer of B with 6^{th} NN, $b = 1.09$, (c) the single layer of B in the trilayer with $J_{AB} = 0.20$, $b = 1.28$ and for (d) $J_{AB} = 0.45$, $b = 1.47$. 8^{th} NN are used to produce (c) and (d).

with the scale T/J_{eff} as this is a comparison between different ranges. The profiles are taken at approximately the same temperatures[§].

One can easily see that the peaks in the magnetisation vs layer profiles are broader

[§]The temperatures for 8^{th} NN are to 2 decimal places after rescaling.

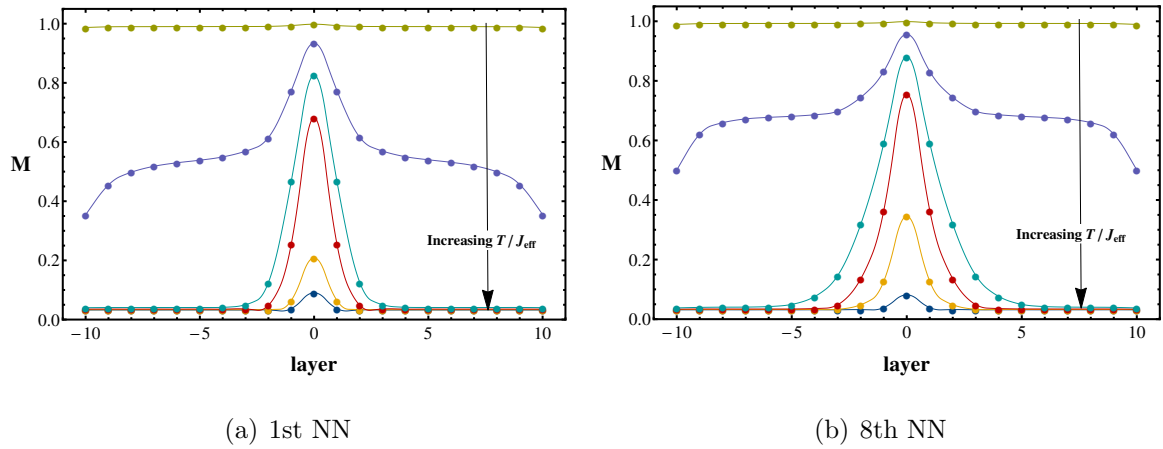


Figure 5.22: Magnetisation vs layer profiles for the trilayer system comparing the range of interactions using $J_{AB} = 0.75$ for (a) NN and (b) 8th NN. Each profile corresponds to one of the temperatures $T/J_{\text{eff}} = 0.01, 0.31, 0.61, 0.91, 1.21, 1.51$ and 1.81 , where these temperatures are to 2 decimal places for 8th NN after re-scaling.

when longer range interactions are used since the magnetic induction extends further within layer A . When the interspecies coupling is simultaneously varied with the range, the critical temperature in the B layer changes as shown in figure 5.23.

Using first nearest neighbour coupling in the trilayer system, shows little variation in $T_c(B)$. The critical temperature of $J_{AB} = 0.75$, found using the fitting method, is lower than for $J_{AB} = 0.60$, whilst $T_c(B)$ increases steadily for the other coupling strengths. The deviation between these two coupling strengths is small and if these T_c 's were extracted from the $\chi(T)$ peaks method, then the T_c trend would be linear, with $T_c = 1.125$ and $T_c = 1.1$ for $J_{AB} = 0.75$ and $J_{AB} = 0.60$, respectively. Due to multiple peaks in the NN $\chi(T)$ plots for some of the couplings, the NN T_c values for all coupling strengths are extracted from the fitting method. Figure 5.23 shows that for further ranged interactions, the critical temperatures differ more between the coupling strengths and alternate with higher and lower T_c values as the range increases. The possible reasoning could be due to the finite size effects, the ‘‘cut off’’ in the decay of interactions and the finite range of interactions, which would be more important for stronger couplings. Following the pattern otherwise, the least variation of $T_c(B)$ with

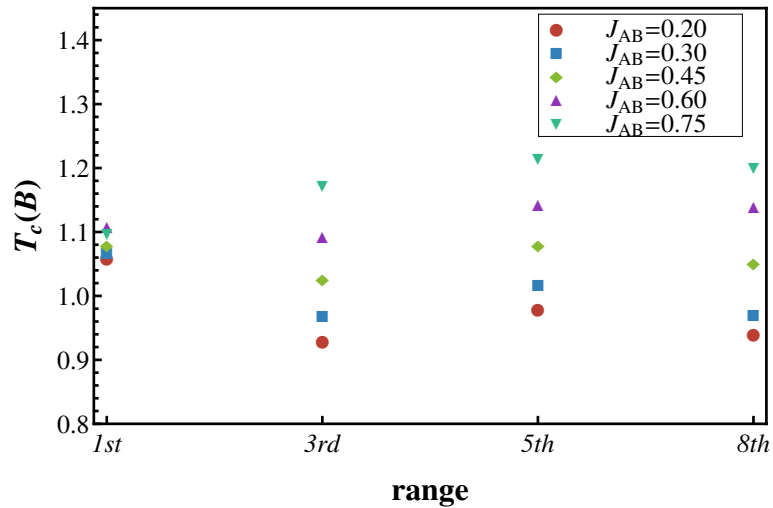


Figure 5.23: $T_c(B)$ vs range for different interspecies coupling strengths in the trilayer. The critical temperatures are found from the peak in $\chi(T)$ of the B layer, except for the NN results, which were found using the fitting method by Ahlberg *et. al.* [20]. This is since multiple peaks in the NN $\chi(T)$ plots for some of the couplings meant it was difficult to extract $T_c(B)$.

range is when $J_{AB} = 0.45$, which could be a limiting observation for $J_{AB} \rightarrow 0.50$.

A mapping produced as in figure 5.23, could prove useful when modelling these magnetic multilayers and help to optimise the range and coupling strength. For instance, it could be considered that the range and interspecies coupling strength that produces the highest $T_c(B)$, is the system where B is most inducing in A and hence the effective thickness of the B layer is greater. Further ranges are required to conclude a general trend.

5.4.4 Simulation results for the ferromagnetic weak/strong coupled multilayer with more repeat units

The experimental study conducted by Ahlberg *et. al.* [71] was for a magnetic multilayer with 10 repeat units and one extra weakly coupled layer for symmetry. The key hypothesis was that providing there are two strongly coupled layers neighbouring a weakly

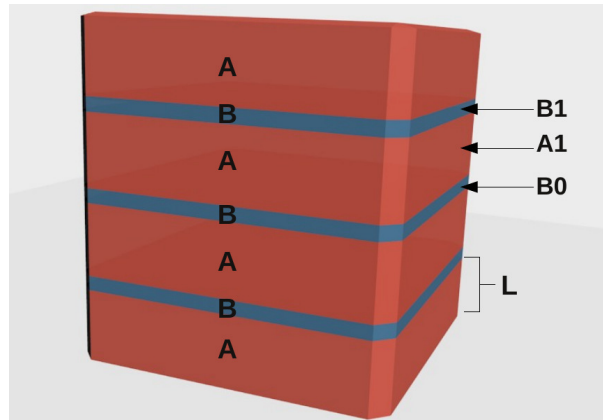


Figure 5.24: A schematic of the multilayer with 3 repeat units and 1 extra A layer for symmetry, as it was in Ahlberg’s work. The parameter, L , which is the thickness of each A layer is indicated on the diagram. $A1$, $B1$ and $B0$ have been highlighted.

coupled layer, either side of it, then when the thickness, L of the weakly coupled layer decreases, indirect interaction between the two strongly coupled layers can occur. This interaction is said to occur through the overlap of proximity effects from the two inducing sources and as a result a dimensionality crossover of the system should be observed. Given this information, the model used in this project is shown in figure 5.24. This has 3 repeat units of A/B with an extra A layer.

Each B layer is a monolayer thick, whilst the thickness of the A layers are varied, as was carried out by Ahlberg *et. al.* The three A thicknesses used here are $L = 3, 6$ and 10 monolayers, using $J_{AB} = 0.75$. The use of a strong coupling is to ensure that the physics of the system can be observed without a limitation on the coupling. In a similar way these multilayers are studied with varying coupling strengths, $J_{AB} = 0, 0.20, 0.45$ and 0.75 , using $L = 6$. This system size was chosen because the range of interactions is up to the 3^{rd} co-ordination cube and hence $L = 6$ is the minimum distance between the two strongly coupled layers before their direct interactions overlap, therefore this should maximise the induction effects which are experienced. The Monte Carlo timings were kept the same as for the trilayer $t_{eq} = 10^4$ MCS/s and $t_{obs} = 10^5$ MCS/s, only MCS/s= $\text{MCS} \times N$ is changed accordingly.

The effect of varying the thickness and interspecies coupling strength in the multilayer

Ahlberg *et. al.* [71] described the strength of the indirect interaction between the B layers as being determined by the relationship of the width of the magnetisation profile, W , with the thickness of the A layers, L . This interaction is determined by the overlap of the induced magnetisation from the B layers. Hence the dependence on W and L is:

- $W > L$, strong interaction
- $W \simeq L$, weak interaction
- $W < L$, no interaction.

Figure 5.25 (a) is the schematic proposed by Ahlberg *et. al.* [71], whilst figures 5.25 (b)-(d) show the m vs layer results for the three different thicknesses of A used in this study. Figures 5.26 (a)-(d) also show the m vs layer results for the four different interspecies coupling strengths used in this study.

Both figures 5.25 and 5.26 show the magnetisation vs layer position in the systems for three temperatures, $T_1 (T < T_c(A))$, $T_2 (T \rightarrow T_c(A))$ and $T_3 (T > T_c(A))$, where $T_c(A)$ was found previously to be 0.91. It is clear to see that the magnetisation profile of the multilayer proposed by Ahlberg *et. al.* [71] is correct with increasing temperature. For T_1 , the magnetisation throughout the A and B layers is the same since there is a spontaneous magnetisation throughout. As the temperature increases to T_2 and approaches T_c , there is evidence of magnetic induction from the B layers, to the A layers which becomes smaller when the A monolayer is further from the inducing source (B layer). At T_3 of figure 5.25 (a), the temperature is much greater than $T_c(A)$ and is beginning to approach $T_c(B)$. In the work by Ahlberg *et. al.*, $T_3 > T_c(B)$, which is not the case in this study and surface effects seem to be omitted in the work by Ahlberg's *et. al.*

Comparing the effects of thickness and coupling strength on the multilayer, one can see that increasing J_{AB} or decreasing L , increases the magnetisation induced in the A

monolayers. For the smallest thickness, $L = 3$, $W > L$ since both central A layers (e.g. A1) are all directly interacting with two B layers, as the range of interactions extend to the 3^{rd} co-ordination sphere of the cubic lattice. As L increases to $L = 6$, it is still

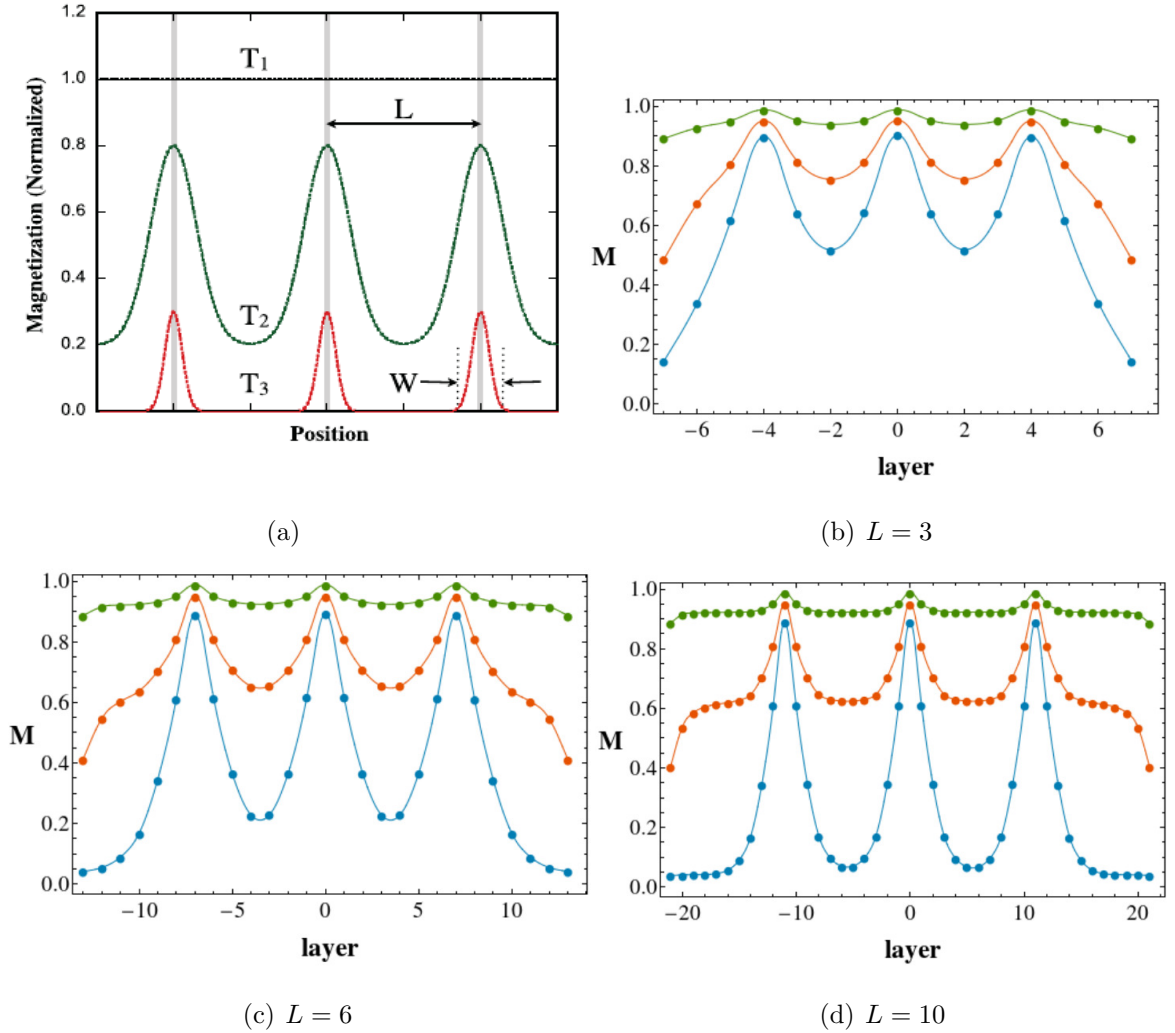


Figure 5.25: Magnetisation vs layer of the A/B multilayer for different L at three different temperatures T_1 ($T < T_c(A)$), T_2 ($T \rightarrow T_c(A)$) and T_3 ($T > T_c(A)$), where $T_c(A)$ was found previously to be 0.91. (a) A proposed schematic of the m vs layer in these multilayers [71]. This indicates L as the width of FeZr layers (or A in this study) and W the width of the magnetisation profile. Thicknesses (b) $L = 3$, (c) $L = 6$ and (d) $L = 10$ with $J_{AB} = 0.75$. The three temperatures are $T = 0.2$, $T = 0.7$, and $T = 1.2$ from green to blue. The points are joined using a second order interpolation.

the case that $W > L$ since both the central A layers are interacting directly with one B layer. For $L = 10$, the relationship of W and L is between $W > L$ and $W \simeq L$ as some A monolayers in the central A layers are not interacting directly with a B layer. Therefore, the overlap of magnetic induction by the B layers become smaller. At some critical L , there is no effective interaction between the B layers as the induced

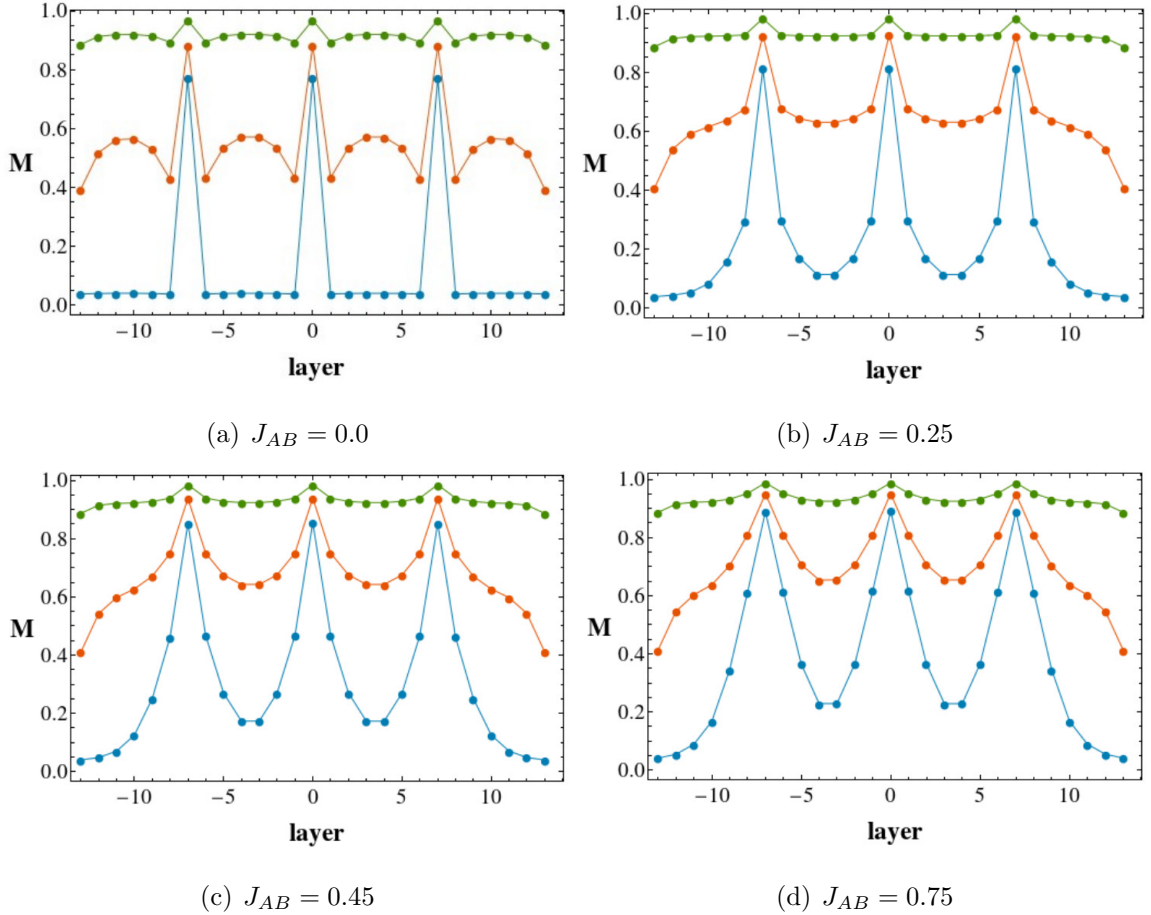


Figure 5.26: Magnetisation vs layer of the A/B multilayer for different J_{AB} , with the same temperature details as figure 5.25 ($T = 0.2$, $T = 0.7$, and $T = 1.2$ from green to blue). (a) $J_{AB} = 0.0$, (b) $J_{AB} = 0.25$, (c) $J_{AB} = 0.45$ and (d) $J_{AB} = 0.75$ for $t(A) = 6$. Points are joined using a first order interpolation.

magnetisation from both B layers no longer overlap since the A thickness is too large.

Changing the interspecies coupling strength in these multilayers is equivalent to varying W . The reason for an increased magnetic induction in the A layers with an increased J_{AB} coupling strength has been discussed quite thoroughly in the trilayer in previous sections. The difference in this multilayer is that there are now more repeat units and so the overlap of the magnetic induction from say $B1$ with $B0$, further enhances the magnetic order in the middle $A1$ monolayers. Also included in this study is $J_{AB} = 0.0$, which shows that no interaction between the A and B layers causes the interface to behave as it would at the surface, which is to decrease the magnetisation. The magnetisation in all the A and B monolayers, in this case, are lower than those in the multilayers where $J_{AB} \neq 0.0$.

Plots of the average magnetisation vs temperature for the $A1$ layer are shown in figures 5.27 (a) and (b) for varying thickness of A and interspecies coupling strength, respectively. Particularly in figure 5.27 (a), one can see that it is very difficult to extract $T_c(A)$, especially when L is small. This is due to the overlap of the magnetic induction from the B layers throughout the system (see figure 5.25), where the magnetisation of the sandwiched A layers (e.g. $A1$) become more like that of the B layers and hence why the A character cannot be distinguished from the B character in these plots.

From figure 5.27 (a), it can be seen that $T_c(A)$ is enhanced when L is small, which is reported by Ahlberg *et. al.* [71]. When the thickness is so small that L is of the order of the range of interactions, as is the case for $L = 3$, the transition temperature of the B layer increases slightly $T_c(B) = 2.60$ (where $L = 6$ and $L = 10$ have $T_c(B) = 2.51$ and $T_c(B) = 2.47$, respectively). As expected, if L is fixed and the coupling is varied, $T_c(B)$ increases with coupling strength (see higher temperature feature in figure 5.27 (b)). Bloch's Law is used to identify the exponent of the $B0$ layer with increasing A thickness: $b = 1.28$ for $L = 3$, $b = 1.32$ for $L = 6$ and $b = 1.36$ for $L = 10$, when fitting T/T_c to the equation $y = ax^b + c$. This is not expected since a system with $L = 3$ would be expected to be more "3d-like" giving $b \rightarrow 1.5$ rather than $L = 10$ due to the overlap of induction throughout the entire system and based on the result from the trilayer,

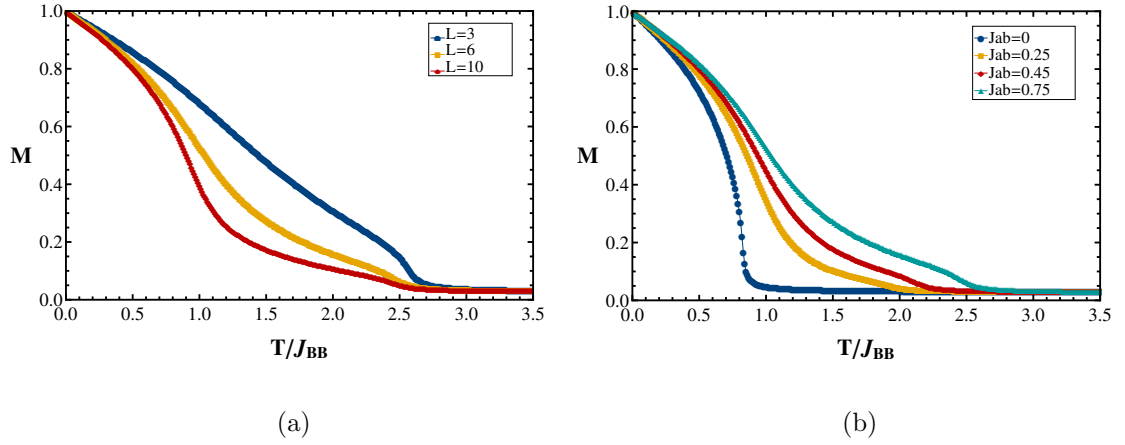


Figure 5.27: Average magnetisation per spin vs T/J_{BB} for the A1 layer of (a) the multilayers HA:XB:HA:XB:HA:XB:HA (3:1:3:1:3:1:3), (6:1:6:1:6:1:6) and (10:1:10:1:10:1:10) with $J_{AB} = 0.75$ and (b) couplings $J_{AB} = 0, 0.25, 0.45$ and 0.75 for the multilayer with $L = 6$.

where the effective thickness of the B layer increases.

From figure 5.27 (b), it is clear that not only is $T_c(A)$ increasing with J_{AB} , but also the decoupling region with the B layers. The critical temperatures for $B0$ with increasing coupling strength are, $T_c(B) = 1.88$, $T_c(B) = 1.98$, $T_c(B) = 2.15$ and $T_c(B) = 2.53$ whilst using Bloch's law, $b = 1.09$, $b = 1.28$, $b = 1.31$ and $b = 1.32$ in the same order. From the trilayer results, this trend is expected, whereby $T_c(A)$ and $T_c(B)$ increase whilst the B layer becomes more “3d-like”. Using the average magnetisation of the A layers is not recommended to study T_c or the exponent since it is not representative of the layers which are most influenced by the B layers. However, fitting $y = ax^b + c$ to T/T_c of the A1 layer gives $b = 1.18$, $b = 1.17$, $b = 1.17$ and $b = 1.17$ for $J_{AB} = 0.0$, $J_{AB} = 0.25$, $J_{AB} = 0.45$ and $J_{AB} = 0.75$, respectively. This would imply that the A monolayers are more 2d than 3d and that the dimensionality of the A spins do not change with interspecies coupling strength, however, this may be different for the monolayers closest to the B layers.

Both figures 5.25 and 5.26 show that the magnetic profile of the multilayer system is also temperature dependent irrespective of whether the interspecies coupling or thickness is varied. At high temperatures, W is small due to strong thermal fluctuations in A spins. If T_c is below some threshold temperature, T' , then perpendicular excitations (z -magnons) will not be accessible in the system and hence $2dXY$ behaviour will be observed, whilst if T_c is above a threshold T'' , then there is enough thermal energy to excite the spin vector out of the plane and enable three-dimensional behaviour [71]. Between these two thresholds, T' and T'' , there is a crossover region of spin dimensionality. Ahlberg *et. al.* [71] found that $T_c < T^{**}$ in their magnetic multilayer because the critical exponents are not completely three-dimensional but neither are they two-dimensional. From the results in this study, the spin dimensionality remains $2d$ in the A layers, but changes from $2d$ to (almost) $3d$ in the B layers when the coupling changes. It could be that $T_c(A) < T^*$ whilst $T' < T_c(B) < T^{**}$. This may imply that the initial design for $J_{AA} = 0.25J_{BB}$ is not suitable for the findings of the work by Ahlberg *et. al.* and hence could require an increase in J_{AA} .

5.4.5 Conclusion

Magnetisation versus monolayer profiles were generated and analysed as a function of temperature for an A/B magnetic multilayer, showing similar profiles to the experiment. A dimensionality crossover, as reported by Ahlberg *et. al.* [71], was found in the trilayer, ABA and was still evident when more repeat units were added. This dimensionality crossover was only found in the strongly coupled B layer due to the difficulty in extracting $T_c(A)$ and hence β , in the weakly coupled A layers. Changing the interspecies coupling strength in the multilayers was found to be equivalent to varying W . Tuning L in the simulations showed a similar effect to that found in the experiment, where $T_c(A)$ is enhanced, however, the dimensionality crossover for the B layers were not as expected and could be due to the intraspecies coupling ratios and T_c with respect to the dimensionality crossover boundaries, T' and T'' . Changing the thickness is related to changing the exchange coupling strength in these multilayers [297] and so it could also be that the theoretical equivalence of experimentally varying the thickness

of one species in these multilayers is by tuning the interspecies coupling strength.

In the introduction of this chapter, it was shown that a strongly coupled ferromagnetic species, B (cobalt in the experiment), with a thickness $L \leq 1$ monolayers, shows no ferromagnetic behaviour. However the results presented here demonstrate that if B is between two layers of a weaker coupled ferromagnetic species, A , so that $J_{BB} = 4J_{AA}$, then this monolayer has the potential to show ferromagnetic behaviour. In these simulations this is shown by an increase in T_c for the monolayer of B in the trilayer compared with the single layer of B , due to an increased effective thickness. In the ABA trilayer, the result is seen when the interspecies exchange coupling strength, J_{AB} is increased and a dimensionality crossover in the B layers is observed from the modelled $2d$ behaviour to an effective $3d$ behaviour. These results are only possible through a double proximity effect of B to A and A to B , where there is a two-way enhancement of the critical temperature in both species.

Chapter 6

Towards modelling the exchange spring effect

In the previous chapter, an A/B magnetic multilayer system was shown to demonstrate a double proximity effect. This is where both layers were affected by the proximity of the other and an enhancement of T_c for both species was identified compared to the stand-alone components. In this chapter, the proximity effect is considered to explain the exchange spring effect observed in an $B/A/C$ multilayer. It is found that the range of interaction is insufficient to conclude the role of the proximity effect with regard to the exchange spring effect, however, does help to visualise and explain the enhancement of T_c in the middle layer as reported in the literature. Additionally, modelling parameters in these multilayer systems are thoroughly discussed.

6.1 An indirect interaction in the trilayer

Experimental work conducted by Magnus [298] has been based on the exchange spring effect in the magnetic trilayer, $\text{Co}_{85}(\text{AlZr})_{15}/\text{Co}_{60}(\text{AlZr})_{40}/\text{Sm}_8\text{Co}_{92}$. The exchange spring effect occurs in multilayers of alternating hard and soft magnetic materials coupled by exchange interactions [299]. The effect refers to the ability of the net magnetic

moments of the monolayers[†] in the soft material to rotate reversibly about the interface of the neighbouring hard magnetic material(s) in the presence of an applied magnetic field perpendicular to the anisotropy of the system [300]. The anisotropy of the system results from the proximity of the hard magnet (see figure 6.2).

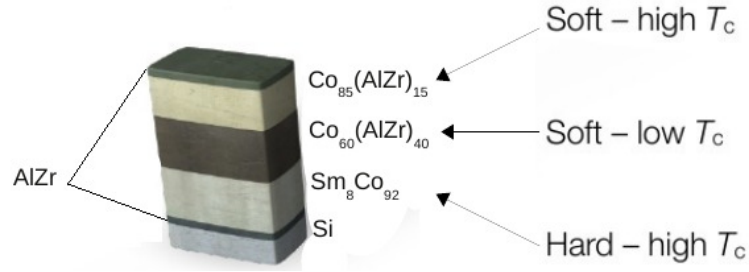


Figure 6.1: A representation of the SmCo/Co(AlZr) multilayer used in the experimental system by Magnus. The hard layer is SmCo whilst the soft layers are the CoAlZr layers. The differing Co concentrations, $\text{Co}_{85}(\text{AlZr})_{15}$ / $\text{Co}_{60}(\text{AlZr})_{40}$ / $\text{Sm}_8\text{Co}_{92}$ from top to bottom in the image, determine how magnetic the material is and the critical temperature of each layer, where $T_c(\text{top layer}) > T_c(\text{central layer}) \ll T_c(\text{bottom layer})$. Image taken from reference [301].

The experimental work has shown that a higher coercivity is observed in the strongly coupled $\text{Co}_{85}(\text{AlZr})_{15}$ layer when the thickness of the weaker coupled $\text{Co}_{60}(\text{AlZr})_{40}$ layer decreases. It is presumed that there is an indirect interaction between the top and bottom layer of the trilayer since the coercivity is related with the anisotropy of the system, however limitations on the experimental analysis only enable one to probe the top layer [302]. Therefore, the aim of the numerical simulations in this project is to construct and test a microscopic model that may account for the experimental observations. Not only is this to shed light on the interaction of the top and bottom layer but also to develop the theoretical understanding on how best to model such trilayers.

[†]Please find the notation given to a *layer*, a *monolayer*, the *interspecies coupling* etc. in section 5.1.

6.2 The exchange spring effect

Magnetic multilayers demonstrating the exchange spring effect are considered to be a way of retaining thermal and field stability in storage media [303–305]. This is because the exchanged coupled alternating hard and soft magnetic materials have the advantage of the high thermal stability of the hard material with the moderate switching field of the soft material [302]. The composition of these alternating hard/soft magnetic multilayers where the exchange spring effect is apparent are usually such that the hard material consists of a rare earth metal mixed with a transition metal (e.g. TbCo [306] or SmCo [307]) and have large coercivities; whilst the soft material generally consists of transition metals which have a large magnetic moment and hence a large saturation magnetisation (e.g. Fe or Co [308, 309]), however, these materials can vary.

The simplest system demonstrating the exchange spring effect is a bilayer of hard/soft magnetic materials, such as FePt/Fe [310]. At a critical thickness of 3 nm of soft iron, the coercivity of the hard FePt decreases through the exchange spring effect [310]. This is because the soft layer effectively tunes the switching field in the hard layer by reversing its own direction of magnetisation first whilst being strongly coupled to the hard layer. In this case one sees continuous in-plane rotations of the soft monolayers (see figure 6.2). Below the critical thickness (of the order of the domain wall width of the hard material [302]), the whole system has a single switching field [311], whilst thicknesses far greater than this critical thickness, there are more soft monolayers with a reversed magnetisation from that given by the hard magnet as the thickness is greater than the range of direct exchange coupling [310].

Domain walls are defined by the boundary between regions of spins aligned in different directions. This would be, for example, the boundary between spins aligned in the $+z$ direction and spins aligned in the $-y$ direction. An analytical indication of the exchange spring effect is where the hysteresis loop, produced in a plot of the magnetisation vs applied field of the multilayer system, shows a characteristic rounded shape

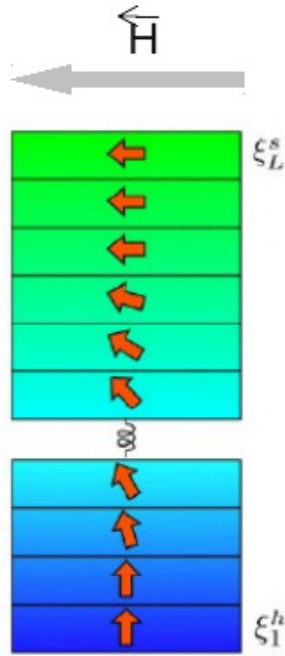


Figure 6.2: A schematic of the exchange spring effect in a magnetic trilayer. The hard/soft layers are indicated below/above the spring and the spring itself represents a non-magnetic layer. There is a twisting of the magnetic moments in the soft monolayers as the proximity to the hard layer decreases and hence increasing the length of the spring reduces the proximity between the hard and soft layers causing them to decouple. The anisotropy of this system is determined by the hard layer and is perpendicular to the plane of the layers and the external field applied. The angle deviation from the easy z axis in monolayer 1 of the hard material is given by ξ_1^h and hence no angle deviation is shown in this monolayer, whilst the angle deviation in monolayer L of the soft material is given by ξ_L^s , showing the largest deviation from the z axis. This image is taken from reference [35].

(see figure 6.3) [312]. If H_n is the nucleation field by which domain walls begin to form and H_i is the irreversibility field (coercive field) of the hard magnet, then for fields in the range $H_n < H < H_i$, the net magnetic moment of the soft magnetic monolayers can rotate reversibly about the hard/soft interface and is the point at which this rounding of the hysteresis loop is observed. Therefore, H_n and H_i effectively correspond to the coercivities of the soft and hard layer, respectively. Sweeping the applied field positively

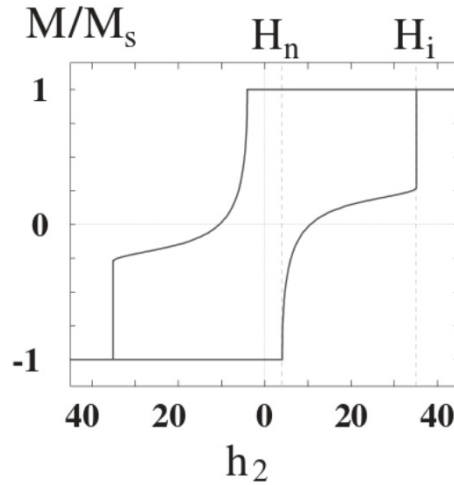


Figure 6.3: Magnetisation M/M_s vs applied field H for a magnetic bilayer demonstrating an exchange spring effect, where $h_2 \equiv HM_{s2}/2K_2$ and M_{s2} and K_2 are the magnetisation and anisotropy energy of the soft layer, respectively. H_n is the nucleation field by which domain walls begin to form and H_i is the irreversibility field (coercive field) of the hard magnet. The exchange spring effect can be identified by the characteristic rounded shape of the hysteresis loop. Image taken from [312].

or negatively enables the domain walls to wind or unwind reversibly.

Investigations of the exchange spring effect can be extended to trilayer systems. This has included investigations of a symmetric hard/soft/hard arrangement [313–316] and those where the coupling between hard and soft magnetic layers is mediated by a non-magnetic interlayer [35, 299, 317] or an antiferromagnetic interlayer [318]. This interlayer acts as a on/off switch for the exchange spring effect depending on its thickness or the temperature in relation to the T_c of the interlayer and hence could be used in heat-assisted magnetic recording (HAMR) [318]. With a non-magnetic interlayer, long range indirect exchange coupling is arguably mediated between the hard and soft layers by RKKY [299] or DM [35] interactions and is similar to the FePt/Fe bilayer where the larger the thickness, in this case of the interlayer, the greater the angle deviation from the anisotropy of the system giving rise to the exchange spring effect. In the case of an antiferromagnetic interlayer, there is no exchange coupling between the hard/soft layer

until temperatures reach above the transition of the interlayer such that it becomes ferromagnetic [318]. At this point exchange coupling between the hard and soft layers mediated by the ferromagnetic interlayer can occur and the exchange spring effect is observed, showing that this effect is controlled by the temperature.

In this chapter we refer to a trilayer system where the interlayer is a soft and weakly coupled ferromagnetic material, whilst the other two layers consist of a soft, strongly coupled ferromagnet and a hard, strongly coupled ferromagnet.

6.3 Experimental background to simulations

In the ferromagnetic bilayer system consisting of $\text{Co}_{85}(\text{AlZr})_{15}$ and $\text{Sm}_8\text{Co}_{92}$, the coercive field and saturation field of the CoAlZr layer are enhanced when the thickness of CoAlZr is reduced [298]. This bilayer system can be complicated further by inserting a softer, lower T_c material, $\text{Co}_{60}(\text{AlZr})_{40}$, between the hard rare earth magnet and the soft higher T_c magnet. Again, experimental analysis of these amorphous thin film multilayers are limited to only probing the top layer (soft, higher T_c material), which provides an observation of how the coercivity changes in the system. The magneto-optical Kerr effect (MOKE) can probe thin layers up to 20 nm [319], however, the size of the multilayers used in the experiment were 15 nm/ L_2 nm/ 20 nm (L_2 is the thickness of the central layer) for the $\text{Co}_{85}(\text{AlZr})_{15}$ / $\text{Co}_{60}(\text{AlZr})_{40}$ / $\text{Sm}_8\text{Co}_{92}$ trilayer and is therefore beyond the thickness resolution of the analytical apparatus.

The materials used in the experimental work are amorphous. This is to be able to tune the magnetic anisotropy (coercivity) and saturation field of the SmCo layer by the amount of Sm content and to also ensure that the lattice mismatch is not as important as for a crystalline material [301]. The critical temperature of the CoAlZr layer is controlled by the zirconium content, where the more Zr, the lower $T_c(\text{CoAlZr})$, which is due to the lower proportion of magnetic material (Co).

Upon changing the thickness of the central layer (soft, lower T_c material), a change in the coercivity of the top layer is observed as shown in figure 6.4. This is proposed to be a consequence of indirect coupling of the top layer with the hard bottom layer, through magnetic induction in the central soft layer [298]. Therefore, the coupling between the top and bottom layer is assumed to become stronger as the thickness of the central layer decreases. This is not as simple as longer range direct interactions becoming more relevant as the distance between top and bottom layers decreases since the experimental work shows that the exchange spring effect is only evident because of the induction in the $\text{Co}_{60}(\text{AlZr})_{40}$ layer [298]. This is proven from figure 6.4, which shows the coercivity of

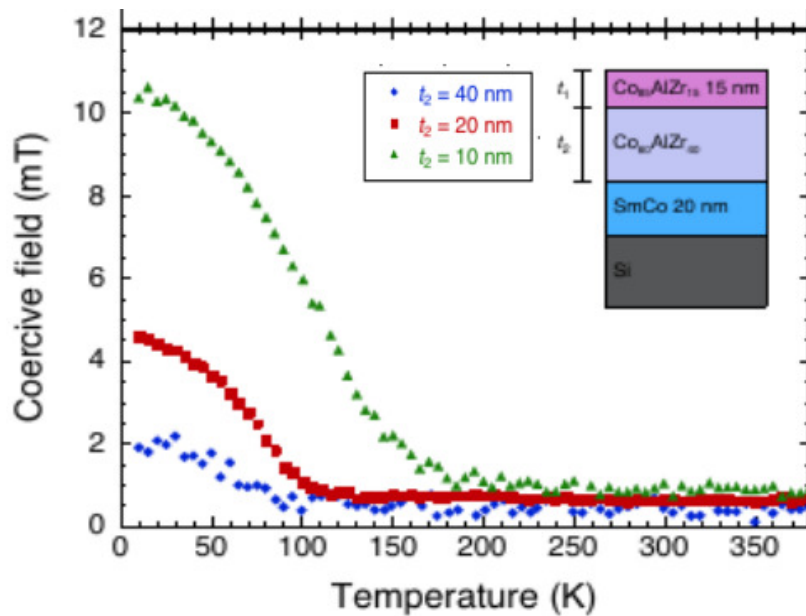


Figure 6.4: Coercive field of the top $\text{Co}_{85}(\text{AlZr})_{15}$ layer vs temperature for different thicknesses of central $\text{Co}_{60}(\text{AlZr})_{40}$ layer in the SmCo/Co(AlZr) multilayers. This is for temperatures up to $T_c(\text{Co}_{60}(\text{AlZr})_{40}) < T < T_c(\text{Co}_{85}(\text{AlZr})_{15})$. The image is from unpublished results by Magnus *et. al.* [298].

the top $\text{Co}_{85}(\text{AlZr})_{15}$ layer with respect to temperature. A strong relationship between the thickness of the central layer and the coercivity of the top layer can be seen when $T_c(\text{Co}_{85}(\text{AlZr})_{15}) > T > T_c(\text{Co}_{60}(\text{AlZr})_{40})$. At the largest thickness of the central layer ($L_2 = 40$ nm), the indirect interaction between the top and bottom layers is considered to be minimal (acting as a bulk system), therefore at the temperature where

the coercivity drops for $L_2 = 40$ nm in figure 6.4, this corresponds to the critical temperature of $\text{Co}_{60}(\text{AlZr})_{40}$. With the smallest thickness, $L_2 = 10$ nm, the coercivity in the top layer remains high where one would note the onset of $T_c(\text{Co}_{60}(\text{AlZr})_{40})$. The induction in $\text{Co}_{60}(\text{AlZr})_{40}$ is considered to play a role since at this point this layer should have become disordered and hence no coercivity increase observed in the $\text{Co}_{85}(\text{AlZr})_{15}$ layer. If there were direct coupling between the top and bottom layers then the coercivity should not fall to zero at temperatures significantly lower than the critical temperatures of the top and bottom layers (reported to be > 380 K [298]). It is therefore proposed that there is an increase in the ordering temperature of the central layer by magnetic induction of the other layers with decreasing thickness and it is at this increased T_c of the central layer that the coercivity in the $\text{Co}_{85}(\text{AlZr})_{15}$ layer declines to zero.

6.4 Simulation details

In the simulations, the multilayer is represented generally as BAC , where B corresponds to the experimental $\text{Co}_{85}(\text{AlZr})_{15}$ layer, A to the $\text{Co}_{60}(\text{AlZr})_{40}$ layer and C to the $\text{Sm}_8\text{Co}_{92}$ layer. A schematic of BAC is shown in figure 6.5 along with the intra- and interspecies couplings.

Previous theoretical studies on the exchange spring effect [35, 299] model the system one-dimensionally (perpendicular to the plane of the system), since within the plane it is assumed that the magnetic properties are invariant [320]. A one-dimensional treatment of the multilayer system could have potentially been used in this study, since the boundaries are periodic in the plane and finite perpendicular to the plane of the layers. However, in this study a more sophisticated approach is required, particularly as I investigate magnetic induction. Parameters which are varied in this study that rely upon the less simplified model are: the range of interaction between spins, which although are further ranged they are also limited; and the rate of decay of interactions, which controls how much weighting an interaction between another spin contributes to

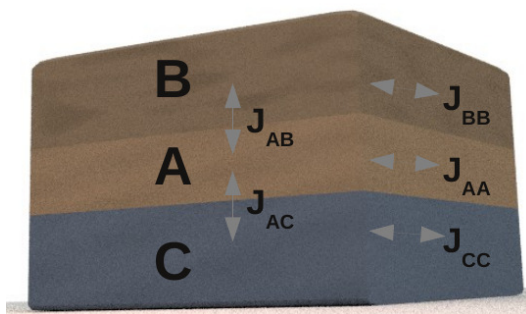


Figure 6.5: Schematic of the *BAC* system such that a layer of *B* has $L_B = 8$ monolayers, *A* has $6 \leq L_A \leq 50$ monolayers and *C* has $L_C = 10$ monolayers. The *B* spins are coupled by $J_{BB} = 1$, *A* spins are coupled by J_{AA} and *C* spins are coupled by $J_{CC} = 1$. The interspecies couplings are given by J_{AB} and J_{AC} and the range of interaction is up to 8^{th} NN.

the energy of the system. Therefore, I model a three-dimensional system.

To determine a model which best describes the experimental system, two approaches are considered: 1) to use the details from the experiment and prior knowledge (see chapter 5) to best imitate the experimental system theoretically and compare the results produced; and 2) to use the experimental results to identify which values of the model parameters of the theoretical system yield the best agreement with the experiment. In this project I start by using method 1), which follows with results of the bilayers, the trilayer and varying L_A . I then revisit the trilayer systems using the second methodical approach. Accordingly, the simulation details and results sections will be divided into two parts.

6.4.1 Method 1- system developed using experimental details

The coupling strengths of the *BAC* multilayer were chosen as $J_{BB} = 1$, $J_{AB} = 0.60$, $J_{AA} = 0.55$, $J_{AC} = 0.60$ and $J_{CC} = 1$. Cobalt is considered to be the source of magnetism in the CoZr layers, whilst both Sm and Co contribute to the magnetic nature

of the SmCo layer. The coupling strengths were chosen according to the cobalt content given by the stoichiometry of the chemical formulas, since there was no found literature relating the magnetic ion coverage with the average coupling strength of an amorphous layer. Though a different property, studies have determined that the coverage of the magnetic material (within the amount reported here) is linearly related to the average magnetic moment of the magnetic ion (see figure 6.6) [321–323]. Using the exact frac-

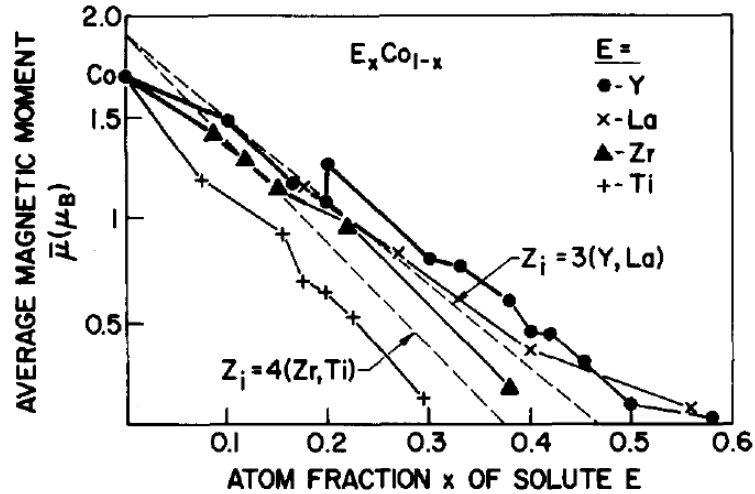


Figure 6.6: Magnetic moment u (denoted as μ in the figure by convention) vs atomic fraction x of alloying solute E for $\text{Co}_{1-x}\text{E}_x$ materials. The key for the different E used is given in the legend. Of interest is when $E = \text{Zr}$, where there is a linear relationship between the magnetic moment and the Zr content. Image taken from reference [321].

tions of Co when normalised to the Co content of the hard layer, then $J_{BB} = 0.92$ and $J_{AA} = 0.65$. It is through the understanding of the experimental details that the B and C layers have ordering temperatures well above the measurement temperature, which is considerably greater than the ordering temperature of A , that J_{BB} is set to one just like J_{CC} . The reasoning for $J_{AA} = 0.55$ for the A layer, is that though the Co content is 60% and the relative coupling to the C layer should be $J_{AA} = 0.65$, figure 6.6 shows the decline in magnetic moment with Zr content is quite steep and the Co content is therefore not likely to yield an equally strong exchange coupling. For the interspecies coupling, the experimental work indicates that the B and C layers influence A and hence we can consider that the J_{AB} coupling must be larger than J_{AA} . This was chosen

as little greater than J_{AA} .

The top layer (denoted as B here) is magnetically soft, however is said to have a high critical temperature. Therefore I have modelled this layer with XY spins (not as magnetically hard as Ising spins) and an intraspecies coupling of 1. The XY spins ensure the spins can rotate within the plane of the layers. The central layer (denoted as A) is also a magnetically soft layer but with a far lower critical temperature than the B spins, I modelled these as Heisenberg spins. Introducing another degree of freedom lowers the ordering temperature of A further from that given by a coupling strength $J_{AA} = 0.55$. The bottom layer (denoted as C) is a hard layer with a strong uniaxial anisotropy, hence this layer is modelled as Ising spins with an intraspecies coupling of 1.

Figure 6.7 is a plot of the susceptibility vs temperature for the components of the BAC multilayer as described so far, with $L_A = 10$. The susceptibility peaks correspond to the critical temperature of the respective layers. As implied by the experimental details [298], $T_c(A)$ must be much lower than $T_c(B)$, to indicate that any significant coercivity of B for $T > T_c(A)$ is due to indirect coupling between B and C , which would not be possible if $T_c(B) \simeq T_c(A)$. In this case, both A and B spins would disorder at the same temperature and no coercivity would be expected at temperatures beyond this. The figure shows that the set of parameters chosen are suitable as there is no overlap of $T_c(A)$ with $T_c(B)$ and a significantly small residual magnetisation of A as $T \rightarrow T_c(B)$.

Assigning the coupling strengths with the respective magnitudes and choosing the dimensionality of the spins in each layer according to how magnetically hard or soft the material is ensures that the experimental system is correctly modelled in the simulations.

The lateral size of the system is fixed as 32×32 spins since, as explained in the previous project, this system size captures the physics of a finite $2d$ XY system quite

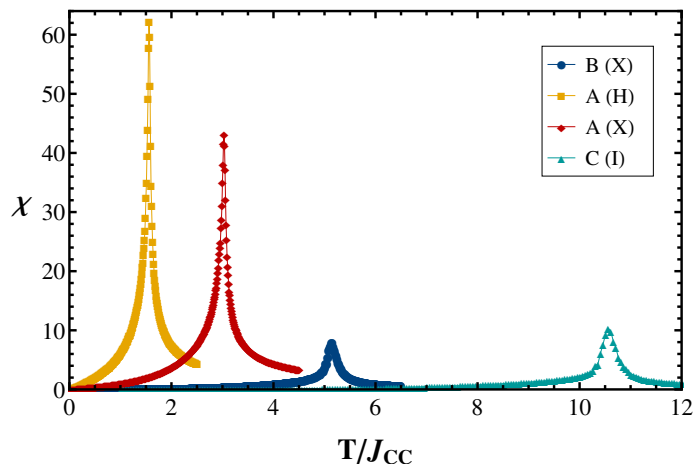


Figure 6.7: χ vs T/J_{CC} for the isolated components of the trilayer. The respective peaks are for 8 monolayers of B , 10 monolayers of A and 10 monolayers of C . The spin dimensionalities for each component are indicated in the legend, where I represents Ising spins, X represents XY spins and H represents Heisenberg spins. Comparison can be made with the peaks of the A layer being treated as XY or Heisenberg spins. Each peak corresponds to $T_c(x)$, where $x = A, B$ or C .

accurately, balanced with computational effort. Though I do not specifically study a $2d$ XY system in this project, important contributions which may result from an insufficient system size should not be overlooked. The number of monolayers were chosen according to the information given in figure 6.4, which shows that $L_C > L_B$, and the thicknesses explored for the A layer were $L_A > L_C > L_B$, $L_A = L_C > L_B$ and $L_C > L_B > L_A$. To compromise on computational effort, layers C and B are chosen as 10 and 8 monolayers, respectively and the number of A monolayers is chosen as $L_A = 6, 7, 10, 20, 30$ and 40 .

All simulations were run with the Hamiltonian used in equation 5.1 in chapter 5, and with 8^{th} NN. As before, $d = 3$ for the $3d$ system and $\sigma = 1$ for a fast decay of attractive interactions. Monte Carlo simulations were run with $t_{eq} = 10^4$ MCS/s and $t_{obs} = 10^5$ MCS/s (remembering that 1 MCS/s corresponds to N attempted single spin flips). The results for the equilibration of the energy can be found in Appendix B.

6.4.2 Method 2- system developed using experimental results

The experimental results indicate that the thickness of the A layer is able to influence the coercivity of the B layer. Also, it has been found that the relationship between the thickness of the central layer (known in the literature as the interlayer) and the coupling strength between the magnetically soft and hard layers is dependent on how strong the anisotropy is within the magnetically soft central layer itself [324]. Therefore I vary both the intra- and interspecies coupling strengths between A and B (and consequently between A and C since $J_{AB} = J_{AC}$), whilst increasing the anisotropy in the A layer with a change in spin dimensionality. As mentioned before, the easy axis and hence anisotropy of this system is defined by the hard material. Method 2 is an iterative process in which to find the parameters which best reproduce the experimental results. One parameter which is fixed in this process is the thickness of the system with $L_B = 8$, $L_A = 10$ and $L_C = 10$. This system size is reasonable for the maximum range of interactions tested as well as limiting the computational effort.

Figure 6.8 shows how varying the intra- and interspecies coupling and the spin dimensionality in the BAC trilayer affects the susceptibility for the A and B layers. The peaks corresponding to the A layer are located at the lower temperatures whilst the peak for the B layer is positioned at higher temperatures. The C peak at even higher temperatures is not shown, however this is of no physical interest.

From this plot, one can see that increasing J_{AA} , shifts the susceptibility peak to higher temperatures signifying an increase in the critical temperature of the A layer. Increasing the interspecies coupling between A and B (and hence the coupling between A and C), decreases the height of the A peaks. A decrease and broadening of the susceptibility peak indicates an inhomogeneous field [325] acting on A , which is most likely due to contributions from B and C when being more strongly coupled to A . Using XY spins rather than Heisenberg spins also shifts the susceptibility peak of the A layer to

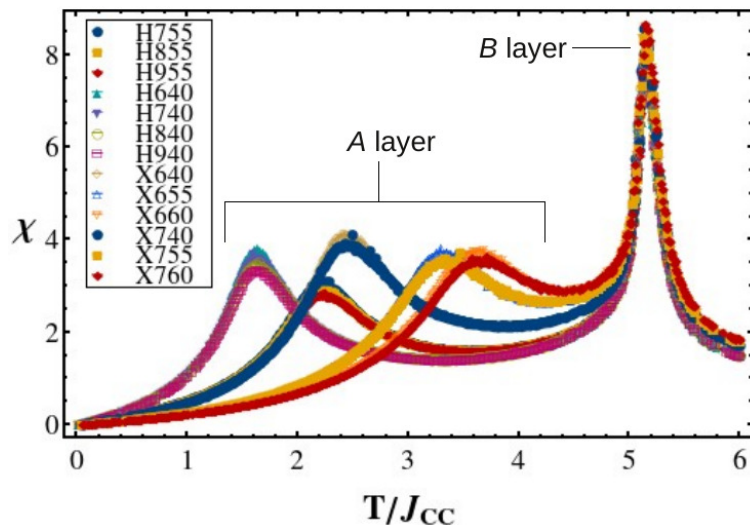


Figure 6.8: χ vs T/J_{CC} for various intra- and interspecies coupling strengths and different spin dimensionalities for the *BAC* trilayer. This plot shows the contributions from each component in the trilayer system, where the simulations do not go to high enough temperatures to reveal the *C* peak. A range of 8^{th} NN is used and fixed couplings were $J_{BB} = 1$ and $J_{CC} = 1$. As indicated in the legend the spin dimensionality is either given as XY denoted by “X”, whilst “H” denotes Heisenberg spins. The next number represents the J_{AB} and J_{AC} couplings which are set as $J_{AB} = J_{AC}$, e.g. a 7 indicates $J_{AB} = J_{AC} = 0.70$ or an 8 is $J_{AB} = J_{AC} = 0.80$. The next two numbers represent the J_{AA} coupling such that e.g. 55 is $J_{AA} = 0.55$ or 40 is $J_{AA} = 0.40$.

higher temperatures. In contrast, the critical temperature of the *B* layer is completely independent of these changes. Therefore with an increase in J_{AA} and a decrease in spin dimensionality, $T_c(A)$ approaches $T_c(B)$ as one would expect.

This result has helped to show that the interspecies coupling is not the major contributor to the amount of induction experienced by the *A* layer. It consequently has shown that the difference between J_{AB} and J_{AA} ($J_{AB} - J_{AA}$) is also not a large contributor to the amount of induction since when the intraspecies coupling is fixed and J_{AB} is varied, $T_c(A)$ stays approximately the same and so it is the magnitude of J_{AA} which is of the most importance. Therefore, it is worth identifying how much more or

less induced the A layer is depending on the J_{AA} magnitude.

Figure 6.9 shows the magnetisation per spin of the first 5 monolayers of the 10 monolayers of A in the BAC multilayer compared with the bulk A magnetisation as a function of temperature, which can otherwise be thought of as the magnetic induction (ΔM vs T/J_{CC}). The bulk magnetisation of A is taken to correspond to the middle monolayer of a 40 monolayered A system to avoid surface effects. The J_{AA} couplings were varied in this investigation and are indicated in the legend of figure 6.9. These plots are produced by spline interpolation on Mathematica, therefore where some of the data points are missing there is some odd behaviour which should be ignored. This is at high temperatures and particularly for the $J_{AA} = 0.55$ results where there are no bulk A data points beyond $T/J_{CC} = 4.50$.

One can easily see that when the intraspecies coupling for A is lowered, then the amount of induction shown in the monolayers is greater. This is particularly evident in the monolayers closest to the interface (figure 6.9 (a)) as opposed to the middle A monolayers (figure 6.9 (e)). The difference in the amount of induction between the three intraspecies couplings becomes smaller when the monolayer is further away from the inducing B source, (e.g. monolayer 5).

The results from chapter 5, showed that increasing J_{AB} so that $J_{AB} \rightarrow 1$ influences the A monolayers to effectively behave like the B layer (similarly, layers A and B were such that $T_c(A) < T_c(B)$ with 8th NN). However this only occurs for the A monolayer immediately neighbouring the B layer. The results in figure 6.8 are the average magnetisation of the trilayers and therefore do not show monolayer specific differences. Therefore with this prior knowledge, it seems that increasing the interspecies coupling alone will not alter the influence that B and C have on the middle monolayers of A , though it will still impact on the interfacial A layers.

Another parameter which could be manipulated to effectively enhance the range of

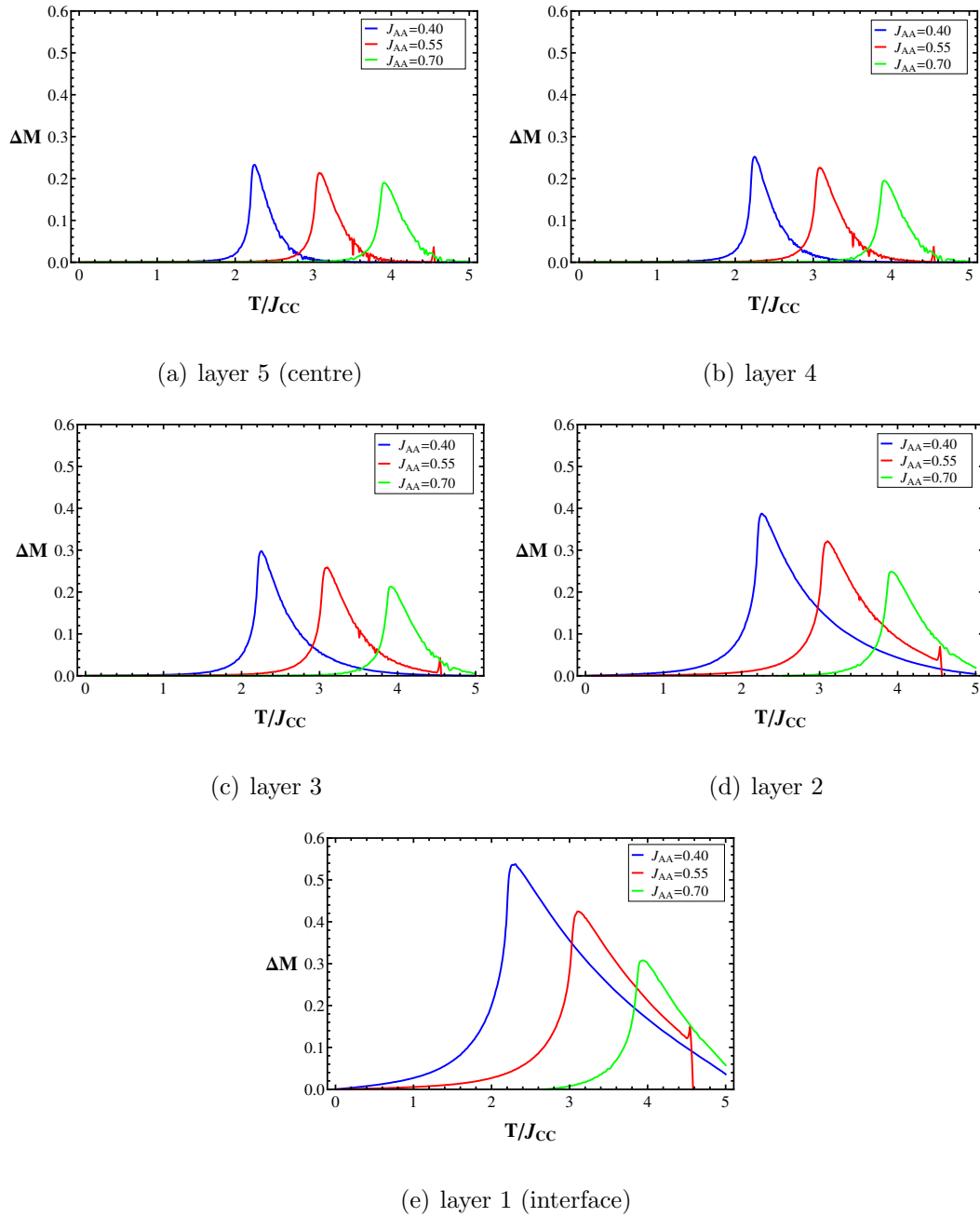


Figure 6.9: Induced magnetisation, ΔM vs T/J_{CC} corresponding to 5 monolayers of the A layer in the BAC trilayer for $J_{AA} = 0.40, 0.55$ and 0.70 (as indicated in the legend). Each monolayer of A in the BAC multilayer from (a) monolayer 5 at the centre of the A slab to (e) monolayer 1 at the A/B interface are modelled with XY spins, couplings of $J_{AB} = J_{AC} = 0.60$ and $J_{AA} = 0.40, 0.55$ and 0.70 (as indicated in the legend). All were simulated with $\sigma = 1$ and 8^{th} NN.

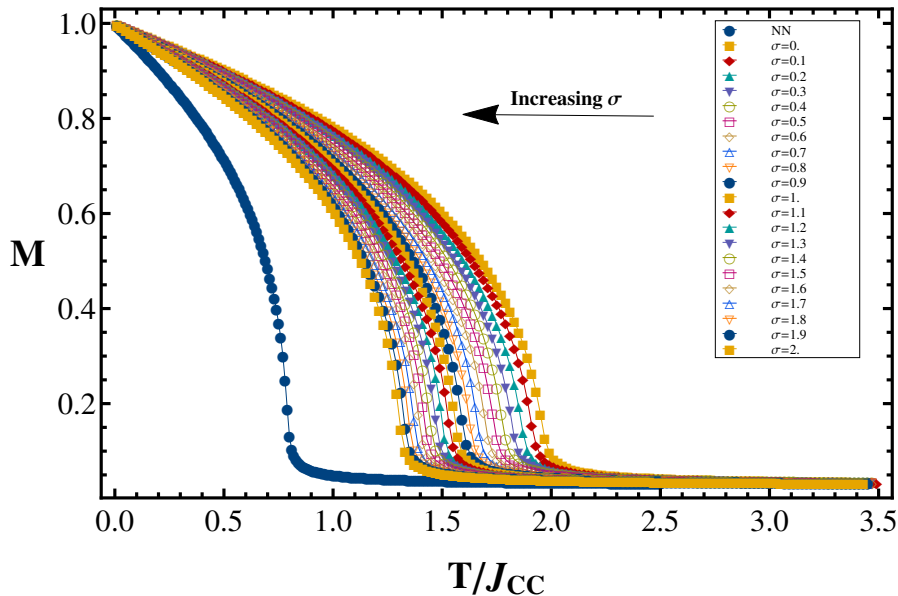


Figure 6.10: Average magnetisation of an A slab with a thickness 40 monolayers vs T/J_{CC} , where $J_{CC} = 1$ and $J_{AA} = 0.55$. This is plotted for varying σ , a parameter in the term $r^{-(d+\sigma)}$ as part of the Hamiltonian shown in equation 5.1. The simulation was conducted with 4^{th} NN and for $\sigma = 0$ to 2 in steps of 0.1, where σ increases from right to left in the plot, as indicated by the arrow in the diagram. The NN result is included for comparison.

induction in the trilayer system is σ . This parameter is part of a term used in the Hamiltonian (shown below for convenience) to control the rate of decay of interactions in the system.

$$\mathcal{H} = -Jr^{-(d+\sigma)} \sum_{\langle i,j \rangle} S_i \cdot S_j. \quad (6.1)$$

Figure 6.10 shows how varying σ from 2 to 0 in steps of 0.1 affects the average magnetisation of 40 monolayers of Heisenberg A spins (slab of A) using 4^{th} NN and $J_{AA} = 0.55$.

One can see that the critical temperature increases with decreasing σ and approaches a NN behaviour (leftmost plot in figure 6.10), which is consistent with the literature

[283]. This is because the rate of decay of interaction is faster with a smaller σ and the spins further away from a spin contribute less to the overall energy of the system than with a slower decay. Figures 6.11 (a)-(c) show how varying σ alters the A layer in the context of the trilayer.

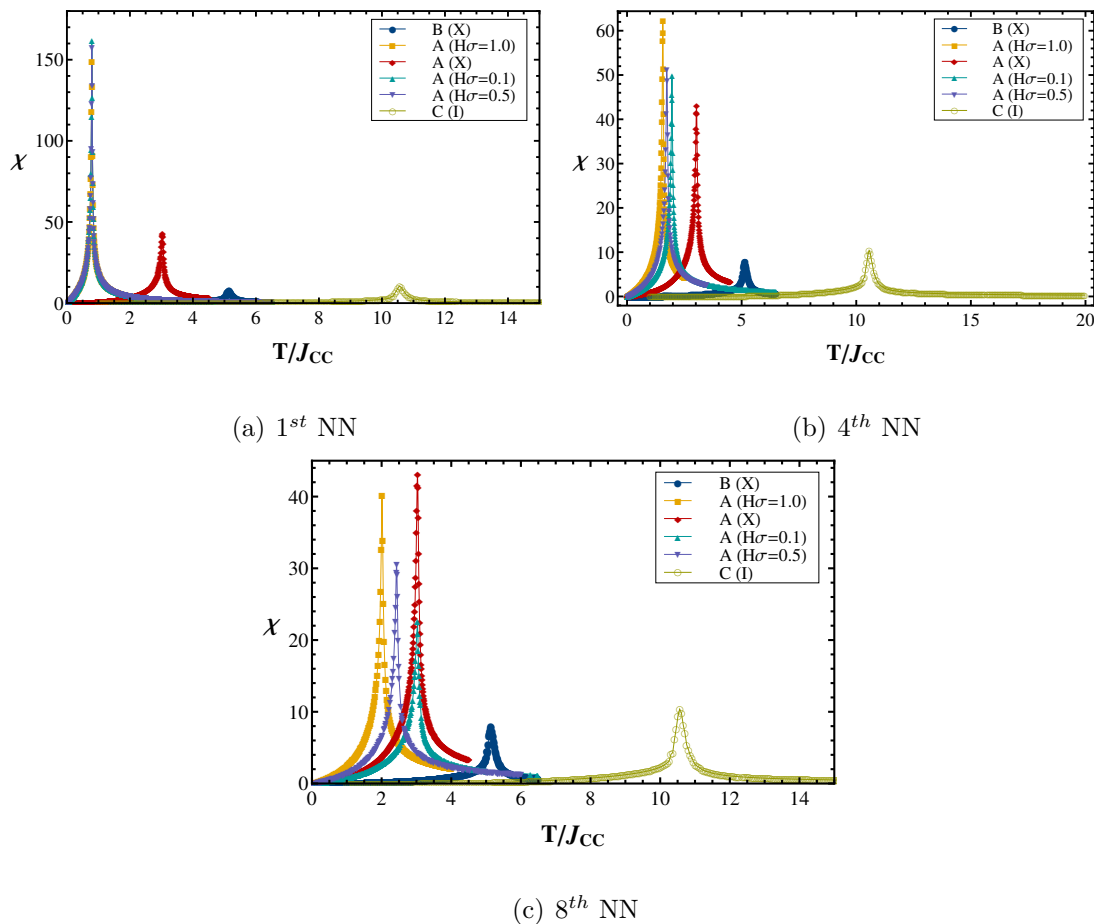


Figure 6.11: χ vs T/J_{CC} for each component of the BAC trilayer. This plot corresponds to slabs of the respective species in the trilayer. The B and C slabs remain the same in the three plots with $J_{BB} = 1$, $J_{CC} = 1$ for 8 monolayers of B and 10 monolayers of C . Also remaining fixed in the three plots is the A slab with 40 monolayers of XY spins, $J_{AA} = 0.55$ and 8th NN. Only the A slab with 40 monolayers of Heisenberg spins with $J_{AA} = 0.55$ and varying σ ($\sigma = 1, 0.5$ or 0.1) changes in the three plots: (a) 1st NN, (b) 4th NN and (c) 8th NN.

Each line in figures 6.11 (a)-(c) represent the susceptibility of each component that makes up the *BAC* multilayer treated as distinct systems. Figures 6.11 (a)-(c) show that as the range of neighbours increases in the Heisenberg *A* system from (a) 1st NN to (c) 8th NN, the σ magnitude becomes more significant in determining $T_c(A)$. In fact, using $\sigma = 0.1$ with 8th NN, sets $T_c(A)$ of the *A* slab with 40 monolayers of Heisenberg spins to approximately that of the *A* slab with 40 monolayers of *XY* spins, $\sigma = 1$, $J_{AA} = 0.55$ and 8th NN.

However, whilst decreasing σ increases the contribution of further ranged interactions to the energy, limiting the range of interactions then has consequences. Using a finite range, r_c , (in this case 8th NN) sets the interaction of a spin with another spin a distance $r > r_c$ away to zero. Neglecting these interactions, which have a higher weighting to the energy when σ is smaller could imply that estimates in the overall magnetisation and other quantities of the system may be subject to approximation.

Figure 6.12 show plots of the magnetisation per spin vs temperature for the bulk Heisenberg *A* system with $J_{AA} = 0.55$ compared with the average of the 10 Heisenberg *A* monolayers in the *BAC* trilayer for different σ . The coupling in the trilayer is set to $J_{AB} = J_{AC} = 0.60$, $J_{AA} = 0.55$, $J_{BB} = 1$ and $J_{CC} = 1$ with all the simulations run with 8th NN. This comparison is to show how the amount of induction from the bulk to the trilayer is dependent on σ . A subtle difference can be realised with $\sigma = 0.1$ showing the smallest amount of induction whilst $\sigma = 0.5$ and $\sigma = 1$ are quite similar. The difference between $\sigma = 0.1$ and the other two σ is likely due to the “cut off” in the range of interactions mentioned previously even though we can see that by decreasing σ there is a greater shift to higher T_c . This is because with further analysis, using $\sigma = 0.1$, the middle monolayers of the *A* layer have a lower magnetisation than the bulk when $T < T_c(A)$.

With the findings presented here, I decided to run the simulations with the following parameters:

- *XY* spins for the *B* and *A* layers and Ising spins for the *C* layer to obtain an

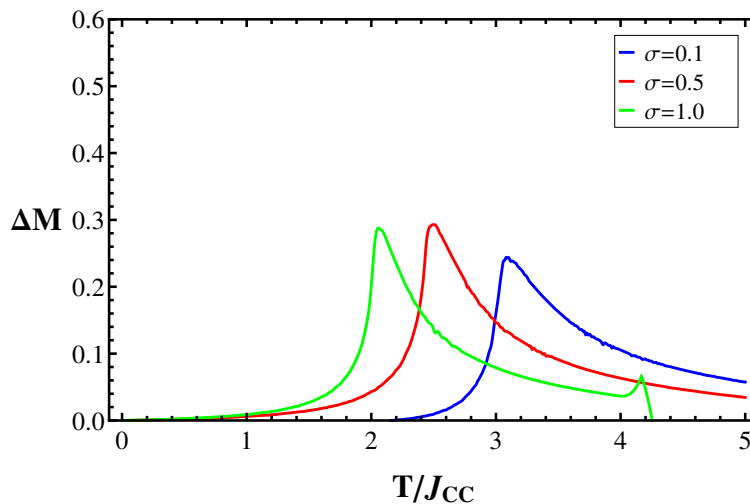


Figure 6.12: Δm vs T/J_{CC} . This is the induced magnetisation as a function of temperature achieved by taking the magnetisation difference of the bulk A system with the 10 monolayers of A in the multilayer. The bulk magnetisation is once again given by the m vs T/J_{CC} of the middle monolayer in a slab of A with 40 monolayers of Heisenberg spins, $J_{AA} = 0.55$ and $\sigma = 0.1, 0.5$ and 1.0 respectively (as indicated in the legend). The A layer in the BAC multilayer are modelled with Heisenberg spins, couplings of $J_{AB} = J_{AC} = 0.60$ and $J_{AA} = 0.55$ and $\sigma = 0.1, 0.5$ and 1.0 (as indicated in the legend). The odd feature at $T/J_{CC} \simeq 4.2$ for $\sigma = 1.0$, is an artefact due to limited data points. All are simulated with 8^{th} NN.

in-plane system and the magnetically hard C layer.

- $J_{AB} = J_{AC} = 0.90$ for a strong influence on the A spins at the A/B and A/C interface, which is appropriate for a system which indicates the B and C layers indirectly couple via the A layer.
- $J_{BB} = J_{CC} = 1$ to treat the B and C layers as high T_c materials.
- $J_{AA} = 0.40$ so B and C can influence A more strongly when the intraspecies coupling of A is low and to treat the A layer as a low T_c material.
- $\sigma = 0.50$ so decay is slower with $r^{-(d+\sigma)}=r^{-3.5}$ this is to effectively increase the range of induction.

- 8th NN also to increase the range of direct coupling.

6.5 Results and discussion

As was mentioned in the previous section, method 1 and method 2 are presented separately since they correspond to two different approaches to modelling the *BAC* trilayer.

Please note that all plots of $m(T)$ which do not compare the range of interactions, will have a temperature scale defined by $J_{CC} = 1$ as the exchange coupling in the *C* layer remains fixed throughout the study and therefore ensures consistency. It is unnecessary to investigate the *C* monolayers independently since they remain unchanged throughout the simulations and are also not used for probing the system in the experimental analysis. In the experimental work the *C* layer can rotate as a single domain in the plane of the multilayer [301], but the angle of its direction relative to the other layers (*A* and *B*) remain fixed. Therefore, to the *A* and *B* layers, the *C* spins remain fixed and this layer will not move in these simulations.

6.5.1 Method 1

These results are presented for the separate components, *A* and *B* of the trilayer and then for the *A/B* and *A/C* bilayers and finally the trilayer.

Results for a soft, low T_c ferromagnetic slab

Using 20 and 40 monolayers of Heisenberg *A* spins, figure 6.13 (a) shows the average magnetisation of each system and the magnetisation of the middle monolayer of each system (see figure 6.13 (b)), which are taken to be monolayer 10 and 20 respectively. One can see that the average magnetisation is slightly different between the system sizes, shown in figure 6.13 (a) whilst the middle monolayer of both system sizes has approximately the same $m(T)$ profile (see figure 6.13 (b)). This is because the average magnetisation of each system size takes into account surface effects, which are more pronounced in smaller system sizes because surface monolayers contribute a greater

proportion to the energy than in larger system sizes (see chapter 5).

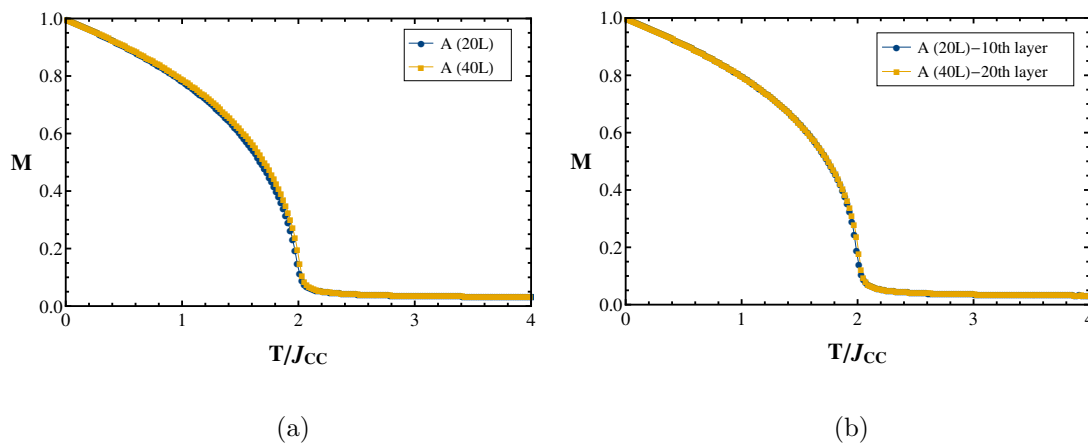


Figure 6.13: m vs T/J_{CC} for an A slab with sizes $32 \times 32 \times 20$ and $32 \times 32 \times 40$. (a) An average magnetisation of the respective system sizes whilst (b) is the magnetisation of the middle monolayer in each system, which is taken to be monolayer 10 and monolayer 20, respectively. As $T_c(A)$ remains constant for the middle monolayer of each system, this is taken to be representative of the bulk $T_c(A)$ value, unaffected by surface effects.

The ordering of spins in the middle monolayer are unaffected by surface effects. Hence, $T_c(A)$ of the middle monolayers represents the ordering temperature of the bulk system. The critical temperature in this case, is found using the maximum peak in the respective $\chi(T)$ plot and is $T_c(A) = 2.03$.

Thickness effects for a soft, high T_c ferromagnetic slab

In chapter 5.4, I investigated a trilayer system which included one monolayer of XY spins and $J = 1$. This was extended to 5 monolayers, as presented in appendix D. Since 8 monolayers of XY spins with $J = 1$ is studied in this project, it is worth investigating how the magnetisation changes for a given thickness of XY spins.

Figure 6.14 shows how the critical temperature of the middle monolayer in the B system changes with the thickness of B . It was important to study the middle mono-

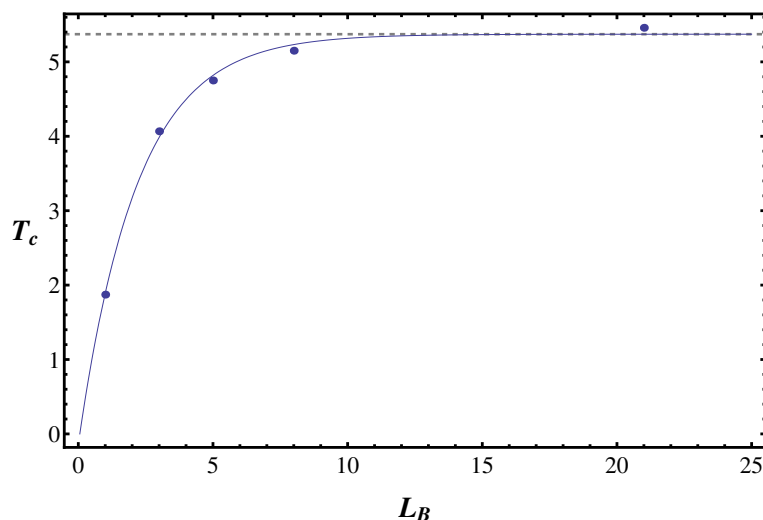


Figure 6.14: $T_c(B)$ vs L_B for thicknesses from 1 to 21. Error bars are obscured by the data points. The dotted line at $T_c/J_{BB} = 5.37$ indicates the maximum / bulk critical temperature of a $3d$ B system with $J_{BB} = 1$ and 8^{th} NN. The fit is achieved using the model $a \exp(-bx) + c$, where $a \rightarrow -5.52$, $b \rightarrow 0.460$ and $c \rightarrow 5.37$.

layer for the same reasons given in the previous section, since when the system becomes large enough the magnetisation in the middle monolayers will have reached the bulk value whilst the average magnetisation will differ between system sizes due to surface effects. The critical temperature increases with thickness but also plateaus clearly for $L_B > 10$. Setting the limiting $T_c(B)$ to $T_c = 5.37$ (3 significant figures), the thickness is found to be $L_B = 17$. Of course, the limiting $T_c(B)$ is not to 3 significant figures and calculating the thickness using more significant figures changes the thickness considerably, but from figure 6.14, $L_B = 17$ is a reasonable approximation to draw conclusions from in relation to the change in $T_c(B)$.

The reason that the smaller thicknesses are lower in ordering temperature is due to the surface effects, which were discussed in the previous chapter and will become clear from the magnetisation profiles of the system. With this in mind, using 8 monolayers of B will have surface effects playing a role in the magnetisation of the B layer. Since the results given here are for the middle monolayers then this also tells us how far extending the surface effects are in the B system. For the 17 monolayers of B spins,

the bulk magnetisation is obtained in monolayer 9. Hence for the 8 monolayers of B used in this trilayer system, the surface effects are expected to permeate throughout the B monolayers and possibly affect any layers directly neighbouring itself.

Results for a (soft high T_c /soft low T_c) ferromagnetic bilayer

The magnetisation per spin vs layer position for an A/B bilayer with $L_A = 40$ monolayers at $T_c(A) = 2.03$ is shown in figure 6.15. This is to see the extent of magnetic induction from the B monolayers into the A monolayers.

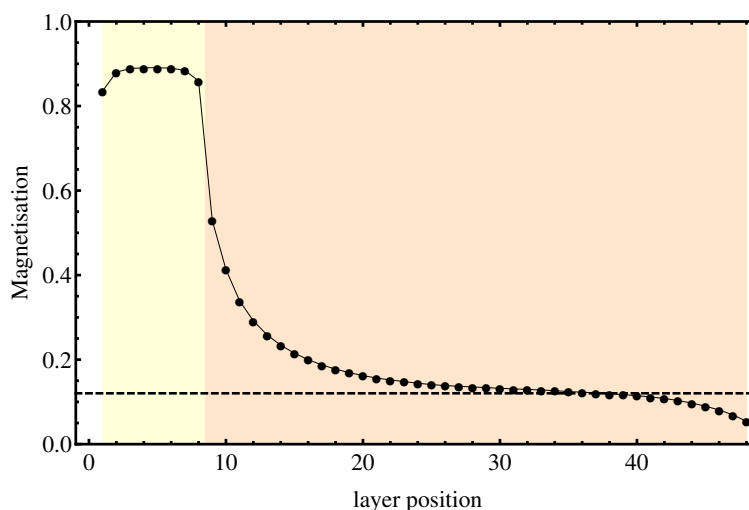


Figure 6.15: Magnetisation per spin vs layer of the A/B bilayer with $L_B = 8$ (yellow shading) and $L_A = 40$ (light orange shading), where $J_{BB} = 1$, $J_{AA} = 0.55$ and $J_{AB} = 0.60$ at $T_c(A)/J_{CC} = 2.03$. The dotted line indicates the magnetisation of the bulk A system. The line through the points is a guide to the eye.

From figure 6.15, one can see the magnetisation of the A monolayer neighbouring the B layer has $m \simeq 0.5$, so that approximately 38% more spins in this monolayer are ordered than there is in the bulk A system at $T_c(A)$ (indicated by the dotted line). The magnetisation at the surface of the A layer is approximately zero, which is lower than the order parameter at $T_c(A)$.

The point where the decay in magnetisation in the A monolayers meets the dotted line in figure 6.15, is the point at which the induction from B ceases, because the bulk magnetisation is obtained at this temperature. In the figure we see this occurs as a small plateau at monolayer 35, which would indicate that if the trilayer system has $L_A \geq 27$, then the coupling of B to C would be insufficient to observe the results as seen in the coercivity if the induction were solely from the B monolayers. However, it is clear to see that only the A monolayers closest to the B layer will play a role in the indirect coupling of B to C . Monolayer 1 and monolayer 8 of the B layer both have a lower magnetisation than the middle B monolayers. This would indicate that the A layer disrupts the order in the B layer as the surface does.

Results for a (soft low T_c /hard) ferromagnetic bilayer

The magnetisation vs layer position for an A/C bilayer with $L_A = 50$ monolayers at $T_c(A) = 2.03$ is shown in figure 6.16. This is to see the extent of magnetic induction from the C monolayers into the A monolayers.

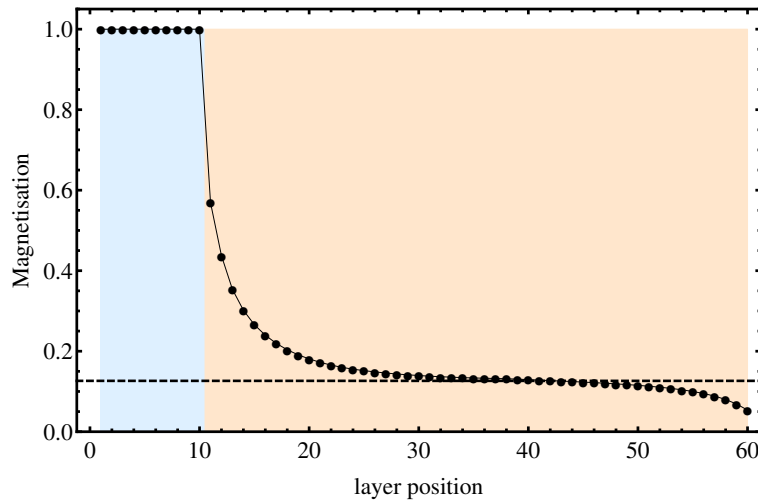


Figure 6.16: Magnetisation per spin vs layer of the A/C bilayer with $L_C = 10$ (blue shading) and $L_A = 50$ (light orange shading), where $J_{CC} = 1$, $J_{AA} = 0.55$ and $J_{AC} = 0.60$ at $T_c(A)/J_{CC} = 2.03$. The dotted line indicates the magnetisation of the bulk A system. The line through the points is a guide to the eye.

Layers B and C only differ by their spin dimensionality, where the C spins are stiffer than the B spins. With such a strong anisotropy from the Ising spins (C), figure 6.16 shows that the A monolayer at the A/C interface now has $m \simeq 0.575$ compared with this monolayer in the A/B bilayer with $m \simeq 0.5$.

The point at which this decay of induction in the A monolayers meet the magnetisation of the bulk $T_c(A)$, occurs at monolayer 44. This would indicate that if the trilayer system has $L_A \geq 36$ and the induction were solely from the C layers, then the coupling between B and C would be insufficient. The stiffness of the C layer is such that the neighbouring A monolayers do not affect the magnetisation in the C layer unlike that of the B layer and the surface monolayer of the C layer is also unaffected by surface effects at this temperature.

From the simulated results thus far, the maximum number of A monolayers that would allow for overlap in the induced order of the B and C layers is $L_A < (36+27)-1 = 62$. The minimum size of L_A , given that direct coupling is up to the third concentric cube, is then $L_A \geq 6$. So overall the limits for the thickness of A is $6 \leq L_A < 62$.

The soft high T_c ferromagnetic layer in different environments

From the bilayer results, it is clear that the A layers reduce the magnetisation in the B monolayer at the A/B interface. However, this increase in coercivity of the B layer could be relative to the thickness size, such that a smaller thickness reduces the magnetisation in the B monolayer less than a thicker A layer. Figure 6.17 (a) shows the average m vs T/J_{CC} for the B layer with varying L_A , whilst figure 6.17 (b) shows this for the B layer at the A/B interface. Both of these plots are compared with the average magnetisation of an 8 layered slab of B .

Figure 6.17 (a) shows that as the thickness of A decreases, the B layer shows no change in the average magnetisation, whilst figure 6.17 (b) shows that the magnetisation of the interfacial B monolayer in the trilayer is not the same as the average value,

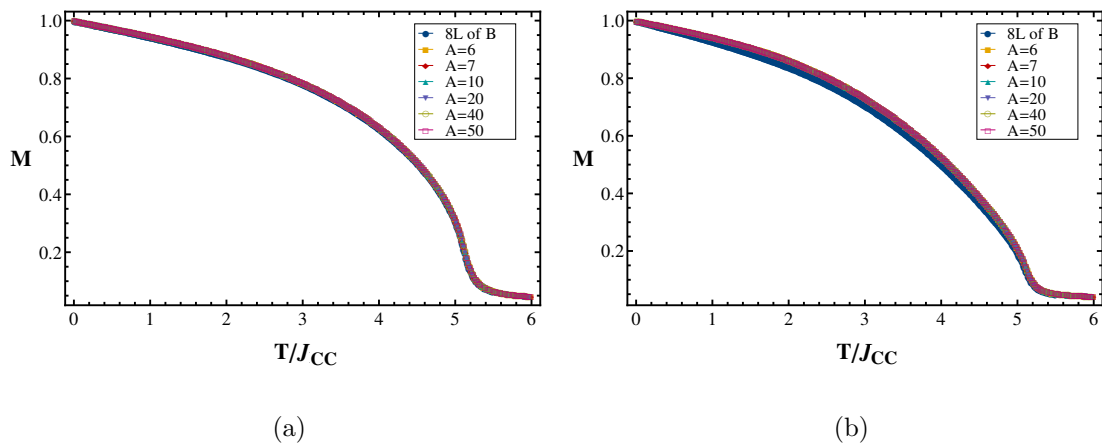


Figure 6.17: (a) Average m vs T/J_{CC} for the 8 monolayers of the B layer in the BAC trilayer. Plotted for $L_A = 6, 7, 10, 20, 40$ and 50 monolayers. (b) m vs T/J_{CC} of the B layer at the A/B interface for the same thicknesses of A are used in (a).

however this value is then independent of the thickness of A . Rather this is just an artefact of the B layer neighbouring an A layer.

Results of a (soft high T_c /soft low T_c /hard) ferromagnetic trilayer with varying thickness

The magnitude of magnetic induction is temperature dependent. Figure 6.18 shows the magnetisation versus monolayer profile of the BAC trilayer at different temperatures for a fixed thickness. By analysing the A monolayers close to the A/B interface, one can see that at temperatures around the critical temperature, $T_c(A) = 2.03$, more monolayers are affected by induced order. This is clear as all the A monolayers should have the same order parameter at the critical temperature and in a slab of A they should be zero. The results coincide with spins fluctuating on all length scales at the critical temperature. Therefore to determine the maximum inducing range of both B and C in the trilayer, observations are made at the critical temperature.

In section 6.5.1 it was found that $6 \leq L_A < 62$ using the plots of m vs layer for the A/B and A/C bilayers. The thickness by which the B and C layers cease to interact by induction can be verified by recording the magnetic order in the middle monolayers

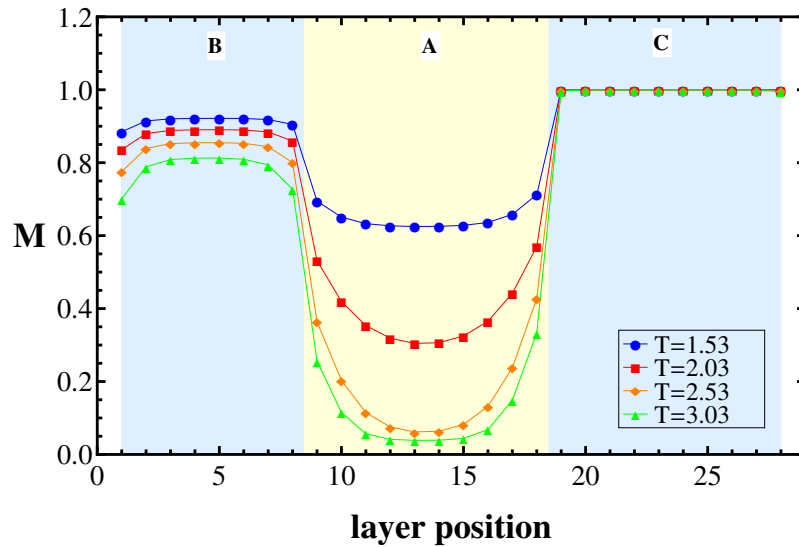


Figure 6.18: Magnetisation per spin vs monolayer profile for the *BAC* trilayer with $L_A = 10$ and 8^{th} NN at different temperatures $T < T_c(A)$, $T = T_c(A) = 2.03$, $T > T_c(A)$ and $T \gg T_c(A)$.

of the trilayer with increasing L_A (figure 6.19). Knowing the order parameter at the critical temperature as a function of thickness size, one can extrapolate the results to find the thickness which yields the same order parameter as the bulk $T_c(A)$ ($m = 0.12$ for $T_c(A) = 2.03$).

In figure 6.19, the dotted line represents the order parameter of the bulk *A* system when $T_c(A) = 2.03$. The point at which the fitted line crosses the dotted line is the thickness whereby the magnetic order in the bulk is obtained in the middle monolayers and hence no further induction in the *A* monolayers is observed. To obtain this point, the equations of the two lines are solved: $0.12 = 0.977x^{-0.509}$. The thickness at this point is found to be 61.6 (to 3 significant figures) and hence $L_A = 62$, which is consistent with the thickness found by adding the *A/B* and *A/C* bilayers.

The *BAC* multilayer has an asymmetry in the magnetic induction from the *B* and *C* layers. Therefore it is not exactly the middle monolayers in the trilayer for which the induction is zero. However, this does not seem to cause any discrepancy between the

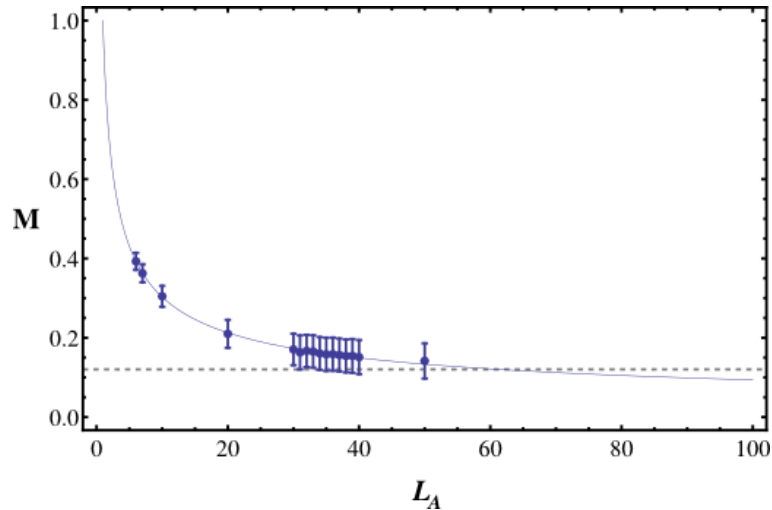


Figure 6.19: Magnetisation per spin in the middle A monolayer vs L_A in the BAC trilayer at $T_c(A) = 2.03$, fitted to a power law given by ax^b where $a \rightarrow 0.977$, $b \rightarrow -0.509$. The average order parameter of the two middle A monolayers is taken for even A thickness sizes. The dotted line represents the magnetisation in the bulk A system.

two methods in finding the maximum thickness for induction (this may only be true for the choice of trilayer given here and may not hold if B and C differed significantly by couplings or degrees of freedom, etc).

Summary of Method 1

Investigating the A and B components independently as well as the A/B and A/C bilayers, one can conclude that only the A layer demonstrates any significant change in magnetic order in the trilayer. It is possible to see this from figure 6.20 which shows how the magnetisation, as a function of temperature, changes with the thickness of A . It is clear to see there is a considerable difference in these plots at temperatures above the critical temperature where induced magnetic order is the sole contributor to any order in the A layer. The smaller the thickness, the more induced order there is at temperatures above $T_c(A)$.

The fact that changes are only seen in the A layer of the trilayer could be due to

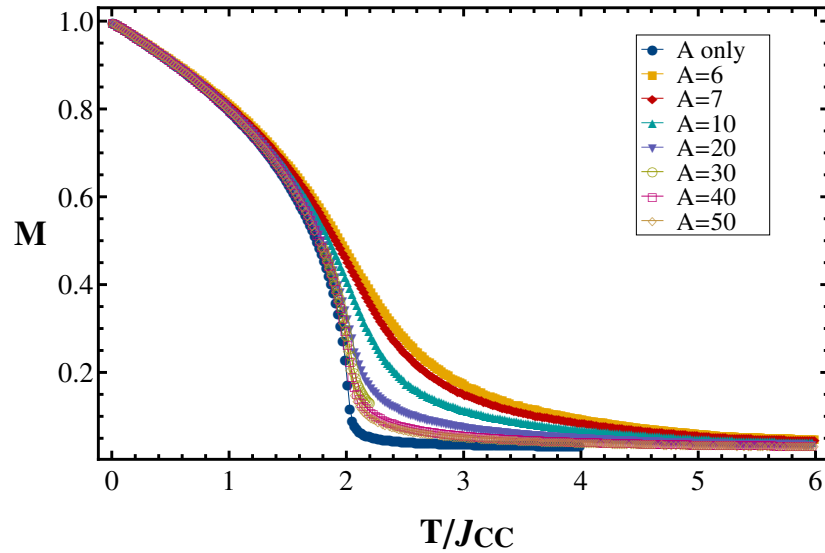


Figure 6.20: Average m vs T/J_{CC} of the A layer when $L_A = 6, 7, 10, 20, 30, 40$ and 50 . The entire temperature range for $L_A = 30$ is not shown as this was part of an investigation to analyse the critical region (see figure 6.19). The magnetic order of the bulk A system is also included in the plot for comparison.

the coupling strength, but also could be a consequence of the range of interactions. In this project 8^{th} NN is used. We can see that range is important for the induction of magnetisation by looking at a plot of the magnetisation vs monolayer profile for different ranges of interaction (figure 6.21).

Figure 6.21 shows the magnetisation as a function of layer position for different range of interaction at the same temperature and energy scale. This shows that with further range interactions, the penetration depth of the magnetic order is greater in the A monolayers than for a shorter range. This is evident from the decay shape.

From the results for Method 1, the magnetic induction in A does not play a role in increasing the T_c of the B layer, which could imply the B spins do not become stiffer and hence neither will there be a change in coercivity as a consequence. This is the case even as the thickness of the A layer decreases and $T_c(A)$ increases. The model is insufficient in capturing the true physics in this trilayer system as the experimental

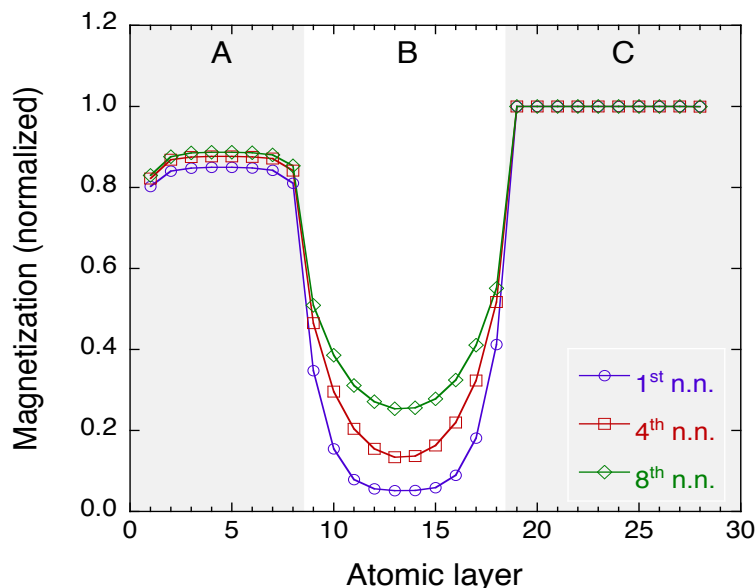


Figure 6.21: Magnetisation vs layer profile for the *BAC* trilayer at $T/J_{\text{eff}} = 1.01$ for varying ranges (1st, 4th and 8th NN). J_{eff} is the scaling factor used to set the energies of the further ranged systems to that of the NN system so that the results are plotted on the same energy scale. $T/J_{\text{eff}} = 1.01$ is chosen as a temperature little beyond the critical temperature of all the ranges to show the extent of induction for each range. This figure was plotted by Magnus, whilst the data is my own.

results indicate that *B* and *C* couple but from these theoretical results this is not the case. Lastly, this may be due to a limitation in the range of interactions as increasing the range of interactions does alter the magnetic order penetration depth in the *A* monolayers (see figure 6.21) and shows that magnetic induction can be sustained for higher temperatures (see figure 6.23).

6.5.2 Method 2

In method 2, an iterative process was used to identify which theoretical parameters would best reproduce the experimental results by varying the spin dimensionality, the inter- and intraspecies couplings and the rate of decay of interactions. The final parameters along with the reasonings were noted at the end of section 6.4.2. The parameters are given again here for convenience: *XY* spins for the *B* and *A* layers and Ising spins

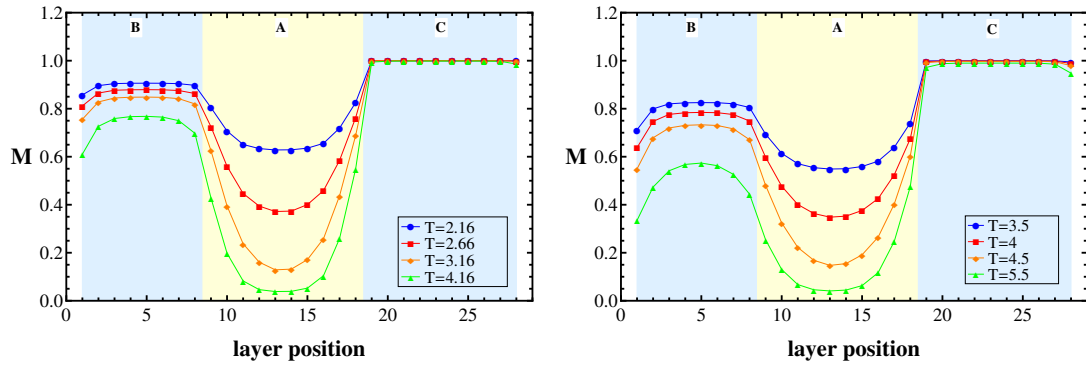
for the C layer, $J_{AB} = J_{AC} = 0.90$, $J_{BB} = J_{CC} = 1$, $J_{AA} = 0.40$, $\sigma = 0.5$ and the range of direct exchange interactions is up to 8^{th} NN. The system size is set as $32 \times 32 \times 28$ with 8 monolayers of B , 10 monolayers of A and 10 monolayers of C .

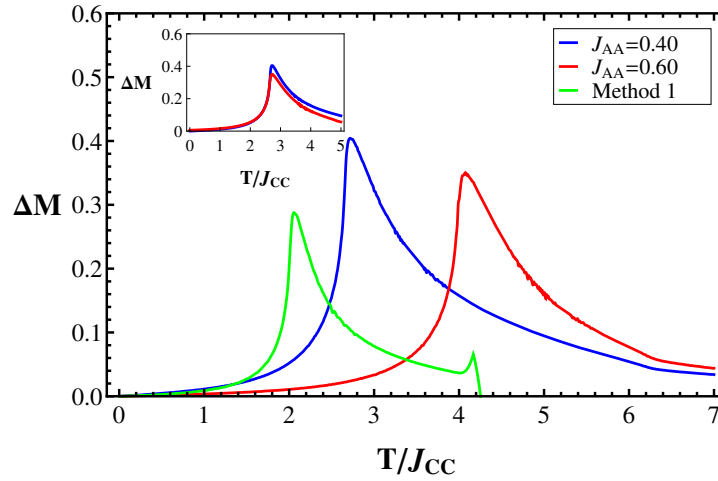
In this section, I compare the trilayer results for method 1 and method 2 using this fixed system size and show which system is more representative of the experimental work.

The efficiency and sustainability of magnetic induction with temperature and range

Figure 6.22 shows m vs monolayer of this BAC trilayer for $T < T_c(A)$, $T = T_c(A) = 2.03$, $T > T_c(A)$ and $T \gg T_c(A)$ for (a) $J_{AA} = 0.40$ and (b) $J_{AA} = 0.60$. I have included $J_{AA} = 0.60$ to show that with a stronger coupling in this system, $T_c(B)$ is not too dissimilar to $T_c(A)$ and would not be suitable for the results needed. Figure 6.22(c) summarises the induction results in plots of ΔM vs T/J_{CC} for the $J_{AA} = 0.40$ and $J_{AA} = 0.60$ systems and also shows a comparison with the result from Method 1 where the parameters differ by Heisenberg spins for the A layer, $J_{AB} = J_{AC} = 0.60$, $J_{AA} = 0.55$ and $\sigma = 1.0$. It is clear to see that not only do the results for $J_{AA} = 0.40$ show the greatest amount of induction in the A layer but it also shows a far greater amount of induction over the temperature range than the system used in Method 1. This is of course expected since a thorough investigation of the parameters were made for Method 2 and parameters were suitably chosen to reproduce the experimental results as closely as possible.

The plots of m as a function of the layer position (monolayers) for these three BAC trilayers are shown for 1^{st} NN, 4^{th} NN and 8^{th} NN in figure 6.23. Each range is plotted for $T = T_c(A) + \Delta T$, where ΔT is arbitrarily chosen here as 0.20 since the magnetisation in the middle monolayers of A using 1^{st} NN interactions in Method 1, reaches a minimum with this shift in temperature. The bulk $T_c(A)$ varies depending on the range. ΔT is used to show the thermal extent each range can sustain induction

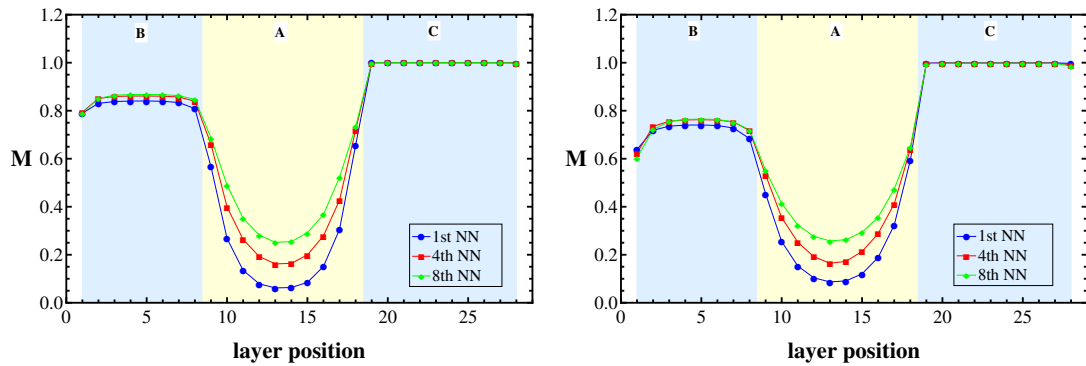

 (a) $J_{AA} = 0.40$

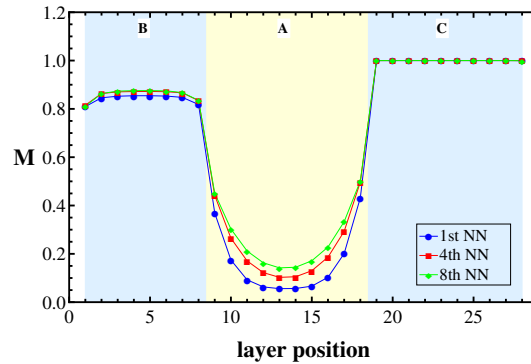
 (b) $J_{AA} = 0.60$


(c)

Figure 6.22: m vs layer of the *BAC* trilayer for temperatures $T < T_c(A)$, $T = T_c(A) = 2.03$, $T > T_c(A)$ and $T \gg T_c(A)$. (a) $J_{AA} = 0.40$ and (b) $J_{AA} = 0.60$ with all other parameters held constant. (c) ΔM vs T/J_{CC} for Method 2 with $J_{AA} = 0.40$ and $J_{AA} = 0.60$ and for Method 1. This is the induced magnetisation as a function of temperature achieved by taking the magnetisation difference of the respective bulk *A* systems from the 10 monolayers of *A* in the multilayer. The inset in (c) shows ΔM vs T/J_{CC} for $J_{AA} = 0.60$ overlaid on the respective plot for $J_{AA} = 0.40$ for an easier comparison.

from *B* and *C* in the *A* layers.


 (a) $J_{AA} = 0.40$

 (b) $J_{AA} = 0.60$


(c) Method 1

Figure 6.23: m vs layer of the *BAC* trilayer for 1st NN, 4th NN and 8th NN. (a) $J_{AA} = 0.40$ and (b) $J_{AA} = 0.60$ with all other parameters held constant, whilst (c) is obtained using the parameters of Method 1. Each range is plotted for $T = T_c(A) + \Delta T$, where ΔT is arbitrarily chosen here as 0.20 and the bulk $T_c(A)$ varies depending on the range ($T = 0.88, T = 1.92, T = 2.66$ for (a); $T = 1.32, T = 2.88, T = 4.00$ for (b) and $T = 0.79, T = 1.57, T = 2.03$ for (c)). A ΔT is chosen as an indication to the sustainability of an induced magnetisation at $T > T_c(A)$.

From figure 6.23(a) and (b), one can see that when using *XY* spins for the *A* layer the decline in magnetisation from *B* to *A* and from *C* to *A* at the interfaces is smaller than when treating the *A* spins as Heisenberg (see figure 6.23(c)). Hence the magnetisation in the other monolayers of *A* is higher than is shown for Method 1. This difference in magnetic order of *A* compared with *B* and *C* is important for ensuring induction penetrates further into the *A* layer but also to maintain the magnetic induc-

tion from the inducing sources B and C at higher temperatures. Comparing figures 6.23(a) and (b), one would think there is a greater induction within the A layers when $J_{AA} = 0.60$ than with $J_{AA} = 0.40$, however, this is not an inductive effect but just a simple consequence of a stronger intraspecies coupling. This is clearly shown in figure 6.22(c), particularly the inset, where ΔM vs T/J_{CC} for $J_{AA} = 0.60$ is overlaid on the respective plot for $J_{AA} = 0.40$. In the inset, one can see that for $J_{AA} = 0.40$, there is a greater maximum induction than in the $J_{AA} = 0.60$ system and the induction is larger over the temperature range. This is because a smaller coupling within the A layer is more magnetically susceptible to influence from stronger coupled B and C layers.

However, even with these improvements to model the behaviour of the experiment, figure 6.24 shows that decreasing the thickness of A causes no noticeable change in the magnetic ordering of the B layer. This can be explained quite simply from the analysis of the A layers, which showed that when the intraspecies coupling is strong, then the susceptibility of the spins to the induced magnetic order is low. One can see that the B layer has a strong J_{BB} coupling and hence is not easily susceptible to magnetic induction from the A layers. The magnetic ordering in the A layer would have to be comparable to the B layer to increase the effective thickness and hence increase T_c of the B layer. From figure 6.14, one must be aware that there is a limit in the thickness of B up to which the T_c increases no further with increasing thickness.

Summary of method 2

The parameters chosen in method 2 are shown to be a significant improvement from the parameters chosen in method 1, as the range of induction and sustainability of induction at higher temperatures is greater, which is more consistent with the results of the experiment [298]. Due to a time constraint on the numerical work in this study, a thorough investigation into the thickness dependence of the B layer magnetisation with these new parameters was not possible, however, preliminary results show that even the improvement in the model does not change the result from method 1, which is that the magnetic order in the B layer is unaffected by the thickness of A in this study. In this

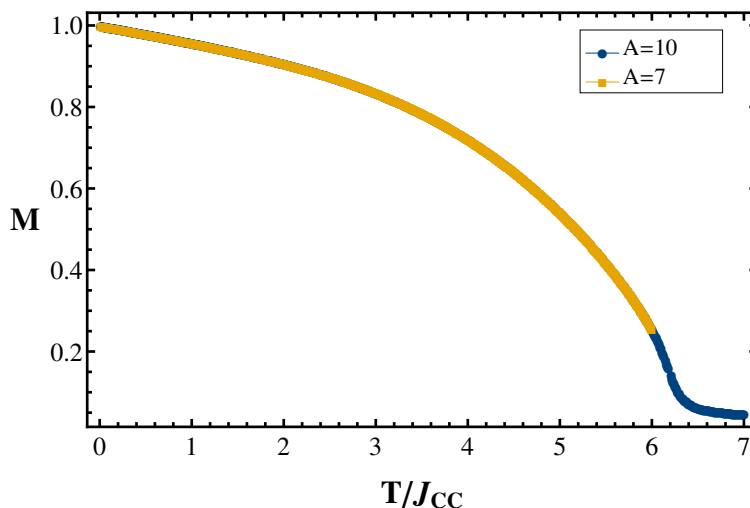


Figure 6.24: m vs T/J_{CC} of the B layer at the A/B interface for $L_A = 7$ monolayers and $L_A = 10$ monolayers. Please note that data for $L_A = 7$ monolayers is recorded up to $T/J_{CC} = 5.99$.

case, only the B monolayer at the A/B interface is considered. One would expect the B layer would show some dependence on L_A since the A layers, as shown in method 1, are clearly increasing in T_c and the decoupling region (A decoupling from B) is also increasing. Hence, one should consider investigating another quantity such as the spin stiffness to identify any other possible consequences of the proximity effect.

6.6 Conclusion

To conclude this chapter, I have modelled the BAC trilayer using two approaches, one to start with the experimental details given about the system and analyse the results, whilst the second is to start from the experimental results in order to identify the best parameters to describe the system. Using both methods I have been able to show magnetisation profiles of the BAC trilayer which demonstrate that there is an overlap of the magnetic induction in A from the B layer and the C layer, with method 1 showing that with a smaller thickness in A , this overlap becomes more significant. As a consequence of this result, the critical temperature of the A layer increases. Though the results in the experiment are regarding the coercivity of the B layer, these results are compli-

mentary in showing that there is an effect in the A layer from the two inducing sources B and C . It does not however, show that the proximity effect causes any changes to the B layer though this could be that the quantity being measured is not suitable. For instance, the spin stiffness is more likely to demonstrate the effects of anisotropy and hence relate more closely with the coercivity results.

Method 1 demonstrates an investigation of the extent of induction and the determination of the thickness by which the inducing effects of B and C no longer overlap. Either by studying the two bilayers A/B and A/C or extrapolating trilayer results to the bulk limit, the same thickness is found as $L_A < 62$ for overlap. This indicates that the range of interactions chosen, 8^{th} NN and the rate of decay of interactions as chosen in this method, $\sigma = 1$, enables the induction to penetrate deep into the trilayer. However, even with this, there is no change in magnetisation of the B layer, not even the B monolayer at the A/B interface with different thicknesses of A . This was thought to be due to the very sharp decline in magnetisation from the B monolayer to the A monolayer at the A/B interface, which is a consequence of the interspecies coupling. Method 2 shows an improvement of the model in Method 1, where the trilayer is in-plane and has very strong interspecies couplings J_{AB} and J_{AC} . The experimental results show that there is a strong magnetic induction, and therefore it is found that a smaller J_{AA} is more susceptible to induction from the harder B and C layers and a longer decay rate $\sigma = 0.5$ is chosen to increase the weighting of magnetisation in neighbours further away from each spin. The alteration improves the sustainability of magnetic induction for higher temperatures than in Method 1, however gives an indication of the reason for why the magnetic order in the B layer is not being affected with thickness, because the intraspecies coupling of the B layer is relatively strong.

Once again, as shown in the previous chapter, the range of direct exchange interactions has a significant impact on the observed physics of the system. A nearest neighbour model would not have been sufficient in identifying the range of induction of the B and C layers in this trilayer.

Part III

Final remarks and perspectives

In this thesis classical spin models have been used together with the Monte Carlo method to study magnetic phases and phase transitions, impacted by lattice geometry, confinement and long-range interactions. This has involved non-uniform finite spin systems with non-homogeneous interactions.

The Coulomb phase has been known to exist in rare earth magnetic pyrochlore systems, when there is an absence of long range magnetic order [205]. However, for the first time, it is shown here that a pyrochlore structure filled with magnetic monopoles and with long range magnetic order can exhibit the Coulomb phase (see figure 4.8). This is through our new conceptual picture known as magnetic moment fragmentation, where in this case, the magnetic moment appears to fragment into a fixed monopolar part and a fluctuating dipolar part. This gives rise to both antiferromagnetism and co-operative paramagnetism coexisting in the monopole crystal we simulate. Additionally, characterisation of the phase transitions in this system (first and second order), has lead to the construction of $\mu^* - T^*$ phase diagrams which demonstrate how the spin ice phase is connected with the monopole crystal phase (see figure 4.6). We expect that the concept of magnetic moment fragmentation will not be limited to monopole crystals but may be relevant generally in experimental systems demonstrating partial ordering whilst in the presence of background magnetic liquid fluctuations.

When the thickness of cobalt is less than or equal to a single monolayer, then as shown experimentally [100], cobalt does not exhibit ferromagnetic behaviour. However, when stacked in a multilayer with a weaker coupled species, cobalt demonstrates ferromagnetism again [71]. The first theoretical explanation for this occurrence is presented in this thesis by analysing the phase transitions in these confined magnetic multilayers as a function of range of interaction and interspecies coupling strength. Bloch's law was used to observe changes in the low temperature region of plots of $M(T/T_c)$ and the β exponent was monitored to observe changes in the critical region in plots of $M(T/T_c)$ (see figure 5.16). A dimensionality crossover is identified in the strongly coupled monolayer, which we describe by an increase in effective thickness resulting

from a developing concept known as the double proximity effect. This effect occurs when there is a two-way enhancement of the critical temperature in both the weaker and strongly coupled species due to their proximity with one another. Understanding the double proximity effect, we believe will be important when designing experimental multilayers and in explaining exceptional behaviour in the monolayer limit.

Developing the models for the magnetic multilayer systems in chapters 5 and 6 clearly show that the choice of parameters for imitating experimental systems can be difficult and sometimes conflicting. Given an A/B multilayer, where A and B have the same spin dimensionality, $T_c(A) < T_c(B)$ and the interspecies coupling, J_{AB} , is strong and fixed; then a weak intraspecies coupling, J_{AA} , has a greater polarisability in the interfacial A monolayers than for a strong J_{AA} . This proximity effect however, does not permeate very well to the bulk A monolayers as for a strong J_{AA} (see chapter 6). Using magnetisation vs monolayer profiles as a function of the range of interaction and coupling strength, were particularly useful when translating the theoretical results to some experimental relevance, especially as experimental studies on these multilayer systems are limited to bulk or single layer analysis (see figure 6.23 for example). These results shed light on the extent of magnetic induction in weakly coupled layers from those with a stronger coupling and clearly indicate interfacial and surface effects.

Long-range interactions have been involved in all the projects presented in this thesis, however, most unique to the studies in thesis is the use of further ranged direct exchange interactions. Long range direct exchange interactions are barely studied since direct exchange is best observed when the orbital overlap is sufficient as a through-bond interaction [1]. Consequently, long range indirect exchange interactions, such as RKKY or DM are preferred in classical spin models. However, in some amorphous systems at room temperature it can be challenged that DM, RKKY and dipolar interactions make little to no contribution [326] and yet NN exchange does not capture the physics properly. Therefore further ranged direct exchange interactions are the next logical step to model and hence is used to study the amorphous systems in chapters 5 and 6.

It was computationally challenging to modify existing code from nearest neighbour interactions to further ranged exchange interactions, whilst ensuring there were periodic boundaries in the xy plane and finite in the z and keeping the computational time low. A test is made between spins in a coordination shell to the spin of interest to identify if it is a neighbour of a particular range or not at all (where the number of coordination shells increase with the range specified). The findings then have to be corrected for the finite z dimension. This is more efficient than searching through $N \times N$ interactions, however, increasing the number of neighbours, increases the equilibration time and has meant a compromise on system sizes in some of the projects. It was also therefore necessary to run most of the simulations using a supercomputer. Modifications to the code also included the ability to use more than one spin dimensionality in one system and to make observations of physical properties for each monolayer in a multilayered system. My code development for each project is summarised in appendix A.

All the simulations conducted on the systems presented in this thesis were carried out using the Monte Carlo method together with the Metropolis algorithm. This is because it is able to efficiently sample large systems and can be suited to sample according to the Boltzmann distribution through importance sampling, finding the lowest energy state (discussed in chapter 3). In most instances, single spin flip dynamics were implemented. However, the limitations of this method are quickly noticed and obtaining metastable states in systems with frustration are prevalent. An occurrence was noted when running the simulations for the system presented in chapter 4, where heating and cooling the sample from the starting configuration showed a discrepancy in the results. It was only with longer equilibration times that the results from heating finally coincided with those from cooling the sample, hence cooling was used to simulate the final results. The use of the Worm algorithm (multiple spin flip dynamics) in chapter 4 by collaborators was used as another solution to avoiding metastable states.

More studies are required in the field of long range direct exchange interactions with a power law decay of attractive interactions ($r^{-(d+\sigma)}$). There seem to be hardly

any recent studies on the consequences of different σ in more complex systems (i.e. for higher spin dimensionalities $n > 1$ and spatial dimensionalities $d > 2$) and also numerical studies on how this changes with the range of interactions. I have shown $2d$ XY results relating T_c with the range for $\sigma = 1$ by an exponent which seems to be the β exponent for the $2d$ XY universality class (see figure 5.8). This is apparently largely as a coincidence of the range of interactions not being sufficient. Additionally since the theoretical results of the magnetic multilayers did not agree perfectly with the experimental results, mainly as a consequence of the range being insufficient, then it would be worthwhile finding the critical range of interactions along with σ that would best imitate the experiment without requiring an infinite range of interactions. Completing this knowledge is clearly important in proximity effects where I have shown that some features would not be observable without further ranged interactions.

The monopole crystal presented in chapter 4 has been an interesting venture, which I would hope to see realised experimentally. As discussed at the end of chapter 4, there are a few methods proposed in which to experimentally create a monopole filled pyrochlore system, however, most of these methods constrain spins in specific, preferred directions, which is problematic for the freedom of the magnetic moments to fragment and hence to observe what is seen in this thesis. Recent studies, which include double charges in the pyrochlore have shown that the best case scenario is with 50% singly charged monopoles and 30% doubly charged monopoles, known as the *staggered charge order* [327, 328], however should still show the magnetic moment fragmentation key characteristics [327]. Studies on monopole filled artificial spin ice has been somewhat more active and kagome ice could lead to greater insight in this area already demonstrating monopole crystallites with simultaneous spin disorder [253, 329].

Appendices

Appendix A

Code development summary

A.1 For chapter 4

Monte Carlo methods with a combination of single spin flip dynamics and the worm algorithm were used in most of the simulations relevant to chapter 4. Existing Fortran 90 code created by Jaubert included a Monte Carlo method with single spin flip dynamics, which specifically kept track of the charges on the diamond lattice, the Landau energy and ensured the formation of doubly charged diamond sites were forbidden. My contribution to this project has been to manipulate this code and include the evaluation of the density of monopoles, the order parameter, the heat capacity and the spin and charge autocorrelation functions. With my preliminary results using single spin flip dynamics, we decided that the density and order parameter of the monopoles as shown in figures 4.3 and 4.5 should be generated using the worm algorithm at low temperatures. I simulated and created the phase diagrams in figure 4.6 and the autocorrelation functions in figures 4.9-4.11.

A.2 For chapters 5 and 6

Existing C++ code created by Banks was used and modified to simulate the multilayer systems in chapters 5 and 6. The relevant sections of the existing Monte Carlo code had incorporated hypercubic lattices with periodic boundaries, single spin flip dynamics and

nearest neighbour interactions. I have modified this code by ensuring a finite boundary in the z direction using a “dummy” layer, which is to set a single layer of spins with $S = 0$ and $J = 0$. Therefore any spin coupling with this layer will effectively not have an interaction. I have also included further range interactions with a power law decay in interaction strength dependent on r . The range is specified by the user in the input file, whilst the code automatically finds the relevant spins within that range. Since all the systems I use in these projects are modelled as simple cubic, then an appropriate maximum concentric shell is chosen for each spin given the range and then only the spins within this shell and smaller are sampled to be neighbours of that spin. The finite and periodic boundaries complicate this method. Once a list of the neighbours for each spin is found, dependent on r , then I ensured that the energy evaluation and updates also included the use of further range interactions.

I incorporated a parameter that enabled one to use more than one spin type in the same system, which could be specified in the input file by the user. This parameter was specific to the species in the input file and would set one or more of the spin dimensions to zero. Additionally, the order parameter and susceptibility could only be evaluated for an average of the entire system in the original code; I modified this so one could evaluate the order parameter and susceptibility of each layer and hence the use of a supercomputer was required in order to handle so much data. The further the range, the longer the simulations for each temperature and therefore, simulations for each temperature were run in parallel for large system sizes.

Appendix B

Equilibration of the energy in Monte Carlo simulations

It is necessary to ensure that all the systems used in this thesis have been equilibrated before running any of the simulations. To determine this, I plot the energy of the system as a function of Monte Carlo time and determine when the energy is constant. Once this is known, then the equilibration time, t_{eq} and the observation time, t_{obs} must be longer than this. The following sections indicate the energy equilibration time for each of the systems investigated in this thesis.

B.1 Equilibration in the modified spin ice system

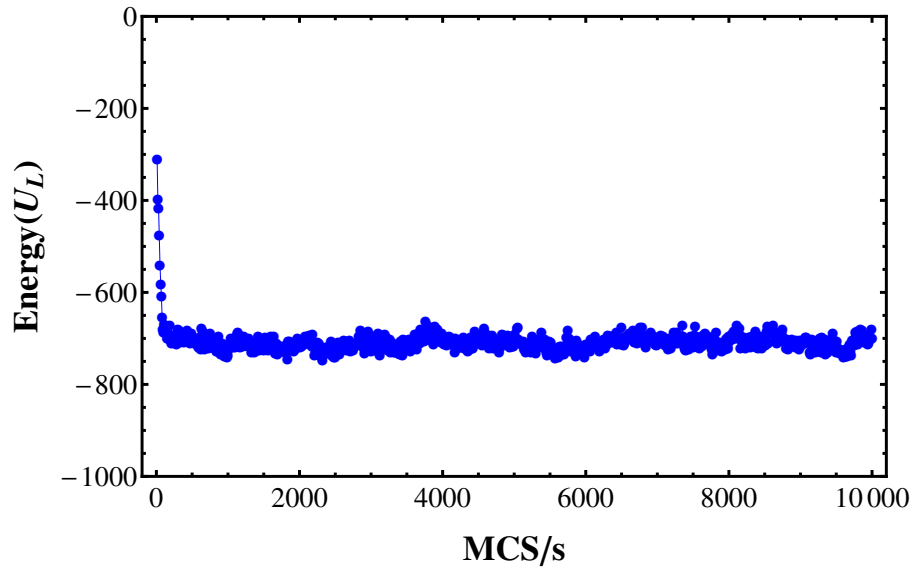


Figure B.1: Equilibration of the Landau energy, U_L , as a function of Monte Carlo steps per spin, MCS/s for the monopole crystal system. This result is found for $L = 5$, $T^* = 0.20$ and $\mu^* = 0.57$. From this result I assume that $t_{eq} = 10^4$ MCS/s is sufficient for the simulations in chapter 4, though I do vary the system size depending on the measurement.

B.2 Equilibration in the magnetic multilayer systems

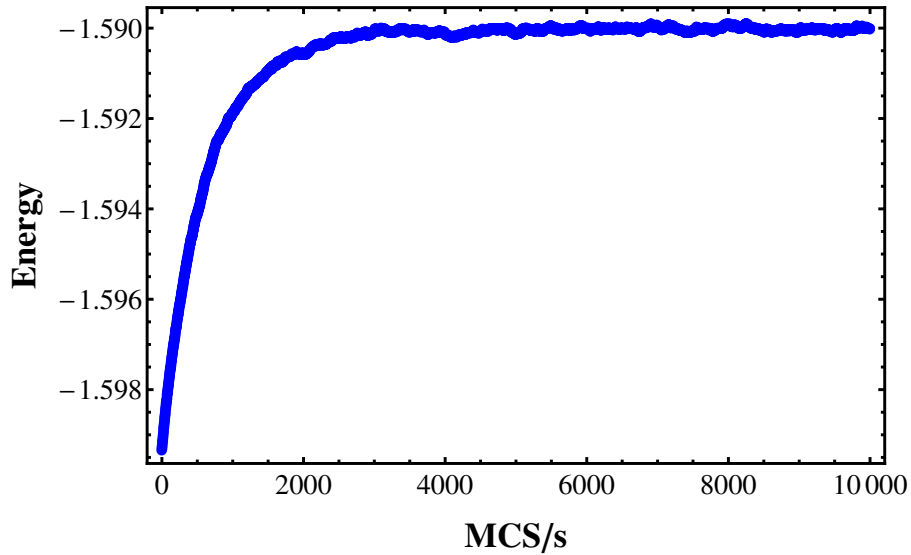


Figure B.2: Equilibration of the energy per spin as a function of Monte Carlo steps per spin, MCS/s for the double proximity multilayer in chapter 5. This result is found for ABA system size $32 \times 32 \times 21$ with $J_{AA} = 0.25$, $J_{BB} = 1$ and $J_{AB} = 0.45$, thickness of both A slabs: $L_A = 10$ and thickness of B layer: $L_B = 1$. The temperature was $T/J_{BB} = 0.01$. From this result I assume that $t_{eq} = 10^4$ MCS/s is sufficient for the simulations in chapter 5.

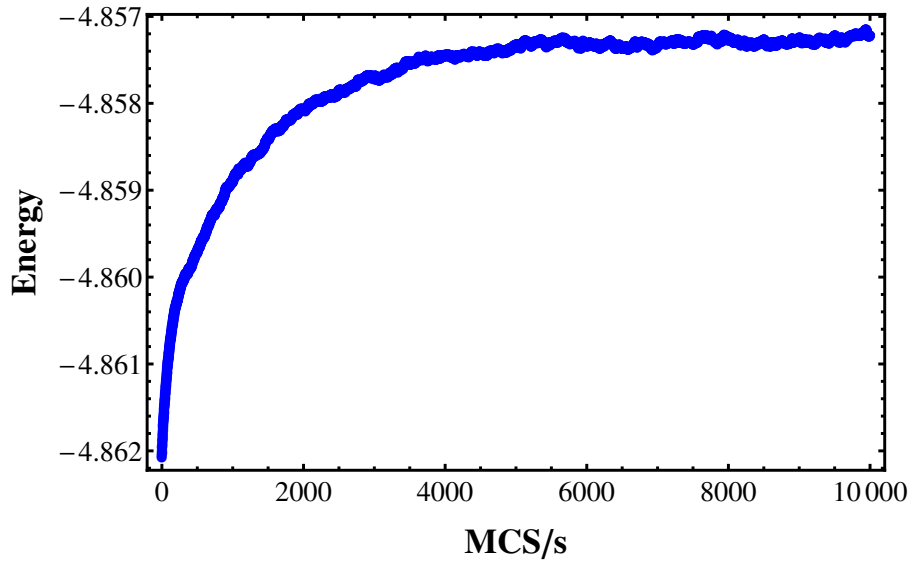


Figure B.3: Equilibration of the energy per spin as a function of Monte Carlo steps per spin, MCS/s for the exchange spring multilayer in chapter 6. This result is found for BAC system size $32 \times 32 \times 29$ of spins with $J_{AA} = 0.55$, $J_{BB} = 1$, $J_{CC} = 1$, $J_{AB} = 0.60$ and $J_{AC} = 0.60$, thickness of B slab: $L_B = 8$, thickness of A slab: $L_A = 10$ and thickness of C slab: $L_C = 10$ at $T/J_{CC} = 0.01$. From this result I assume that $t_{eq} = 10^4$ MCS/s is sufficient for the simulations in chapter 6.

Appendix C

Neutron scattering theory

To explain the background of neutron scattering this report will follow the account of Furrer [330]. The fundamental result of neutron scattering is finding the probability that the incident beam of neutrons, with a wave vector \mathbf{k} , is scattered with a new wavevector \mathbf{k}' . A wavevector, \mathbf{Q} is defined as the difference between the wavevectors of the neutron before and after scattering:

$$\mathbf{Q} = \mathbf{k} - \mathbf{k}' \quad (\text{C.1})$$

Where \mathbf{Q} is the scattering vector in reciprocal space, \mathbf{k} and \mathbf{k}' are wavevectors such that $k = 2\pi/\lambda$ and λ is the wavelength. Since the incident wavelength of the beam corresponds to the de Broglie wavelength, $\lambda = h/p$, then the momentum, p , of the neutrons can be related to the wavevector by:

$$\mathbf{p} = \hbar\mathbf{k} \quad (\text{C.2})$$

and the energy is expressed as:

$$E = \frac{\hbar^2 k^2}{2m} \quad (\text{C.3})$$

where $\hbar = h/2\pi$, h is Planck's constant and m is the mass. Therefore the energy transfer to the material upon scattering the beam of neutrons is given by:

$$\delta E = \hbar\omega = \frac{\hbar^2(k^2 - k'^2)}{2m} \quad (\text{C.4})$$

where $\omega = 2\pi f$ (i.e. $\delta E = hf$).

When $k = k'$, then $\hbar\omega = 0$ (i.e. there is no energy transfer): this is known as elastic scattering. When $\delta E \neq 0$, then this is inelastic scattering and is where,

$$\mathbf{Q} = (\mathbf{k} - \mathbf{k}') + \mathbf{q} \quad (\text{C.5})$$

where \mathbf{q} is the wavevector of an elementary excitation.

For elastic scattering, $\mathbf{Q} = \mathbf{k} - \mathbf{k}' = \tau = (4\pi \sin \theta)/\lambda$ and a coherent scattering is obtained since $\mathbf{Q} \cdot \mathbf{d} = 2\pi n$, where n is an integer [3]. Together these conditions correspond to Bragg's law, which is:

$$n\lambda = 2d \sin \theta \quad (\text{C.6})$$

where θ is the angle of incidence from the lattice and in the case of elastic scattering, the angle of reflection should be the same magnitude as the angle of incidence. $n\lambda$ indicates the path difference between the beams scattered by adjacent lattice planes with equivalent indices [331]. This determines constructive or destructive interference between plane waves.

In neutron scattering, the distribution of neutrons scattered by the sample is measured. The cross-section of scattering is dependent on the scatterer/ target. For nuclear scattering, this is dependent on the position of the lattice points, whilst for magnetic scattering, this is also dependent on the vectors of the spins [330]. The scattering cross-section, σ , is the number of neutrons scattered per second divided by the flux of the incident neutrons. The scattering information is then obtained for a small angle $d\Omega$ and for an energy transfer between $\hbar\omega$ and $\hbar(\omega+d\omega)$. Therefore, the second derivative of the cross section is taken with $d\Omega$ and $d\omega$ to find $\frac{d^2\sigma}{d\Omega d\omega}$. The reason for evaluating within an angle $d\Omega$ is because experiments can only measure a small region at any one time.

The cross section dependence on the angle and energy is most usually calculated from Fermi's "golden rule" of lowest-order time dependent perturbation theory [26].

Included in this equation, is the interaction operator, \hat{U} . For magnetic scattering this is a dipole interaction between neutrons and electrons,

$$\hat{U}_m = \hat{u} \cdot \mathbf{H} \quad (\text{C.7})$$

where \hat{u} is the magnetic moment operator of the neutron and \mathbf{H} is the magnetic field with which the neutron interacts, generated by the unpaired electrons of the material. The complexity is that this interaction of the neutron with the material needs to be considered for the initial and final states of all the magnetic atoms in the material. With mathematical manipulation, one can obtain the cross-section formula for an unpolarised beam of neutrons in terms of the spin correlation functions:

$$\frac{d\sigma}{d\Omega d\omega} = (\gamma r_0)^2 \frac{k'}{k} F^2(\mathbf{Q}) \exp\{-2W(\mathbf{Q})\} \sum_{\alpha,\beta} \left(\delta_{\alpha\beta} - \frac{Q_\alpha Q_\beta}{Q^2} \right) S^{\alpha\beta}(\mathbf{Q}, \omega) \quad (\text{C.8})$$

Where γ is the gyromagnetic ratio, r_0 is the classical electron radius, $F(\mathbf{Q})$ is the Fourier transform of the spin density, otherwise known as the form factor; $\exp\{-2W(\mathbf{Q})\}$ is the Debye-Waller factor, α and β correspond to the x, y, z cartesian coordinates and $S^{\alpha\beta}(\mathbf{Q}, \omega)$ is the static magnetic scattering function which contains the pair correlation function calculated in simulations. It is also defined as [3]:

$$S^{\alpha\beta}(\mathbf{Q}) = \frac{1}{N} \langle \mathbf{M}^\alpha(\mathbf{Q}) \cdot \mathbf{M}^\beta(-\mathbf{Q}) \rangle \quad (\text{C.9})$$

where,

$$\mathbf{M}(\mathbf{Q}) = \sum_r \mathbf{S}_r \exp(i\mathbf{Q} \cdot \mathbf{r}) \quad (\text{C.10})$$

A neutron scattering event is characterised by (\mathbf{Q}, ω) where Q gives us information about the miller indices of the material (hkl) and ω gives us information about the energy as previously shown in equation C.4. The $\left(\delta_{\alpha\beta} - \frac{Q_\alpha Q_\beta}{Q^2} \right)$ term in equation C.8 indicates that the neutrons can only couple to the magnetic moments which are perpendicular to \mathbf{Q} . If \mathbf{Q} is parallel to the neutron spin direction ($\mathbf{Q} \parallel \hat{u}$), then no magnetic scattering will be observed, but if the neutron spin direction has a non-zero perpendicular component ($\mathbf{Q} \perp \hat{u}$), then magnetic scattering will be observed. For an ordered antiferromagnet, each plane of ordered spins will only have nuclear scattering since

$\mathbf{Q} \parallel \hat{u}$, whilst between magnetic planes $\mathbf{Q} \perp \hat{u}$.

From Bragg's law, it is necessary to know the lattice planes of the material and therefore to define the axes and the positions of the lattice sites/ vectors of the magnetic moments. In real space the sites are given by positions (r) [3]:

$$\mathbf{r} = m\mathbf{a} + n\mathbf{b} + p\mathbf{c}. \quad (\text{C.11})$$

The lattice basis vectors are \mathbf{a} , \mathbf{b} and \mathbf{c} , whilst m , n and p are integers. These positions in reciprocal space, which is achieved by a Fourier transform of the real space and is how results are produced in neutron scattering, have sites at positions (R):

$$\mathbf{R} = h\mathbf{A} + k\mathbf{B} + l\mathbf{C} \quad (\text{C.12})$$

where in the same way h , k and l are integers and are the miller indices of a crystal.

Appendix D

Proximity effects in the strong/weak coupled trilayer: beyond the monolayer

Figure D.1 shows results of the ABA trilayer with an increased B layer thickness. This is for a $HA : XB : HA$ system with (10:5:10) compared with the original (10:1:10) trilayer. The results in figure D.1 (a), do not show a low temperature feature “bump” as there was in figure 5.16. This feature representing the decoupling region, implied that there was an increase in effective thickness in the B layer, however, in this case the β exponent is now $\beta = 0.33$ for monolayer 0 (representative of $3d$ behaviour), which corresponds to a different universality class from the previous $\beta = 0.25$ in the 10:1:10 system (representative of a $2d$ system). It can be shown in experiments also that without the increase in effective thickness or in actual thickness, the B layer is otherwise two dimensional. An example is in δ -doped Pd(Fe) [288], whereby an increase from 0.5 ML to 1 ML of Fe shows a crossover in the spin dimensionality of the Fe, by the polarisation in the neighbouring palladium layers causing an increase in effective thickness of Fe.

The B spins in the 10:5:10 system are in a $3d$ XY environment rather than just an “effective” environment as in the 10:1:10 system caused by the induced A monolayers. As a result, there is a large difference in the transition temperatures of the B layer

comparing the 10:1:10 system ($T_c = 2.17$) and of the average of the B layers in the 10:5:10 system ($T_c = 4.80$). The increase in transition temperature of the B layers is shown to affect the A layers very little (see figure D.1 (b)).

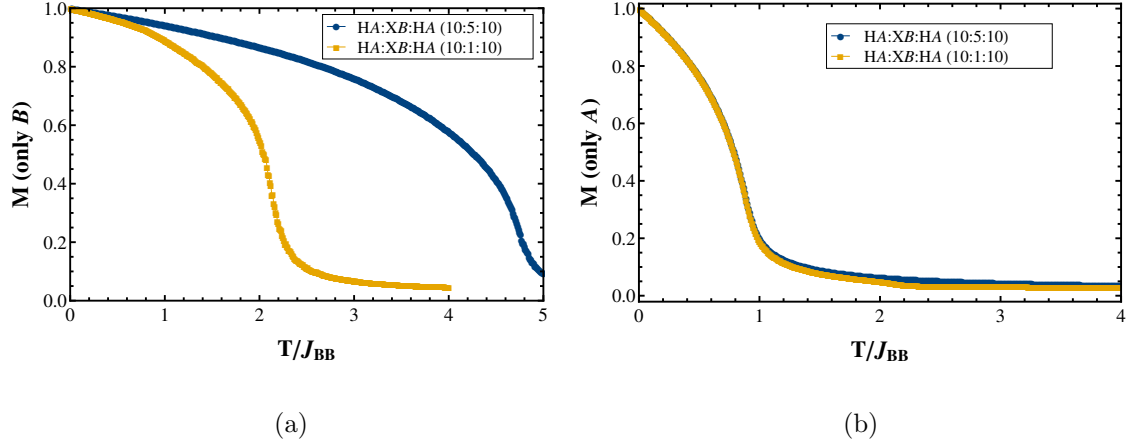


Figure D.1: (a) Average M vs T/J_{BB} of the B layer in the trilayers HA:XB:HA (10:1:10) and (10:5:10) with $J_{AB} = 0.45$. (b) The average M vs T/J_{BB} for one A layer in the respective trilayer systems.

This means the A monolayers neighbouring the 5 B monolayers most likely still behave like XY B spins as shown before, however, their effect of changing the spin dimensionality in B does not occur because the increased thickness of the B layer ensures a $3d$ XY behaviour to begin with.

References

- [1] S. Blundell. *Magnetism in condensed matter*. OUP, 7th edition, pages 1–6, 74–81, 115–116, 122–126, 140–157, 2008.
- [2] C. Kittel. *Introduction to Solid State physics*. John Wiley and Sons Inc., 7th edition, pages 61–63, 305–308, 463–466, 644–647, 1996.
- [3] A. Harman-Clarke. *Topological constraints and ordering in model frustrated magnets/Contraintes topologiques et ordre dans les systèmes modèle pour le magnétisme frustré*. PhD thesis, University College London, 2012.
- [4] A. I. M. Rae. *Quantum Mechanics*. CRC Press, 5th edition, page 132, 2007.
- [5] B. Odom, D. Hanneke, B. D’Urso, and G. Gabrielse. New measurement of the electron magnetic moment using a one-electron quantum cyclotron. *Phys. Rev. Lett.*, 97:030801, 2006.
- [6] R. Boča. *Theoretical Foundations of Molecular Magnetism*. Current Methods in Inorganic Chemistry. Elsevier Science, page 347, 1999.
- [7] J. Stöhr and H. C. Siegmann. *Magnetism: From Fundamentals to Nanoscale Dynamics*. Springer Series in Solid-State Sciences. Springer Berlin Heidelberg, pages 172–176, 2007.
- [8] G. Cappellini, M. Mancini, G. Pagano, P. Lombardi, L. Livi, M. Siciliani de Cumis, P. Cancio, M. Pizzocaro, D. Calonico, F. Levi, C. Sias, J. Catani, M. Inguscio, and L. Fallani. Direct observation of coherent inter-orbital spin-exchange dynamics. *Phys. Rev. Lett.*, 113:120402, 2014.

-
- [9] M. Gitterman. *Phase Transitions: Modern Applications*. World Scientific Publishing Co Pte Ltd, 2nd edition edition, pages 1,9,15–16, 2013.
- [10] M. J. Oliveira. *Equilibrium Thermodynamics*. Graduate Texts in Physics. Springer Berlin Heidelberg, page 106, 2014.
- [11] S. J. Blundell and K. M. Blundell. *Concepts in Thermal Physics*. OUP Oxford, page 320, 2010.
- [12] J. M. Yeomans. *Statistical Mechanics of Phase Transitions*. Clarendon Press, pages 22,102, 1992.
- [13] H. B. Callen. *Thermodynamics and an Introduction to Thermostatistics*. Wiley, pages 222–223,257–258,261–265, 1985.
- [14] L. D. Landau and E. M. Lifshitz. *Statistical Physics*. Number v. 5. Elsevier Science, pages 446–511, 2013.
- [15] J. J. Binney, N. J. Dowrick, A. J. Fisher, and M. E. J. Newman. *The Theory of Critical Phenomena: An Introduction to the Renormalization Group*. Oxford Science Publ. Clarendon Press, pages 9–11, 1992.
- [16] W. Bietenholz, M. Bögli, F. Niedermayer, M. Pepe, F. G. Rejón-Barrera, and U. J. Wiese. Topological lattice actions for the 2d XY model. *Journal of High Energy Physics*, 2013(3):1–23, 2013.
- [17] P. Davies. *The New Physics*. Cambridge University Press, page 213, 1992.
- [18] M. E. J. Newman and G. T. Barkema. *Monte Carlo Methods in Statistical Physics*. Clarendon Press, pages 5–17,31–42,51,82, 1999.
- [19] R. Erdem and G. Gülpnar. *Nonequilibrium Thermodynamics of Ising Magnets, Thermodynamics - Systems in Equilibrium and Non-Equilibrium*.
- [20] M. Ahlberg. *Critical Phenomena and Exchange Coupling in Magnetic Heterostructures*. PhD thesis, 2012.

-
- [21] M. Tuckerman. *Magnetic systems and the Ising model and Overview of critical phenomena (1999)*. Date accessed: 07/10/2014. http://www.nyu.edu/classes/tuckerman/stat.mech/lectures/lecture_25/node3.html and http://www.nyu.edu/classes/tuckerman/stat.mech/lectures/lecture_25/node1.html.
- [22] T. Kaneyoshi. *Introduction to Surface Magnetism*. Taylor & Francis, pages 119–120, 1990.
- [23] P. Atkins and J. de Paula. *Atkins' Physical Chemistry*. OUP Oxford, pages 77–81,113–117,122–123,138–139, 2010.
- [24] H.E. Stanley. *Introduction to phase transitions and critical phenomena*. International series of monographs on physics. Oxford University Press, 1st edition, pages 1–8,18–21, 1971.
- [25] S. T. Bramwell and M. J. P. Gingras. Spin ice state in frustrated magnetic pyrochlore materials. *Science*, 294(5546):1495–1501, 2001.
- [26] N. W. Ashcroft and N. D. Mermin. *Solid State Physics*. Cengage Learning India Private Limited, pages 40–45, 402–405, 702, 715–719, 759, 790–795, 2011.
- [27] M. Plischke and B. Bergersen. *Equilibrium Statistical Physics*, volume 1 of *Equilibrium Statistical Physics*. World Scientific, pages 40–43,63–65,199–209,396–400,466, 1994.
- [28] R. J. Baxter. *Exactly Solved Models in Statistical Mechanics*. Dover Books on Physics. Dover Publications, pages 11–13, 39–41, 128, 2013.
- [29] P. Weiss. L'hypothèse du champ moléculaire et la propriété ferromagnétique. *J. Phys. Theor. Appl.*, 6(1):661–690, 1907.
- [30] J. L. Cardy. *Scaling and Renormalization in Statistical Physics*. Cambridge University Press, pages 5–10, 16–21, 111–112, 1996.

-
- [31] TU Graz. *Landau theory of second order phase transitions*. http://lamp.tu-graz.ac.at/hadley/ss2/landau/second_order.php. Date accessed: 23/01/2014.
- [32] J. H. Moon, S. M. Seo, K. J. Lee, K. W. Kim, J. Ryu, H. W. Lee, R. D. McMichael, and M. D. Stiles. Spin-wave propagation in the presence of interfacial Dzyaloshinskii-Moriya interaction. *Phys. Rev. B*, 88:184404, 2013.
- [33] A. A. Tsirlin. Spin-chain magnetism and uniform Dzyaloshinsky-Moriya anisotropy in BaV_3O_8 . *Phys. Rev. B*, 89:014405, 2014.
- [34] A. Ikeda and H. Kawamura. Ordering of the pyrochlore ising model with the long-range RKKY interaction. *Journal of the Physical Society of Japan*, 77(7):073707, 2008.
- [35] A. F. Franco and H. Kachkachi. Spin configuration of magnetic multilayers: effect of exchange, dipolar and Dzyalozhinski-Moriya interactions. *Journal of Physics: Condensed Matter*, 25(31):316003, 2013.
- [36] B. Skubic, E. Holmström, D. Iuşan, O. Bengone, O. Eriksson, R. Brucas, B. Hjörvarsson, V. Stanciu, and P. Nordblad. Competing exchange interactions in magnetic multilayers. *Phys. Rev. Lett.*, 96:057205, 2006.
- [37] S. V. Grigoriev, D. Lott, Y. O. Chetverikov, A. T. D. Grünwald, R. C. C. Ward, and A. Schreyer. Interplay of RKKY, Zeeman, and Dzyaloshinskii-Moriya interactions and the nonzero average spin chirality in Dy/Y multilayer structures. *Phys. Rev. B*, 82:195432, 2010.
- [38] C. Lacroix, P. Mendels, and F. Mila. *Introduction to Frustrated Magnetism: Materials, Experiments, Theory*. Springer Series in Solid-State Sciences. Springer, pages 70, 184, 284–285, 298, 316, 2011.
- [39] K. H. Fischer and J. A. Hertz. *Spin Glasses*. Cambridge Studies in Magnetism. Cambridge University Press, page 180, 1993.

-
- [40] K. Matan, B. M. Bartlett, J. S. Helton, V. Sikolenko, S. Mat'aš, K. Prokeš, Y. Chen, J. W. Lynn, D. Grohol, T. J. Sato, M. Tokunaga, D. G. Nocera, and Y. S. Lee. Dzyaloshinskii-moriya interaction and spin reorientation transition in the frustrated kagome lattice antiferromagnet. *Phys. Rev. B*, 83:214406, 2011.
- [41] R. Wiesendanger. <http://www.nanoscience.de/nanojoom/index.php/en/research/current-topics/noncollinear-spins/94-noncollinear-spins.html>. Date accessed: 14/01/2015.
- [42] D. Khomskii. *Transition Metal Compounds*. Cambridge University Press, pages 146–148, 2014.
- [43] H. Tashiro, M. Nishiyama, A. Oyamada, T. Itou, S. Maegawa, M. Yano, T. Ono, and H. Tanaka. Effect of DM interaction in a quantum antiferromagnet on a deformed kagome lattice, $\text{Rb}_2\text{Cu}_3\text{SnF}_{12}$. *Journal of Physics: Conference Series*, 320(1):012052, 2011.
- [44] D. C. Mattis. *The Theory of Magnetism Made Simple: An Introduction to Physical Concepts and to Some Useful Mathematical Methods*. World Scientific, page 395, 2006.
- [45] J. B. Parkinson and D. J. J. Farnell. *An Introduction to Quantum Spin Systems*. Lecture Notes in Physics. Springer, pages 7–13, 2010.
- [46] J. M. D. Coey. *Magnetism and Magnetic Materials*. Cambridge University Press, pages 9,168–172, 2010.
- [47] U. R. Alim, A. Entezari, and T. Moeller. The Lattice-Boltzmann Method on Optimal Sampling Lattices. *IEEE Transactions on Visualization and Computer Graphics*, 15(4):630–641, 2009.
- [48] E. Ising. Beitrag zur theorie des ferromagnetismus. *Zeitschrift fur Physik*, 31:253–258, 1925.

-
- [49] S. T. Bramwell and P. C. W. Holdsworth. Magnetization and universal sub-critical behaviour in two-dimensional XY magnets. *Journal of Physics: Condensed Matter*, 5(4):L53, 1993.
- [50] J. C. Le Guillou and J. Zinn-Justin. Critical exponents from field theory. *Phys. Rev. B*, 21:3976–3998, 1980.
- [51] M. Campostrini, M. Hasenbusch, A. Pelissetto, P. Rossi, and E. Vicari. Critical behavior of the three-dimensional XY universality class. *Phys. Rev. B*, 63:214503, 2001.
- [52] M. Campostrini, M. Hasenbusch, A. Pelissetto, P. Rossi, and E. Vicari. Critical exponents and equation of state of the three-dimensional Heisenberg universality class. *Phys. Rev. B*, 65:144520, 2002.
- [53] A. Piróth and J. Sólyom. *Fundamentals of the Physics of Solids: Volume 1: Structure and Dynamics*. Fundamentals of the Physics of Solids. Springer London, pages 551–557, 2007.
- [54] M. Ferer, M. A. Moore, and M. Wortis. Critical Indices and Amplitudes of Classical Planar Models in Finite Field for Temperatures Greater than T_c . *Phys. Rev. B*, 8:5205–5212, 1973.
- [55] P. M. Chaikin and T. C. Lubensky. *Principles of Condensed Matter Physics*. Cambridge University Press, pages 542–546, 2000.
- [56] N. D. Mermin and H. Wagner. Absence of ferromagnetism or antiferromagnetism in one- or two-dimensional isotropic Heisenberg models. *Phys. Rev. Lett.*, 17:1133–1136, 1966.
- [57] L. Onsager. Crystal Statistics. I. A Two-Dimensional Model with an Order-Disorder Transition. *Phys. Rev.*, 65:117–149, 1944.
- [58] T. Horiguchi. A spin-one Ising model on a honeycomb lattice. *Phys. Lett. A*, 113(8):425 – 428, 1986.

-
- [59] T. Morita. Exactly Solved Two-Dimensional Ising Model with Spin S Greater than $1/2$. *Journal of the Physical Society of Japan*, 62(12):4218–4223, 1993.
- [60] S. Henneberger, E. Frey, P. G. Maier, F. Schwabl, and G. M. Kalvius. Critical dynamics of a uniaxial and dipolar ferromagnet. *Phys. Rev. B*, 60:9630–9649, 1999.
- [61] W. Low and H. Ehrenreich. *Solid State Physics*, volume 2. Elsevier Science, pages 113–122, 1956.
- [62] O. Lavrentovich and North Atlantic Treaty Organization (Scientific Affairs Division). *Defects in Liquid Crystals: Computer Simulations, Theory and Experiments: Computer Simulations, Theory, and Experiments*. Springer Netherlands, page 4, 2001.
- [63] S. Komineas. Rotating Vortex Dipoles in Ferromagnets. *Phys. Rev. Lett.*, 99:117202, 2007.
- [64] J. M. Kosterlitz and D. J. Thouless. Ordering, metastability and phase transitions in two-dimensional systems. *Journal of Physics C: Solid State Physics*, 6(7):1181, 1973.
- [65] P. Archambault, S. T. Bramwell, and P. C. W. Holdsworth. Magnetic fluctuations in a finite two-dimensional XY model. *Journal of Physics A: Mathematical and General*, 30(24):8363, 1997.
- [66] S. V. Maleev. Dipole forces in two-dimensional and layered ferromagnets. *Sov. Phys. JETP*, 43(6):1240 – 1247, 1976.
- [67] L. A. S. Mól and B. V. Costa. Phase transition in the two-dimensional dipolar planar rotator model. *Journal of Physics: Condensed Matter*, 22(4):046005, 2010.
- [68] S. Teitel and C. Jayaprakash. Phase transtions in frustrated two-dimensional XY models. *Phys. Rev. B*, 27:598–601, 1983.

-
- [69] P. G. Maier and F. Schwabl. Novel phase transition in two-dimensional XY -models with long-range interaction. *Condensed Matter Physics*, 8(1):103–111, 2005.
- [70] P. G. Maier and F. Schwabl. Ferromagnetic ordering in the two-dimensional dipolar XY model. *Phys. Rev. B*, 70:134430, 2004.
- [71] M. Ahlberg, P. Korelis, G. Andersson, and B. Hjörvarsson. Effect of ferromagnetic proximity on critical behavior. *Phys. Rev. B*, 85(22):224425, 2012.
- [72] H. T. Diep. *Frustrated Spin Systems*. World Scientific Publishing Company, Incorporated, pages 369, 381, 393–398, 419–423, 2004.
- [73] K. Lenz, S. Zander, and W. Kuch. Magnetic proximity effects in antiferromagnet/ferromagnet bilayers: The impact on the néel temperature. *Phys. Rev. Lett.*, 98:237201, 2007.
- [74] M. Kiwi. Origin of the magnetic proximity effect. In *Symposia Q/R—Magnetoelectronics—Novel Magnetic Phenomena in Nanostructures—Advanced Characterization of Artificially Structured Magnetic Materials*, volume 746 of *MRS Proceedings*, 2002.
- [75] D. Liu, Y. Hu, H. Guo, and X. F. Han. Magnetic proximity effect at the molecular scale: First-principles calculations. *Phys. Rev. B*, 78:193307, 2008.
- [76] I. Vobornik, U. Manju, J. Fujii, F. Borgatti, P. Torelli, D. Krizmancic, Y. S. Hor, R. J. Cava, and G. Panaccione. Magnetic proximity effect as a pathway to spintronic applications of topological insulators. *Nano Letters*, 11(10):4079–4082, 2011.
- [77] V. Kapaklis, U. B. Arnalds, A. Harman-Clarke, E. Th Papaioannou, M. Karimipour, P. Korelis, A. Taroni, P. C. W. Holdsworth, S. T. Bramwell, and B. Hjörvarsson. Melting artificial spin ice. *New Journal of Physics*, 14(3):035009, 2012.

-
- [78] S. Krongelb. *Magnetic Materials Processes and Devices 11*. Number 34 in ECS transactions. Electrochemical Society, 2011.
- [79] T. Ono, H. Miyajima, K. Shigeto, and T. Shinjo. Magnetization reversal in submicron magnetic wire studied by using giant magnetoresistance effect. *Applied Physics Letters*, 72(9):1116–1117, 1998.
- [80] L. You, R. C. Sousa, S. Bandiera, B. Rodmacq, and B. Dieny. Co/Ni multilayers with perpendicular anisotropy for spintronic device applications. *Applied Physics Letters*, 100(17):172411, 2012.
- [81] N. D. Rizzo, M. DeHerrera, J. Janesky, B. Engel, J. Slaughter, and S. Tehrani. Thermally activated magnetization reversal in submicron magnetic tunnel junctions for magnetoresistive random access memory. *Applied Physics Letters*, 80(13), 2002.
- [82] M. T. Johnson, P. J. H. Bloemen, F. J. A. den Broeder, and J. J. de Vries. Magnetic anisotropy in metallic multilayers. *Reports on Progress in Physics*, 59(11):1409, 1996.
- [83] G. Asti, M. Carbucicchio, M. Ghidini, M. Rateo, G. Ruggiero, M. Solzi, F. DORazio, and F. Lucari. Microstructural and magnetic properties of exchange-coupled Co/Fe multilayers. *Journal of Applied Physics*, 87(9), 2000.
- [84] R. Bali, B. B. Nelson-Cheeseman, A. Scholl, E. Arenholz, Y. Suzuki, and M. G. Blamire. Competing magnetic anisotropies in an antiferromagnet-ferromagnet-antiferromagnet trilayer. *Journal of Applied Physics*, 106(11):–, 2009.
- [85] A. Paul, N. Paul, J. Jutimoosik, R. Yimmirun, S. Rujirawat, B. Höpfner, I. Lauer-mann, M. Lux-Steiner, S. Mattauch, and P. Böni. Change in interface magnetism of an exchange-coupled system due to the presence of nonmagnetic spacers. *Phys. Rev. B*, 87:014431, 2013.
- [86] P. J. H. Bloemen, W. J. M. de Jonge, and F. J. A. den Broeder. The temperature

- dependence of the magnetization of magnetic multilayers. *Journal of Magnetism and Magnetic Materials*, 93(0):105 – 108, 1991.
- [87] P. Kappenberger, S. Martin, Y. Pellmont, H. J. Hug, J. B. Kortright, O. Hellwig, and Eric E. Fullerton. Direct imaging and determination of the uncompensated spin density in exchange-biased CoO/(CoPt) multilayers. *Phys. Rev. Lett.*, 91:267202, 2003.
- [88] S. V. Halilov, J. Henk, T. Scheunemann, and R. Feder. Model calculation of magnetic surface states in multilayer systems. *Surface Science*, 343(12):148 – 156, 1995.
- [89] R. K. Das, R. Misra, S. Tongay, R. Rairigh, and A. F. Hebard. Finite size effects with variable range exchange coupling in thin-film Pd/Fe/Pd trilayers. *Journal of Magnetism and Magnetic Materials*, 322(17):2618 – 2621, 2010.
- [90] D. Wang, J. M. Daughton, K. Bussmann, and G. A. Prinz. Magnetic properties of very thin single and multilayer NiFeCo and CoFe films deposited by sputtering. *Journal of Applied Physics*, 83(11):7034–7036, 1998.
- [91] G. Andersson and B. Hjörvarsson. Effects of strain on magnetic anisotropy in Fe- and Co-based heterostructures. *Phase Transitions*, 81(7-8):679–701, 2008.
- [92] L. Wei, L. Xiong-Hua, C. Wei-Bin, G. Wen-Jie, and Z. Zhi-Dong. Exchange couplings in magnetic films. *Chinese Physics B*, 22(2):027104, 2013.
- [93] A. Fert, G. Güntherodt, B. Heinrich, and E. E. Marinero. *Magnetic Thin Films, Multilayers and Superlattices*. European Materials Research Society Symposia Proceedings. Elsevier Science, 1991.
- [94] A. Chikina, M. Höppner, S. Seiro, K. Kummer, S. Danzenbächer, A. Generalov, M. Güttler, Y. Kucherenko, E. V. Chulkov, Y. M. Koroteev, K. Köpernik, C. Geibel, M. Shi, M. Radovic, C. Laubschat, and D. V. Vyalikh. Strong ferromagnetism at the surface of an antiferromagnet caused by buried magnetic moments. *Nature Communications*, 5, 2014.

-
- [95] K. Mibu and T. Shinjo. Magnetic anisotropy in Fe/rareearth multilayers. *Hyperfine Interactions*, 113(1-4):287–293, 1998.
- [96] E. Weschke, H. Ott, E. Schierle, C. Schüßler-Langeheine, D. V. Vyalikh, G. Kaindl, V. Leiner, M. Ay, T. Schmitte, H. Zabel, and P. J. Jensen. Finite-size effect on magnetic ordering temperatures in long-period antiferromagnets: Holmium thin films. *Phys. Rev. Lett.*, 93:157204, 2004.
- [97] K. Binder. Monte Carlo study of thin magnetic Ising films. *Thin Solid Films*, 20(2):367 – 381, 1974.
- [98] P. J. Jensen, H. Dreyssé, and K. H. Bennemann. Thickness dependence of the magnetization and the Curie temperature of ferromagnetic thin films. *Surface Science*, 269270(0):627 – 631, 1992.
- [99] H. S. Nalwa. *Handbook of Thin Films*, volume 5-Volume Set of *Handbook of thin film materials*. Elsevier Science, page 388, 2001.
- [100] F. Huang, M. T. Kief, G. J. Mankey, and R. F. Willis. Magnetism in the few-monolayers limit: A surface magneto-optic Kerr-effect study of the magnetic behavior of ultrathin films of Co, Ni, and Co-Ni alloys on Cu(100) and Cu(111). *Phys. Rev. B*, 49:3962–3971, 1994.
- [101] P. Chapon and P. Yvon. *Surface and thin film analysis methods*. <http://www.horiba.com/fileadmin/uploads/Scientific/Documents/Emission/GD26.pdf>. Date accessed: 07/05/2014, page 2.
- [102] A. Braun. Conversion of thickness data of thin films with variable lattice parameter from monolayers to angstroms: An application of the epitaxial bain path. *Surface Review and Letters*, 10(6):889–894, 2003.
- [103] M. T. Johnson, P. J. H. Bloemen, F. J. A. den Broeder, and J. J. de Vries. Magnetic anisotropy in metallic multilayers. *Reports on Progress in Physics*, 59(11):1409, 1996.

-
- [104] R. Wu and A. J. Freeman. Spinorbit induced magnetic phenomena in bulk metals and their surfaces and interfaces. *Journal of Magnetism and Magnetic Materials*, 200(13):498 – 514, 1999.
- [105] J. Camarero, J. J. de Miguel, A. Hernando, and R. Miranda. Effects of reduced dimensionality on the magnetic properties of ultrathin (Co/Cu)[111] films. *Journal of Applied Physics*, 89(11):7150–7152, 2001.
- [106] J. Camarero, T. Graf, J. J. de Miguel, R. Miranda, W. Kuch, M. Zharnikov, A. Dittschar, C. M. Schneider, and J. Kirschner. Surfactant-mediated modification of the magnetic properties of Co/Cu(111) thin films and superlattices. *Phys. Rev. Lett.*, 76:4428–4431, 1996.
- [107] E. Weschke, E. Schierle, H. Ott, C. Schüßler-Langeheine, and G. Kaindl. *Magnetic structures and phase transitions in nanostructured materials*. Freie Universität Berlin, page 55.
- [108] E. L. Lee, P. E. Bolduc, and C. E. Violet. Magnetic ordering and critical thickness of ultrathin iron films. *Phys. Rev. Lett.*, 13:800–802, 1964.
- [109] C. Domb. Critical temperature of finite systems in d dimensions. *Journal of Physics A: Mathematical, Nuclear and General*, 6(9):1296, 1973.
- [110] J. T. Ou, W. Lai, D. L. Lin, and F. Lee. Interface effects on the critical temperature of heterostructures of magnetic films. *Journal of Physics: Condensed Matter*, 9(18):3687, 1997.
- [111] H. J. Elmers, J. Hauschild, G. H. Liu, and U. Gradmann. Critical phenomena in the two-dimensional XY magnet Fe(100) on W(100). *Journal of Applied Physics*, 79(8), 1996.
- [112] M. E. McHenry, M. A. Willard, and D. E. Laughlin. *Amorphous and Nanocrystalline Materials for Applications as Soft Magnets*. Progress in materials science. Pergamon, page 387, 1999.

-
- [113] W. R. Branford, S. Ladak, D. E. Read, K. Zeissler, and L. F. Cohen. Emerging Chirality in Artificial Spin Ice. *Science*, 335(6076):1597–1600, 2012.
- [114] P. Korelis. *Uncovering Magnetic Order in Nanostructured Disordered Materials: A Study of Amorphous Magnetic Layered Structures*. Uppsala Universitet, Uppsala, pages 17–18,36–38,96, 2011.
- [115] A. J. Freeman, H. Krakauer, S. Ohnishi, D. S. Wang, M. Weinert, and E. Wimmer. Magnetism at surfaces and interfaces. *Journal of Magnetism and Magnetic Materials*, 38(3):269 – 272, 1983.
- [116] A. J. Freeman. Electronic structure and magnetism of surfaces and interfaces. *Journal of Magnetism and Magnetic Materials*, 35(13):31 – 36, 1983.
- [117] S. V. Halilov, J. Henk, T. Scheunemann, and R. Feder. Surface states and photoemission of magnetic multilayer systems. *Phys. Rev. B*, 52:14235–14244, 1995.
- [118] J. M. Wesselinowa. Influence of magnetic surface anisotropy on the dynamic properties in ferromagnetic thin films. *Journal of Physics: Condensed Matter*, 18(35):8169, 2006.
- [119] M. G. Cottam and D. R. Tilley. *Introduction to Surface and Superlattice Excitations*. page 91, 1989.
- [120] L. Liu, W. Sheng, J. Bai, J. Cao, Y. Lou, Y. Wang, F. Wei, and J. Lu. Magnetic properties and magnetization reversal process of L1₀ FePt/Fe bilayers magnetic thin films. *Applied Surface Science*, 258(20):8124 – 8127, 2012.
- [121] P. Srivastava, F. Wilhelm, A. Ney, M. Farle, H. Wende, N. Haack, G. Ceballos, and K. Baberschke. Magnetic moments and Curie temperatures of Ni and Co thin films and coupled trilayers. *Phys. Rev. B*, 58:5701–5706, 1998.
- [122] J. S. Jiang, Eric E. Fullerton, M. Grimsditch, C. H. Sowers, and S. D. Bader. Exchange-spring behavior in epitaxial hard/soft magnetic bilayer films. *Journal of Applied Physics*, 83(11), 1998.

-
- [123] M. Labruno and H. Niedoba. Dipolar coupling effect in magnetic bilayer system. *The European Physical Journal B - Condensed Matter and Complex Systems*, 27(1):103–109, 2002.
- [124] E. Talbot, D. Ledue, and P. E. Berche. Magnetization reversal in amorphous Fe/Dy multilayers: A Monte Carlo study. *Journal of Applied Physics*, 106(2):–, 2009.
- [125] K. C. Schuermann, J. D. Dutson, S. Z. Wu, S. D. Harkness, B. Valcu, H. J Richter, R. W. Chantrell, and K. O’Grady. Exchange-coupling effects in perpendicular composite materials. *Journal of Applied Physics*, 99(8):08Q904–08Q904–3, 2006.
- [126] M. Gierlings, M. J. Prandolini, M. Gruyters, T. Funk, D. Riegel, and W. D. Brewer. A study of the induced magnetism in the Au spacer layer of Co/Au/CoO exchange-bias trilayers and related systems. *The European Physical Journal B - Condensed Matter and Complex Systems*, 45(1):137–146, 2005.
- [127] U. Bovensiepen, F. Wilhelm, P. Srivastava, P. Pouloupoulos, M. Farle, A. Ney, and K. Baberschke. Two susceptibility maxima and element specific magnetizations in indirectly coupled ferromagnetic layers. *Phys. Rev. Lett.*, 81:2368–2371, 1998.
- [128] W. E. Bailey, A. Ghosh, S. Auffret, E. Gautier, U. Ebels, F. Wilhelm, and A. Rogalev. Pd magnetism induced by indirect interlayer exchange coupling. *Phys. Rev. B*, 86:144403, 2012.
- [129] W. L. Lim, N. Ebrahim-Zadeh, J. C. Owens, H. G. E. Hentschel, and S. Urazhdin. Temperature-dependent proximity magnetism in Pt. *Applied Physics Letters*, 102(16):162404–162404–4, 2013.
- [130] A. F. Kravets, A. N. Timoshevskii, B. Z. Yanchitsky, M. A. Bergmann, J. Buhler, S. Andersson, and V. Korenivski. Temperature-controlled interlayer exchange coupling in strong/weak ferromagnetic multilayers: A thermomagnetic Curie switch. *Phys. Rev. B*, 86:214413, 2012.

-
- [131] B. Y. Wang, C. C. Chiu, W. C. Lin, and M. T. Lin. Enhanced perpendicular magnetic anisotropy in Fe/Mn bilayers by incorporating ultrathin ferromagnetic underlayer through magnetic proximity effect. *Applied Physics Letters*, 103(4):–, 2013.
- [132] Q. L. Lv, J. W. Cai, S. L. He, and L. Sun. Perpendicular magnetic anisotropy and magnetic proximity effect in $\text{Pt}_{1-\delta}\text{Fe}_\delta/\text{Co}$ multilayer films. *Journal of Magnetism and Magnetic Materials*, 323(5):465 – 470, 2011.
- [133] U. Köbler and R. Schreiber. Exploring the $2d$ to $3d$ dimensionality crossover in thin iron films. *Journal of Magnetism and Magnetic Materials*, 300(2):519–524, 2006.
- [134] Yi Li and K. Baberschke. Dimensional crossover in ultrathin Ni(111) films on W(110). *Phys. Rev. Lett.*, 68:1208–1211, 1992.
- [135] P. Schilbe, S. Siebentritt, and K. H. Rieder. Monte carlo calculations on the dimensional crossover of thin ising films. *Phys. Lett. A*, 216(15):20 – 25, 1996.
- [136] E. Th Papaioannou, V. Kapaklis, A. Taroni, M. Marcellini, and B. Hjörvarsson. Dimensionality and confinement effects in δ -doped Pd(Fe) layers. *Journal of Physics: Condensed Matter*, 22(23):236004, 2010.
- [137] P. W. Anderson. Ordering and antiferromagnetism in ferrites. *Phys. Rev.*, 102:1008–1013, 1956.
- [138] T. Fennell, P. P. Deen, A. R. Wildes, K. Schmalzl, D. Prabhakaran, A. T. Boothroyd, R. J. Aldus, D. F. McMorrow, and S. T. Bramwell. Magnetic Coulomb Phase in the Spin Ice $\text{Ho}_2\text{Ti}_2\text{O}_7$. *Science*, 326(5951):415–417, 2009.
- [139] L. Hozoi, H. Gretarsson, J. P. Clancy, B.-G. Jeon, B. Lee, K. H. Kim, V. Yushankhai, Peter Fulde, D. Casa, T. Gog, Jungho Kim, A. H. Said, M. H. Upton, Y. J. Kim, and J. van den Brink. Longer-range lattice anisotropy strongly competing with spin-orbit interactions in pyrochlore iridates. *Phys. Rev. B*, 89:115111, 2014.

-
- [140] S. Rosenkranz, A. P. Ramirez, A. Hayashi, R. J. Cava, R. Siddharthan, and B. S. Shastry. Crystal-field interaction in the pyrochlore magnet $\text{Ho}_2\text{Ti}_2\text{O}_7$. *Journal of Applied Physics*, 87(9):5914–5916, 2000.
- [141] D. Pomaranski, L. R. Yaraskavitch, S. Meng, K. A. Ross, H. M. L. Noad, H. A. Dabkowska, B. D. Gaulin, and J. B. Kycia. Absence of pauling’s residual entropy in thermally equilibrated $\text{Dy}_2\text{Ti}_2\text{O}_7$. *Nature Physics*, 9(6):353–356, 2013.
- [142] L. Bovo, X. Moya, D. Prabhakaran, Y. A. Soh, A. T. Boothroyd, N. D. Mathur, G. Aeppli, and S. T. Bramwell. Restoration of the third law in spin ice thin films. *Nature Communications*, 5, 2014.
- [143] D. P. Leusink, F. Coneri, M. Hoek, S. Turner, H. Idrissi, G. Van Tendeloo, and H. Hilgenkamp. Thin films of the spin ice compound $\text{Ho}_2\text{Ti}_2\text{O}_7$. *APL Materials*, 2(3), 2014.
- [144] R. Siddharthan, B. S. Shastry, A. P. Ramirez, and A. Hayashi. Ising pyrochlore magnets: low-temperature properties, “ice rules” and beyond. *Phys. Rev. Lett.*, 83(9):1854–1857, 1999.
- [145] R. F. Wang, C. Nisoli, R. S. Freitas, J. Li, W. McConville, B. J. Cooley, M. S. Lund, N. Samarth, C. Leighton, V. H. Crespi, and P. Schiffer. Artificial ‘spin ice’ in a geometrically frustrated lattice of nanoscale ferromagnetic islands. *Nature*, 446(7131):102–102, 2007.
- [146] S. Ladak, D. E. Read, G. K. Perkins, L. F. Cohen, and W. R. Branford. Direct observation of magnetic monopole defects in an artificial spin-ice system. *Nature Physics*, 6(5):359–363, 2010.
- [147] C. Nisoli, J. Li, X. Ke, D. Garand, P. Schiffer, and V. H. Crespi. Effective temperature in an interacting vertex system: Theory and experiment on artificial spin ice. *Phys. Rev. Lett.*, 105:047205, 2010.
- [148] J. P. Morgan, A. Stein, S. Langridge, and C. H. Marrows. Thermal ground-state

- ordering and elementary excitations in artificial magnetic square ice. *Nature Physics*, 7(1):75–79, 2011.
- [149] C. Phatak, M. Pan, A. K. Petford-Long, S. Hong, and M. De Graef. Magnetic interactions and reversal of artificial square spin ices. *New Journal of Physics*, 14(7):075028, 2012.
- [150] A. S. Wills, R. Ballou, and C. Lacroix. Model of localized highly frustrated ferromagnetism: the *kagomé* spin ice. *Phys. Rev. B*, 66:144407, 2002.
- [151] S. T. Bramwell and M. J. Harris. Frustration in Ising-type spin models on the pyrochlore lattice. *Journal of Physics: Condensed Matter*, 10(14):L215, 1998.
- [152] L. J. Heyderman and R. L. Stamps. Artificial ferroic systems: novel functionality from structure, interactions and dynamics. *Journal of Physics: Condensed Matter*, 25(36):363201, 2013.
- [153] K. Zeissler, S. K. Walton, S. Ladak, D. E. Read, T. Tylizszczak, L. F. Cohen, and W. R. Branford. The non-random walk of chiral magnetic charge carriers in artificial spin ice. *Scientific reports*, 3, 2013.
- [154] Y. Shen, O. Petrova, P. Mellado, S. Daunheimer, J. Cumings, and O. Tchernyshyov. Dynamics of artificial spin ice: a continuous honeycomb network. *New Journal of Physics*, 14(3):035022, 2012.
- [155] S. D. Pollard, V. Volkov, and Y. Zhu. Propagation of magnetic charge monopoles and dirac flux strings in an artificial spin-ice lattice. *Phys. Rev. B*, 85:180402, 2012.
- [156] G. M. Wysin, W. A. Moura-Melo, L. A. S. Mól, and A. R. Pereira. Dynamics and hysteresis in square lattice artificial spin ice. *New Journal of Physics*, 15(4):2, 2013.
- [157] S. Ladak, D. E. Read, W. R. Branford, and L. F. Cohen. Direct observation and control of magnetic monopole defects in an artificial spin-ice material. *New Journal of Physics*, 13(6):063032, 2011.

-
- [158] S. Ladak, D. Read, T. Tyliczszak, W. R. Branford, and L. F. Cohen. Monopole defects and magnetic coulomb blockade. *New Journal of Physics*, 13(2):023023, 2011.
- [159] J. P. Morgan, A. Stein, S. Langridge, and C. H. Marrows. Magnetic reversal of an artificial square ice: dipolar correlation and charge ordering. *New Journal of Physics*, 13(10):105002, 2011.
- [160] U. B. Arnalds, A. Farhan, R. V. Chopdekar, V. Kapaklis, A. Balan, E. Th. Papaioannou, M. Ahlberg, F. Nolting, L. J. Heyderman, and B. Hjörvarsson. Thermalized ground state of artificial kagome spin ice building blocks. *Applied Physics Letters*, 101(11):112404, 2012.
- [161] V. Kapaklis, U. B. Arnalds, A. Farhan, R. V. Chopdekar, A. Balan, A. Scholl, L. J. Heyderman, and B. Hjörvarsson. Thermal fluctuations in artificial spin ice. *Nature Nanotechnology*, 9(7):514–519, 2014.
- [162] C. Enss and S. Hunklinger. *Low-Temperature Physics*. SpringerLink: Springer e-Books. Springer, page 246, 2005.
- [163] L. D. C. Jaubert and P. C. W. Holdsworth. Magnetic monopole dynamics in spin ice. *Journal of Physics: Condensed Matter*, 23(16):164222, 2011.
- [164] D. L. Bergman, G. A. Fiete, and L. Balents. Ordering in a frustrated pyrochlore antiferromagnet proximate to a spin liquid. *Phys. Rev. B*, 73:134402, 2006.
- [165] M. J. P. Gingras, B. C. den Hertog, M. Faucher, J. S. Gardner, S. R. Dunsiger, L. J. Chang, B. D. Gaulin, N. P. Raju, and J. E. Greedan. Thermodynamic and single-ion properties of Tb^{3+} within the collective paramagnetic-spin liquid state of the frustrated pyrochlore antiferromagnet $\text{Tb}_2\text{Ti}_2\text{O}_7$. *Phys. Rev. B*, 62:6496–6511, 2000.
- [166] G. Ehlers, A. L. Cornelius, T. Fennell, M. Koza, S. T. Bramwell, and J. S. Gardner. Evidence for two distinct spin relaxation mechanisms in ‘hot’ spin ice $\text{Ho}_2\text{Ti}_2\text{O}_7$. *Journal of Physics: Condensed Matter*, 16(11):S635, 2004.

-
- [167] L. D. C. Jaubert. *Topological constraints and defects in spin ice*. PhD thesis, Ecole normale supérieure de lyon, 2009.
- [168] J. Cumings. Frustrated magnets: Artificial ice goes thermal. *Nature Physics*, 7:7–8, 2011.
- [169] T. L. Malkin, B. J. Murray, A. V. Brukhno, J. Anwar, and C. G. Salzmann. Structure of ice crystallized from supercooled water. *Proceedings of the National Academy of Sciences*, 109(4):1041–1045, 2012.
- [170] B. J. Murray, D. A. Knopf, and A. K. Bertram. The formation of cubic ice under conditions relevant to earth’s atmosphere. *Nature*, 434(7030):202–205, 2005.
- [171] B. J. Murray and A. K. Bertram. Formation and stability of cubic ice in water droplets. *Physical Chemistry Chemical Physics*, 8(1):186–192, 2006.
- [172] E. Mayer and A. Hallbrucker. Cubic ice from liquid water. *Nature*, 325(6105):601–602, 1987.
- [173] L. Pauling. The structure and entropy of ice and of other crystals with some randomness of atomic arrangement. *Journal of the American Chemical Society*, 57(12):2680–2684, 1935.
- [174] W. F. Giauque and J. W. Stout. The Entropy of Water and the Third Law of Thermodynamics. The Heat Capacity of Ice from 15 to 273° K. *Journal of the American Chemical Society*, 58(7):1144–1150, 1936.
- [175] J. D. Bernal and R. H. Fowler. A theory of water and ionic solution, with particular reference to hydrogen and hydroxyl ions. *The Journal of Chemical Physics*, 1(8), 1933.
- [176] G. Möller and R. Moessner. Artificial square ice and related dipolar nanoarrays. *Phys. Rev. Lett.*, 96:237202, 2006.
- [177] G. W. Chern, C. Reichhardt, and C. Nisoli. Realizing three-dimensional artificial spin ice by stacking planar nano-arrays. *Applied Physics Letters*, 104(1):–, 2014.

-
- [178] R. G. Melko, B. C. den Hertog, and M. J. P. Gingras. Long-range order at low temperatures in dipolar spin ice. *Phys. Rev. Lett.*, 87:067203, 2001.
- [179] C. Wengel, C. L. Henley, and A. Zippelius. Spin-glass and antiferromagnet critical behavior in a diluted FCC antiferromagnet. *Phys. Rev. B*, 53:6543–6553, 1996.
- [180] J. S. Gardner, B. D. Gaulin, S.-H. Lee, C. Broholm, N. P. Raju, and J. E. Greedan. Glassy statics and dynamics in the chemically ordered pyrochlore antiferromagnet $\text{Y}_2\text{Mo}_2\text{O}_7$. *Phys. Rev. Lett.*, 83:211–214, 1999.
- [181] N. P. Raju, E. Gmelin, and R. K. Kremer. Magnetic-susceptibility and specific-heat studies of spin-glass-like ordering in the pyrochlore compounds $\text{R}_2\text{Mo}_2\text{O}_7$ ($\text{R} = \text{Y}, \text{Sm}, \text{or Gd}$). *Phys. Rev. B*, 46:5405–5411, 1992.
- [182] J. S. Gardner, B. D. Gaulin, A. J. Berlinsky, P. Waldron, S. R. Dunsiger, N. P. Raju, and J. E. Greedan. Neutron scattering studies of the cooperative paramagnet pyrochlore $\text{Tb}_2\text{Ti}_2\text{O}_7$. *Phys. Rev. B*, 64:224416, 2001.
- [183] I. Mirebeau, I. N. Goncharenko, P. Cadavez-Peres, S. T. Bramwell, M. J. P. Gingras, and J. S. Gardner. Pressure-induced crystallization of a spin liquid. *Nature*, (6911):5457, 2002.
- [184] B. C. den Hertog and M. J. P. Gingras. Dipolar interactions and origin of spin ice in ising pyrochlore magnets. *Phys. Rev. Lett.*, 84:3430–3433, 2000.
- [185] L. D. C. Jaubert and P. C. W. Holdsworth. Signature of magnetic monopole and dirac string dynamics in spin ice. *Nature Physics*, 5(4):258–261, 2009.
- [186] C. Castelnovo, R. Moessner, and S. L. Sondhi. Magnetic monopoles in spin ice. *Nature Letters*, 451(06433), 2008.
- [187] C. Castelnovo, R. Moessner, and S. L. Sondhi. Thermal quenches in spin ice. *Phys. Rev. Lett.*, 104:107201, 2010.

-
- [188] E. Mengotti, L. J. Heyderman, A. F. Rodriguez, F. Nolting, R. V. Huegli, and H. B. Braun. Real-space observation of emergent magnetic monopoles and associated Dirac strings in artificial kagome spin ice. *Nature Physics*, 7(1):68–74, 2011.
- [189] A. Rajantie. Introduction to magnetic monopoles. *Contemporary Physics*, 53(3):195–211, 2012.
- [190] L. A. S. Mól, W. A. Moura-Melo, and A. R. Pereira. Conditions for free magnetic monopoles in nanoscale square arrays of dipolar spin ice. *Phys. Rev. B*, 82(5), 2010.
- [191] L. A. Mól, R. L. Silva, R. C. Silva, A. R. Pereira, W. A. Moura-Melo, and B. V. Costa. Magnetic monopole and string excitations in two-dimensional spin ice. *Journal of Applied Physics*, 106(6):–, 2009.
- [192] P. A. M. Dirac. Quantised singularities in the electromagnetic field. *Proceedings of the Royal Society of London Series A- Containing papers of a Mathematical and Physical Character*, 133(821):60–72, 1931.
- [193] C. Moore, M. G. Nordahl, N. Minar, and C. R. Shalizi. Vortex dynamics and entropic forces in antiferromagnets and antiferromagnetic potts models. *Phys. Rev. E*, 60:5344–5351, 1999.
- [194] G. Möller and R. Moessner. Magnetic multipole analysis of kagome and artificial spin-ice dipolar arrays. *Phys. Rev. B*, 80:140409, 2009.
- [195] R. Wentzcovitch and L. Stixrude. Theoretical and computational methods in mineral physics:geophysical applications. *Reviews in Mineralogy and Geochemistry*, 71:129–130, 2010.
- [196] D. Ceperley, G. V. Chester, and M. H. Kalos. Monte Carlo simulation of a many-fermion study. *Phys. Rev. B*, 16:3081–3099, 1977.

-
- [197] N. Metropolis, A. W. Rosenbluth, M. N. Rosenbluth, A. H. Teller, and E. Teller. Equation of state calculations by fast computing machines. *The Journal of Chemical Physics*, 21(6):1087–1092, 1953.
- [198] P. P. Ewald. The calculation of optical and electrostatic grid potential. *Annalen Der Physik*, 64(3):253–287, 1921.
- [199] N. Prokof’ev and B. Svistunov. Worm algorithms for classical statistical models. *Phys. Rev. Lett.*, 87:160601, 2001.
- [200] M. J. P. Gingras and P. A. McClarty. Quantum spin ice: a search for gapless quantum spin liquids in pyrochlore magnets. *Reports on Progress in Physics*, 77(5):056501, 2014.
- [201] L. D. C. Jaubert, M. Haque, and R. Moessner. Analysis of a fully packed loop model arising in a magnetic coulomb phase. *Phys. Rev. Lett.*, 107:177202, 2011.
- [202] E. L. Pollock and D. M. Ceperley. Path-integral computation of superfluid densities. *Phys. Rev. B*, 36:8343–8352, 1987.
- [203] G. T. Barkema and M. E. J. Newman. Monte carlo simulation of ice models. *Phys. Rev. E*, 57:1155–1166, 1998.
- [204] Q. Liu, Y. Deng, T. M. Garoni, and H. W. J. Blöte. The loop model on a three-dimensional lattice. *Nuclear Physics B*, 859(2):107 – 128, 2012.
- [205] C. L. Henley. The “coulomb phase” in frustrated systems. *Annual Review of Condensed Matter Physics*, 1(1):179–210, 2010.
- [206] S. V. Isakov, K. Gregor, R. Moessner, and S. L. Sondhi. Dipolar spin correlations in classical pyrochlore magnets. *Phys. Rev. Lett.*, 93:167204, 2004.
- [207] A. Sen, R. Moessner, and S. L. Sondhi. Coulomb phase diagnostics as a function of temperature, interaction range, and disorder. *Phys. Rev. Lett.*, 110:107202, 2013.

-
- [208] L. Liang, R. Rinaldi, and H. Schober. *Neutron Applications in Earth, Energy and Environmental Sciences*. Neutron Scattering Applications and Techniques. Springer, pages 15–17, 2008.
- [209] T. Fennell, O. A. Petrenko, B. Fåk, S. T. Bramwell, M. Enjalran, T. Yavors’kii, M. J. P. Gingras, R. G. Melko, and G. Balakrishnan. Neutron scattering investigation of the spin ice state in $\text{Dy}_2\text{Ti}_2\text{O}_7$. *Phys. Rev. B*, 70:134408, 2004.
- [210] T. Brückel and Institut für Festkörperforschung (Jülich) Neutronenstreuung. *Neutron Scattering: Lectures of the JCNS Laboratory Course Held at Forschungszentrum Jülich and the Research Reactor FRM II of TU Munich*. Schriften des Forschungszentrums Jülich / Reihe Schlüsseltechnologien: Reihe Schlüsseltechnologien. Forschungszentrum, Zentralbibliothek, page 8.2, 2010.
- [211] T. Fennell, O. A. Petrenko, G. Balakrishnan, S. T. Bramwell, J. D. M. Champion, B. Fåk, M.J. Harris, and D. McK. Paul. Field-induced partial order in the spin ice Dysprosium Titanate. *Applied Physics A*, 74(1):s889–s891, 2002.
- [212] R. Moessner and J. T. Chalker. Low-temperature properties of classically frustrated antiferromagnets. *Phys. Rev. B*, 58:12049–12062, 1998.
- [213] M. E. Brooks-Bartlett, S. T. Banks, L. D. C. Jaubert, A. Harman-Clarke, and P. C. W. Holdsworth. Magnetic-Moment Fragmentation and Monopole Crystallization. *Phys. Rev. X*, 4:011007, 2014.
- [214] J. N. Reimers, J. E. Greedan, and M. Björgvinsson. Critical properties of highly frustrated pyrochlore antiferromagnets. *Phys. Rev. B*, 45:7295–7306, 1992.
- [215] A. B. Chen and A. Sher. *Semiconductor Alloys: Physics and Materials Engineering*. Language of Science. Plenum Press, page 2, 1995.
- [216] Wolfram Research Inc. Mathematica. Version 9.0, 2012.
- [217] D. Henderson, M. Holovko, and A. Trokhymchuk. *Ionic Soft Matter: Modern Trends in Theory and Applications*. NATO science series: Mathematics, physics, and chemistry. Springer, 2005.

-
- [218] K. Binder and D. Heermann. *Monte Carlo Simulation in Statistical Physics: An Introduction*. Graduate Texts in Physics. Springer-Verlag, pages 56–59, 2010.
- [219] L. D. C. Jaubert, M. J. Harris, T. Fennell, R. G. Melko, S. T. Bramwell, and P. C. W. Holdsworth. Topological-Sector Fluctuations and Curie-Law Crossover in Spin Ice. *Phys. Rev. X*, 3:011014, 2013.
- [220] I. A. Ryzhkin. Magnetic relaxation in rare-earth oxide pyrochlores. *Journal of Experimental and Theoretical Physics*, 101(3):481–486, 2005.
- [221] A. P. Sazonov, A. Gukasov, I. Mirebeau, and P. Bonville. Double-layered monopolar order in the $\text{Tb}_2\text{Ti}_2\text{O}_7$ spin liquid. *Phys. Rev. B*, 85:214420, 2012.
- [222] Z. Hiroi, K. Matsuhira, and M. Ogata. Ferromagnetic ising spin chains emerging from the spin ice under magnetic field. *Journal of the Physical Society of Japan*, 72(12):3045–3048, 2003.
- [223] R. Moessner and S. L. Sondhi. Theory of the [111] magnetization plateau in spin ice. *Phys. Rev. B*, 68:064411, 2003.
- [224] D. I. Khomskii. Electric dipoles on magnetic monopoles in spin ice. *Nature Communications*, 3, 2012.
- [225] A. A. Zvyagin. New physics in frustrated magnets: Spin ices, monopoles, etc. (review article). *Low Temperature Physics*, 39(11):901–922, 2013.
- [226] L. Savary and L. Balents. Coulombic quantum liquids in spin-1/2 pyrochlores. *Phys. Rev. Lett.*, 108:037202, 2012.
- [227] L. J. Chang, S. Onoda, Y. Su, Y. J. Kao, K. D. Tsuei, Y. Yasui, K. Kakurai, and M. R. Lees. Higgs transition from a magnetic coulomb liquid to a ferromagnet in $\text{Yb}_2\text{Ti}_2\text{O}_7$. *Nature Communications*, 3, 2012.
- [228] Lucile Savary and Leon Balents. Spin liquid regimes at nonzero temperature in quantum spin ice. *Phys. Rev. B*, 87:205130, 2013.

-
- [229] H. D. Zhou, S. T. Bramwell, J. G. Cheng, C. R. Wiebe, G. Li, L. Balicas, J. A. Bloxsom, H. J. Silverstein, J. S. Zhou, J. B. Goodenough, and J. S. Gardner. High pressure route to generate magnetic monopole dimers in spin ice. *Nature Communications*, 2, 2011.
- [230] O. Sikora, F. Pollmann, N. Shannon, K. Penc, and P. Fulde. Quantum liquid with deconfined fractional excitations in three dimensions. *Phys. Rev. Lett.*, 103:247001, 2009.
- [231] J. S. Gardner, S. R. Dunsiger, B. D. Gaulin, M. J. P. Gingras, J. E. Greedan, R. F. Kiefl, M. D. Lumsden, W. A. MacFarlane, N. P. Raju, J. E. Sonier, I. Swainson, and Z. Tun. Cooperative paramagnetism in the geometrically frustrated pyrochlore antiferromagnet $\text{Tb}_2\text{Ti}_2\text{O}_7$. *Phys. Rev. Lett.*, 82:1012–1015, 1999.
- [232] H. R. Molavian, M. J. P. Gingras, and B. Canals. Dynamically induced frustration as a route to a quantum spin ice state in $\text{Tb}_2\text{Ti}_2\text{O}_7$ via virtual crystal field excitations and quantum many-body effects. *Phys. Rev. Lett.*, 98:157204, 2007.
- [233] T. Fennell, M. Kenzelmann, B. Roessli, H. Mutka, J. Ollivier, M. Ruminy, U. Stuhr, O. Zaharko, L. Bovo, A. Cervellino, K. Haas, M. and J. Cava, R. Magnetoelastic excitations in the pyrochlore spin liquid $\text{Tb}_2\text{Ti}_2\text{O}_7$. *Phys. Rev. Lett.*, 112:017203, 2014.
- [234] J. S. Gardner, A. Keren, G. Ehlers, C. Stock, E. Segal, J. M. Roper, B. Fåk, M. B. Stone, P. R. Hammar, D. H. Reich, and B. D. Gaulin. Dynamic frustrated magnetism in $\text{Tb}_2\text{Ti}_2\text{O}_7$ at 50 mK. *Phys. Rev. B*, 68:180401, 2003.
- [235] T. Fennell, M. Kenzelmann, B. Roessli, M. K. Haas, and R. J. Cava. Power-law spin correlations in the pyrochlore antiferromagnet $\text{Tb}_2\text{Ti}_2\text{O}_7$. *Phys. Rev. Lett.*, 109:017201, 2012.
- [236] S. Petit, P. Bonville, J. Robert, C. Decorse, and I. Mirebeau. Spin liquid correlations, anisotropic exchange, and symmetry breaking in $\text{Tb}_2\text{Ti}_2\text{O}_7$. *Phys. Rev. B*, 86:174403, 2012.

-
- [237] Y. Yasui, M. Kanada, M. Ito, H. Harashina, M. Sato, H. Okumura, K. Kakurai, and H. Kadowaki. Static correlation and dynamical properties of Tb^{3+} -moments in $\text{Tb}_2\text{Ti}_2\text{O}_7$ neutron scattering study. *Journal of the Physical Society of Japan*, 71(2):599–606, 2002.
- [238] E. Lhotel, C. Paulsen, P. Dalmas de Réotier, A. Yaouanc, C. Marin, and S. Vanishri. Low-temperature magnetization in geometrically frustrated $\text{Tb}_2\text{Ti}_2\text{O}_7$. *Phys. Rev. B*, 86:020410, 2012.
- [239] M. L. Dahlberg, M. J. Matthews, P. Jiramongkolchai, R. J. Cava, and P. Schiffer. Low-temperature dynamic freezing and the fragility of ordering in $\text{Tb}_2\text{Sn}_2\text{O}_7$. *Phys. Rev. B*, 83:140410, 2011.
- [240] P. A. McClarty, P. Stasiak, and M. J. P. Gingras. Soft dipolar spin ice physics and the ordered phase of the frustrated $\text{Tb}_2\text{Sn}_2\text{O}_7$ pyrochlore magnet. *ArXiv e-prints*, 2010.
- [241] Z. L. Dun, E. S. Choi, H. D. Zhou, A. M. Hallas, H. J. Silverstein, Y. Qiu, J. R. D. Copley, J. S. Gardner, and C. R. Wiebe. $\text{Yb}_2\text{Sn}_2\text{O}_7$: A magnetic coulomb liquid at a quantum critical point. *Phys. Rev. B*, 87:134408, 2013.
- [242] R. M. D’Ortenzio, H. A. Dabkowska, S. R. Dunsiger, B. D. Gaulin, M. J. P. Gingras, T. Goko, J. B. Kycia, L. Liu, T. Medina, T. J. Munsie, D. Pomaranski, K. A. Ross, Y. J. Uemura, T. J. Williams, and G. M. Luke. Unconventional magnetic ground state in $\text{Yb}_2\text{Ti}_2\text{O}_7$. *Phys. Rev. B*, 88:134428, 2013.
- [243] J. A. Hodges, P. Bonville, A. Forget, A. Yaouanc, P. Dalmas de Réotier, G. André, M. Rams, K. Królas, C. Ritter, P. C. M. Gubbens, C. T. Kaiser, P. J. C. King, and C. Baines. First-order transition in the spin dynamics of geometrically frustrated $\text{Yb}_2\text{Ti}_2\text{O}_7$. *Phys. Rev. Lett.*, 88:077204, 2002.
- [244] J. S. Gardner, G. Ehlers, N. Rosov, R. W. Erwin, and C. Petrovic. Spin-spin correlations in $\text{Yb}_2\text{Ti}_2\text{O}_7$: A polarized neutron scattering study. *Phys. Rev. B*, 70:180404, 2004.

-
- [245] K. A. Ross, L. R. Yaraskavitch, M. Laver, J. S. Gardner, J. A. Quilliam, S. Meng, J. B. Kycia, D. K. Singh, Th. Proffen, H. A. Dabkowska, and B. D. Gaulin. Dimensional evolution of spin correlations in the magnetic pyrochlore $\text{Yb}_2\text{Ti}_2\text{O}_7$. *Phys. Rev. B*, 84:174442, 2011.
- [246] J. Lago, I. Živković, J. O. Piatek, P. Álvarez, D. Hüvonen, F. L. Pratt, M. Díaz, and T. Rojo. Glassy dynamics in the low-temperature inhomogeneous ferromagnetic phase of the quantum spin ice $\text{Yb}_2\text{Sn}_2\text{O}_7$. *Phys. Rev. B*, 89:024421, 2014.
- [247] S. Ninet, F. Datchi, P. Dumas, M. Mezouar, G. Garbarino, A. Mafety, C. J. Pickard, R. J. Needs, and A. M. Saitta. Experimental and theoretical evidence for an ionic crystal of ammonia at high pressure. *Phys. Rev. B*, 89:174103, 2014.
- [248] W. Zhang, A. R. Oganov, A. F. Goncharov, Q. Zhu, S. E. Boulfelfel, A. O. Lyakhov, E. Stavrou, M. Somayazulu, V. B. Prakapenka, and Z. Konôpková. Unexpected stable stoichiometries of sodium chlorides. *Science*, 342(6165):1502–1505, 2013.
- [249] A. D. Fortes, J. P. Brodholt, I. G. Wood, and L. Vočadlo. Hydrogen bonding in solid ammonia from ab initio calculations. *The Journal of chemical physics*, 118(13):5987–5994, 2003.
- [250] S. Ninet, F. Datchi, and A. M. Saitta. Proton disorder and superionicity in hot dense ammonia ice. *Phys. Rev. Lett.*, 108:165702, 2012.
- [251] C. J. Pickard and R. J. Needs. Highly compressed ammonia forms an ionic crystal. *Nature Materials*, 7(10):775–779, 2008.
- [252] S. Zhang, I. Gilbert, C. Nisoli, G. W. Chern, M. J. Erickson, L. O’Brien, C. Leighton, P. E. Lammert, V. H. Crespi, and P. Schiffer. Crystallites of magnetic charges in artificial spin ice. *Nature*, 500(7464):553–557, 2013.
- [253] G. W. Chern and O. Tchernyshyov. Magnetic charge and ordering in kagome spin ice. *Philosophical Transactions of the Royal Society A: Mathematical, Physical and Engineering Sciences*, 370(1981):5718–5737, 2012.

-
- [254] F. Montaigne, D. Lacour, I. A. Chioar, N. Rougemaille, D. Louis, S. Mc Murtry, H. Riahi, B. Santos Burgos, T. O. Montes, A. Locatelli, B. Canals, and M. Hehn. Size distribution of magnetic charge domains in thermally activated but out-of-equilibrium artificial spin ice. *Scientific Reports*, 4, 2014.
- [255] G. W. Chern, P. Mellado, and O. Tchernyshyov. Two-stage ordering of spins in dipolar spin ice on the kagome lattice. *Phys. Rev. Lett.*, 106:207202, 2011.
- [256] A. J. Macdonald, P. C. W. Holdsworth, and R. G. Melko. Classical topological order in kagome ice. *Journal of Physics: Condensed Matter*, 23(16):164208, 2011.
- [257] M. Udagawa, M. Ogata, and Z. Hiroi. Exact result of ground-state entropy for ising pyrochlore magnets under a magnetic field along [111] axis. *Journal of the Physical Society of Japan*, 71(10):2365–2368, 2002.
- [258] D. A. King and D. P. Woodruff. *Growth and Properties of Ultrathin Epitaxial Layers*. The Chemical Physics of Solid Surfaces. Elsevier Science, page 587, 1997.
- [259] F. Thorpe and L. Tichý. *Properties and Applications of Amorphous Materials*. NATO science series: Mathematics, physics, and chemistry. pages 1–3.
- [260] W. Zhang, I. Ronneberger, Y. Li, and R. Mazzarello. Magnetic properties of crystalline and amorphous phase-change materials doped with 3d impurities. *Advanced Materials*, 24(32):4387–4391, 2012.
- [261] T. C. Hufnagel and F. Hellman. Structural and magnetic length scales in amorphous TbFe₂. *Journal of Magnetism and Magnetic Materials*, 256(13):322 – 327, 2003.
- [262] W. P. O’Leary. Partial structure factors and pair correlation functions for an amorphous magnetic alloy. *Journal of Physics F: Metal Physics*, 5(11):L175, 1975.
- [263] A. Garcia-Arribas, M. L. Fdez-Gubieda, I. Orúe, J. M. Barandiarán, J. Herreros, and F. Plazaola. Correlation between structure and magnetic behavior of Fe-P amorphous alloys. *Phys. Rev. B*, 52:12805–12812, 1995.

-
- [264] Y.Q. Cheng and E. Ma. Atomic-level structure and structure-property relationship in metallic glasses. *Progress in Materials Science*, 56(4):379 – 473, 2011.
- [265] H. Geisler, U. Herr, T. Lorenz, and K. Samwer. Thickness- and concentration-dependent crystal-to-amorphous transition of $\text{Fe}_{100-x}\text{Zr}_x$ in $\text{Zr}/\text{Fe}_{100-x}\text{Zr}_x/\text{Zr}$ trilayers. *Thin Solid Films*, 275(12):176 – 179, 1996.
- [266] S. G. Mayr and K. Samwer. Surface morphology, stress, and volume change during growth and crystallization of interface-stabilized amorphous $\text{Fe}_{100-x}\text{Zr}_x$ films. *Phys. Rev. B*, 65:115408, 2002.
- [267] Y. Shimada and H. Kojima. Sputtering of amorphous CoZr and CoHf films with soft magnetic properties. *Journal of Applied Physics*, 53(4), 1982.
- [268] A. Tago, C. Nishimura, and K. Yanagisawa. Magnetic properties of ion beam sputtered Co-Zr and Co-Zr-RE amorphous films. *Magnetics, IEEE Transactions on*, 21(5):2032–2034, 1985.
- [269] P. Hansen, C. Clausen, G. Much, M. Rosenkranz, and K. Witter. Magnetic and magneto-optical properties of rare-earth transition metal alloys containing Gd, Tb, Fe, Co. *Journal of Applied Physics*, 66(2):756–767, 1989.
- [270] S. Honda and M. Nawate. Magnetization characteristics and Curie temperature of Y/Fe and Tb/Fe multilayers. *Journal of Magnetism and Magnetic Materials*, 136(12):163 – 175, 1994.
- [271] J. H. Park and B. I. Min. Electronic structures and noncollinear magnetic properties of structurally disordered Fe. *Journal of Magnetism*, 15(1):1–6, 2010.
- [272] H. J. H. Brouwers. Packing of crystalline structures of binary hard spheres: An analytical approach and application to amorphization. *Phys. Rev. E*, 76:041304, 2007.
- [273] H. Li and B. P. Tonner. Direct experimental identification of the structure of ultrathin films of BCC iron and metastable BCC and FCC cobalt. *Phys. Rev. B*, 40:10241–10248, 1989.

-
- [274] S. Minakawa, D. Suzuki, M. Ohtake, N. Inaba, and M. Futamoto. Co thin film with metastable BCC structure formed on GaAs(111) substrate. In *EPJ Web of Conferences*, volume 75, page 01004. EDP Sciences, 2014.
- [275] E. Luijten and H. W. J. Blöte. Monte carlo method for spin models with long-range interactions. *International Journal of Modern Physics C*, 06(03):359–370, 1995.
- [276] M. E. Fisher, S. K. Ma, and B. G. Nickel. Critical exponents for long-range interactions. *Phys. Rev. Lett.*, 29:917–920, 1972.
- [277] E. Korutcheva and N. Tonchev. Finite-size effects in a field-theoretic model with long-range exchange interaction. *Journal of Statistical Physics*, 62(3-4):553–562, 1991.
- [278] P. A. Morais, J. S. Andrade, E. M. Nascimento, and M. L. Lyra. Geometrical and anderson transitions in harmonic chains with constrained long-range couplings. *Phys. Rev. E*, 84:041110, 2011.
- [279] M. E. Fisher and V. Privman. First-order transitions in spherical models: Finite-size scaling. *Communications in Mathematical Physics*, 103(4):527–548, 1986.
- [280] M. Aizenman and R. Fernandez. Critical exponents for long-range interactions. *Letters in Mathematical Physics*, 16(1):39–49, 1988.
- [281] T. Blanchard, M. Picco, and M. A. Rajabpour. Influence of long-range interactions on the critical behavior of the Ising model. *EPL*, 101(5):56003, 2013.
- [282] B. P. Lee and J. L. Cardy. Phase ordering in one-dimensional systems with long-range interactions. *Phys. Rev. E*, 48:5–11, 16–22, 72–75, 2452–2465, 1993.
- [283] H. Hayakawa, Z. Rácz, and T. Tsuzuki. Ordering kinetics in systems with long-range interactions. *Phys. Rev. E*, 47:1499–1505, 1993.

-
- [284] F. Borgonovi and G. L. Celardo. Enhancement of the magnetic anisotropy barrier in critical long range spin systems. *Journal of Physics: Condensed Matter*, 25(10):106006, 2013.
- [285] Z. Glumac and K. Uzelac. Finite-range scaling study of the $1d$ long-range Ising model. *Journal of Physics A: Mathematical and General*, 22(20):4439, 1989.
- [286] J. K. Bhattacharjee, J. L. Cardy, and D. J. Scalapino. $O(n)$ heisenberg model with long-range interactions. *Phys. Rev. B*, 25:1681–1687, 1982.
- [287] M. Perez, C. H. Marrows, and B. J. Hickey. Influence of δ -layers on indirect exchange coupling in giant magnetoresistance multilayers. *Europhysics Letters*, 54(2):262, 2001.
- [288] M. Pärnaste, M. Marcellini, E. Holmström, N. Bock, J. Fransson, O. Eriksson, and B. Hjörvarsson. Dimensionality crossover in the induced magnetization of Pd layers. *Journal of Physics: Condensed Matter*, 19(24):246213, 2007.
- [289] C. Kawabata and A. R. Bishop. A Monte Carlo study of the two-dimensional Heisenberg model with easy-plane symmetry. *Solid State Communications*, 60(2):169 – 171, 1986.
- [290] M. Kim, D. Jeong, H. W. Kwon, and M. Y. Choi. Information exchange dynamics of the two-dimensional xy model. *Phys. Rev. E*, 88:052134, 2013.
- [291] E. Luijten, H. W. J. Blöte, and K. Binder. Medium-range interactions and crossover to classical critical behavior. *Phys. Rev. E*, 54:4626–4636, 1996.
- [292] E. Luijten and H. W. J. Blöte. Classical critical behavior of spin models with long-range interactions. *Phys. Rev. B*, 56:8945–8958, 1997.
- [293] V. L. Pokrovskii and G. V. Uimin. Magnetic properties of plane and layer systems. *Soviet Journal of Experimental and Theoretical Physics*, 38:847, 1974.
- [294] M. Ahlberg and B. Hjörvarsson. private communication, 2012.

-
- [295] R. B. Griffiths. Dependence of critical indices on a parameter. *Phys. Rev. Lett.*, 24:1479–1482, 1970.
- [296] F. Maccherozzi, M. Sperl, G. Panaccione, J. Minár, S. Polesya, H. Ebert, U. Wurstbauer, M. Hochstrasser, G. Rossi, G. Woltersdorf, W. Wegscheider, and C. H. Back. Evidence for a magnetic proximity effect up to room temperature at Fe/(Ga,Mn)As interfaces. *Phys. Rev. Lett.*, 101:267201, 2008.
- [297] M. A. Moskalenko, V. M. Uzdin, and H. Zabel. Manipulation by exchange coupling in layered magnetic structures. *Journal of Applied Physics*, 115(5):–, 2014.
- [298] F. Magnus, M. E. Brooks-Bartlett, Moubah R., Andersson G. Procter, R. A., T. Hase, S. T. Banks, and B. Hjörvarsson. Long-range magnetic interactions and proximity effects in an amorphous exchange-spring magnet (unpublished). 2015.
- [299] T. Klein, R. Röhlberger, O. Crisan, K. Schlage, and E. Burkel. Magnetic structure and interlayer exchange coupling in spring magnets studied via nuclear resonant scattering. *Thin Solid Films*, 515(4):2531 – 2534, 2006.
- [300] I. P. Krug. *Magnetic Proximity Effects in Highly-ordered Transition Metal Oxide Heterosystems - a Study by Soft-x-ray Photoemission Microscopy*. Schriften des Forschungszentrums Jülich / Reihe Information: Reihe Information. Forschungszentrum, Zentralbibliothek, pages 48–52, 2008.
- [301] F. Magnus. private communication- poster. 2014.
- [302] V. R. Reddy, O. Crisan, A. Gupta, A. Banerjee, and V. Kuncser. Tuning exchange spring effects in FePt/Fe(Co) magnetic bilayers. *Thin Solid Films*, 520(6):2184 – 2189, 2012.
- [303] D. Suess, T. Schrefl, R. Dittrich, M. Kirschner, F. Dorfbauer, G. Hrkac, and J. Fidler. Exchange spring recording media for areal densities up to 10 Tbit/in². *Journal of Magnetism and Magnetic Materials*, 290291, Part 1(0):551 – 554, 2005. Proceedings of the Joint European Magnetic Symposia (JEMS' 04) .

-
- [304] R. H. Victora and X. Shen. Composite media for perpendicular magnetic recording. *Magnetics, IEEE Transactions on*, 41(2):537–542, 2005.
- [305] B. Lengsfeld, T. Olson, J. Park, and A.F. Torabi. A general energy barrier model for switching of exchange spring media in an external field. *Magnetics, IEEE Transactions on*, 50(3):56–61, 2014.
- [306] J. Ph. Jay, F. Petit, J. Ben Youssef, M. V. Indenbom, A. Thiaville, and J. Militat. Magnetostrictive hysteresis of TbCoCoFe multilayers and magnetic domains. *Journal of Applied Physics*, 99(9):–, 2006.
- [307] S. Demirtas, M. R. Hossu, M. Arikan, A. R. Koymen, and M. B. Salamon. Tunable negative and positive coercivity for SmCo(CoGd) exchange springs investigated with SQUID magnetometry. *Phys. Rev. B*, 76:214430, 2007.
- [308] E. E. Fullerton, J. S. Jiang, M. Grimsditch, C. H. Sowers, and S. D. Bader. Exchange-spring behavior in epitaxial hard/soft magnetic bilayers. *Phys. Rev. B*, 58:12193–12200, 1998.
- [309] M. J. Pechan, N. Teng, J. D. Stewart, J. Z. Hilt, E. E. Fullerton, J. S. Jiang, C. H. Sowers, and S. D. Bader. Anisotropy determination in epitaxial SmCo/Fe exchange springs. *Journal of Applied Physics*, 87(9):6686–6688, 2000.
- [310] L. S. Huang, J. F. Hu, and J. S. Chen. Critical Fe thickness for effective coercivity reduction in FePt/Fe exchange-coupled bilayer. *Journal of Magnetism and Magnetic Materials*, 324(6):1242 – 1247, 2012.
- [311] R. Pellicelli, C. Pernechele, M. Solzi, M. Ghidini, F. Casoli, and F. Albertini. Modeling and characterization of irreversible switching and viscosity phenomena in perpendicular exchange-spring Fe-FePt bilayers. *Phys. Rev. B*, 78:184434, 2008.
- [312] A. Bill and H. B. Braun. Magnetic properties of exchange springs. *Journal of Magnetism and Magnetic Materials*, 272276, Part 2(0):1266 – 1267, 2004. Proceedings of the International Conference on Magnetism (ICM 2003).

-
- [313] M. Amato, M. G. Pini, and A. Rettori. Optimization study of the nanostructure of hard/soft magnetic multilayers. *Phys. Rev. B*, 60:3414–3420, 1999.
- [314] Z. Wang, X. Ma, H. Huang, H. Xiao, and T. Li. Micromagnetic simulation of domain walls in exchange spring trilayers. *Advances in Condensed Matter Physics*, 2014.
- [315] P. Saravanan, J. H. Hsu, Reddy G. L. N., S. Kumar, and S. V. Kamat. Annealing induced compositional changes in $\text{SmCo}_5/\text{Fe}/\text{SmCo}_5$ exchange spring trilayers and its impact on magnetic properties. *Journal of Alloys and Compounds*, 574:191 – 195, 2013.
- [316] D. Suess. Multilayer exchange spring media for magnetic recording. *Applied Physics Letters*, 89(11), 2006.
- [317] A. Gayen, B. Biswas, A. K. Singh, P. Saravanan, and A. Perumal. High temperature magnetic properties of indirect exchange spring $\text{FePt}/\text{M}(\text{Cu}, \text{C})/\text{Fe}$ trilayer thin films. *Journal of Nanomaterials*, 2013.
- [318] T. J. Zhou, K. Cher, J. F. Hu, Z. M. Yuan, and B. Liu. The concept and fabrication of exchange switchable trilayer of $\text{FePt}/\text{FeRh}/\text{FeCo}$ with reduced switching field. *Journal of Applied Physics*, 111(7), 2012.
- [319] G. Gubbiotti, G. Carlotti, J. Weston, G. Zangari, D. C. Crew, and R. L. Stamps. Asymmetry in the static and dynamic magnetic properties of a weak exchange spring trilayer. *Journal of Magnetism and Magnetic Materials*, 286(0):479 – 483, 2005. Proceedings of the 5th International Symposium on Metallic Multilayers.
- [320] M. Amato, A. Rettori, and M. G. Pini. Exchange-spring behavior of hard/soft magnetic multilayers: optimization study of the nanostructure. *Physica B: Condensed Matter*, 275(13):120 – 123, 2000.
- [321] A. P. Malozemoff, A. R. Williams, K. Terakura, V. L. Moruzzi, and K. Fukamichi. Magnetism of amorphous metal-metal alloys. *Journal of Magnetism and Magnetic Materials*, 35(13):192 – 198, 1983.

-
- [322] R. Ristić and E. Babić. Thermodynamic properties and atomic structure of amorphous zirconium. *Materials Science and Engineering: A*, 449451(0):569 – 572, 2007. Proceedings of the 12th International Conference on Rapidly Quenched; Metastable Materials.
- [323] S. Krongelb and Electrochemical Society. *Magnetic Materials, Processes, and Devices VI: Applications to Storage and Microelectromechanical Systems (MEMS) : Proceedings of the International Symposium*. Proceedings (Electrochemical Society). Electrochemical Society, pages 150–152, 2001.
- [324] L. Saharan, C. Morrison, J. J. Miles, T. Thomson, T. Schrefl, and G. Hrkac. Modelling interfacial coupling in thin film magnetic exchange springs at finite temperature. *Journal of Applied Physics*, 114(15):–, 2013.
- [325] A. Samoson, T. Tuherm, and Z. Gan. High-field high-speed MAS resolution enhancement in ¹H NMR spectroscopy of solids. *Solid State Nuclear Magnetic Resonance*, 20(34):130–136, 2001.
- [326] G. N. Kakazei, N. M. Santos, C. Quiros, M. Velez, J. I. Martin, J. M. Alameda, V. O. Golub, O. Y. Saliuk, Yu. G. Pogorelov, J. B. Sousa, M. C. Carmo, and N. A. Sobolev. Magnetic properties of amorphous Co_{0.74}Si_{0.26}/Si multilayers with different numbers of periods. *Low Temperature Physics*, 36(8), 2010.
- [327] P. C. Guruciaga, S. A. Grigera, and R. A. Borzi. Monopole ordered phases in dipolar and nearest-neighbors ising pyrochlore: From spin ice to the all-in–all-out antiferromagnet. *Phys. Rev. B*, 90:184423, 2014.
- [328] R. A. Borzi, D. Slobinsky, and S. A. Grigera. Charge ordering in a pure spin model: Dipolar spin ice. *Phys. Rev. Lett.*, 111:147204, 2013.
- [329] I. A. Chioar, B. Canals, D. Lacour, M. Hehn, B. Santos Burgos, T. O. Mentes, A. Locatelli, F. Montaigne, and N. Rougemaille. Kinetic pathways to the magnetic charge crystal in artificial dipolar spin ice. *Phys. Rev. B*, 90:220407, 2014.

- [330] A. Furrer. *Magnetic Neutron Scattering*. World Scientific Publishing Co Pte Ltd, pages 3–4, 1995.
- [331] J. P. Glusker and K. N. Trueblood. *Crystal Structure Analysis: A Primer*. IUCr texts on crystallography. OUP Oxford, 2010.